Large Eddy Simulation of Supersonic Twin-Jet Impingement Using a Fifth-Order WENO Scheme

by

Hoong Thiam Toh

Dissertation submitted to the Faculty of Virginia Polytechnic Institute and State University
in partial fulfillment of the requirements for the degree of

Doctor of Philosophy
in
Engineering Mechanics

Dr. Saad A. Ragab, Chairman
Dr. Slimane Adjerid
Dr. Muhammad R. Hajj
Dr. Scott L. Hendricks
Dr. Demetri P. Telionis
Dr. Surot Thangjitham

September 5, 2003
Blacksburg, Virginia

Keywords: LES, Twin-Jet Impingement, WENO

Large Eddy Simulation of Supersonic Twin-Jet Impingement Using a Fifth-Order WENO Scheme

Hoong Thiam Toh

ABSTRACT

A three-dimensional flow field produced by supersonic twin-jet impingement is studied using a large eddy simulation (LES). The numerical model consists of two parallel axisymmetric jets of diameter D^*, $3D^*$ apart, issuing from a plane which is at a distance $H^* = 4D^*$ above the ground. The jet diameter D^*, mean velocity W_o^*, mean density ρ_o^* and mean temperature T_o^* at the jet center in the exit plane are used as reference values. The Mach number and Reynolds number of the jets are $M = 1.5$ and $Re = 5.5 \times 10^5$, respectively. This model is closely related to the experimental setup of Elavarasan *et al.* [23].

The three-dimensional time-dependent compressible Navier-Stokes equations are solved using the method of lines. The convective terms are discretized using a fifth-order WENO scheme, whereas the viscous terms are discretized using a fourth-order central-differencing scheme. A low-storage five-stage fourth-order Runge-Kutta scheme is used to advance the solution in time. Code verification is achieved by comparison with flat-plate boundary-layer linear stability analysis, and computational data by Bendiks *et al.* [5] for a compressible turbulent round jet.

Instantaneous flow, mean flow and Reynolds stresses for the twin-jet impingement are presented and discussed. The results reveal the existence of flapping behavior in the fountain. The flapping fountain is the vortical structure formed by the alternating merging of a primary vortex tube with a secondary vortex tube induced by the neighboring primary vortex tube. The nondimensional period of flapping is found to be $7D^*/W_o^*$. High unsteadiness and strong interaction between the fountain and the jets are also observed. Due to the high diffusion and spreading rate of the fountain, the interaction between the fountain and the jets is only significant up to a height which is less than $3D^*$. It is found that the mean peak velocity in the fountain is $0.40406W_o^*$ and it occurs at $0.536607D^*$ from the ground.

The suitability of the fifth-order WENO scheme to simulate turbulent flow field with embedded shocks is also demonstrated by its capability to capture unsteady shock waves in the impingement regions.

Dedication

I would like to dedicate this dissertation to my parents for their understanding and sacrifices to our family during my stay in the United States.

Acknowledgments

First of all, I would like to thank my advisor, Dr Saad A. Ragab, to whom I owe a big debt of gratitude. This dissertation would not have been completed without his guidance, help and patience.

Thanks are also due to Dr. Slimane Adjerid, Dr. William Greenberg, Dr. Muhammad R. Hajj, Dr. Scott L. Hendricks, Dr. Demetri P. Telionis, and Dr. Surot Thangjitham for their service on my committee.

I would also like to express my gratitude to the Department of Engineering Science and Mechanics for providing me financial support through Graduate Teaching Assistantship during my studies in the department.

Last but not least, I would like to thank Mr. Yasser El-Okda and, once again, Dr Saad A. Ragab for their help in creating the animation for the present project.

Contents

List of Figures

List of Tables

Chapter 1

INTRODUCTION

1.1 Background

While hovering in close proximity to the ground, a V/STOL (Vertical/Short Take-off and Landing) aircraft powered by twin lift jets produces a complex three-dimensional flow field as shown in Figure 1.1.

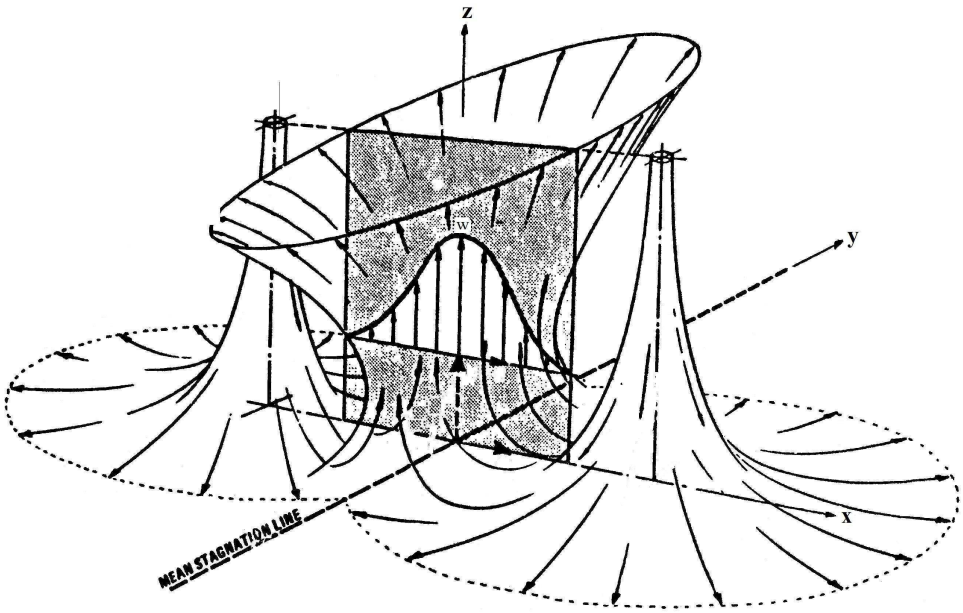

Figure 1.1: Three dimensional flow field produced by a V/STOL aircraft in hovering mode (taken from [25]).

This flow field involves strong interactions between the vehicle surface, the lift jets and the ground. The characteristic features of the flow field are shown schematically in Figure 1.2.

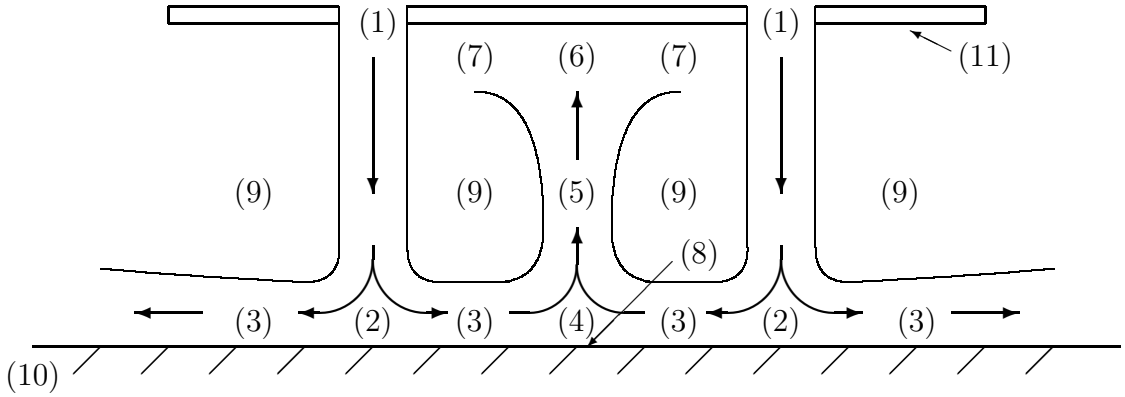

(1) Lift jet
(2) Jet impingement region
(3) Lower wall jet
(4) Fountain formation region
(5) Fountain upwash region
(6) Fountain impingement region
(7) Upper wall jet
(8) Stagnation line region
(9) Entrainment region
(10) Ground plane
(11) Aircraft undersurface

Figure 1.2: Flow structure of twin impinging jets

On impinging the ground, each of the impinging jets (lift jets) spreads radially outward from the impinging point along the ground surface in the form of a wall jet (which is a wall-bounded shear layer). As the lift jets expand, they entrain the surrounding air, causing a reduction in the pressure on the lower surface of the aircraft. The lowering of pressure creates a force opposite to the jet thrust and causes the aircraft to experience a suckdown force and hence a loss in lift. The loss of lift is further increased by the entrainment action of the wall jets flowing outward from the impinging point.

The opposite wall jets in the middle then collide with each other to form a fountain upwash flow. The fan-shaped fountain spreads radially outward in all directions with increasing width away from the ground [37, 64]. The fountain upwash flow when impinges on the aircraft may contribute to its lift. However, the fountain flow may also cause a reduction in the pressure between the jets and the fountain. In addition, the impinging fluid may flow along the fuselage and eventually make its way into the engine inlets. As the temperature of the fountain flow is much hotter than the ambient air, it raises fuselage skin temperature and its ingestion by the engine can reduce the power and cause thermal stresses in the engine components [37, 51, 80, 78, 65].

These problems become severer as the speed of jets increases and can be detrimental to

the performance and safety during the aircraft's vertical operations. Therefore, a proper understanding and prediction of this flow field is of great importance to the design of V/STOL aircraft powered by supersonic lift jets (e.g. the Joint Strike Fighter).

The overall flow field of the jet impingement problem is three-dimensional and involves unsteady strong turbulence. The experimental study of this flow field is very difficult and may be unreliable since the measurement of fluctuating velocities and pressure in the rather violent collision region is very difficult. In particular, the mechanism which lead to the high spreading rate of upwash flow is poorly understood.

As experimental study is difficult and expensive, numerical simulation is therefore an indispensable tool in studying and predicting the flow field of twin-jet impingement.

1.2 Numerical Simulation of Turbulent Flows

In order to capture the complete physical phenomena of the a turbulent flow, numerical simulation must be based on the Navier-Stokes equations, which take into account the effects of convective and viscous mechanisms as well as thermal effects [62]. There are three approaches to numerical simulation of turbulent flows, namely, Direct Numerical Simulation (DNS), solution of Reynolds Averaged Navier-Stokes equations (RANS), and Large Eddy Simulation (LES) [58].

In the DNS approach, all the temporal and spatial scales (from the large energetic scales to the small dissipative scales) of motion are calculated explicitly by solving the full unsteady Navier-Stokes equations without using any model. In a turbulent flow, the ratio of the largest to the smallest scales is of the order of $Re^{\frac{3}{4}}$, where the Reynolds number, Re, is defined by $v\ell/\nu$. Here ℓ is the characteristics length associated with the large energetic eddies of turbulence, v is the characteristic fluctuating velocity, and ν is the kinematic molecular viscosity. In order to resolve all of the scales of motion in a three-dimensional flow field, a refined mesh with the number of grid points of the order of $Re^{\frac{9}{4}}$ is thus required [41]. Due to the limited capacity of the computers available today, it is impossible to resolve all the scales of motion for a flow with high Reynolds number.

The RANS approach is a fully statistical method. In this approach, flow variables are decomposed into time mean and fluctuating components. The Reynolds averaged quantities are computed by time-averaging the Navier-Stokes equations, whereas all the high-order statistical moments of the variables (the turbulence scales) are modeled. Since all large and small scales of turbulence are modeled, the mesh of the resolution as needed by DNS are not required. However, this approach is well adapted only for predictive studies of the mean quantities [62].

The LES is a compromise between the DNS and the RANS approaches. In this approach, large-scale eddies are computed whereas small scales are modeled. Since the small-scale

eddies have an isotropic and homogeneous structure, simpler and more universal subgrid scale models than the models required for RANS can be used. As the large-scale turbulence is to be computed, the resolution requirement for the mesh are much more than in RANS, but not as demanding as in DNS because the small scales are modeled.

Due to the limitations of the DNS and RANS approaches described above, the LES approach is used in the present study for the simulation of supersonic twin-jet impingement at high Reynolds number.

1.3 Literature Review of Twin-Jet Impingement Flow

The flow field of twin-jet impingement is different from that of single-jet impingement. Also, the structures of two-dimensional and three-dimensional flow fields are not the same. Therefore only research papers on three-dimensional twin-jet impingement will be reviewed as this is the focus of the present research. A review of research papers on single-jet impingement for both three-dimensional and two-dimensional cases can be found in Chuang *et al.* [18] and Behrouzi [4].

1.3.1 Experimental Studies of Twin-Jet Impingement

Due to the limitation of computing capabilities, the majority of the research work in the investigation of the flow field produced by twin impinging jets has been experimental. Much efforts have been conducted to gain understanding of the development and structure of the upwash fountain and to determine the parameters that influence these characteristics by using a simple two-dimensional flow configuration.

Gilbert [31] conducted an experimental study of a two-dimensional upwash formed by the collision of two opposed two-dimensional wall jets. The measurements indicate the presence of symmetry in the upwash turbulence energy profiles and high upwash spreading rate. The turbulence level and mixing layer growth of the upwash are larger than those found in a free two-dimensional jet.

Elbana and Sabbagh [24] carried out an experimental study of the impingement of two two-dimensional jets against a normal ground plane. Their hot-wire measurements showed that the rate of jet decay in a twin-jet impingement flow is greater than that for a single jet impingement flow and for a free jet.

Saripalli [63] conducted a visualization experiment using water as the working medium for twin jets without a blocking plate. Bower *et al.* conducted a visualization experiment using water as the working medium [6] for twin jets with a blocking plate. They successfully described the features of the three-dimensional flow field and their response to parametric changes in the variables that characterize the configurations.

The first data on turbulence and near ground mean velocity measurements in the three-dimensional fountain flow was reported by Saripalli [64]. With water as the working medium, Saripalli used a two-component LDV (Laser Doppler velocimeter) to measure the instantaneous velocities in the plane of symmetry connecting the nozzle centerlines. The distribution of mean velocity components and various turbulence quantities, including the turbulence intensity and the Reynolds shear stress was derived from the basic instantaneous velocity data. The "twin-jet fountain" configuration consisted of two round jets of diameter D^* spaced at $9D^*$ and impinging on a base plate $3D^*$ below the plane of jet exits in a water tank. The Reynolds number of the jet is 1.70×10^5, taken $1.5mm$ below the nozzle exit. The findings of Saripalli's study are:

(1) The distributions of mean velocity and turbulence quantities across the fountain show self-similarity when nondimensionalized with proper parameters.

(2) The growth of the fountain was linear.

(3) The fountain flow is highly turbulent($\approx 50\%$ turbulent intensity)

The experimental investigation of three-dimensional flow field generated by two axisymmetric supersonic impinging jets has been carried out recently by Elavarasan and *et al.* [23] using PIV (Particle Image Velocimetry). Denote the nozzle exit diameter by D^* and the height of the nozzle exit from the ground by H, the main findings from their experimental study can be summarized as follows:

(1) The fountain upwash induced by the interaction of the two jets has significance only when the distance between the lift and ground plane is small. The fountain upwash reduces the lift loss significantly (nearly 100%) when $H^*/D^* < 3$.

(2) The average peak velocity in the fountain flow is 0.4261 and it occurs at $H^*/D^* \approx 0.7692$ from the ground plane.

(3) In the region $H^*/D^* > 4$, the flow is highly unsteady and consists of large-scale vortical structures.

(4) The maximum effect of the fountain flow occurs along the perpendicular direction to the plane containing the two main jets.

(5) The large scale structures in the free and wall bounded shear layers increase the entrainment of the ambient flow resulting in higher suction pressure on the lift plate.

1.3.2 Analytical Studies of Twin-Jet Impingement

As the flow field resulting from the impingement of twin jets is highly three-dimensional and turbulent, an analytical solution of this flow field cannot be obtained. Therefore, theoretical

analysis of this flow field requires some assumptions to be made on the flow field. By assuming that the flow field was two-dimensional, incompressible, inviscid and isothermal, Siegel and Marvin [71, 72] obtained the first analytical solution of the flow field using the method of comformal mapping. Their analytical solution was later extended by Houlihan and Thompson [33] to include tilted jet configuration.

Because of the difficulty and limitation of theoretical analysis, more research efforts have been directed to numerical investigations when the advances in computer capabilities made it feasible to perform an analysis on a more realistic flow model.

1.3.3 Numerical Studies of Twin-Jet Impingement

In contrast with the research work in the numerical simulation of single jet impingement, numerical investigations of twin-jet impingement are comparatively fewer.

1.3.3.1 Simulation Based on Two-Equation k-ϵ Turbulence Model

The first attempt to model the twin-jet impingement flow field by solving the three-dimensional incompressible Navier-Stokes equations was carried out by Bower *et al.* [8]. The turbulent upwash flow produced by two interacting incompressible planar jets was simulated by solving the time-averaged Navier-Stokes equations in conjunction with the k-ϵ turbulence model using a second-order-accurate finite-difference scheme. This work was later improved by Bower [7] by discretizing the resulting system of equations using a third-order-accurate upwind-difference scheme. Due to computer limitations, they were not able to resolve the flow domain with enough grid points such that the numerical errors in the solution are essentially negligible.

Since Bower's work, several numerical simulations of twin-jet impingement based on the solution of the Reynolds-Averaged Navier-Stokes (RANS) equations using the two-equation k-ϵ turbulence model had been carried out.

The first three-dimensional numerical simulation for compressible twin-jet impingement flow field was conducted by Childs and Nixon [15]. The simulation was done by solving the three-dimensional time-dependent compressible Reynolds-averaged Navier-Stokes equations and a k-ϵ turbulence model. The equations were discretized using the explicit/implicit MacCormack method [45], which is second order accurate in space and time. In order to reduce the computational time, they modified the MacCormack scheme such that the integration of the viscous term is only first order accurate in time and the implicit part of the algorithm is only used in the direction normal to the wall in a small region near the wall. Artificial dissipation was used to minimize spurious oscillations near sharp gradients. The modeled configuration consisted of twin jets in still air with $H^*/D^* = 4$ and $S^*/D^* = 6$, where S^* is the distance between the jet axes. The simulation was performed on a $64 \times 32 \times 21$

grid. To permit maximum resolution at the fountain, symmetry was used in three planes. One symmetry plane is through the centerlines of both jets. The other two symmetry planes are perpendicular to the first, one through each jet centerline. This configuration corresponds to an infinite one-dimensional array of jets in the physical space. Their results indicate that the fountain is asymmetric, tilting about 5° to the right of vertical. The results were not compared with experiments. The authors did not state if the numerical results were grid-independent.

Pigues [55] simulated the fountain upwash flow based on Saripalli's [64] experiment. However, their simulations were based on square jets instead of the round jets in Saripalli's experiment. Only one-fourth of the total geometry was simulated because they imposed symmetry. The steady, incompressible, Reynolds-averaged Navier-Stokes equations and the k-ϵ turbulence model were solved on a $64 \times 32 \times 32$ grid using a multigrid based first/second order hybrid differencing scheme of Spalding [76]. Comparison with Saripalli's data showed that the mean velocities were predicted with reasonable accuracy, whereas the turbulent kinetic energies were seriously in error. They attributed the discrepancy to the unsteadiness of the impingement region that cannot be represented by the Reynolds-averaged Navier-Stokes equations.

Cho and Park [17] also pointed to the need of an unsteady computation for accurate prediction of a two-dimensional upwash jet arising from two opposing plane wall jets. Using various eddy viscosity models, namely, the standard k-ϵ model, the RNG k-ϵ model [86], and the Bardina's model [3], they found that the flow characteristics of the upwash jet were poorly predicted if the steady version of the Reynolds averaged Navier-Stokes equations was employed. As a result, the velocity profiles of the upwash jet were in very poor agreement with the experimental data. However, if an oscillatory behavior of the merged upwash jet was assumed and the unsteady version of the standard k-ϵ model of Kato and Launder [36] was used in solving the full Reynolds averaged Navier-Stokes equations, the spreading rate estimating from the time-averaged velocity was in much better agreement with the experimental data of Gilbert [31].

Behrouzi [4] studied the behavior of turbulent twin-jet impingement by solving the incompressible Reynolds-Averaged Navier-Stokes(RANS) equations using the standard k-ϵ turbulence model, together with log-law based wall functions [22]. The equations were solved numerically using the modified version of the finite volume pressure-correction-based code that had been used by Barata *et al.* [2]. The results of their computations using a second-order QUICK scheme showed that the velocity field was close to the LDV experimental results in the majority of the flow regions. However, the fountain growth rate and the decay of fountain maximum velocity were grossly underpredicted by about 60% and 50%, respectively.

Chuang *et al.* [18] analyzed the three-dimensional turbulent impinging square twin-jet flow field by solving the steady, isothermal, incompressible, time-averaged Navier-Stokes equations in conjunction with k-ϵ turbulence model using the CFD code PHOENICS which adopts

the SIMPLEST algorithm. The Reynolds number of the flow was $105,000$. They reported that the calculated mean velocities in the plane through the centerline of both jets were in good agreement with the experimental data of Barata *et al.* [2]. However, no results for the fountain spreading rate and the decay of fountain maximum velocity were presented. There were no comparisons with the experimental data for the flow parameters in the fountain upwash and impingement regions.

1.3.3.2 Simulation Based on Modified k-ϵ Turbulence Model

The failure of the standard k-ϵ model to accommodate the effects of streamline curvature, sudden changes in strain rate and secondary motion, etc. has led to the extensions of the k-ϵ model to include the effects of streamline curvature by several researchers. As it is known that the turbulent flow field in the impingement region is characterized by strong streamline curvature [12], several investigators have sought to improve the simulation of twin-jet impinging flow field by using a modified k-ϵ model.

Childs [12] used a modified k-ϵ turbulence model that takes into account the effects of streamline curvature, large scale mixing and anisotropy in a Reynolds-averaged model to study the planar upwash generated by the head-on collision of two equal-strength incompressible planar wall jets. Although there was improvement over the standard k-ϵ turbulence model, the upwash spreading rate and the maximum shear stress were still only 50% and 55%, respectively, of Saripalli's [64] experimental values.

Three turbulence models that extend the standard k-ϵ model to include the curvature effects, namely, the Park-Chung model [53, 19], the Childs-Caruso model [14], and the Leschziner-Rodi Model [40] have been used by Roberts and Imlay [60] to model the upwash fountain of the two-dimensional twin impinging jet flow field investigated by Elbana and Sabbagh [24]. The simulation was done by incorporating the turbulence models into the existing 3D compressible Reynolds-averaged Navier-Stokes code. Since symmetry condition was imposed, only half of the flow domain was modeled using a stretched grid with 55×40 cells. Both jets have the same subsonic speed corresponding to a Reynolds number of $Re = 16,600$. Their results showed that the upwash spreading rate was grossly underpredicted by all the models. The peak velocity and spreading rate in the impinging jet were also not accurately modeled by all the models. They reported that no improvement over the results was obtained when Rodi's ARSM was used.

An assessment of one- and two-equation turbulence models for the computation of incompressible and compressible twin-jet impingement flow field have been performed by Ladd and Korakianitis [38] using the McDonnell Douglas Navier-Stokes solver NASTD that employs second order accurate (in space) finite volume scheme. The turbulence models used by them are the one-equation model of Spalart and Allmaras (SA) [74], the low-Reynolds-number k-ϵ model of Chien (CH) [10], and the Shear Stress Transport model (SST) of Menter [50]. Ideal gas was assumed and the Prandtl number of $Pr = 0.72$ and the turbulent Prandtl number

of $Pr_t = 0.9$ were used in their computations. Only the incompressible (low Mach number) predictions were compared with the LDV measurements in the impingement and upwash fountain regions. Their main findings are:

(1) The growth of the fountain half width was substantially underpredicted by the CH and SST two-equation turbulence models and fairly well predicted (slightly overpredicted by the SA turbulence model.

(2) All of the models overpredicted the upwash velocities near the center of the fountain.

(3) The computed vertical mean velocity profiles from all the models exhibit strong self-similarity in the fountain region. This is consistent with the experiment.

(4) All of the models overpredicted the lateral velocities near the wall in the fountain formation region by a factor of 2.0.

(5) The CH and SST two-equation turbulence models adequately predicted the vertical core velocities and growth of the jet shear layer near the impingement region.

(6) In general the two-equation turbulence models are in better agreement with experiment data than the one-equation turbulence model.

1.3.3.3 Simulation Based on Reynolds Stress Transport Model (RSTM)

It is known that in the upwash fountain, an important chain of events involves the production and convection of anisotropic normal stresses [13]. In this type of complex flow, the eddy viscosity may be strongly directional. The standard isotropic k-ϵ turbulence model has no means of representing this physics and, therefore, cannot model this flow accurately. Since Reynolds Stress Transport Model(RSTM) can resolves this convection, it should, in principle, provide significant improvement over the k-ϵ model in modeling the impinging jet flows. However, investigations by several researchers showed that RSTM generally give poor accuracy because the models for the pressure-strain term are inadequate.

Childs [13] tested the accuracy of Reynolds-stress transport model in modeling the upwash fountain by evaluating the performance of various models for pressure-strain term. Three models were investigated, namely, the models proposed by Gibson and Launder [28], Gibson and Younis [29], and by Sarkar and Speziale [66]. The simulation was performed by solving the turbulence model equations and the 3-D compressible Navier-Stokes equations with an explicit finite volume solver. The solver used an explicit Runge-Kutta scheme with spatially variable time stepping to integrate the solutions to a steady state. The accuracy of the spatial discretization for the inviscid terms is fourth order, while that for the viscous terms is second order. A blend of fourth and second order artificial dissipation was used to stabilize the mean and turbulence solutions. The planar upwash were generated by the collision of two equal-strength planar wall jets. Due to symmetry, only half of the upwash fountain was

modeled. The grid contained 60×80 points in the streamwise and vertical directions. The inlet jet Mach number is $M = 0.5$. Poor results were obtained from all the models, with the shear stresses underpredicted by an order of magnitude.

The effect of the diffusion term in the Reynolds Stress Model to the spreading rate of a two-dimensional upwash jet resulting from the collision of two planar wall jets was investigated by Cho and Park [17]. In their study, the steady, incompressible Reynolds-averaged Navier-Stokes equations were solved using the Reynolds Stress models with different diffusion term models. The three diffusion models used were: the Daly and Harlow model [20], the Hanjalic and Launder model [32],and the Mellor and Herring model [49].

The dissipation model of Launder *et al.* [39] and the pressure-strain model of Sarkar and Speziale [66, 77] were used with all the diffusion models. All the models showed rather poor agreement with the experimental data.

1.3.3.4 Simulation Based on Algebraic Reynolds Stress Model

While Reynolds-stress transport model is more accurate for complex flows, it is computationally more expensive. To capture many important features of the flow without adding special modifications to the model, Rodi [61] proposed the Algebraic Reynolds Stress Model (ASRM) which reduces the RSTM to six algebraic non-linear algebraic equations by assuming that the convection and diffusion terms in the RSTM are proportional to the turbulence kinetic energy. These algebraic equations are then solved together with the k-ϵ turbulence model.

Childs and Patel [11] compared the performance of the standard k-ϵ turbulence model with Rodi's Algebraic Reynolds Stress Transport Model (ARSM) in predicting the mean flow field and Reynolds stresses of Saripalli's "twin-jet fountain" configuration [64]. The simulation was done by solving the three-dimensional, steady, incompressible, Navier-Stokes equations together with one of these turbulence models. The SIMPLE (Semi-Implicit Iterative Scheme) of Patankar [54] was used to solve the governing equations numerically.

Due to the symmetry, only 1/4 of the domain in Saripalli's experiment was actually modeled. The twin jet flow field was modeled in a rectangular domain of size $10D^* \times 3D^* \times 5D^*$ using three different staggered grids: coarse ($42 \times 14 \times 22$), medium ($54 \times 20 \times 26$) and fine ($70 \times 30 \times 30$). The jet inlets were simulated by square inlets having the same cross-sectional as the actual round jet. Turbulent wall function was used on all solid surface, and the jet inlet velocities were assumed uniform with turbulent intensities of 10% (based on Saripalli's measurements). Based on their simulations, the authors claimed that:

(1) The k-ϵ and ARSM models adequately predict the mean velocities, turbulent kinetic energy k, turbulent viscosity μ_t and the Reynolds shear stress $-\overline{u'v'}$.

(2) The k-ϵ model overpredicts $-\overline{u'^2}$ and underpredicts $-\overline{v'^2}$.

(3) The ASM and the k-ϵ models break down at the impingement zone.

(4) The ASM model results are not significantly different from the k-ϵ model.

However, as pointed out by Ladd [38] the validity of their conclusions is hardly convincing as there is no evidence that their square jets truely represent the round jets that are being simulated.

1.3.3.5 Simulation Based on Very Large Eddy Simulation (VLES)

Childs and Nixon [16] used the Very Large Eddy Simulation (VLES) approach to simulate a planar upwash fountain by colliding two opposite planar wall jets and permitting the upwash to develop naturally. In this approach, only the very large scale unsteady motions are resolved and the small scale turbulence is modeled by a sub-grid scale (SGS) fixed mixing length turbulence model. Each wall jet was approximated by an unsteady inflow profiles which was allowed to evolve in the streamwise direction before colliding with another wall jet. The maximum inflow Mach number for the wall jets was 0.65. The Reynolds number based on maximum velocity and half inflow velocity thickness was $20,000$. The governing equations were solved by integrating the three-dimensional time-dependent compressible Reynolds averaged Navier-Stokes equations using the numerical algorithm described in Child and Nixon [15]. The simulations were performed on a Cartesian grid with stretching in the x- and y-directions. The grid has $40 \times 32 \times 25$ points in the fountain region and $32 \times 32 \times 32$ points in the wall jet region. The primary jets were not directly modeled. The results of their simulation can be summarized as follows:

(1) High spreading rate of the fountain was predicted and compared reasonably well with the experimental data of Gilbert [30] in the range of 24% to 36%.

(2) High Reynolds stresses were also predicted and were in moderately good agreement with experimental data.

Childs and Patel [11] pointed out that the spreading rate obtained by Child and Nixon [16] was higher than that obtained from the water tank experiment by Saripalli [64]. Since the impinging twin jets were not simulated, they hypothesized that the twin jet may have an inhibiting effect on the spreading of the fountain. This effect was also missing in Gilbert's experiment.

1.3.3.6 Simulation Based on Large Eddy Simulation (LES)

Rizk and Menon [59] performed a large eddy simulation(LES) to investigate the responses of an upwash fountain to various azimuthal and axisymmetric excitations applied at the

exits of two impinging jets separated at a distance of $3D^*$, where D^* is the jet diameter. The LES solver was based on the three-dimensional, time-dependent, incompressible Navier-Stokes equations and the Smagorinsky's eddy viscosity model. The governing equations were solved on a domain of $6D^* \times 6D^* \times 3D^*$ using a finite difference scheme that is second order accurate in space and time. Since periodic boundary conditions were applied in the x-direction, they were actually simulating an infinite rows of impinging jets. In addition, as their uniform $64 \times 64 \times 32$ staggered grid was not fine enough to resolve the viscous sublayer, the solution in the wall region was patched to the first point in the computational domain using Spalding's expression [75].

Tang *et al.* [79] conducted a simulation of an impinging jet in crossflow based on LES approach. Their results show that details of the turbulence in the immediate vicinity of the impingement point are better captured by the LES approach compared to the RANS approach based on the standard k-ϵ turbulence model.

These studies showed that LES has much promising potential in the simulation of jet impingement flow field as the unsteadiness is taken into consideration. To the authors knowledge, the present study may be the first attempt to carry out a large eddy simulation of the twin-jet impingement based on the compressible model which includes both the jets and the fountain in one model.

1.4 Motivation

Previous numerical studies of the flow field associated with twin-jet impingement suffer from one or more of the following limitations:

(1) Simulations were based on simplified hypotheses such as planar upwash. The simulations were focused on two-dimensional upwash formed by the collision of two opposing wall jets. The twin-impinging jets were not modeled.

(2) Simulations were based on incompressible flow model.

(3) Modeling was based on the RANS approach using the standard or modified k-ϵ model as turbulence closure.

(4) Unsteadiness of the flow were not considered in the RANS modeling.

(5) Numerical schemes used in the simulations were second-order accurate in time and space.

Turbulence modeling based on the RANS approach has not been successful so far for the twin-jet impingement problem. The failure of the existing turbulence models to predict the large spreading rate of the upwash jet indicates that unsteadiness of the flow has to be taken

into account in addition to the various terms in the turbulence models. This suggests that in order to obtain an accurate prediction of the twin-jet impingement flow field, the unsteadiness in the impingement region must be properly modeled. Therefore, the calculations should be based on the full three-dimensional unsteady Navier-Stokes equations. Hence, time-accurate simulations based on LES maybe more appropriate for accurate calculations of this type of flow. In addition, a fine grid is also required in order to resolve the turbulent scales sufficiently. To relax the requirement on the density of the grid, which is seriously restricted by computer resources, a high-order numerical scheme is required.

1.5 Objectives

The present study is an attempt to address the issues which have thus been neglected in the previous simulations. To this end, a fifth-order WENO scheme (for spatial discretization) in conjunction with a low-storage fourth-order Runge-Kutta scheme (for temporal discretization) will be used to solve the full unsteady Navier-Stokes equations based on the LES approach.

The objectives of the present study are:

(1) To investigate the capability of the fifth-order weighted essentially non-oscillatory (WENO) schemes of G. S. Jiang and C.-W. Shu [34] in the numerical simulation of supersonic twin impinging jets with possible embedded shock waves.

(2) To identify the spatial and temporal characteristics of the large scale structures in the supersonic twin jet impingement flow field.

1.6 Contributions

The main contributions of the present work are:

(1) It is the first attempt to simulate the supersonic twin-jet impingement flow based on the LES approach using high-order numerical schemes.

(2) It is the first simulation based on unsteady compressible flow model that simulates both twin impinging jets and the fountain flow in one numerical model. It will provide more realistic information of the flow field as three-dimensionality and unsteadiness of the flow field are both taken into consideration in the simulation.

(3) The new filtered dynamic subgrid-scale model proposed by Zhang and Chen [87] for incompressible flow model is extended to the compressible flow model used in the present study.

(4) The performance of the fifth-order WENO scheme for the numerical simulation of subsonic and supersonic turbulent flows is evaluated.

Chapter 2

MATHEMATICAL FORMULATION

2.1 Numerical Model

Introducing a set of right-handed Cartesian axes, x_i^*, $(i = 1, 2, 3)$, fixed in space, the numerical model for the simulation of twin-jet impingement is defined as shown in Figure 2.1.

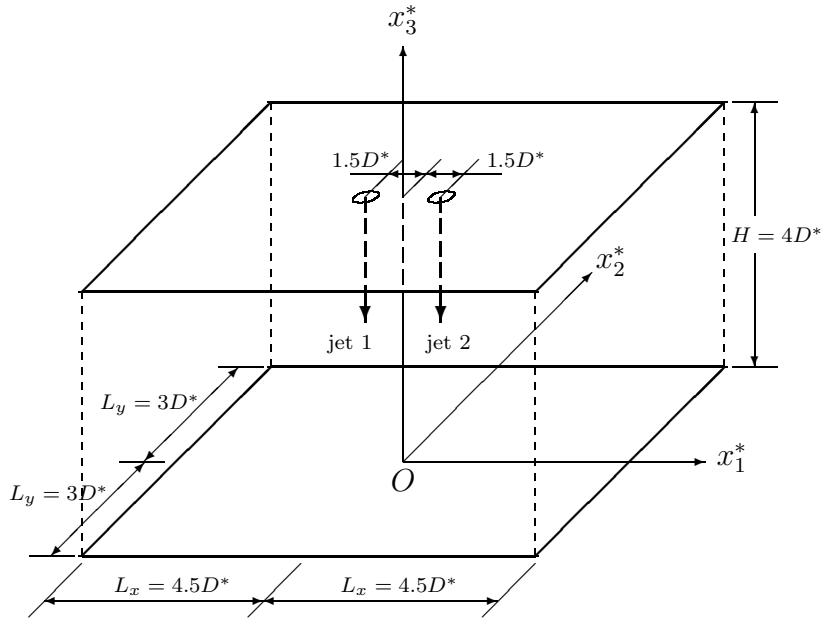

Figure 2.1: Numerical model for twin-jet impingement

The basic configuration of the numerical model consists of two parallel axisymmetric jets issuing from a plane which is at a distance $H^* = 4D^*$ above the ground, where D^* is the jet exit diameter. The axes of the two jets are separated by a distance of $3D^*$. The jet diameter D^*, mean velocity W_o^*, mean density ρ_o^* and mean temperature T_o^* at the center of the jet in the jet exit plane are used as reference values. The Mach number and Reynolds numbers of the jets are $M = 1.5$ and $Re = 5.5 \times 10^5$, respectively. This model is closely related to the experimental setup of Elavarsan *et al.* [23].

2.2 Governing Equations

At time t^*, let u_i^*, ρ^*, p^*, T^*, μ^*, and κ^* represent, respectively, the velocity components, density, pressure, temperature, dynamic viscosity, and thermal conductivity of the fluid particle at position x_i^*. By neglecting body forces and assuming that air is a perfect gas, and an isotropic, homogeneous, Newtonian fluid, the governing equations of the flow field, viz., the continuity equation, the Navier-Stokes equation, the total energy equation and equation of state, are given by:

Continuity Equation:

$$\frac{\partial \rho^*}{\partial t^*} + \frac{\partial (\rho^* u_j^*)}{\partial x_j^*} = 0, \tag{2.1}$$

Momentum Equation:

$$\frac{\partial (\rho^* u_i^*)}{\partial t^*} + \frac{\partial}{\partial x_j^*}(\rho^* u_i^* u_j^* + p^* \delta_{ij}) = \frac{\partial \sigma_{ij}^*}{\partial x_j^*} \tag{2.2}$$

Energy Equation:

$$\frac{\partial (\rho^* E^*)}{\partial t^*} + \frac{\partial}{\partial x_j^*}\left[(\rho^* E^* + p^*) u_j^*\right] = \frac{\partial}{\partial x_j^*}(\sigma_{ij}^*\, u_i^* - q_j^*) \tag{2.3}$$

Equation of State:

$$p^* = \rho^* R^* T^*, \tag{2.4}$$

where

$$E^* = \frac{p^*}{(\gamma - 1)\rho^*} + \frac{1}{2} u_i^* u_i^*, \tag{2.5}$$

$$\sigma_{ij}^* = \mu^* \left(\frac{\partial u_i^*}{\partial x_j^*} + \frac{\partial u_j^*}{\partial x_i^*} - \frac{2}{3} \frac{\partial u_k^*}{\partial x_k^*} \delta_{ij} \right), \tag{2.6}$$

$$q_j^* = -\kappa^* \frac{\partial T^*}{\partial x_j^*}, \tag{2.7}$$

The terms σ_{ij}^*, E^*, q_j^* are the stress tensor, total specific energy and heat flux vector, respectively.

The gas constant R^* and the ratio of specific heats γ are given by

$$\gamma = \frac{c_p^*}{c_v^*} = 1.4 \ , \tag{2.8}$$

and

$$R^* = c_p^* - c_v^* = 287.06 \ J\, kg^{-1} K^{-1} \tag{2.9}$$

respectively. Here the specific heat at constant pressure c_p^* and the specific heat at constant volume c_v^* are assumed to be constants.

The dynamic viscosity and thermal conductivity are determined by the Sutherland law [81]:

$$\mu^* = \mu_0^* \left(\frac{T^*}{T_0^*} \right)^{\frac{3}{2}} \left(\frac{T_0^* + S_\mu^*}{T^* + S_\mu^*} \right), \tag{2.10}$$

$$\kappa^* = \kappa_0^* \left(\frac{T^*}{T_0^*} \right)^{\frac{3}{2}} \left(\frac{T_0^* + S_\kappa^*}{T^* + S_\kappa^*} \right), \tag{2.11}$$

with $T_0^* = 273 \ K$, $\mu_0^* = 1.716 \times 10^{-5} \ N \cdot s/m^2$, $\kappa_0^* = 0.0241 \ W/m \cdot K$, $S_\mu^* = 111 \ K$, and $S_\kappa^* = 194 \ K$.

2.3 Governing Equations in Nondimensional Form

Let the jet mean flow variables at the center of the jet in the jet exit plane be given by

$$\begin{aligned}
x_3 - \text{component velocity} &: u_{3_{jet}}^* = W_o^*, \\
\text{density} &: \rho_{jet}^* = \rho_o^*, \\
\text{temperature} &: T_{jet}^* = T_o^*, \\
\text{dynamic viscosity} &: \mu_{jet}^* = \mu_o^*, \\
\text{specific heat at constant pressure} &: c_{p_{jet}}^* = c_{p_o}^*, \\
\text{thermal conductivity} &: \kappa_{jet}^* = \kappa_o^*
\end{aligned} \tag{2.12}$$

Using the jet diameter (D^*) and the above flow variables as reference values, one can define the following dimensionless variables:

$$t = \frac{t^*\, W_o^*}{D^*}, \quad x_i = \frac{x_i^*}{D^*}, \quad u_i = \frac{u_i^*}{W_o^*}, \quad \rho = \frac{\rho^*}{\rho_o^*}, \quad p = \frac{p^*}{\rho_o^* W_o^{*2}},$$

$$T = \frac{T^*}{T_o^*}, \quad E = \frac{E^*}{W_o^{*2}}, \quad \mu = \frac{\mu^*}{\mu_o^*}, \quad \kappa = \frac{\kappa^*}{\kappa_o^*}, \quad c_p = \frac{c_p^*}{c_{p_o}^*} = 1$$

Using the above dimensionless variables, the governing equations from Eq. (2.1) to Eq. (2.4) can be expressed in nondimensional form as follows:

Continuity Equation:

$$\frac{\partial \rho}{\partial t} + \frac{\partial (\rho u_j)}{\partial x_j} = 0, \tag{2.15}$$

Momentum Equations:

$$\frac{\partial (\rho u_i)}{\partial t} + \frac{\partial (\rho u_i u_j + p\delta_{ij})}{\partial x_j} = \frac{1}{Re}\frac{\partial \sigma_{ij}}{\partial x_j}, \tag{2.16}$$

Energy Equation:

$$\frac{\partial (\rho E)}{\partial t} + \frac{\partial \left[(\rho E + p)\, u_j\right]}{\partial x_j} = \frac{1}{Re}\frac{\partial}{\partial x_j}\left[\sigma_{ij}\, u_i - \frac{1}{Pr\, (\gamma - 1)\, M^2}\, q_j\right] \tag{2.17}$$

Equation of State:

$$p = \rho\, R\, T, \tag{2.18}$$

with

$$E = \frac{p}{(\gamma - 1)\rho} + \frac{1}{2} u_i u_i, \tag{2.19}$$

$$\sigma_{ij} = \mu \left(\frac{\partial u_i}{\partial x_j} + \frac{\partial u_j}{\partial x_i} - \frac{2}{3}\frac{\partial u_k}{\partial x_k}\delta_{ij} \right), \tag{2.20}$$

$$q_j = -\kappa \frac{\partial T}{\partial x_j}. \tag{2.21}$$

The dimensionless parameters of the jet, viz., the Reynolds number Re, the Mach number M and the Prandtl number Pr are given by

$$Re = \frac{\rho_o^* \, W_o^* \, D^*}{\mu_o^*}, \tag{2.22}$$

$$M = \frac{W_o^*}{\sqrt{\gamma R^* T_o^*}}, \tag{2.23}$$

$$Pr = \frac{\mu_o^* \, c_{p_o}^*}{\kappa_o^*}. \tag{2.24}$$

The nondimensional gas constant are given by

$$R = \frac{R^* \, T_o^*}{W_o^{*^2}} \; = \frac{1}{\gamma M^2} \tag{2.25}$$

2.4 Large Eddy Simulation

In LES, the large scale motion is resolved directly, while the small-scale components of motion are modeled [62]. In order to extract the large scale motion from the small eddies in a flow quantity $\Phi(x_i, t)$, it is multiplied by a spatial filter function $G(x_i - x_i')$, where $x_i - x_i'$ is the relative position in space. The large-scale flow quantity which is the filtered value is then obtained by integrating the product over the entire flow domain Ω [48, 57, 56].

$$\bar{\Phi}(\mathbf{x}, t) = \int_{\Omega} G(\mathbf{x} - \mathbf{x}')\, \Phi(\mathbf{x}, t)\, d^3\mathbf{x}' \tag{2.26}$$

where the filter function G is defined as

$$G(\mathbf{x} - \mathbf{x}') = \prod_{\alpha=1}^{3} g_i(x_\alpha - x_\alpha') \tag{2.27}$$

The filter function must satisfy the following relation in order to deliver a consistent value for $\Phi =$ constant :

$$\int_{\Omega} G(\mathbf{x} - \mathbf{x}')\, d^3\mathbf{x}' = 1 \tag{2.28}$$

In the present study, we use the top hat filter (or box filter), which is defined by

$$g(x_i - x_i') = \begin{cases} \frac{1}{\Delta_i} & \text{for } x_i - \frac{\Delta_i}{2} \le x_i' \le x_i + \frac{\Delta_i}{2}, \\ \\ 0 & \text{otherwise} \end{cases} \tag{2.29}$$

where Δ_i is the filter width in the x_i-direction.

As a result of filtering, Φ is decomposed as follows :

$$\Phi = \overline{\Phi} + \phi' \tag{2.30}$$

where $\bar{\Phi}$ is the large-scale (grid-scale) component, and ϕ' is the subgrid-scale (SGS) component which is the fluctuation of scale smaller than the grid scale.

The filtering process obeys the following rules:

$$\overline{\Phi + \Psi} = \overline{\Phi} + \overline{\Psi} \tag{2.31}$$

$$\overline{c \cdot \Phi} = c \cdot \overline{\Phi} \tag{2.32}$$

Since differentiation in time always commutes with space averaging, and spatial differentiation also commutes with space averaging, we have

$$\overline{\frac{\partial \Phi}{\partial t}} = \frac{\partial \overline{\Phi}}{\partial t} \tag{2.33}$$

$$\overline{\frac{\partial \Phi}{\partial x_i}} = \frac{\partial \overline{\Phi}}{\partial x_i} \tag{2.34}$$

For compressible flows, the large-scale field equations are operationally simpler when the flow variables are expressed in term of Favre-filtered quantities, where a Favre-filtered variable is defined as

$$\widetilde{\Phi} = \frac{\overline{\rho\,\Phi}}{\bar{\rho}} \tag{2.35}$$

Using the Favre-filter, a flow variable may then be decomposed according to

$$\Phi = \widetilde{\Phi} + \Phi^{'} \tag{2.36}$$

The Favre-filtering process satisfies the following relations:

$$\widetilde{\Phi^{'}} \neq 0, \tag{2.37}$$

and

$$\widetilde{\widetilde{\Phi}} \neq \widetilde{\Phi} \tag{2.38}$$

Applying these definitions to the governing equations, the following Favre-filtered governing equations for the resolved scales are obtained.

Continuity Equation:

$$\frac{\partial \bar{\rho}}{\partial t} + \frac{\partial (\bar{\rho}\widetilde{u}_j)}{\partial x_j} = 0, \tag{2.39}$$

Momentum Equation:

$$\frac{\partial (\bar{\rho}\widetilde{u}_i)}{\partial t} + \frac{\partial (\bar{\rho}\widetilde{u}_i\widetilde{u}_j + \bar{p}\delta_{ij})}{\partial x_j} = \frac{1}{Re}\frac{\partial \widetilde{\sigma}_{ij}}{\partial x_j} - \frac{\partial \tau_{ij}}{\partial x_j} \tag{2.40}$$

Energy Equation:

$$\begin{aligned}\frac{\partial(\bar{\rho}\widetilde{E})}{\partial t}+\frac{\partial[(\bar{\rho}\widetilde{E}+\bar{p})\widetilde{u}_j]}{\partial x_j} &= \frac{1}{Re}\frac{\partial}{\partial x_j}\left[\widetilde{\sigma}_{ij}\widetilde{u}_i-\frac{1}{Pr\,(\gamma-1)\,M^2}\,\widetilde{q}_j\right] \\ &+ \frac{1}{Re}\frac{\partial \mathcal{D}_j}{\partial x_j}-\frac{\partial}{\partial x_j}\left[c_p\mathcal{Q}_j+\frac{1}{2}\mathcal{T}_j\right],\end{aligned} \tag{2.41}$$

Equation of State:

$$\bar{p}=\bar{\rho}\,R\,\widetilde{T}, \tag{2.42}$$

where

$$\widetilde{E}=\frac{\bar{p}}{(\gamma-1)\bar{\rho}}+\frac{1}{2}\widetilde{u}_i\widetilde{u}_i, \tag{2.43}$$

$$\widetilde{\sigma}_{ij}=\widetilde{\mu}\left(\frac{\partial\widetilde{u}_i}{\partial x_j}+\frac{\partial\widetilde{u}_j}{\partial x_i}-\frac{2}{3}\frac{\partial\widetilde{u}_k}{\partial x_k}\delta_{ij}\right), \tag{2.44}$$

$$\widetilde{q}_j=-\widetilde{\kappa}\,\frac{\partial\widetilde{T}}{\partial x_j}, \tag{2.45}$$

$$\tau_{ij}=\bar{\rho}\,(\widetilde{u_iu_j}-\widetilde{u}_i\widetilde{u}_j) \tag{2.46}$$

$$\mathcal{Q}_j=\bar{\rho}\left(\widetilde{u_jT}-\widetilde{u}_j\widetilde{T}\right) \tag{2.47}$$

$$\mathcal{T}_j=\bar{\rho}\left(\widetilde{u_ju_ku_k}-\widetilde{u}_j\widetilde{u_ku_k}\right) \tag{2.48}$$

$$\mathcal{D}_j=\overline{\sigma_{ij}u_i}-\widetilde{\sigma}_{ij}\widetilde{u}_i \tag{2.49}$$

Here τ_{ij}, $\mathcal{Q}_j$, $\frac{\partial\mathcal{T}_j}{\partial x_j}$, $\frac{\partial\mathcal{D}_j}{\partial x_j}$ represent the SGS stress tensor, SGS heat flux, SGS turbulent diffusion and SGS viscous diffusion, respectively. They are unclosed terms that need to be modeled in order to close the system of equations.

As the usual practice [47], it has been assumed in the above equations that $\bar{\sigma}_{ij}-\widetilde{\sigma}_{ij}=0$ and $\bar{q}_j-\tilde{q}_j=0$.

2.5 Subgrid-scale Model for Momentum Equation

There is only one unclosed term in the momentum equation, i.e., the SGS stress τ_{ij}. The dynamic version of the Smagorinsky's eddy-viscosity model [73] introduced by Germano *et al.* [26] is used to model the SGS stress.

2.5.1 SGS Stress

For dynamic model the spectral data contained in the resolved field is utilized by introducing a "test filter" ($\hat{G}$) that has a larger filter width ($\widehat{\Delta}_i$) than the resolved grid filter (Δ_i) to generate a second field with scales larger than the resolved field [52].

Upon applying the test filter to the momentum equation, the test-filtered SGS stress is obtained

$$\widehat{\tau}_{ij} = \widehat{\bar{\rho}\widetilde{u_i u_j}} - \widehat{\bar{\rho}\widetilde{u}_i\widetilde{u}_j} = \widehat{\overline{\rho u_i u_j}} - \left(\frac{\widehat{\overline{\rho u_i}\,\overline{\rho u_j}}}{\bar{\rho}}\right) \tag{2.50}$$

By analogy to SGS stress τ_{ij}, a subtest-scale (STS) stress $\mathscr{T}_{ij}$ is defined as follows:

$$\mathscr{T}_{ij} = \widehat{\overline{\rho u_i u_j}} - \frac{\widehat{\overline{\rho u_i}}\,\widehat{\overline{\rho u_j}}}{\widehat{\bar{\rho}}} \tag{2.51}$$

The resolved turbulent stress associated with scales of motion between the test scale and grid scale is given by the Germano identity:

$$\mathcal{L}_{ij} = \mathscr{T}_{ij} - \widehat{\tau}_{ij} \tag{2.52}$$

or

$$\mathcal{L}_{ij} = \widehat{\bar{\rho}\,\widetilde{u}_i\,\widetilde{u}_j} - \frac{\widehat{\bar{\rho}\,\widetilde{u}_i}\,\widehat{\bar{\rho}\,\widetilde{u}_j}}{\widehat{\bar{\rho}}}\ , \tag{2.53}$$

The SGS and STS stresses are then modeled by splitting them into isotropic and anisotropic parts. The anitropic parts of both STS and SGS stresses are parametrized using Smagorinsky's eddy viscosity model

$$\tau_{ij} - \frac{1}{3}\tau_{kk}\delta_{ij} = -2C\bar{\rho}\bar{\Delta}^2\,|\widetilde{S}|\,\left(\widetilde{S}_{ij} - \frac{1}{3}\widetilde{S}_{kk}\delta_{ij}\right) \tag{2.54}$$

$$\mathscr{T}_{ij} - \frac{1}{3}\mathscr{T}_{kk}\delta_{ij} = -2C\widehat{\bar{\rho}}\widehat{\Delta}^2\,|\widehat{\widetilde{S}}|\,\left(\widehat{\widetilde{S}}_{ij} - \frac{1}{3}\widehat{\widetilde{S}}_{kk}\delta_{ij}\right) \tag{2.55}$$

where

$$\widetilde{S}_{ij} = \frac{1}{2}\left(\frac{\partial \widetilde{u}_i}{\partial x_j} + \frac{\partial \widetilde{u}_j}{\partial x_i}\right), \tag{2.56}$$

$$|\widetilde{S}| = \left(2\widetilde{S}_{ij}\widetilde{S}_{ij}\right)^{\frac{1}{2}}, \tag{2.57}$$

$$\bar{\Delta} = (\Delta_1\,\Delta_2\,\Delta_3)^{\frac{1}{3}}, \tag{2.58}$$

$$\widehat{\Delta} = (\widehat{\Delta}_1\,\widehat{\Delta}_2\,\widehat{\Delta}_3)^{\frac{1}{3}}. \tag{2.59}$$

Here C is the Smagorinsky coefficient that is assumed to be independent of filter width. In the present study, $\widehat{\Delta}_i = 2\bar{\Delta}_i$ is used.

The isotropic parts of SGS and STS stresses are modeled separately as

$$\tau_{kk} = 2C_I\,\bar{\rho}\,\bar{\Delta}^2\,|\widetilde{S}|^2\ , \tag{2.60}$$

$$\mathscr{T}_{kk} = 2C_I\,\widehat{\bar{\rho}}\,\widehat{\bar{\Delta}}^2\,|\widehat{\widetilde{S}}|^2\ . \tag{2.61}$$

Applying the test filter to Eq. (2.54) and subtracting the result from Eq. (2.55) yields

$$\mathcal{L}_{ij} - \frac{1}{3}\mathcal{L}_{kk}\delta_{ij} = C\mathcal{M}_{ij}\ , \tag{2.62}$$

where

$$\mathcal{M}_{ij} = -2\widehat{\Delta}^2\widehat{\bar{\rho}}|\widehat{\widetilde{S}}|\widehat{\widetilde{S}^d_{ij}} + 2\bar{\Delta}^2\widehat{\bar{\rho}|\widetilde{S}|\widetilde{S}^d_{ij}}\ , \tag{2.63}$$

$$\widehat{\widetilde{S}^d_{ij}} = \widehat{\widetilde{S}}_{ij} - \frac{1}{3}\widehat{\widetilde{S}}_{kk}\delta_{ij}\ , \tag{2.64}$$

$$\widetilde{S}^d_{ij} = \widetilde{S}_{ij} - \frac{1}{3}\widetilde{S}_{kk}\delta_{ij}\ . \tag{2.65}$$

Eq. (2.62) represents five independent equations in one unknown and therefore no value of C can be chosen. However its error can be minimized by applying the least square approach [43].

Define

$$\mathcal{A} = \left(\mathcal{L}_{ij} - \frac{1}{3}\mathcal{L}_{kk}\delta_{ij} - C\mathcal{M}_{ij}\right)^2 \tag{2.66}$$

Then C can be determined by requiring that

$$\frac{\partial \mathcal{A}}{\partial C} = 0 \tag{2.67}$$

which gives

$$C = \frac{\left(\mathcal{L}_{ij} - \frac{1}{3}\mathcal{L}_{kk}\delta_{ij}\right)\mathcal{M}_{ij}}{\mathcal{M}_{ij}\mathcal{M}_{ij}} \tag{2.68}$$

Since the isotropic parts must satisfy the Germano identity, we have

$$\mathcal{L}_{kk} = \mathscr{T}_{kk} - \widehat{\tau}_{kk} = C_I \left(2\,\widehat{\Delta}^2\widehat{\overline{\rho}}|\widehat{\overline{S}}|^2 - 2\,\bar{\Delta}^2\widehat{\overline{\rho}|\overline{S}|}\right) \tag{2.69}$$

Using the least square approach, we define

$$\mathcal{A}_I = \left[\mathcal{L}_{kk} - C_I \left(2\,\widehat{\Delta}^2\widehat{\overline{\rho}}|\widehat{\overline{S}}|^2 - 2\,\bar{\Delta}^2\widehat{\overline{\rho}|\overline{S}|}\right)\right]^2 \tag{2.70}$$

By setting $\frac{\partial \mathcal{A}_I}{C_I} = 0$, C_I is obtained as follows:

$$C_I = \frac{\mathcal{L}_{kk}}{\left(2\,\widehat{\Delta}^2\widehat{\overline{\rho}}|\widehat{\overline{S}}|^2 - 2\,\bar{\Delta}^2\widehat{\overline{\rho}|\overline{S}|}\right)} \tag{2.71}$$

To avoid the large fluctuations in the values of C and C_I that may cause the instability of numerical solutions, Zhang and Chen [87] proposed a new filtered dynamic subgrid-scale model for incompressible large-eddy simulation of indoor airflow [88, 89]. Following their approach, the value of C and C_I are then determined as follows:

$$C = \frac{\widehat{\overline{\mathcal{L}_{ij}^d}\overline{\mathcal{M}_{ij}}}}{\widehat{\overline{\mathcal{M}_{ij}}\overline{\mathcal{M}_{ij}}}}, \qquad \mathcal{L}_{ij}^d = \mathcal{L}_{ij} - \frac{1}{3}\mathcal{L}_{kk}\delta_{ij} \tag{2.72}$$

$$C_I = \frac{\widehat{\overline{\mathcal{L}}}_{kk}}{2\,\widehat{\Delta}^2\widehat{\overline{\rho}}\,\widehat{\overline{|\overline{S}|^2}} - 2\,\bar{\Delta}^2\widehat{\overline{\rho}|\overline{S}|^2}} \tag{2.73}$$

where the symbol $\widehat{\bar{}}$ represents double filtering, i.e., a grid filter ($\bar{}$) is applied first followed by a test filter ($\widehat{}$).

2.6 Subgrid-scale Model for Energy Equation

The unclosed terms in the total energy equation is the SGS heat flux $\mathcal{Q}_j$, the SGS turbulent diffusion $\frac{\partial \mathcal{T}_j}{\partial x_j}$ and the SGS viscous diffusion $\frac{\partial \mathcal{D}_j}{\partial x_j}$. The SGS turbulent diffusion is comparable with the divergence of SGS heat flux, while the SGS viscous diffusion is one order of magnitude smaller than the other terms [47].

2.6.1 SGS Heat Flux

From the definition of Favre-filter, the SGS heat flux $\mathcal{Q}_j$ defined in Eq. (2.47) can be written as

$$\mathcal{Q}_j = \overline{\rho u_j T} - \frac{\overline{\rho u_j}\,\overline{\rho T}}{\bar{\rho}} \tag{2.74}$$

The STS heat flux is defined as

$$\mathscr{Q}_j = \widehat{\overline{\rho u_j T}} - \frac{\widehat{\overline{\rho u_j}}\,\widehat{\overline{\rho T}}}{\widehat{\bar{\rho}}} \tag{2.75}$$

Using the Smagorinsky's eddy-diffusivity model, $\mathcal{Q}_j$ and $\mathscr{Q}_j$ are modeled as

$$\mathcal{Q}_j = \frac{\bar{\rho}\nu_T}{Pr_T}\frac{\partial \widetilde{T}}{\partial x_j} = -C\frac{\Delta^2 \bar{\rho}\,|\widetilde{S}|}{Pr_T}\frac{\partial \widetilde{T}}{\partial x_j} \tag{2.76}$$

$$\mathscr{Q}_j = -C\frac{\widehat{\Delta}^2 \bar{\rho}\,|\widetilde{S}|}{Pr_T}\frac{\partial \widetilde{T}}{\partial x_j} \tag{2.77}$$

where C is the eddy-viscosity coefficient given by Eq. (2.68) and Pr_T is the turbulent Prandtl number.

The "test-window" heat flux is defined by

$$\mathcal{K}_j = \mathscr{Q}_j - \widehat{\mathcal{Q}}_j \tag{2.78}$$

or

$$\mathcal{K}_j \;=\; \left(\frac{\widehat{\overline{\rho u_j}\,\overline{\rho T}}}{\bar{\rho}}\right) - \frac{\widehat{\overline{\rho u_j}}\,\widehat{\overline{\rho T}}}{\widehat{\bar{\rho}}} \;=\; \widehat{\bar{\rho}\widetilde{u}_j\widetilde{T}} - \frac{\widehat{\bar{\rho}\widetilde{u}_j}\,\widehat{\bar{\rho}\widetilde{T}}}{\widehat{\bar{\rho}}} \tag{2.79}$$

Test-filtering Eq. (2.76) and subtracting the result from Eq. (2.77) yields

$$\mathscr{Q}_j - \widehat{\mathcal{Q}}_j = C\frac{\mathcal{N}_j}{Pr_T} \tag{2.80}$$

where

$$\mathcal{N}_j = -\widehat{\Delta}^2\widehat{\bar{\rho}}\,|\widehat{\widetilde{S}}|\frac{\partial\widehat{\widetilde{T}}}{\partial x_j} + \Delta^2\widehat{\bar{\rho}|\widetilde{S}|\frac{\partial\widetilde{T}}{\partial x_j}} \tag{2.81}$$

From Eq. (2.78) and Eq. (2.80), we have

$$C\frac{\mathcal{N}_j}{Pr_T} = \mathcal{K}_j \tag{2.82}$$

or

$$\mathcal{K}_j\ Pr_T - C\mathcal{N}_j = 0 \tag{2.83}$$

Applying the least-square approach, we define

$$\mathcal{B} = (\mathcal{K}_j\ Pr_T - C\mathcal{N}_j)^2. \tag{2.84}$$

The turbulent Prandtl number Pr_T is then obtained by requiring that

$$\frac{\partial\mathcal{B}}{\partial C} = 2(\mathcal{K}_j\ Pr_T - C\mathcal{N}_j)\mathcal{N}_j = 0. \tag{2.85}$$

Solving the above equation for Pr_T and applying the filtered averaging process, we have

$$Pr_T = \frac{C\widehat{\overline{\mathcal{N}_j}\,\overline{\mathcal{N}_j}}}{\widehat{\overline{\mathcal{K}_k}\,\overline{\mathcal{N}_k}}} \tag{2.86}$$

2.6.2 SGS Turbulent Diffusion

Many researchers have ignored the SGS turbulent diffusion term. Martin *et al.* [47] modeled this term by using a dynamic scale-similar model based on the generalized central moments of Germano [27].

Knight *et al.* argued that $\widetilde{u}_i \simeq \widetilde{\widetilde{u}}_i$ and proposed a model of the form

$$\mathcal{T}_j = \widetilde{u}_k\tau_{jk} \tag{2.87}$$

An *a priori* study by Martin *et al.* [47] show that both their model and Knight's model perform well for $\bar{\Delta}/\Delta \leq 16$, while neither is accurate for $\bar{\Delta}/\Delta = 32$.

In the present work, this term will be ignored.

2.6.3 SGS Viscous Diffusion

The SGS viscous diffusion $\frac{\partial \mathcal{D}_j}{\partial x_j}$ is the smallest term [47] in the total energy equation. It is about 5% of the divergence of the SGS heat flux $\mathcal{Q}_j$ [47] . The only attempt to model $\mathcal{D}_j$ was that by Martin *et al.* [47]. They parametrized it using a scale-similar model. Their model gives a poor correlation and poor agreement for the prediction of the rms magnitude.

As the usual practice, this term is also ignored in the present study.

Chapter 3

STRETCHED GRID AND COORDINATE TRANSFORMATION

In order to resolve the flow field effectively, it is necessary to have more grid points in the region of interest. Therefore a stretched grid is required. On the other hand, the finite difference scheme used to solve the governing equations requires that the computation be conducted on a uniform grid. Therefore a coordinate transformation from the physical space (stretched grid) to the computational space (uniform grid) is required.

3.1 Stretched Grid

The grid points are concentrated in the middle region surrounding the twin jets. The mesh consists of three regions: uniform region in the middle, a stretched region, and a narrow uniform region near the boundaries as shown in Figure 3.1.

The physical domain $x_{1_1} \leq x_1 \leq x_{1_M}$, $x_{2_1} \leq x_2 \leq x_{2_M}$, $x_{3_1} \leq x_3 \leq x_{3_N}$ is mapped into the computational domain $-1 \leq \xi_1 \leq 1$, $-1 \leq \xi_2 \leq 1$, $0 \leq \xi_3 \leq 1$ as shown in Figure 3.2.

Uniform mesh in computational space is given by

$$\xi_{1_\ell} = -1 + 2\,\frac{\ell - 1}{N_1 - 1}, \qquad \ell = 1, \ldots, N_1 \tag{3.1}$$

$$\xi_{2_m} = -1 + 2\,\frac{m - 1}{N_2 - 1}, \qquad m = 1, \ldots, N_2 \tag{3.2}$$

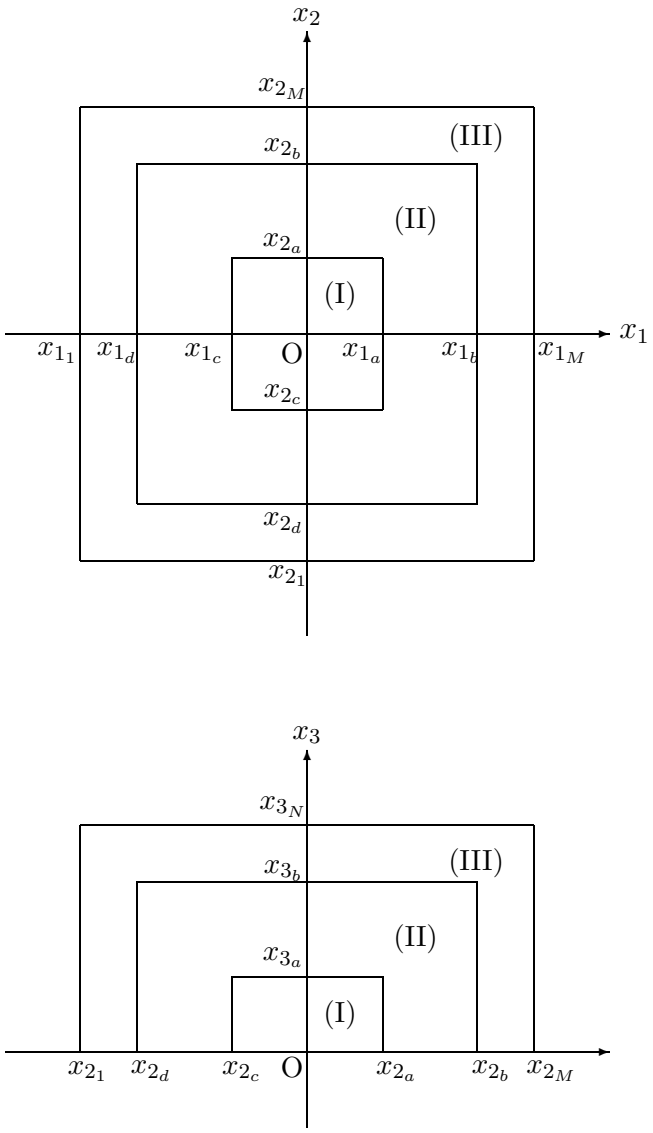

(I) uniform region (smallest spacing)
(II) stretched region
(III) uniform region (largest spacing)

Figure 3.1: Stretched and uniform regions in a stretched grid

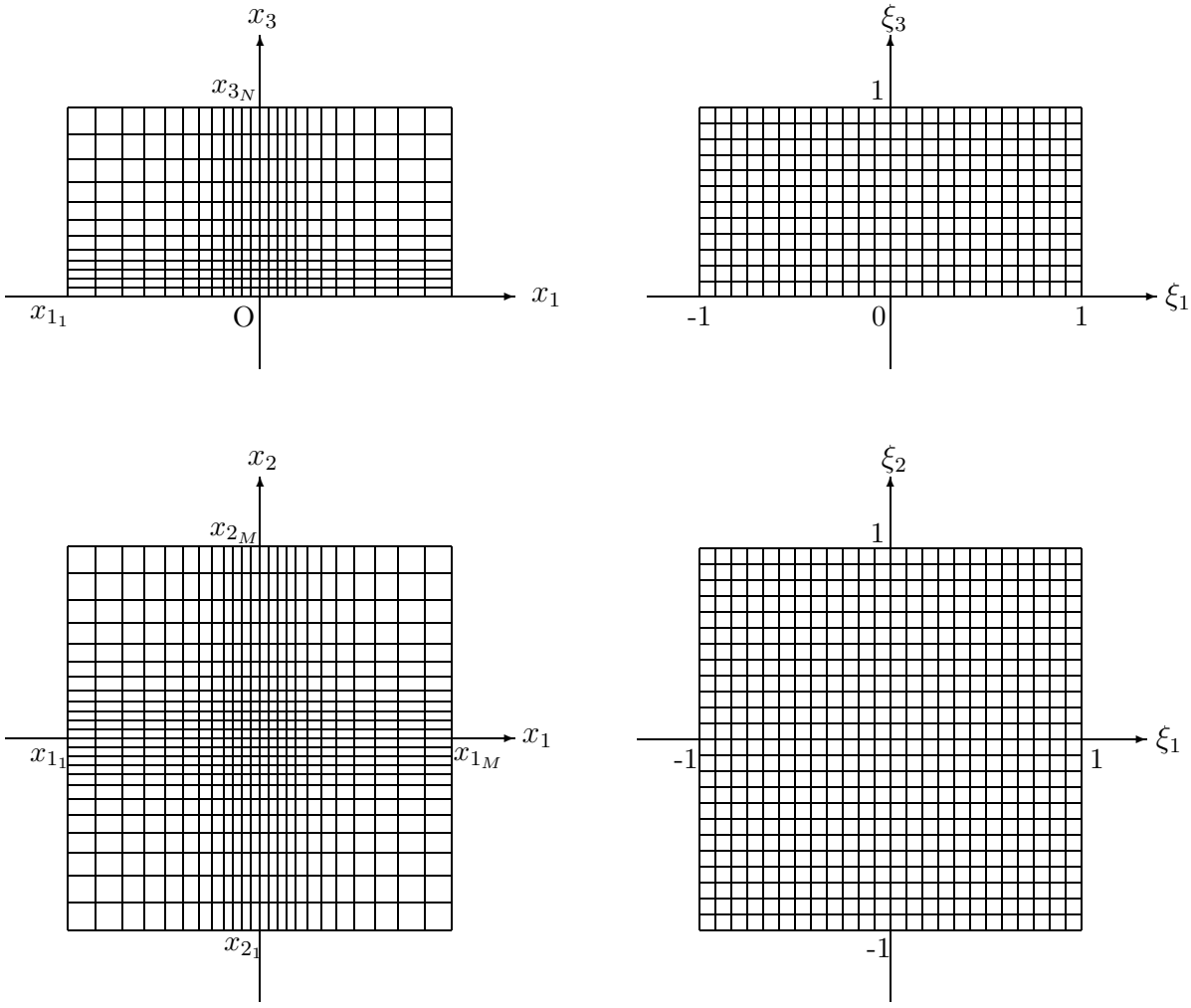

Figure 3.2: Coordinate transformation

$$\xi_{3_n} = \frac{n-1}{N_3-1}, \qquad n{=}1,\ \ldots,\ N_3 \tag{3.3}$$

The non-uniform mesh in the physical space is then obtained by means of coordinate transformation. Since the fifth-order WENO scheme will be used to approximate the spatial derivatives in the governing equations, $x_i(\xi_i)$ must have at least five continuous derivatives. This requirement is met by the following transformation :

$$x_i = \frac{f(\xi_{i_\ell}) - f(\xi_{i_1})}{f(\xi_{i_M}) - f(\xi_{i_1})}(x_{i_M} - x_{i_1}) + x_{i_1}, \quad i = 1, 2,\ \ell = 1, \ldots,\ N_1 \text{ or } N_2 \tag{3.4}$$

$$x_3 = \frac{g(\xi_{3_\ell}) - g(\xi_{3_1})}{g(\xi_{3_N}) - g(\xi_{3_1})}(x_{3_N} - x_{3_1}) + x_{3_1}, \tag{3.5}$$

where

$$f(\xi_{i_\ell}) = \begin{cases} s_1\xi_{i_c} + f_{cd}(\xi_{i_d}) + s_2(\xi_{i_\ell} - \xi_{i_d}) & \text{for } \xi_{i_\ell} < \xi_{i_d}, \\ s_1\xi_{i_c} + f_{cd}(\xi_{i_\ell}) & \text{for } \xi_{i_d} \le \xi_{i_\ell} < \xi_{i_c}, \\ s_1\xi_{i_\ell} & \text{for } \xi_{i_c} \le \xi_{i_\ell} \le \xi_{i_a}, \\ s_1\xi_{i_a} + f_{ab}(\xi_{i_\ell}) & \text{for } \xi_{i_a} < \xi_{i_\ell} \le \xi_{i_b}, \\ s_1\xi_{i_a} + f_{ab}(\xi_{i_b}) + s_2(\xi_{i_\ell} - \xi_{i_b}) & \text{for } \xi_{i_\ell} > \xi_{i_b}, \end{cases} \tag{3.6}$$

with

$$\begin{aligned} f_{cd}(\xi_{i_\ell}) = {} & \frac{1}{13}a_1(\xi_{i_\ell} - \xi_{i_c})^{13} + \frac{1}{12}a_2(\xi_{i_\ell} - \xi_{i_c})^{12} + \frac{1}{11}a_3(\xi_{i_\ell} - \xi_{i_c})^{11} \\ & + \frac{1}{10}a_4(\xi_{i_\ell} - \xi_{i_c})^{10} + \frac{1}{9}a_5(\xi_{i_\ell} - \xi_{i_c})^{9} + \frac{1}{8}a_6(\xi_{i_\ell} - \xi_{i_c})^{8} \\ & + \frac{1}{7}a_7(\xi_{i_\ell} - \xi_{i_c})^{7} + s_1(\xi_{i_\ell} - \xi_{i_c}), \end{aligned} \tag{3.7}$$

$$\begin{aligned} f_{ab}(\xi_{i_\ell}) = {} & \frac{1}{13}b_1(\xi_{i_\ell} - \xi_{i_a})^{13} + \frac{1}{12}b_2(\xi_{i_\ell} - \xi_{i_a})^{12} + \frac{1}{11}b_3(\xi_{i_\ell} - \xi_{i_a})^{11} \\ & + \frac{1}{10}b_4(\xi_{i_\ell} - \xi_{i_a})^{10} + \frac{1}{9}b_5(\xi_{i_\ell} - \xi_{i_a})^{9} + \frac{1}{8}b_6(\xi_{i_\ell} - \xi_{i_a})^{8} \\ & + \frac{1}{7}b_7(\xi_{i_\ell} - \xi_{i_a})^{7} + s_1(\xi_{i_\ell} - \xi_{i_a}), \end{aligned} \tag{3.8}$$

and

$$g(\xi_{3_\ell}) = \begin{cases} s_3\xi_{3_\ell} & \text{for } 0 \le \xi_{3_\ell} \le \xi_{3_a}, \\ s_3\xi_{3_a} + g_{ab}(\xi_{3_\ell}) & \text{for } \xi_{3_a} < \xi_{3_\ell} \le \xi_{3_b}, \\ s_3\xi_{3_a} + g_{ab}(\xi_{3_b}) + s_4(\xi_{3_\ell} - \xi_{3_b}) & \text{for } \xi_{3_\ell} > \xi_{3_b}, \end{cases} \tag{3.9}$$

with

$$g_{ab}(\xi_{i_\ell}) = \frac{1}{13}c_1(\xi_{3_\ell} - \xi_{3_a})^{13} + \frac{1}{12}c_2(\xi_{3_\ell} - \xi_{3_a})^{12} + \frac{1}{11}c_3(\xi_{3_\ell} - \xi_{3_a})^{11} + \frac{1}{10}c_4(\xi_{3_\ell} - \xi_{3_a})^{10} + \frac{1}{9}c_5(\xi_{3_\ell} - \xi_{3_a})^{9} + \frac{1}{8}c_6(\xi_{3_\ell} - \xi_{3_a})^{8} + \frac{1}{7}c_7(\xi_{3_\ell} - \xi_{3_a})^{7} + s_3(\xi_{3_\ell} - \xi_{3_a}), \tag{3.10}$$

The coefficients of the polynomials, $a_\ell,\ b_\ell,\ c_\ell,\ (i = 1,\ \ldots,\ 7)$ in the above equations are given by:

$$\begin{aligned} a_1 &= -462\tfrac{(s_1-s_2)}{(\xi_{i_d}-\xi_{i_c})^{12}}, & a_2 &= 3024\tfrac{(s_1-s_2)}{(\xi_{i_d}-\xi_{i_c})^{11}}, \\ a_3 &= -8316\tfrac{(s_1-s_2)}{(\xi_{i_d}-\xi_{i_c})^{10}}, & a_4 &= 12320\tfrac{(s_1-s_2)}{(\xi_{i_d}-\xi_{i_c})^{9}}, \\ a_5 &= -10395\tfrac{(s_1-s_2)}{(\xi_{i_d}-\xi_{i_c})^{8}}, & a_6 &= 4752\tfrac{(s_1-s_2)}{(\xi_{i_d}-\xi_{i_c})^{7}}, \\ a_7 &= -924\tfrac{(s_1-s_2)}{(\xi_{i_d}-\xi_{i_c})^{6}}, \end{aligned} \tag{3.11}$$

$$\begin{aligned} b_1 &= -462\tfrac{(s_1-s_2)}{(\xi_{i_b}-\xi_{i_a})^{12}}, & b_2 &= 3024\tfrac{(s_1-s_2)}{(\xi_{i_b}-\xi_{i_a})^{11}}, \\ b_3 &= -8316\tfrac{(s_1-s_2)}{(\xi_{i_b}-\xi_{i_a})^{10}}, & b_4 &= 12320\tfrac{(s_1-s_2)}{(\xi_{i_b}-\xi_{i_a})^{9}}, \\ b_5 &= -10395\tfrac{(s_1-s_2)}{(\xi_{i_b}-\xi_{i_a})^{8}}, & b_6 &= 4752\tfrac{(s_1-s_2)}{(\xi_{i_b}-\xi_{i_a})^{7}}, \\ b_7 &= -924\tfrac{(s_1-s_2)}{(\xi_{i_b}-\xi_{i_a})^{6}}, \end{aligned} \tag{3.12}$$

$$\begin{aligned} c_1 &= -462\tfrac{(s_3-s_4)}{(\xi_{i_b}-\xi_{i_a})^{12}}, & c_2 &= 3024\tfrac{(s_3-s_4)}{(\xi_{i_b}-\xi_{i_a})^{11}}, \\ c_3 &= -8316\tfrac{(s_3-s_4)}{(\xi_{i_b}-\xi_{i_a})^{10}}, & c_4 &= 12320\tfrac{(s_3-s_4)}{(\xi_{i_b}-\xi_{i_a})^{9}}, \\ c_5 &= -10395\tfrac{(s_3-s_4)}{(\xi_{i_b}-\xi_{i_a})^{8}}, & c_6 &= 4752\tfrac{(s_3-s_4)}{(\xi_{i_b}-\xi_{i_a})^{7}}, \\ c_7 &= -924\tfrac{(s_3-s_4)}{(\xi_{i_b}-\xi_{i_a})^{6}}. \end{aligned} \tag{3.13}$$

Here s_1 and s_2 are the stretching parameters that control the spacing in regions (I) and (III), respectively, in both x_1- and x_2- directions. The terms, s_3 and s_4 are the stretching parameters that control the spacing in regions (I) and (III), respectively, in the x_3- direction.

3.2 Transformation of Governing Equations

Transformation from the x_i coordinate system in the physical space to the ξ_i coordinate system in the computational space will be operationally more convenient if the governing equations in the previous chapter are expressed in the so-called "strong conservation" form as follows:

$$\frac{\partial \mathcal{U}}{\partial t} + \frac{\partial(\mathcal{F}_1 - \mathcal{F}_{v_1})}{\partial x_1} + \frac{\partial(\mathcal{F}_2 - \mathcal{F}_{v_2})}{\partial x_2} + \frac{\partial(\mathcal{F}_3 - \mathcal{F}_{v_3})}{\partial x_3} = 0 \tag{3.14}$$

where $\mathcal{U}$, $\mathcal{F}_j$, $\mathcal{F}_{v_j}$, $j = 1,\ 2,\ 3$, are the vectors of conserved variables, convective flux, and viscous flux, respectively, in the x_j coordinate system, i.e.,

$$\mathcal{U} = \begin{bmatrix} \bar{\rho} \\ \bar{\rho}\widetilde{u_1} \\ \bar{\rho}\widetilde{u_2} \\ \bar{\rho}\widetilde{u_3} \\ \bar{\rho}\widetilde{E} \end{bmatrix}, \tag{3.15}$$

$$\mathcal{F}_j = \begin{bmatrix} \bar{\rho}\widetilde{u_j} \\ \bar{\rho}\widetilde{u_1}\widetilde{u_j} + \bar{p}\delta_{1j} \\ \bar{\rho}\widetilde{u_2}\widetilde{u_j} + \bar{p}\delta_{2j} \\ \bar{\rho}\widetilde{u_3}\widetilde{u_j} + \bar{p}\delta_{3j} \\ (\bar{\rho}\tilde{E} + \bar{p})\widetilde{u_j} \end{bmatrix}, \tag{3.16}$$

$$\mathcal{F}_{v_j} = \frac{1}{Re} \begin{bmatrix} 0 \\ \widetilde{\sigma}_{1j} - Re\ \tau_{1j} \\ \widetilde{\sigma}_{2j} - Re\ \tau_{2j} \\ \widetilde{\sigma}_{3j} - Re\ \tau_{3j} \\ \widetilde{\sigma}_{1j}\widetilde{u_1} + \widetilde{\sigma}_{2j}\widetilde{u_2} + \widetilde{\sigma}_{3j}\widetilde{u_3} - \frac{1}{Pr(\gamma-1)M^2}\,\widetilde{q}_j - Re\ c_p\ Q_j \end{bmatrix} \tag{3.17}$$

Let the transformation from the physical space (x_i, t) to the computational space (ξ_i, t) be defined by

$$\xi_i = \xi_i(x_i)\ , \qquad i = 1,\ 2,\ 3 \tag{3.18}$$

Then the transformation Jacobian J is given by

$$J = \frac{\partial(\xi_1, \xi_2, \xi_3)}{\partial(x_1, x_2, x_3)} = \epsilon_{kij}\frac{\partial \xi_k}{\partial x_1}\frac{\partial \xi_i}{\partial x_2}\frac{\partial \xi_j}{\partial x_3} = \left(\frac{\partial x_1}{\partial \xi_1}\frac{\partial x_2}{\partial \xi_2}\frac{\partial x_3}{\partial \xi_3}\right)^{-1} \tag{3.19}$$

Applying chain rule, Eq. (3.14) can be written as

$$\frac{\partial U}{\partial t}+\frac{\partial \xi_1}{\partial x_1}\frac{\partial (F_1-F_{v_1})}{\partial \xi_1}+\frac{\partial \xi_2}{\partial x_2}\frac{\partial (F_2-F_{v_2})}{\partial \xi_2}+\frac{\partial \xi_3}{\partial x_3}\frac{\partial (F_3-F_{v_3})}{\partial \xi_3}=0 \tag{3.20}$$

Multiplying Eq. (3.20) by $\frac{1}{J}$, the transformed system of equation in strong conservation form is obtained as follows:

$$\frac{\partial U}{\partial t}+\frac{\partial (F_1-F_{v_1})}{\partial \xi_1}+\frac{\partial (F_2-F_{v_2})}{\partial \xi_2}+\frac{\partial (F_3-F_{v_3})}{\partial \xi_3}=0 \tag{3.21}$$

where

$$U=\frac{1}{J}\begin{bmatrix}\bar{\rho}\\ \bar{\rho}\widetilde{u_1}\\ \bar{\rho}\widetilde{u_2}\\ \bar{\rho}\widetilde{u_3}\\ \bar{\rho}\widetilde{E}\end{bmatrix}, \tag{3.22}$$

$$F_1=\frac{1}{J}\frac{\partial \xi_1}{\partial x_1}\begin{bmatrix}\bar{\rho}\widetilde{u_1}\\ \bar{\rho}\widetilde{u_1}^2+\bar{p}\\ \bar{\rho}\widetilde{u_2}\widetilde{u_1}\\ \bar{\rho}\widetilde{u_3}\widetilde{u_1}\\ (\bar{\rho}\tilde{E}+\bar{p})\widetilde{u_1}\end{bmatrix}, \tag{3.23}$$

$$F_2=\frac{1}{J}\frac{\partial \xi_2}{\partial x_2}\begin{bmatrix}\bar{\rho}\widetilde{u_2}\\ \bar{\rho}\widetilde{u_1}\widetilde{u_2}\\ \bar{\rho}\widetilde{u_2}^2+\bar{p}\\ \bar{\rho}\widetilde{u_3}\widetilde{u_2}\\ (\bar{\rho}\tilde{E}+\bar{p})\widetilde{u_2}\end{bmatrix}, \tag{3.24}$$

$$F_3=\frac{1}{J}\frac{\partial \xi_3}{\partial x_3}\begin{bmatrix}\bar{\rho}\widetilde{u_3}\\ \bar{\rho}\widetilde{u_1}\widetilde{u_3}\\ \bar{\rho}\widetilde{u_2}\widetilde{u_3}\\ \bar{\rho}\widetilde{u_3}^2+\bar{p}\\ (\bar{\rho}\tilde{E}+\bar{p})\widetilde{u_3}\end{bmatrix}, \tag{3.25}$$

$$F_{v_1}=\frac{1}{J}\frac{\partial \xi_1}{\partial x_1}\frac{1}{Re}\begin{bmatrix}0\\ \widetilde{\sigma}_{11}-Re\ \tau_{11}\\ \widetilde{\sigma}_{21}-Re\ \tau_{21}\\ \widetilde{\sigma}_{31}-Re\ \tau_{31}\\ \widetilde{\sigma}_{11}\widetilde{u_1}+\widetilde{\sigma}_{21}\widetilde{u_2}+\widetilde{\sigma}_{31}\widetilde{u_3}-\frac{1}{Pr(\gamma-1)M^2}\widetilde{q}_1-Re\ c_p\ Q_1\end{bmatrix} \tag{3.26}$$

$$F_{v_2} = \frac{1}{J}\frac{\partial \xi_2}{\partial x_2}\frac{1}{Re}\begin{bmatrix} 0 \\ \widetilde{\sigma}_{12} - Re\ \tau_{12} \\ \widetilde{\sigma}_{22} - Re\ \tau_{22} \\ \widetilde{\sigma}_{32} - Re\ \tau_{32} \\ \widetilde{\sigma}_{12}\widetilde{u_1} + \widetilde{\sigma}_{22}\widetilde{u_2} + \widetilde{\sigma}_{32}\widetilde{u_3} - \frac{1}{Pr(\gamma-1)M^2}\,\widetilde{q}_2 - Re\ c_p\ Q_2 \end{bmatrix} \tag{3.27}$$

$$F_{v_3} = \frac{1}{J}\frac{\partial \xi_3}{\partial x_3}\frac{1}{Re}\begin{bmatrix} 0 \\ \widetilde{\sigma}_{13} - Re\ \tau_{13} \\ \widetilde{\sigma}_{23} - Re\ \tau_{23} \\ \widetilde{\sigma}_{33} - Re\ \tau_{33} \\ \widetilde{\sigma}_{13}\widetilde{u_1} + \widetilde{\sigma}_{23}\widetilde{u_2} + \widetilde{\sigma}_{33}\widetilde{u_3} - \frac{1}{Pr(\gamma-1)M^2}\,\widetilde{q}_3 - Re\ c_p\ Q_3 \end{bmatrix} \tag{3.28}$$

with

$$\widetilde{\sigma}_{ij} = \widetilde{\mu}\left(\frac{\partial \xi_l}{\partial x_j}\frac{\partial \widetilde{u}_i}{\partial \xi_l} + \frac{\partial \xi_l}{\partial x_i}\frac{\partial \widetilde{u}_j}{\partial \xi_l} - \frac{2}{3}\frac{\partial \xi_l}{\partial x_k}\frac{\partial \widetilde{u}_k}{\partial \xi_l}\delta_{ij}\right), \tag{3.29}$$

$$\widetilde{q}_j = -\widetilde{\kappa}\,\frac{\partial \xi_l}{\partial x_j}\frac{\partial \widetilde{T}}{\partial \xi_l}, \tag{3.30}$$

and

$$\frac{\partial \xi_l}{\partial x_j} = 0 \quad \text{for} \quad l \neq j. \tag{3.31}$$

The SGS stress tensor τ_{ij} is given by

$$\tau_{ij} = -2C\bar{\rho}(\frac{\bar{\Delta}_\xi}{J^{\frac{1}{3}}})^2\,|\widetilde{S}|\,\left(\widetilde{S}_{ij} - \frac{1}{3}\widetilde{S}_{kk}\delta_{ij}\right) + \frac{1}{3}\tau_{kk}\delta_{ij} \tag{3.32}$$

with

$$\tau_{kk} = 2C_I\,\bar{\rho}\,(\frac{\bar{\Delta}_\xi}{J^{\frac{1}{3}}})^2\,|\widetilde{S}|^2 \tag{3.33}$$

where

$$C = \frac{\widehat{\overline{\mathcal{L}_{ij}^d}\overline{\mathcal{M}_{ij}}}}{\widehat{\overline{\mathcal{M}_{km}}\overline{\mathcal{M}_{km}}}}, \qquad \mathcal{L}_{ij}^d = \mathcal{L}_{ij} - \frac{1}{3}\mathcal{L}_{kk}\delta_{ij} \tag{3.34}$$

$$C_I = \frac{\widehat{\overline{\mathcal{L}_{kk}}}}{2\,(\frac{\hat{\bar{\Delta}}_\xi}{J^{\frac{1}{3}}})^2\,\widehat{\bar{\rho}}\,\widehat{\overline{|\widetilde{S}|^2}} - 2\,\widehat{\overline{(\frac{\bar{\Delta}_\xi}{J^{\frac{1}{3}}})^2\bar{\rho}|\widetilde{S}|^2}}} \tag{3.35}$$

$$\mathcal{L}_{ij} = \widehat{\bar{\rho}\widetilde{u}_i\widetilde{u}_j} - \frac{\widehat{\bar{\rho}\widetilde{u}_i}\,\widehat{\bar{\rho}\widetilde{u}_j}}{\widehat{\bar{\rho}}} \tag{3.36}$$

$$\mathcal{M}_{ij} = -2(\frac{\widehat{\Delta}_\xi}{J^{\frac{1}{3}}})^2\widehat{\bar{\rho}}|\widehat{\widetilde{S}}|\widehat{\widetilde{S}^a_{ij}} + 2(\frac{\bar{\Delta}_\xi}{J^{\frac{1}{3}}})^2\widehat{\bar{\rho}|\widetilde{S}|\widetilde{S}^a_{ij}} \tag{3.37}$$

$$\widetilde{S}_{ij} = \frac{1}{2}\left(\frac{\partial\xi_l}{\partial x_j}\frac{\partial\widetilde{u}_i}{\partial\xi_l} + \frac{\partial\xi_l}{\partial x_i}\frac{\partial\widetilde{u}_j}{\partial\xi_l}\right), \tag{3.38}$$

$$\widetilde{S}^a_{ij} = \widetilde{S}_{ij} - \frac{1}{3}\widetilde{S}_{ij}\delta_{ij} \tag{3.39}$$

$$|\widetilde{S}_{ij}| = \sqrt{\frac{1}{2}}\left(\frac{\partial\xi_l}{\partial x_j}\frac{\partial\widetilde{u}_i}{\partial\xi_l} + \frac{\partial\xi_l}{\partial x_i}\frac{\partial\widetilde{u}_j}{\partial\xi_l}\right). \tag{3.40}$$

$$\bar{\Delta}_\xi = (\Delta_{\xi_1}\,\Delta_{\xi_2}\,\Delta_{\xi_3})^{\frac{1}{3}} \tag{3.41}$$

$$\widehat{\Delta}_\xi = 2\bar{\Delta}_\xi \tag{3.42}$$

Here Δ_{ξ_i} is the grid size in the ξ_i-direction in the computational domain.

The SGS heat flux is given by

$$\mathcal{Q}_j = -C\frac{(\bar{\Delta}_\xi/J^{\frac{1}{3}})^2\bar{\rho}\,|\widetilde{S}|}{Pr_T}\frac{\partial\xi_l}{\partial x_j}\frac{\partial\widetilde{T}}{\partial\xi_l} \tag{3.43}$$

where

$$Pr_T = \frac{C\widehat{\overline{\mathcal{N}_j}\,\overline{\mathcal{N}_j}}}{\widehat{\overline{\mathcal{K}_k}\,\overline{\mathcal{N}_k}}} \tag{3.44}$$

$$\mathcal{N}_j = -(\frac{\widehat{\Delta}}{J})^2\,\widehat{\bar{\rho}}\,|\widehat{\widetilde{S}}|\frac{\partial\xi_l}{\partial x_j}\frac{\partial\widehat{\widetilde{T}}}{\partial\xi_l} + (\frac{\bar{\Delta}}{J})^2\left(\bar{\rho}\widehat{|\widetilde{S}|\frac{\partial\xi_l}{\partial x_j}\frac{\partial\widetilde{T}}{\partial\xi_l}}\right) \tag{3.45}$$

$$\mathcal{K}_j \;=\; \widehat{\bar{\rho}\widetilde{u}_j\widetilde{T}} - \frac{\widehat{\bar{\rho}\widetilde{u}_j}\,\widehat{\bar{\rho}\widetilde{T}}}{\widehat{\bar{\rho}}} \tag{3.46}$$

Chapter 4

NUMERICAL METHOD

Using the method of lines [67], temporal and spatial discretization of Eq. (3.21) are carried out independently. The discretization can be written in the semi-discrete form as

$$\frac{dU}{dt} = -L(U) \tag{4.1}$$

where $L(U)$ is the high-order discrete representation of

$$\frac{\partial(F_1 - F_{v_1})}{\partial \xi_1} + \frac{\partial(F_2 - F_{v_2})}{\partial \xi_2} + \frac{\partial(F_3 - F_{v_3})}{\partial \xi_3} \tag{4.2}$$

4.1 Spatial Discretization

The spatial derivatives can be approximated dimension by dimension; for example, when approximating $\frac{\partial(F_1 - F_{v_1})}{\partial \xi_1}$, one fixes ξ_j, $j = 2, 3$ and uses a one-dimensional approximation in the direction of ξ_1. Hence, for simplicity we restrict our attention to one direction and consider only the approximation of $\frac{\partial(F - F_v)}{\partial \xi}$, in which the subscript "j" has been dropped.

The spatial derivatives of the inviscid flux F and viscous flux F_v will be approximated separately. The former will be approximated using the fifth-order WENO scheme of G. S. Jiang and C.-W. Shu [34, 68, 70], whereas the latter is approximated using a fourth-order central-difference scheme.

4.1.1 Numerical Approximation to the Spatial Derivatives of Inviscid Flux

Following Shu [69], we consider the following one-dimensional hyperbolic system of conservation laws:

$$\frac{\partial U}{\partial t} + \frac{\partial F(U)}{\partial \xi} = 0 \tag{4.3}$$

where $U = (u_1, \ldots, u_m)$ is the vector of conserved variables, $F(U) = (f_1, \ldots, f_m)$ is a flux vector. Let the domain be discretized into a uniform grid

$$\xi_i = i\Delta\xi, \quad i = 1, \ldots, N.$$

with $I_i \equiv \left[\xi_{i-\frac{1}{2}},\ \xi_{i+\frac{1}{2}}\right]$ define a typical cell on the grid. Then at every node ξ_i, the semi-discrete finite difference scheme for Eq. (4.3) is of the form

$$\frac{dU}{dt} = -L(U)\ , \tag{4.4}$$

where $L(U)$ is the spatial approximations to the spatial derivative $\frac{\partial F_i}{\partial \xi}$.

The spatial operator can be written in conservative form as

$$L(U_i) = \frac{1}{\Delta\xi}\left[\hat{F}_{i+\frac{1}{2}} - \hat{F}_{i-\frac{1}{2}}\right] \tag{4.5}$$

where $\hat{F}_{i+\frac{1}{2}}$ and $\hat{F}_{i-\frac{1}{2}}$ are the numerical fluxes to be computed using the fifth-order WENO scheme.

4.1.1.1 Reconstruction Procedure for Numerical Flux

To illustrate how the numerical flux $f_{i+\frac{1}{2}}$ is constructed, we use the following one-dimensional scalar conservation law as an example [69]:

$$\frac{\partial u}{\partial t} + \frac{\partial f}{\partial \xi} = 0, \tag{4.6}$$

Eq. (4.6) can be written in a semi-discrete form as

$$\frac{du}{dt} = -L(u)\ , \tag{4.7}$$

where $L(u)$ is the spatial approximation to the spatial derivative $\frac{\partial f}{\partial \xi}$.

If at each discrete point $\xi_i = i\Delta\xi,\ (i = 1,\ 2,\ \ldots,\ N)$ on a uniform grid, there exists a function $h(x)$ such that

$$f_i = \frac{1}{\Delta\xi} \int_{\xi_{i-\frac{1}{2}}}^{\xi_{i+\frac{1}{2}}} h(\eta)\ d\eta, \tag{4.8}$$

then

$$\frac{\partial f_i}{\partial \xi} = \frac{1}{\Delta\xi} \left[h(\xi_{i+\frac{1}{2}}) - h(\xi_{i-\frac{1}{2}}) \right] \tag{4.9}$$

Therefore, the r-th order accurate approximation to $\frac{\partial f}{\partial \xi}$ can be obtained if $h(\xi_{i+\frac{1}{2}})$ is approximated to a r-th order accuracy by a numerical flux $\hat{f}_{i+\frac{1}{2}}$. Hence we have

$$\frac{\partial f_i}{\partial \xi} = \frac{1}{\Delta\xi} \left[\hat{f}(\xi_{i+\frac{1}{2}}) - \hat{f}(\xi_{i-\frac{1}{2}}) \right] + O(\Delta\xi^r) \tag{4.10}$$

The primitive function of $h(\xi)$ in Eq. (4.9) may be defined by

$$H(\xi) = \int_{-\infty}^{\xi} h(\eta)\ d\eta, \tag{4.11}$$

which implies that

$$H(\xi_{i+\frac{1}{2}}) \ = \ \int_{-\infty}^{\xi_{i+\frac{1}{2}}} h(\eta)\ d\eta \ = \ \sum_{j=-\infty}^{i} \int_{\xi_{j-\frac{1}{2}}}^{\xi_{j+\frac{1}{2}}} h(\eta) d\eta \ = \Delta\xi \sum_{j=-\infty}^{i} f_j \tag{4.12}$$

Eq. (4.12) indicates that by identifying the given point values $\{f_i\}$ as the cell average of another function $h(\xi)$, the primitive function $H(\xi)$ is known exactly at the cell interfaces $\xi = \xi_{i+\frac{1}{2}}$.

Further, if we let $P(\xi)$ be the unique polynomial of degree at most r that interpolates $H(\xi)$ at the following $r+1$ points:

$$\xi_{i-r-\frac{1}{2}},\ \ldots,\ \xi_{i+s+\frac{1}{2}},$$

i.e.,

$$P(\xi) = H(\xi) + O(\Delta\xi^{r+1}), \tag{4.13}$$

where

$$P(\xi_{j+\frac{1}{2}}) = H(\xi_{j+\frac{1}{2}}), \qquad j = i-r,\ \ldots,\ i+s, \tag{4.14}$$

then the derivative of $P(\xi)$, denoted by $p(\xi)$, which is of degree r-1, approximates $h(\xi)$, i.e.,

$$h(\xi) = p(\xi) + O(\Delta\xi^r), \tag{4.15}$$

Thus, the numerical flux $\hat{f}_{i+\frac{1}{2}}$ needed to approximate $\hat{h}_{i+\frac{1}{2}}$ is given by $p(\xi_{i+\frac{1}{2}})$, i.e.

$$\hat{f}_{i+\frac{1}{2}} = p(\xi_{i+\frac{1}{2}}) \tag{4.16}$$

The polynomial $p(\xi)$ may be obtained using the Lagrange interpolation formula and the numerical flux $\hat{f}_{i+\frac{1}{2}}$ can then be expressed as

$$\hat{f}_{i+\frac{1}{2}} = \sum_{j=0}^{r-1} c_{kj}\ f_{i-k+j}, \quad k = 0,\ \ldots,\ r-1 \tag{4.17}$$

where c_{kj} are predetermined constants. The values of c_{kj} for the order of accuracy between r=1 and r=7 can be found in [68, 69].

4.1.1.2 Construction of High-Order Numerical Flux Using the Fifth-Order WENO Scheme

Eq. (4.17) indicates that there are r candidate stencils given by [69]:

$$S_i^{(k)} = \{\xi_{i-k},\ \xi_{i-k+(r-2)},\ \ldots,\ \xi_{i-k+(r-1)}\}, \qquad k = 0,\ 1,\ \ldots,\ r-1. \tag{4.18}$$

that one can use to construct an r-th order interpolating function for $\hat{f}_{i+\frac{1}{2}}$. Instead of using only one of the candidate stencils to form a r-th order numerical flux, the WENO scheme of Liu *et al.* [44] takes a convex combination of all $\hat{f}_{i+\frac{1}{2}}^{(k)}$ to obtain a $(2r-1)$-th order numerical flux [44, 34]. The WENO approximation of $\hat{f}_{i+\frac{1}{2}}$ assumes the form

$$\hat{f}_{i+\frac{1}{2}} = \sum_{k=0}^{r-1} w_k\ \hat{f}_{i+\frac{1}{2}}^{(k)}, \qquad k = 0, \ldots, r-1 \tag{4.19}$$

where w_r are the weights that satisfy the following conditions

$$w_k \geq 0, \qquad \sum_{k=0}^{r-1} w_k = 1 \tag{4.20}$$

The choice of the weights are based on the following two properties of WENO approximation [35]:

(1) If $h(x)$ is smooth near $\xi_{i+\frac{1}{2}}$, the approximated value $\hat{f}_{i+\frac{1}{2}}$ of $h(\xi_{i+\frac{1}{2}})$ satisfies

$$\hat{f}_{i+\frac{1}{2}} = h(\xi_{i+\frac{1}{2}}) + O(\triangle\xi^{2r-1})$$

(2) If $h(x)$ is discontinuous near $\xi_{i+\frac{1}{2}}$, no Gibbs phenomena (i.e., spurious oscillations) occur.

By requiring that the weights be C^∞ smooth functions and computationally efficient, Jiang and Shu [34, 70] define the weights as:

$$w_k = \frac{\hat{w}_k}{\sum_{l=0}^{r-1} \hat{w}_l}, \qquad k = 0, \ldots, r-1 \tag{4.21}$$

with

$$\hat{w}_k = \frac{d_k}{(\epsilon + IS_k)^2} \tag{4.22}$$

where $\epsilon > 0$ is introduced to prevent the denominator from becoming 0. Here we set $\epsilon = 10^{-10}$.

The smooth indicator IS_k of the stencil $S_i^{(k)}$ is defined by

$$IS_k = \sum_{l=1}^{r-1} \int_{\xi_{i-\frac{1}{2}}}^{\xi_{i+\frac{1}{2}}} \triangle\xi^{2l-1} \left(\frac{\partial^l p_k(\xi)}{\partial \xi^l} \right)^2 d\xi \tag{4.23}$$

For the 5th-order WENO scheme, $r = 3$; therefore a five-point stencil that consists of three 3-point sub-stencils as shown in Fig.4.1 is required.

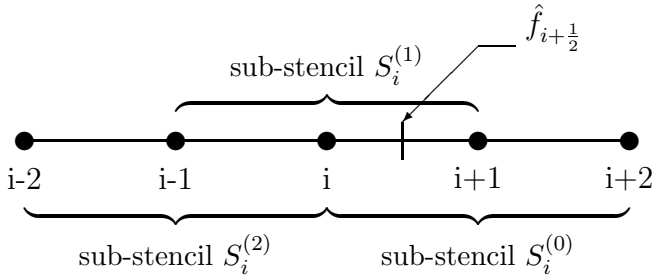

Figure 4.1: Stencil for 5th-order WENO scheme

The third-order accurate approximations $\hat{f}_{i+\frac{1}{2}}^{(k)}$ for each sub-stencil $S_i^{(k)}$, $(k = 0,\ 1,\ 2)$ are given by

$$\begin{aligned}
\hat{f}^{(0)}_{i+\frac{1}{2}} &= \tfrac{1}{3}f(u_{i-2}) - \tfrac{7}{6}f(u_{i-1}) + \tfrac{11}{6}f(u_i), \\
\hat{f}^{(1)}_{i+\frac{1}{2}} &= -\tfrac{1}{6}f(u_{i-1}) + \tfrac{5}{6}f(u_i) + \tfrac{1}{3}f(u_{i+1}), \\
\hat{f}^{(2)}_{i+\frac{1}{2}} &= \tfrac{1}{3}f(u_i) + \tfrac{5}{6}f(u_{i+1}) - \tfrac{1}{6}f(u_{i+2})
\end{aligned} \tag{4.24}$$

The nonlinear weights w_k are given by

$$w_k = \frac{\hat{w}_k}{\sum_{l=0}^{2} \hat{w}_l}, \qquad \hat{w}_k = \frac{d_k}{(\epsilon + IS_k)^2}, \quad k = 0, 1, 2 \tag{4.25}$$

where the linear weights d_k are given by

$$d_0 = \frac{3}{10}, \quad d_1 = \frac{3}{5}, \quad d_2 = \frac{1}{10} \tag{4.26}$$

and the smoothness indicators IS_k are given by

$$\begin{aligned}
IS_0 &= \tfrac{13}{12}\left[f(u_i) - 2f(u_{i+1}) + f(u_{i+2})\right]^2 + \tfrac{1}{4}\left[3f(u_i) - 4f(u_{i+1}) + f(u_{i+2})\right]^2, \\
IS_1 &= \tfrac{13}{12}\left[f(u_{i-1}) - 2f(u_i) + f(u_{i+1})\right]^2 + \tfrac{1}{4}\left[f(u_{i-1}) - 4f(u_{i+1})\right]^2, \\
IS_2 &= \tfrac{13}{12}\left[f(u_{i-2}) - 2f(u_{i-1}) + f(u_i)\right]^2 + \tfrac{1}{4}\left[f(u_{i-2}) - 4f(u_{i-1}) + 3f(u_i)\right]^2.
\end{aligned} \tag{4.27}$$

4.1.1.3 Local Characteristic Decomposition

The nonlinear system of conservation laws in Eq. (4.3) can be written in the quasilinear form as:

$$\frac{\partial U}{\partial t} + A(U)\,\frac{\partial U}{\partial \xi} = 0 \tag{4.28}$$

where $A(U) = \frac{\partial F}{\partial U}$ is the 5×5 Jacobian matrix.

Eq. (4.28) can be linearized locally at each cell interface $\xi_{i+\frac{1}{2}}$ to produce a constant coefficient linear hyperbolic system of the form

$$\frac{\partial U}{\partial t} + \bar{A}\,\frac{\partial U}{\partial \xi} = 0 \tag{4.29}$$

where $\bar{A} = A(U_{i+\frac{1}{2}})$ is the Roe-average Jacobian matrix which approximates $A(U)$ at the Roe-average state $U_{i+\frac{1}{2}}$. The matrix $\bar{A}$ is required to satisfy the following conditions [42] :

$$\begin{array}{ll} (i) & \bar{A}(U_i, U_{i+1})\,(U_{i+1} - U_i) = F(U_{i+1}) - F(U_i), \\ (ii) & \bar{A}(U_i, U_{i+1}) \text{ is diagonalizable with real eigenvalues,} \\ (iii) & \bar{A}(U_i, U_{i+1}) \;\rightarrow\; F'(U_{i+\frac{1}{2}}) \text{ smoothly as } U_i,\; U_{i+1} \;\rightarrow\; U_{i+\frac{1}{2}} \end{array} \tag{4.30}$$

Based on the conditions in Eq. (4.30), Roe-average quantities, namely, the Roe-average density $\rho_{i+\frac{1}{2}}$, velocities $u_{1_{i+\frac{1}{2}}}$, $u_{2_{i+\frac{1}{2}}}$, $u_{3_{i+\frac{1}{2}}}$ and total specific enthalpy $h_{T_{i+\frac{1}{2}}}$ are given by :

$$\rho_{i+\frac{1}{2}} = \sqrt{\rho_{i+1}\;\rho_i} \tag{4.31}$$

$$u_{1_{i+\frac{1}{2}}} = \frac{\sqrt{\rho_{i+1}}\;u_{1_{i+1}} \;+\; \sqrt{\rho_i}\;u_{1_i}}{\sqrt{\rho_{i+1}} \;+\; \sqrt{\rho_i}} \tag{4.32}$$

$$u_{2_{i+\frac{1}{2}}} = \frac{\sqrt{\rho_{i+1}}\;u_{2_{i+1}} \;+\; \sqrt{\rho_i}\;u_{2_i}}{\sqrt{\rho_{i+1}} \;+\; \sqrt{\rho_i}} \tag{4.33}$$

$$u_{3_{i+\frac{1}{2}}} = \frac{\sqrt{\rho_{i+1}}\;u_{3_{i+1}} \;+\; \sqrt{\rho_i}\;u_{3_i}}{\sqrt{\rho_{i+1}} \;+\; \sqrt{\rho_i}} \tag{4.34}$$

$$h_{T_{i+\frac{1}{2}}} = \frac{\sqrt{\rho_{i+1}}\;h_{Ti+1} \;+\; \sqrt{\rho_i}\;h_{T_i}}{\sqrt{\rho_{i+1}} \;+\; \sqrt{\rho_i}} \tag{4.35}$$

Using these Roe-average quantities, the vector $U_{i+\frac{1}{2}}$ and the matrix $\bar{A}$ can then be determined.

Since Eq. (4.29) is hyperbolic, $\bar{A}$ is diagonalizable with real eigenvalues, so that

$$\bar{A} = R\Lambda R^{-1} \tag{4.36}$$

where $\Lambda = \Lambda(U_{i+\frac{1}{2}}) = diag(\lambda_1,\;\lambda_2,\;\ldots,\;\lambda_5)$ is a diagonal matrix of eigenvalues and $R = R(U_{i+\frac{1}{2}}) = [r_1,\;r_2,\;\ldots,\;r_5]$ is the matrix of right eigenvectors (r_i).

It follows that Eq. (4.29) can be decomposed into 5 independent equations at each cell interface $\xi_{i+\frac{1}{2}}$ by left multiplying Eq. (4.29) by matrix R^{-1}. The characteristic flux F^c is then given by

$$F^c = R^{-1} \cdot F \tag{4.37}$$

Therefore, the characteristic numerical flux at cell interface $\hat{F}^c_{i+\frac{1}{2}}$ can be interpolated component by component according to the procedure discussed in the previous section. The

numerical flux $\hat{F}_{i+\frac{1}{2}}$ in Eq. (4.5) can then be obtained by projecting $\hat{F}^c_{i+\frac{1}{2}}$ from the characteristic space to the original "physical space" by

$$\hat{F}_{i+\frac{1}{2}} = R \cdot \hat{F}^c_{i+\frac{1}{2}} \tag{4.38}$$

4.1.1.4 Flux Splitting and Upwinding

For achieving numerical stability and for avoiding entropy violating solutions, upwinding and flux splitting approaches are needed in constructing the flux.

In the flux splitting approach, the flux is written as [34, 35, 69]

$$F(U) = F^+(U) + F^-(U), \tag{4.39}$$

where

$$\frac{dF^+(U)}{dU} \geq 0, \qquad \frac{dF^-(U)}{dU} \leq 0. \tag{4.40}$$

so that for the equation $U_t + F^+_\xi = 0$, waves propagate in the increasing ξ direction, while for $U_t + F^-_\xi = 0$, waves propagate in the negative ξ direction.

Therefore, the characteristic numerical flux is written as

$$F^c = F^{c^+} + F^{c^-} \tag{4.41}$$

The splitting is performed using the Local Lax-Friedrichs(LLF) scheme given by [1] :

$$f^{c^+}_{s;i} = l_{s;\, i+\frac{1}{2}} \cdot \frac{1}{2}(F^c_i + \hat{\lambda}_{s;\, i+\frac{1}{2}}\, U_i)\ ; \tag{4.42}$$

$$f^{c^-}_{s;i} = l_{s;\, i+\frac{1}{2}} \cdot \frac{1}{2}(F^c_{i+1} - \hat{\lambda}_{s;\, i+\frac{1}{2}}\, U_{i+1})\ ; \tag{4.43}$$

$$\hat{\lambda}_{s;\, i+\frac{1}{2}} = \chi\ max(|\lambda_{s;\, i+\frac{1}{2}}|,\ |\lambda_{s;\, i}|,\ |\lambda_{s;\, i+1}|). \tag{4.44}$$

where $f^{c^+}_{s;i}$ and $f^{c^-}_{s;i}$ are the s-th component of $F^{c^+}_i$ and $F^{c^-}_i$ respectively. The eigenvalue $\lambda_{s;\, i+\frac{1}{2}}$ is the s-th component of the matrix $\Lambda(U_{i+\frac{1}{2}})$. The left eigenvector $l_{s;\, i+\frac{1}{2}}$ corresponding to the eigenvalue $\lambda_{s;\, i+\frac{1}{2}}$ is the s-th row of the matrix $R^{-1}(U_{i+\frac{1}{2}})$. The amount of dissipation in the scheme is controlled by the value of χ which is typically in the range of 1.1 to 1.3.

The WENO approximation procedure is then applied to $f^{c^+}_{s;i}$ and $f^{c^-}_{s;i}$ to obtain $\hat{f}^+_{s;\, i+\frac{1}{2}}$ and $\hat{f}^-_{s;\, i+\frac{1}{2}}$ respectively. Finally, the characteristic numerical flux $\hat{f}^c_{s;\, i+\frac{1}{2}}$ required in Eq. (4.37) is obtained by summing up these positive and negative fluxes:

$$\hat{f}^{c}_{s;\, i+\frac{1}{2}} = \hat{f}^{c^+}_{s;\, i+\frac{1}{2}} + \hat{f}^{c^-}_{s;\, i+\frac{1}{2}}. \tag{4.45}$$

Since the physical domain of dependence lies to the left for right-running waves and to the right for left-running waves, numerical scheme must model this behavior by using upwind-biased stencils. Therefore the numerical stencils for computing $\hat{f}^{c^+}_{s;\, i+\frac{1}{2}}$ and $\hat{f}^{c^-}_{s;\, i+\frac{1}{2}}$ are different. For the fifth-order WENO scheme, the stencils for computing positive and negative numerical fluxes at cell interface are shown in Figure 4.2.

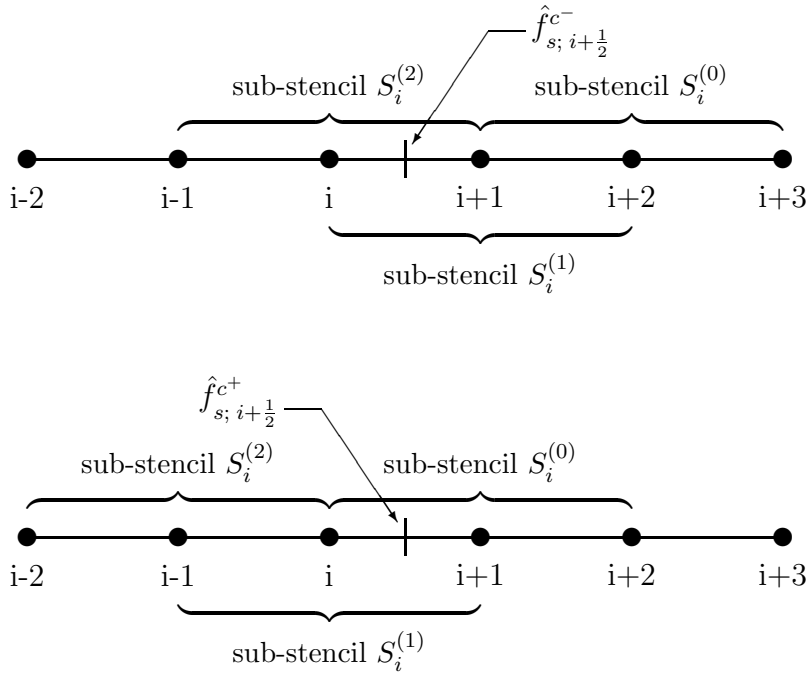

Figure 4.2: Upwind-biased stencil for $\hat{f}^{c^+}_{s;\, i+\frac{1}{2}}$ and $\hat{f}^{c^-}_{s;\, i+\frac{1}{2}}$

4.1.1.5 Boundary Treatment for WENO Scheme

It was shown in the previous section that numerical approximation to the spatial derivatives at each grid point requires a five-point stencil. Therefore, functional values outside the computational domain will be required when approximating the spatial derivatives near the boundaries. To satisfy this requirement, the computational domain is augmented by adding external boundary points, called the ghost points as shown in Figure 4.3. For the fifth-order WENO scheme, three extra points are required. In order to enforce the physical boundary conditions, numerical boundary conditions have to be applied to these ghost points. For solid boundary, the reflective boundary condition is employed. For inflow/outflow boundary, the non-reflective boundary condition is implemented [85, 69].

(a) Ghost points for reflective boundary

In order to impose the no-penetration boundary condition at a solid boundary, the solid boundary is treated as a reflective boundary (cf. Figure 4.3). Let B_0, B_{-1} and B_{-2} denote the ghost points which are the mirror images along the ξ_3-direction of the first three points in the computational domain, B_2, B_3 and B_4, respectively. Then, the values at the ghost points are given by:

$$
\begin{array}{lll}
\text{Density :} & \rho|_{B_0} = \rho|_{B_2}, \\
& \rho|_{B_{-1}} = \rho|_{B_3}, \\
& \rho|_{B_{-2}} = \rho|_{B_4}, \\
\\
\xi_1\text{-velocity :} & u_1|_{B_0} = u_1|_{B_2}, \\
& u_1|_{B_{-1}} = u_1|_{B_3}, \\
& u_1|_{B_{-2}} = u_1|_{B_4}, \\
\\
\xi_2\text{-velocity :} & u_2|_{B_0} = u_2|_{B_2}, \\
& u_2|_{B_{-1}} = u_2|_{B_3}, \\
& u_2|_{B_{-2}} = u_2|_{B_4}, \\
\\
\xi_3\text{-velocity :} & u_3|_{B_0} = -u_3|_{B_2}, \\
& u_3|_{B_{-1}} = -u_3|_{B_3}, \\
& u_3|_{B_{-2}} = -u_3|_{B_4}, \\
\\
\text{Pressure :} & p|_{B_0} = p|_{B_2}, \\
& p|_{B_{-1}} = p|_{B_3}, \\
& p|_{B_{-2}} = p|_{B_4}
\end{array}
\tag{4.46}
$$

Similarly, at the upper solid boundary, the states of the ghost points are the reflected state of their respective mirror image about the solid boundary in the computational domain.

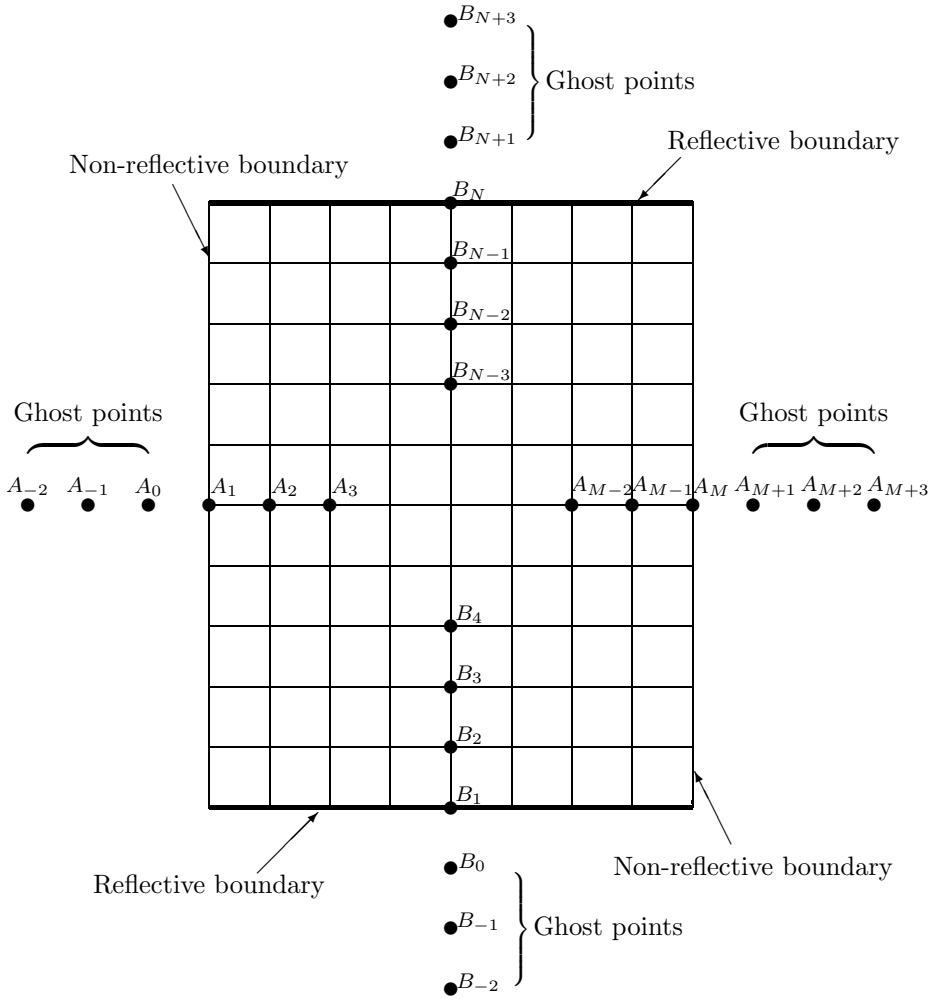

Ghost points for reflective boundary:

(1) States at points B_0, B_{-1}, B_{-2} are reflected states of B_2, B_3, B_4 , respectively.

(2) States at points $B_{N+1}, B_{N+2}, B_{N+3}$ are reflected states of $B_{N-1}, B_{N-2}, B_{N-3}$, respectively.

Ghost points for non-reflective boundary:

(1) Inflow : $A_{-2} = A_{-1} = A_0 = A_1$; $A_{M+3} = A_{M+2} = A_{M+1} = A_M$.

(2) Outflow : States at A_0 are extrapolated from interior points A_1, A_2, A_3.
States at A_{M+1} are extrapolated from interior points A_M, A_{M-1}, A_{M-2}.

Figure 4.3: Ghost points for non-reflective and reflective boundaries

(b) Ghost points for non-reflective boundary

The edge of flow field in the ξ_1 and ξ_2 directions are inflow/outflow boundaries. (cf. Figure 4.3). For inflow boundaries, the states at the ghost points are set to those of the boundary points. For outflow boundaries, the states at the ghost points are determined by third-order extrapolation from the interior points.

4.1.2 Numerical Approximation to the Spatial Derivatives of Viscous Flux

The derivative of viscous flux, $\frac{\partial F_v}{\partial \xi}$, is discretized using the following fourth-order finite-difference formula:

$$\left(\frac{\partial \phi}{\partial \xi}\right)_i = \frac{-\phi_{i+2} + 8\phi_{i+1} - 8\phi_{i-1} + \phi_{i-2}}{12\Delta\xi} + O(\Delta\xi^4), \quad i = 2, \ \ldots, \ N-1 \tag{4.47}$$

$$\left(\frac{\partial \phi}{\partial \xi}\right)_1 = \frac{-11\phi_1 + 18\phi_2 - 9\phi_3 + 2\phi_4}{6\Delta\xi} + O(\Delta\xi^3), \tag{4.48}$$

$$\left(\frac{\partial \phi}{\partial \xi}\right)_2 = \frac{-2\phi_1 - 3\phi_2 + 6\phi_3 - \phi_4}{6\Delta\xi} + O(\Delta\xi^3), \tag{4.49}$$

$$\left(\frac{\partial \phi}{\partial \xi}\right)_{N-1} = \frac{2\phi_N + 3\phi_{N-1} - 6\phi_{N-2} + \phi_{N-3}}{6\Delta\xi} + O(\Delta\xi^3), \tag{4.50}$$

$$\left(\frac{\partial \phi}{\partial \xi}\right)_N = \frac{11\phi_N - 18\phi_{N-1} + 9\phi_{N-2} - 2\phi_{N-3}}{6\Delta\xi} + O(\Delta\xi^3), \tag{4.51}$$

where $\phi = F_v$.

4.2 Temporal Discretization

The temporal discretization is done by means of the five-stage fourth-order explicit Runge-Kutta (RK) scheme proposed by Carpenter and Kennedy [9, 84]. This scheme is based on the low-storage RK scheme of Williamson [83]. The scheme is low-storage as only two storage locations (one for the time derivative and one for the variable itself) are required for time advancement.

m	a^m	b^m
1	0	0.14965902
2	-0.41789047	0.37921031
3	-1.19215169	0.82295502
4	-1.69778469	0.69945045
5	-1.51418344	0.15305724

Table 4.1: Coefficients of a five-stage fourth-order Runge-Kutta scheme [84]

Eq. (4.1) is advanced from time level, n to $n+1$, in 5 substages (denoted by m) using a fourth-order explicit RK scheme. The advancement from substage m to $m+1$ is defined by:

$$U^{m+1} = U^m + b^{m+1}\,\Delta t\; L(U^m), \qquad m = 0,\ \ldots,\ 4 \tag{4.52}$$

where Δt is the time step, b^{m+1} is a coefficient of the RK scheme and $L(U^m)$ is given by Eq. (4.2). The substage $m = 0$ is equivalent to the n-th time level and the substage $m = 4$ is equivalent to the $(n+1)$-th time level.

The low-storage requirement is accomplished by continuously overwriting the storage location for the time derivatives and unknown variables at each substage:

$$L(U^m) \leftarrow a^m L(U^{m-1}), \qquad m = 1,\ \ldots,\ 5 \tag{4.53}$$

where the notation $\leftarrow$ is used to indicate that the storage locations U^m, $L(U^{m-1})$ are overwritten by U^{m+1}, $L(U^m)$, respectively.

The values of a^m and b^m for the five-stage fourth-order Runge-Kutta scheme are given in Table 4.1.

4.3 Boundary Conditions

The side boundaries of the computational domain represent the farfield of the actual flow field. At each point on the boundaries, the boundary conditions are allowed to switch between nonreflecting inflow and outflow depending on the sign of the instantaneous normal velocity. The numerical implementation of the farfield boundary conditions has to satisfy the requirement that any outgoing disturbances must not be reflected back into the flow field. To satisfy this requirement, the farfield boundary conditions are implemented based on the concepts of characteristic variables. The type of boundary conditions to be imposed on these boundaries depends on the direction and speed (subsonic or supersonic) of the flow at the boundary. Since the flow at the side boundaries are subsonic, only subsonic boundary conditions would be discussed in the following section.

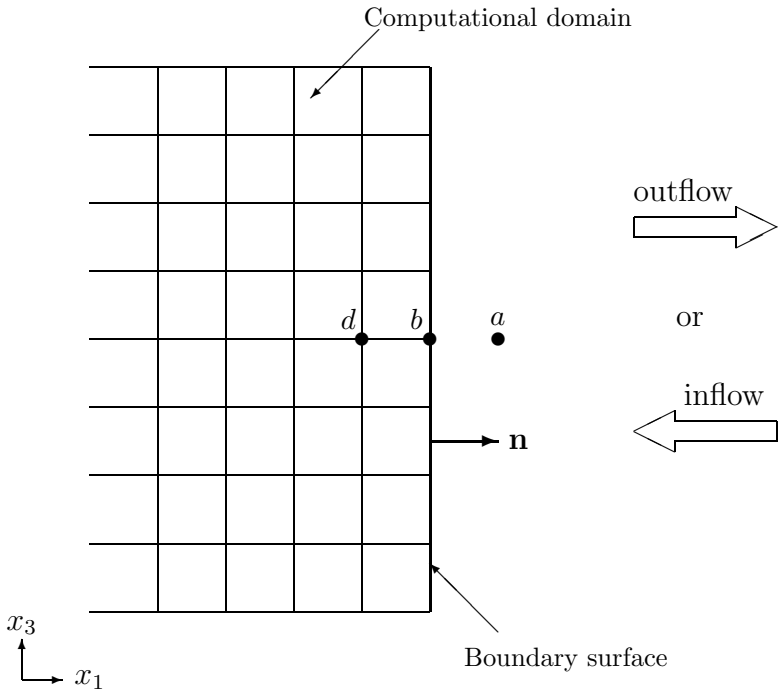

Figure 4.4: Boundary Condition Terminology

4.3.1 Inflow Boundary Conditions

According to the concept of characteristic variables, the information in x_i-direction ($i = 1,\ 2,\ 3$) is transported into or out of the computational domain along the characteristics depending on the sign of the eigenvalues of the convective flux jacobian: $\lambda_1 = u_i - c$, $\lambda_2 = \lambda_3 = \lambda_4 = u_i$, and $\lambda_5 = u_i + c$, where c is the local speed of sound.

Consider the boundary surface shown in Figure 4.4. Here a is the exterior point next to the boundary, b is the point at the boundary and d is the interior point next to the boundary. For subsonic inflow, there are four incoming characteristics and one outgoing characteristics. Since information is transported into the computational domain from outside at the inflow boundary, the number of boundary conditions to be imposed at the inflow boundary must be equal to the number of incoming characteristics. Therefore, one characteristic variable must be interpolated from the solution inside the computational domain. The interpolation is carried out using the Riemann invariants defined by:

$$\mathcal{R}^+ = \mathbf{u} \cdot \mathbf{n} + \frac{2c}{\gamma - 1} \tag{4.54}$$

$$\mathcal{R}^- = \mathbf{u} \cdot \mathbf{n} - \frac{2c}{\gamma - 1} \tag{4.55}$$

where $\mathcal{R}^+$ and $\mathcal{R}^-$ are incoming and outgoing Remainn invariants respectively, c is the local speed of sound and $\mathbf{n}$ is the outward unit normal.

Setting $\mathcal{R}_b^+ = \mathcal{R}_d^+$ and $\mathcal{R}_b^- = \mathcal{R}_a^-$, then the normal velocity component, u_{1_b}, and the local speed of sound, c_b, at the boundary are given by :

$$u_{1_b} = \mathbf{u}_b \cdot \mathbf{n} = \frac{1}{2}\left(\mathcal{R}_b^+ + \mathcal{R}_b^-\right) \tag{4.56}$$

and

$$c_b = \frac{\gamma - 1}{4}\left(\mathcal{R}_b^+ + \mathcal{R}_b^-\right) \tag{4.57}$$

where

$$\mathcal{R}_b{}^+ = \mathbf{u_d} \cdot \mathbf{n} + \frac{2c_d}{\gamma - 1} \tag{4.58}$$

$$\mathcal{R}_b{}^- = \mathbf{u_a} \cdot \mathbf{n} - \frac{2c_a}{\gamma - 1} \tag{4.59}$$

The other two velocity components at the boundary are specified as follows:

$$u_{2_b} = u_{2_a} \tag{4.60}$$

$$u_{3_b} = u_{3_a} \tag{4.61}$$

The pressure and density at the boundary are determined by assuming constant entropy as follows:

$$p_b = p_a \left(\frac{c_b}{c_a}\right)^{\left(\frac{2\gamma}{\gamma-1}\right)} \tag{4.62}$$

$$\rho_b = \rho_a \left(\frac{c_b}{c_a}\right)^{\left(\frac{2}{\gamma-1}\right)} \tag{4.63}$$

The temperature is determined using the equation of state as

$$T_b = \frac{p_b}{R\rho_b} \tag{4.64}$$

4.3.2 Outflow Boundary Conditions

For subsonic outflow, there are four outgoing characteristics and one incoming characteristics. Hence one boundary condition (pressure) has to be imposed at the boundary. The remaining four boundary conditions are interpolated from the interior of the computational domain.

Hence, the pressure is specified to be equal to the farfield pressure. The remaining primitive variables are interpolated from the interior using linear interpolation as follows:

$$p_b = p_a \tag{4.65}$$

$$u_{1_b} = u_{1_d} \tag{4.66}$$

$$u_{2_b} = u_{2_d} \tag{4.67}$$

$$u_{3_b} = u_{3_d} \tag{4.68}$$

$$\rho_b = \rho_d \tag{4.69}$$

The temperature at the boundary is determined as given in Eq. (4.64)

4.3.3 Wall Boundary Conditions

The top and bottom boundaries of the computational domain represent the solid walls. At these boundaries, the no-penetration condition

$$u_3|_{wall} = \mathbf{u} \cdot \mathbf{n} = 0 \tag{4.70}$$

and the noslip boundary condition

$$u_1|_{wall} = u_2|_{wall} = 0 \tag{4.71}$$

are implemented.

In addition, it is assumed that the walls are adiabatic. This means that the heat flux is zero at the walls

$$q_3 = 0 \tag{4.72}$$

which implies that

$$\frac{\partial T}{\partial \xi_3} = 0 \tag{4.73}$$

The pressure at the wall is extrapolated from the interior of the computational domain. In the present study, first order extrapolation was employed.

Chapter 5

CODE VERIFICATION

In order to verify the new code developed in this study, two simulations were performed. In the first case, numerical simulation of a subsonic three-dimensional compressible turbulent round jet was conducted and the results were compared with published data in the literature. In the second case, direct numerical simulations of boundary layer instability waves were compared with the result obtained from linear stability analysis.

In the following sections and subsequent chapters, we will use the following notations. For Cartesian coordinate system, we let

$$\begin{aligned} x_1 = x, \quad x_2 = y, \quad x_3 = z, \\ u_1 = u, \quad u_2 = v, \quad u_3 = w. \end{aligned} \tag{5.1}$$

For cylindrical coordinate system, we denote

$$\begin{aligned} r &= \text{radial coordinate}, \\ \theta &= \text{azimuthal (circumferential) coordinate}, \\ z &= \text{axial coordinate}, \\ u_r &= \text{radial velocity}, \\ u_\theta &= \text{azimuthal velocity}, \\ u_z &= \text{axial velocity}. \end{aligned} \tag{5.2}$$

5.1 Simulation of Mach 0.9 Turbulent Jet

The subsonic three-dimensional compressible turbulent round jet with Mach number of $M = 0.9$ and Reynolds number of $Re = 36,000$ investigated by Bendiks *et al.* [5] was simulated. The Mach number is based on the ambient speed of sound and the jet mean centerline velocity W_o^*. The Reynolds number is based on the jet diameter D^* and jet mean centerline velocity W_o^*. As discussed in Chapter 2, the governing equations are nondimensionalized using the jet diameter D^* and the mean centerline velocity of the jet W_o^* as reference values. Therefore, in nondimensional form, the jet diameter is given by $D = 1$. The inflow velocity profile, in cylindrical coordinates, is given by

$$u_z(r,\theta,0,t) = \frac{1}{2} - \frac{1}{2}\, tanh\left[2.8\left(\frac{r}{r_o} - \frac{r_o}{r}\right)\right]\left[1 + \epsilon\, sin\,(St\, t)\right] \tag{5.3}$$

where r_o is the nondimensional jet radius. This inflow velocity profile u_z as a function of radial distance r is shown in Figure 5.1 for $t = 0$.

In Eq. (5.3) the Strouhal number $St = 2\, R_o^*\, f/W_o^*$ is 0.45, where R_o^* is the jet radius. The amplitude of ϵ is 0.0025. A very small random forcing given by

$$u_\theta(r,\theta,0) = 0.025\, exp\left[-3\left(1 - \frac{r}{r_o}\right)^2\right]\, ran \tag{5.4}$$

is applied in the circumferential direction in the initial shear layer to trigger three-dimensional instabilities. The term ran in the above equation is a random number generated uniformly between -0.5 and 0.5. The velocity component in the radial direction is set to zero ($u_r = 0$).

The size of the physical domain for the simulation is $-4D \le x \le 4D$, $-4D \le y \le 4D$, $0 \le z \le 21.25D$ as shown in Figure 5.2. The physical domain is discretized into a stretched grid of size $n_x \times n_y \times n_z = 81 \times 81 \times 161$ as shown in Figure 5.3 and Figure 5.4. The grid has uniform spacing in the z-direction, and in the region $-1.5D \le x \le 1.5D$ and $-1.5D \le y \le 1.5D$. The grid size in the z-direction is $\Delta z = 0.0132813$. The grid sizes for the uniform region surrounding the jets in the x- and y-directions are $\Delta x = \Delta y = 0.0563991$.

The grid used here is Cartesian and is different from the cylindrical grid used by Bendiks *et al.* [5]. In their study, Bendiks *et al.* used a finer grid of size $192 \times 128 \times 64$, in the axial, radial and azimuthal directions, respectively. Their grid is slightly stretched in the axial direction, and uniform in both circumferential and radial directions. Since the grid used in the present study is Cartesian, there is imperfection in the circular profile of the jet. This imperfection is absent in the grid of Bendiks *et al.* [5] as it is cylindrical.

In their numerical simulation, Bendiks *et al.* used a sixth order compact finite difference scheme for spatial discretization and a fourth order Runge-Kutta scheme for temporal discretization. At the boundaries of their computational domain, they added sponge layers to

force the flow to the self-similarity solution for an incompressible jet. In the present study, no sponge layers are used.

Therefore, due to the differences in the grid resolution, the type of grid (Cartesian versus cylindrical) and the boundary treatment, one would expect some discrepancies between the results of the present study and those of Bendiks *et al.* [5].

In the present study, simulation was carried out in three stages. In the first stage, $4,000$ time steps were used to allow the transient response to exit the domain. In the second stage, $5,000$ time steps were used to obtain the mean velocities. In the third stage, $7,000$ time steps were used to obtain statistically stationary Reynolds stresses. The mean flow was also updated during these $7,000$ steps. The time step size varies between 2.1×10^{-2} and 2.3×10^{-2} such that $CFL = 1.4$.

Before comparing the results from the present study with those of Bendiks *et al.* [5], we highlight the difference in the notations used by Bendiks *et al.* as the results of Bendiks *et al.* presented here are replicas of the figures in their paper [5]. In Bendiks *et al.* [5], the variables are nondimensionalized based on the ambient speed of sound and the jet radius R_o. The difference in the notations used in these two studies are tabulated in Table 5.1. The equivalent variables used by these two studies are shown in Table 5.2. Note that in the present study, all symbols with asterisk (*) are dimensional variables, whereas those without asterisk are nondimensional variables.

Variable	Bendiks *et al.* [5]	Present study
Jet mean centerline velocity	U_o	W_o^*
Jet radius	R_o	R_o^*
Reference velocity	speed of sound, a_o	jet mean centerline velocity, W_o^*
Reference length	R_o	D^*

Table 5.1: Notations used by Bendiks *et al.* [5] and the corresponding notations in the present study

Non-dimensional variable	Bendiks *et al.* [5]	Present study
Axial distance	x/R_o	z^*/R_o^* or $2z$
Radial distance	r/R_o	r^*/R_o^* or $2r$
Mean axial velocity	U/U_o	MU_z
Reynolds shear stress	$\overline{u_r'u_z'}$	$M^2\ \overline{u_r'u_z'}$
Axial rms stress	$(u')_{rms}$	$M(u_z')_{rms}$

Table 5.2: Equivalent quantities used in the present study and Bendiks *et al.* [5]

Figure 5.5 shows the centerline decay of the axial velocity obtained in the present study. Here U_z is the mean axial velocity. In order to show the effect of grid resolution, another simulation was performed using a coarser grid of size $61 \times 61 \times 97$. From the figure, it can be seen that with the fine grid, the mean centerline velocity starts to decay at $z^*/R_o^* \approx 16$. However, with the coarse grid, the mean centerline velocity starts to decay at $z^*/R_o^* \approx 19$. Thus, one can conclude that transition to turbulence is delayed if the grid resolution is coarse.

Figure 5.6 shows the centerline decay of the axial velocity obtained by Bendiks *et al.* [5]. Comparing Figures 5.5 and 5.6, one can see that the result from the present study agrees qualitatively with that of Bendiks *et al.* [5]. However, according to Bendiks' result, the centerline velocity starts to decay at $r/R_o \approx 13$. This discrepancy in the position at which the axial velocity starts to decay is due to the difference in the grid resolution used in the simulations. Bendiks *et al.* used a finer grid than the present study. As the study on the effect of grid resolution shown in Figure 5.5 indicates, it is believed that if the grid of the present study is further refined, the results will be closer to that of Bendiks *et al.* [5].

Figure 5.7 shows the mean axial velocity profile as a function of radius at various axial locations downstream of the jet exit as obtained in the present study. The corresponding results obtained by Bendiks *et al.* [5] are shown in Figure 5.8. The velocity profiles in these two figures are in agreement qualitatively. Since in the present study, the mean axial velocity starts to decay only at $z^*/R_o^* \approx 16$, the magnitude of the mean axial velocity when $r^*/R_o^* = 0$ at $z^* = 13.0R_o^*$ is very close to that at $z^* = 3.2R_o^*$. This is not the case in Figure 5.8 which shows a decrease in the mean axial velocity from $x = 3.2R_o$ to $x = 13.0R_o$ as the mean axial velocity starts to decay at $x/R_o = 13.0$. However, the overall agreement is satisfactory considering the coarser grid used here.

Figures 5.9 and 5.10 are plots of the Reynolds shear stresses as a function of the radial coordinate at various downstream locations. The former shows the results obtained by the present study, whereas the latter shows the results obtained by Bendiks *et al.* [5]. The results from the two studies agree qualitatively. Since the difference in the mean velocities affects the calculation of the Reynolds shear stresses, the discrepancies in the Reynolds shear stress profiles are expected.

Figure 5.11 shows the axial rms profiles $M(u_z')_{rms} = M\sqrt{\overline{u_z'^2}}$ for various downstream locations obtained in the present study. The axial rms profiles obtained by Bendiks *et al.* [5] is shown in Figures 5.12. From these figures, it can be seen that for $z^* = 19.5R_o^*$, the value of $M(u_z')_{rms}$ in the present study is in better agreement with the DNS data than that of Bendiks *et al.* [5]. For other locations, the results are generally in reasonably good agreement with those of Bendiks *et al.* [5].

The distribution of the Reynolds shear stress $M^2\,\overline{u_r'u_z'}$ in the r-z plane obtained in the present study can be seen in the contour plot for Reynolds shear stresses shown in Figure 5.14. From the figure, one can see that the Reynolds shear stress has a maximum value of 0.011

at $(r, z) \approx (1, 10)$. The contour plot for $M(u'_z)_{rms}$ in the r-z plane in Figure 5.13 shows the distribution of $M(u'_z)_{rms}$ in the present study. From the figure, one can see that the maximum $M(u'_z)_{rms}$ occurs at $(r, z) \approx (0.6, 11)$, with a value of ≈ 0.16. Thess two figures also indicate that transition to turbulence starts at $z \approx 5D$.

Figure 5.15 shows the snapshot of instantaneous vorticity contours at $t = 261.65$. Note that the potential core of the jet starts to break up around $z \approx 8$ ($z^*/R_o^* \approx 16$). This is the location where the axial velocity begins to decay as shown in Figure 5.5.

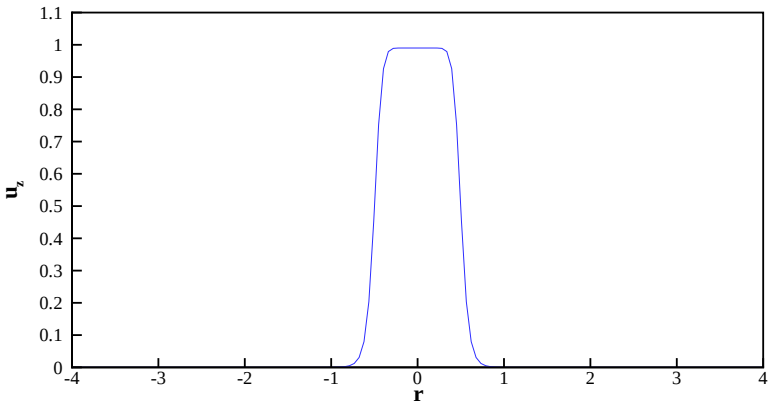

Figure 5.1: Mean inflow velocity profile for free jet.

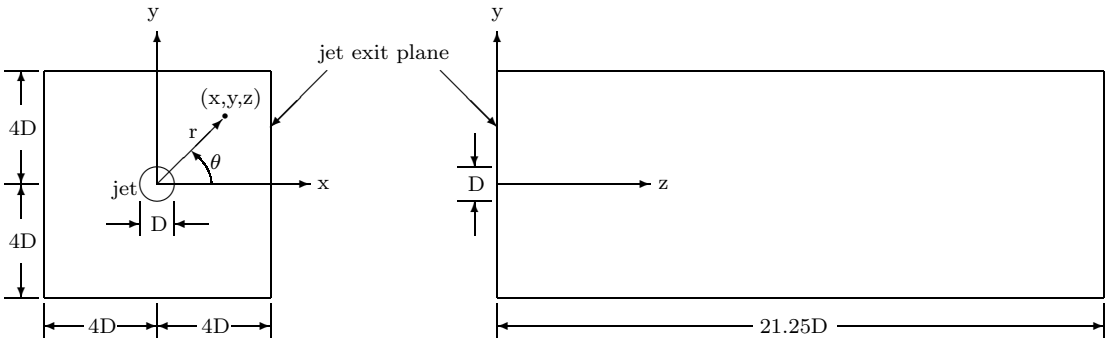

Figure 5.2: Schematic of the computational domain for free jet simulation

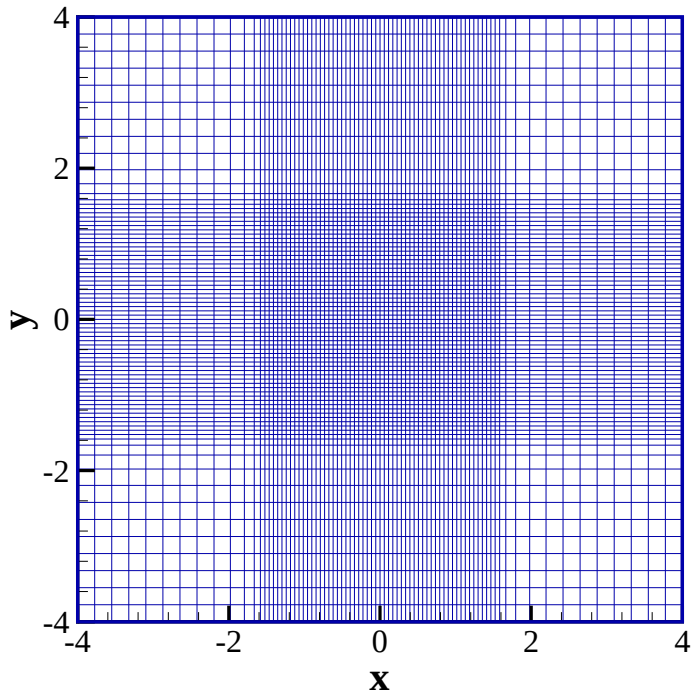

Figure 5.3: Grid in the xy-plane of computational domain.

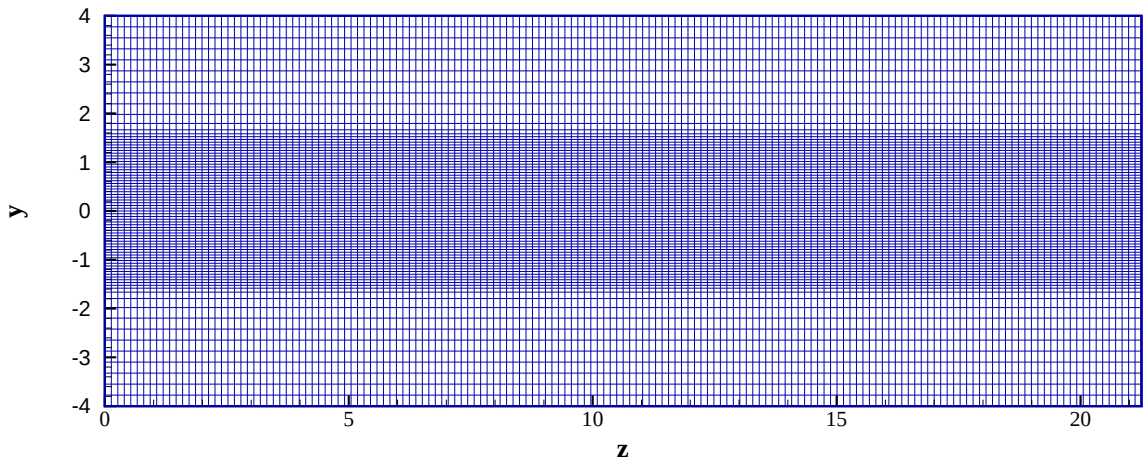

Figure 5.4: Grid in the yz-plane of computational domain.

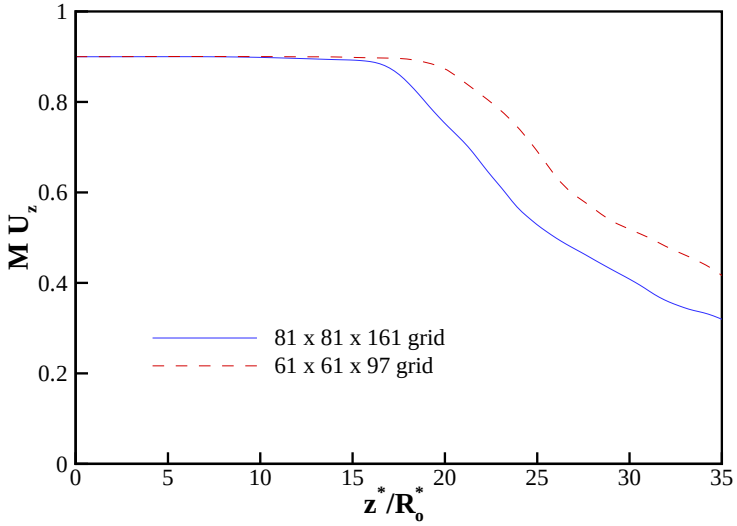

Figure 5.5: The centerline decay of the mean axial velocity obtained in the present study.

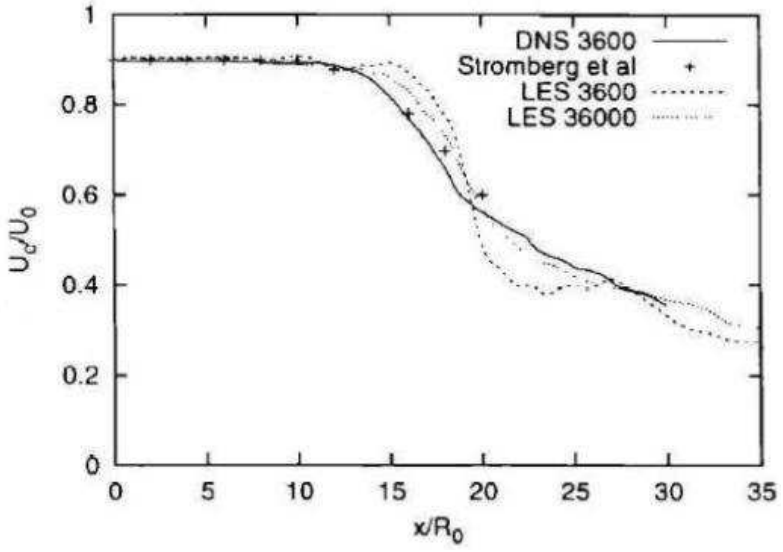

Figure 5.6: The centerline decay of the mean axial velocity obtained by Bendiks *et al.* [5] (DNS: Re=3600, LES: Re=36000).

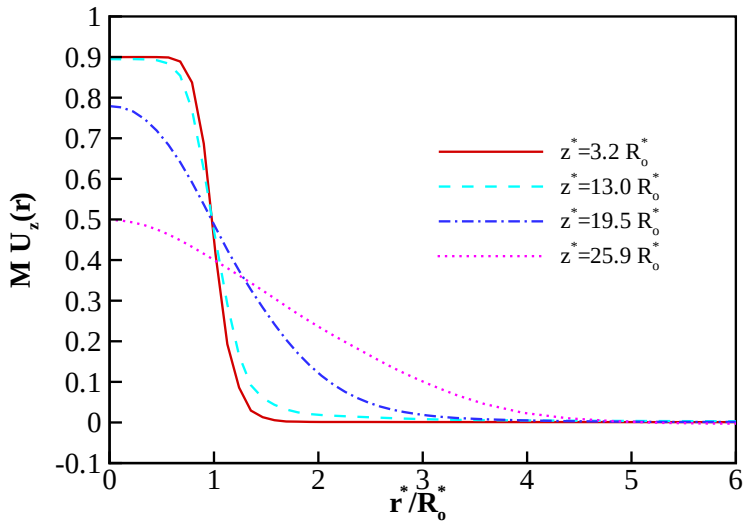

Figure 5.7: The mean axial velocity profile as a function of the radial position at different downstream locations obtained in the present study.

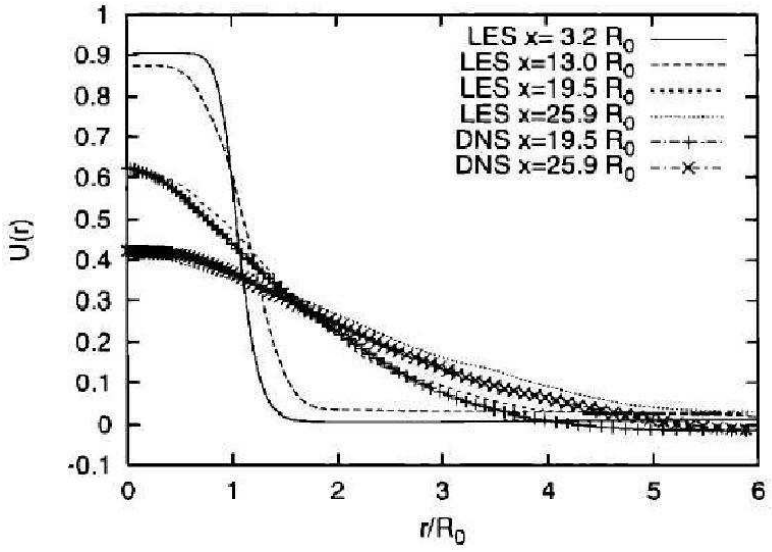

Figure 5.8: The mean axial velocity profile as a function of the radial position at different downstream locations obtained by Bendiks *et al.* [5] (DNS: Re=3600, LES: Re=36000).

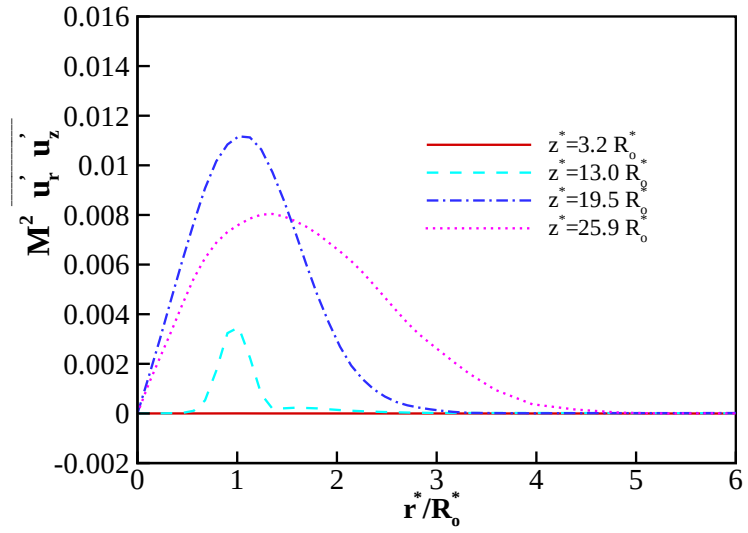

Figure 5.9: The Reynolds shear stress profiles as a function of the radial position at different downstream locations of the jet orifice obtained in the present study.

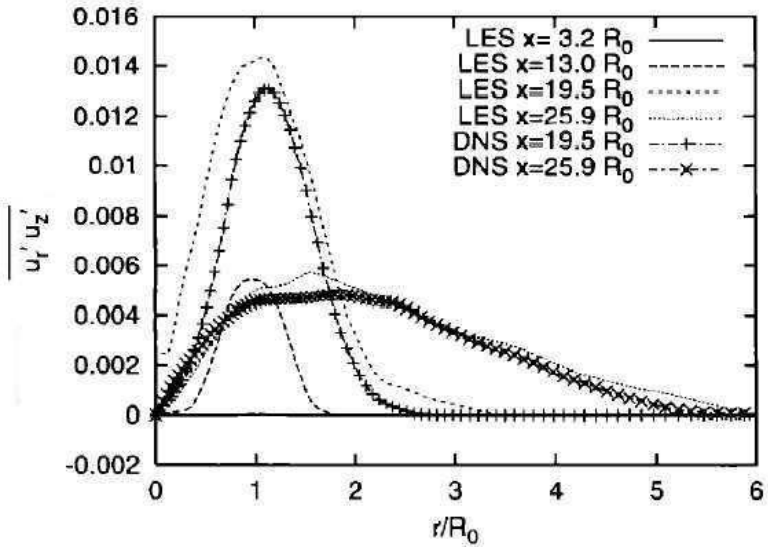

Figure 5.10: The Reynolds shear stress profiles as a function of the radial position at different downstream locations of the jet orifice obtained by Bendiks*et al.* [5] (DNS: Re=3600, LES: Re=36000).

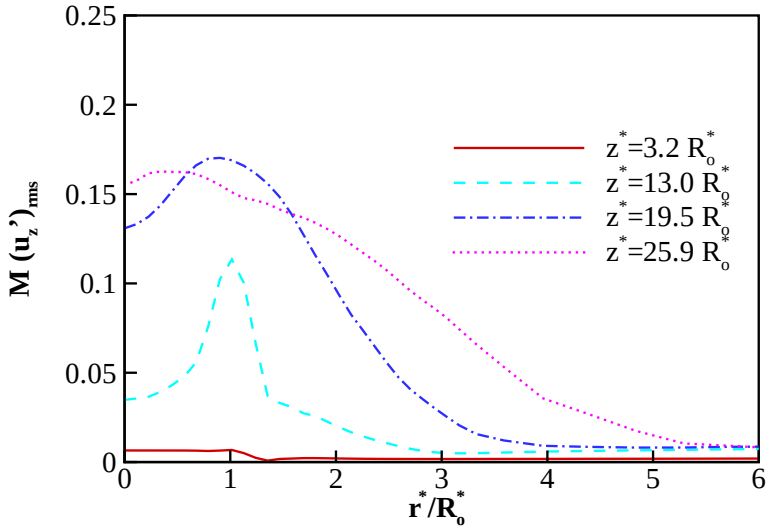

Figure 5.11: The axial root mean square profile as a function of the radial position at different downstream locations obtained in the present study.

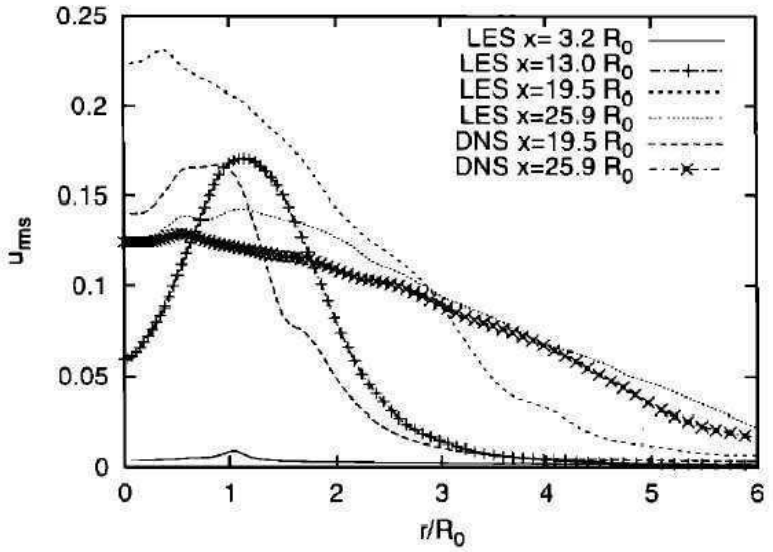

Figure 5.12: The axial root mean square profile as a function of the radial position at different downstream locations obtained by Bendiks *et al.* [5] (DNS: Re=3600, LES: Re=36000) (Note : Using the notation in the present study, $u_{rms} \equiv w'_{rms}$.)

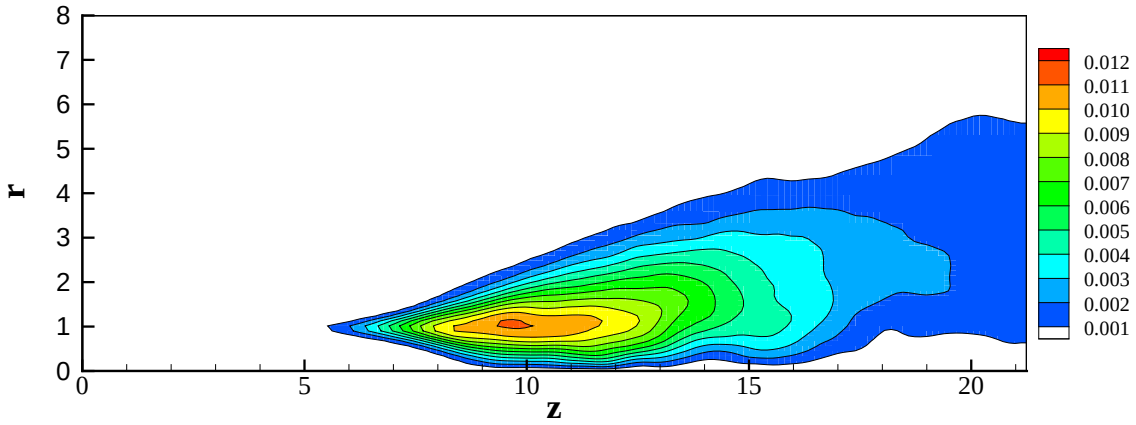

Figure 5.13: Contour plot for Reynolds shear stress $M^2\ \overline{u_r' u_z'}$.

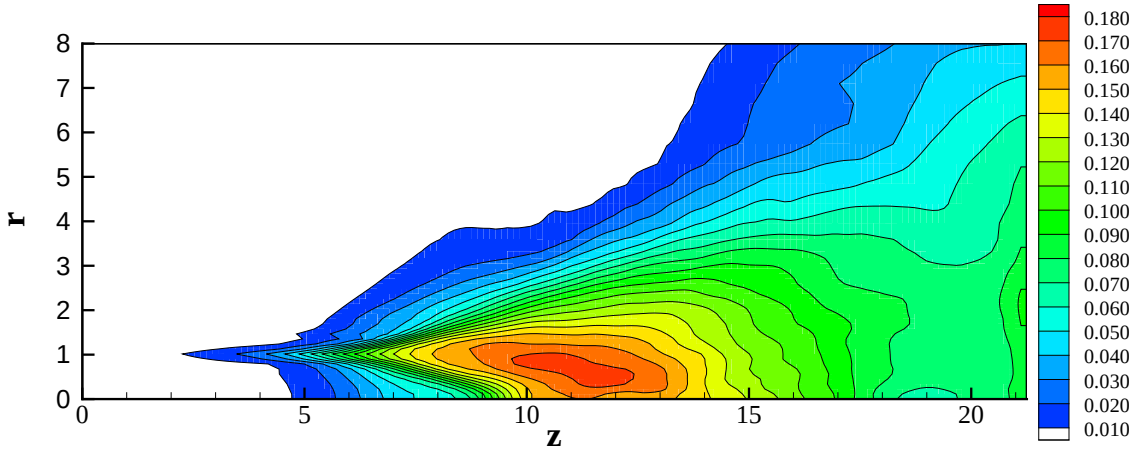

Figure 5.14: Contour plot for axial velocity root mean square $M(u_z')_{rms}$.

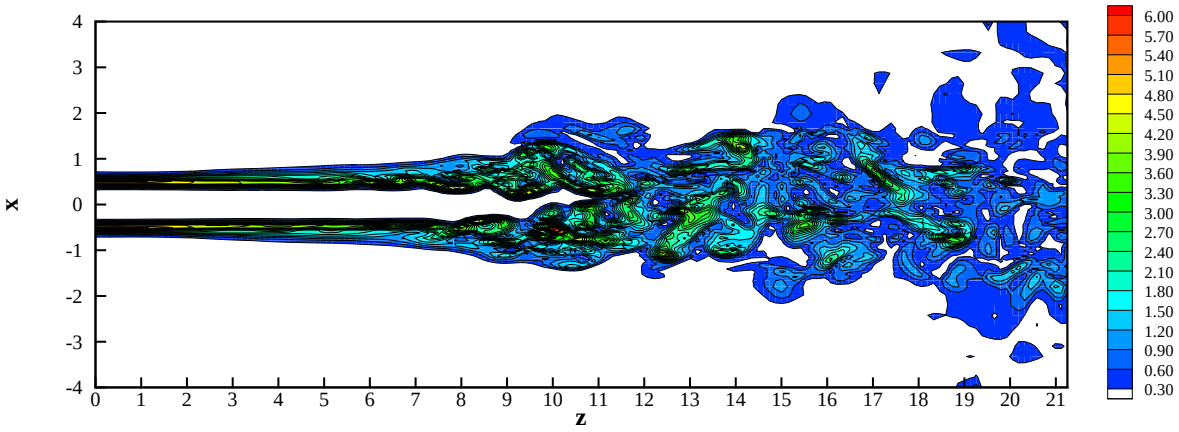

Figure 5.15: Contour plot for snapshot of instantaneous vorticity magnitude at $t = 261.65$.

5.2 Comparison With Linear Stability Analysis

5.2.1 Linear Stability Theory

In this section we will consider the stability of a three dimensional compressible boundary layer flow. Let a Cartesian coordinate system x, y, z be oriented in such a way that the y axis is normal to the solid boundary, and the x, z axes are parallel to it. Further, let the x axis be in the free stream direction and the z axis be along the span. According to linear stability theory, all time-dependent flow quantities are split into a steady (basic state) component and an unsteady fluctuation component. If u, v, w are the x, y, z components of the instantaneous velocity, respectively, and p and T are instantaneous pressure and temperature, then assuming that the base flow is locally parallel, we have [46]

$$u(x,y,z,t) = U_0(y) + \tilde{u}(y)e^{i(\alpha x+\beta z-\omega t)} \tag{5.5}$$

$$v(x,y,z,t) = \tilde{v}(y)e^{i(\alpha x+\beta z-\omega t)} \tag{5.6}$$

$$w(x,y,z,t) = W_0(y) + \tilde{w}(y)e^{i(\alpha x+\beta z-\omega t)} \tag{5.7}$$

$$p(x,y,z,t) = \tilde{p}(y)e^{i(\alpha x+\beta z-\omega t)} \tag{5.8}$$

$$T(x,y,z,t) = T_0(y) + \tilde{T}(y)e^{i(\alpha x+\beta z-\omega t)} \tag{5.9}$$

where α and β are nondimensional wave numbers in the x and z directions, respectively, and ω is the frequency. Here U_0, W_0, and T_0 represent the steady unperturbed boundary layer, and quantities with tildes denote complex disturbance amplitudes.

Substitution of Eqs. (5.5)-(5.9) into the compressible Navier-Stokes equations yields the following system of ordinary differential equations:

$$\left(A\frac{d^2}{dy^2} + B\frac{d}{dy} + C)\right)\vec{\phi} = 0 \tag{5.10}$$

where $\vec{\phi}$ is a five element vector define by

$$\{\alpha\tilde{u} + \beta\tilde{w},\ \tilde{v},\ \tilde{p},\ \tilde{T},\ \alpha\tilde{w} - \beta\tilde{u}\}^T \tag{5.11}$$

Here A, B, C are 5×5 matrices whose elements are given in Malik and Orszag [46].

The boundary conditions for Eq. (5.10) are

$$\begin{aligned} y = 0, &\quad \phi_1 = \phi_2 = \phi_4' = \phi_5 = 0 \\ y \to \infty, &\quad \phi_1,\ \phi_2,\ \phi_4,\ \phi_5 \to 0 \end{aligned} \tag{5.12}$$

where ϕ_1, ϕ_2, ϕ_3, ϕ_4 and ϕ_5 are the components of vector $\vec{\phi}$.

Equations (5.10)-(5.12) constitute an eigenvalue problem for ω, α, and β. In general, α, β and ω are complex. For temporal stability analysis, α and β are real, and ω is complex ($\omega = \omega_r + i\omega_i$). The disturbances grow if $\omega_i > 0$ and decay if $\omega_i < 0$. For selected values of α and β, the above problem results in a linear eigenvalue problem for ω.

5.2.2 Direct Numerical Simulation of Flat-Plate Boundary-Layer Instability

To validate the code developed for the present study, direct numerical simulations of flat-plate boundary layer instability were conducted. Both subsonic and supersonic boundary layers were considered. For subsonic boundary layers, three cases were considered. The first two cases involved two-dimensional instability waves with different values of α. In the third case, three-dimensional instability wave was studied. For supersonic case, only two-dimensional instability wave was considered. The details of these four cases under study are summarized in Table 5.3. The reference length is $\sqrt{\nu x_o/U_\infty}$, where x_o is the x-coordinate corresponding to the local basic state U_o, W_o and T_o.

Description	Case 1	Case 2	Case 3	Case 4
Type of Flow	subsonic	subsonic	subsonic	supersonic
Mach No.	0.5	0.5	0.5	4.5
Reynolds No.	860	860	860	1550
Prandtl No.	0.7075	0.7075	0.7075	0.7075
Freestream Temperature	273 K	273 K	273 K	120 K
Wave no. in x−direction, α	0.14	0.21	0.14	0.248
Wave no. in z−direction, β	0	0	0.1	0

Table 5.3: Direct numerical simulation of flat-plate instability: The four cases under study

For three-dimensional case, the size of the physical domain is given by $L_x \times L_y \times L_z = 2\pi/\alpha \times 22 \times 2\pi/\beta$. For two-dimensional case, the size of the physical domain is given by $L_x \times L_y = 2\pi/\alpha \times 22$. Two types of stretched grid were used to discretize the physical domain. The first type, denoted as type I, has uniform region from $y = 0$ to $y = 0.3$ and stretched region from $y = 0.3$ to $y = 22$. The second type, denoted as type II, has uniform region from $y = 0$ to $y = 0.6$ and stretched region from $y = 0.6$ to $y = 22$. Both types of grid are uniform in x and z directions. Grid type II was used only in Case No. 3. To study the effect of the grid resolution on the values of ω_i, numerical simulations were conducted on four different resolutions for both grid types.

In the numerical simulation, the flow quantities were initialized as follows :

$$u(x,y,z,0) = U_0(y) + A \text{ Re}\left[\tilde{u}(y)e^{i(\alpha x+\beta z-\omega t)}\right] \tag{5.13}$$

$$v(x,y,z,0) = A \text{ Re}\left[\tilde{v}(y)e^{i(\alpha x+\beta z-\omega t)}\right] \tag{5.14}$$

$$w(x,y,z,0) = W_0(y) + A \text{ Re}\left[\tilde{w}(y)e^{i(\alpha x+\beta z-\omega t)}\right] \tag{5.15}$$

$$p(x,y,z,0) = A \text{ Re}\left[\tilde{p}(y)e^{i(\alpha x+\beta z-\omega t)}\right] \tag{5.16}$$

$$T(x,y,z,0) = T_0(y) + A \text{ Re}\left[\tilde{T}(y)e^{i(\alpha x+\beta z-\omega t)}\right] \tag{5.17}$$

Here $U_0(y)$, $W_0(y)$ and $T_0(y)$ took the values of the Blasius compressible boundary layer. The disturbances, namely, $\tilde{u}$, $\tilde{v}$, $\tilde{w}$, $\tilde{p}$ and $\tilde{T}$ are the eigenfunctions obtained from the solution of the linear stability equations, and the amplitude A is 0.02.

To determine the growth rate, ω_i, only one time step is required. The numerical solution was then analyzed using Fourier Transform to extract the value of ω_i. The values of ω_i were computed at the value of y for which the kinetic energy of the disturbance is maximum.

The values of $\omega = \omega_r + \omega_i$ obtained by solving the linear stability equations using an existing linear stability analysis code are tabulated in Table 5.4. The values of ω_i obtained from the direct numerical simulation are tabulated in Table 5.5. From Table 5.5, it can be seen that for Cases No. 1, 2 and 3 the values of ω_i converged to those of the linear stability theory as the grid is refined. Although Case No. 3 does not show absolute convergence, the errors of only 0.36% (for the finest grid of grid type I) and 0.33% (for the finest grid of grid type II) are acceptable. In conclusion, the close agreement of the values of ω_i between the direct numerical simulation and the linear stability theory indicates that the performance of the present simulation code is satisfactory.

Case No.	$(\omega_r)_{LS}$	$(\omega_i)_{LS}$
1	4.895000×10^{-2}	2.011600×10^{-3}
2	7.818100×10^{-2}	-5.812900×10^{-3}
3	5.177834×10^{-2}	8.338080×10^{-4}
4	2.259200×10^{-1}	2.425600×10^{-3}

Table 5.4: Wave frequencies obtained by solving the linear stability equations

Case No.	Grid Type	Grid Size	$(\omega_i)_{NS}$	$(\omega_i)_{NS}/(\omega_i)_{LS}$
1	I	$9 \times 171 \times 9$	-3.5303×10^{-3}	-1.7550
		$17 \times 171 \times 9$	1.7509×10^{-3}	0.87040
		$33 \times 171 \times 9$	-2.0023×10^{-3}	0.99538
		$65 \times 171 \times 9$	-2.0114×10^{-3}	0.99990
2	I	$9 \times 171 \times 9$	-1.4118×10^{-2}	2.4287
		$17 \times 171 \times 9$	-6.2022×10^{-3}	1.0670
		$33 \times 171 \times 9$	-5.8270×10^{-3}	1.0024
		$65 \times 171 \times 9$	-5.8134×10^{-3}	1.0001
3	I	$65 \times 171 \times 9$	-1.1069×10^{-3}	-1.32760
		$65 \times 171 \times 17$	7.3590×10^{-4}	0.88257
		$65 \times 171 \times 33$	8.3039×10^{-4}	0.99590
		$65 \times 171 \times 65$	8.3685×10^{-4}	1.00360
	II	$65 \times 211 \times 9$	-1.1310×10^{-3}	-1.35640
		$65 \times 211 \times 17$	7.3432×10^{-4}	0.88068
		$65 \times 211 \times 33$	8.3005×10^{-4}	0.99549
		$65 \times 211 \times 65$	8.3659×10^{-4}	1.00330
4	I	$9 \times 171 \times 9$	7.2871×10^{-6}	0.00300
		$17 \times 171 \times 9$	2.3049×10^{-3}	0.95024
		$33 \times 171 \times 9$	2.4120×10^{-3}	0.99439
		$65 \times 171 \times 9$	2.4157×10^{-3}	0.99591

Table 5.5: ω_i obtained from direct numeircal simulation of flat-plate instability

Chapter 6

RESULTS AND DISCUSSION

As mentioned in previous chapter, we will use the following notations in this chapter. For Cartesian coordinate system, we let

$$\begin{aligned} x_1 = x, \quad x_2 = y, \quad x_3 = z, \\ u_1 = u, \quad u_2 = v, \quad u_3 = w. \end{aligned} \tag{6.1}$$

For cylindrical coordinate system, we denote

$$\begin{aligned} r &= \text{radial coordinate}, \\ \theta &= \text{azimuthal (circumferential) coordinate}, \\ z &= \text{axial coordinate}, \\ u_r &= \text{radial velocity}, \\ u_\theta &= \text{azimuthal velocity}, \\ u_z &= \text{axial velocity}. \end{aligned} \tag{6.2}$$

In addition, we recall from Chapter 2 that all symbols with asterisk (*) are dimensional variables, whereas those without asterisk are nondimensional variables. The nondimensional variables are obtained by using the jet diameter, D^*, and the following flow variables of the jet center at the jet exit plane ($z = 4$) as reference values:

$$\begin{aligned} z - \text{component velocity} &: W_o^*, \\ \text{density} &: \rho_o^*, \\ \text{temperature} &: T_o^*, \\ \text{dynamic viscosity} &: \mu_o^*, \\ \text{specific heat at constant pressure} &: c_{p_o}^*, \\ \text{thermal conductivity} &: \kappa_o^* \end{aligned} \tag{6.3}$$

In the numerical simulation of twinjet-jet impingement, a stretched grid of size $n_x \times n_y \times n_z = 151 \times 91 \times 111$ as shown in Figures 6.1 through 6.3 is used. The grid has uniform spacing in the regions defined by $-3 \leq x \leq 3$ and $-1.5 \leq y \leq 1.5$, and in the region defined by $0 \leq z \leq 0.05$. The grid sizes for the uniform region surrounding the jets in the $x-$ and $y-$ directions are $\Delta x = \Delta y = 0.05$. The uniform spacing in the $z-$direction is $\Delta z = 0.005745$.

The simulation is conducted at a Mach number of $M = 1.5$ and a Reynolds number of $Re = 5.5 \times 10^5$. The inflow boundary conditions (at $z = 4$) for the impinging jets are given by

$$u(x, y, z, t) = -u_\theta \, sin\theta \tag{6.4}$$
$$v(x, y, z, t) = u_\theta \, cos\theta \tag{6.5}$$
$$w(x, y, z, t) = u_z(r) \left[1 + 0.04 \, f_z \, \epsilon_2(x, y, t)\right] \tag{6.6}$$
$$\rho(x, y, z, t) = 1 \tag{6.7}$$
$$T(x, y, z, t) = 1 \tag{6.8}$$

The instantaneous circumferential velocity u_θ and the mean axial velocity $u_z(r)$ are defined, respectively, by

$$u_\theta(r, t) = 0.04 \, f_r \, \epsilon_1(x, y, t), \tag{6.9}$$

$$u_z(r) = -w_o \, \left[1 - (r/r_o)^6\right], \tag{6.10}$$

$$f_r = e \left(\frac{1 - r/r_o}{1 - b/r_o}\right) \, e^{\left(-\frac{1-r/r_o}{1-b/r_o}\right)}, \qquad b = 0.84 r_o, \tag{6.11}$$

$$f_z = f_r / 0.74. \tag{6.12}$$

where the value of the nondimensional jet radius, r_o, is 0.5 and the nondimensional jet centerline velocity at the exit plane is $w_o = 1$.

In the above equations, f_r and f_z are random forcings applied in the circumferential and axial directions, respectively, to the initial shear layer to trigger three-dimensional instabilities. The terms ϵ_1 and ϵ_2 are random numbers generated uniformly between -0.5 and 0.5.

Figure 6.4 shows the w-velocity profile as a function of x at the jet exit plane (z=4). Figure 6.5 shows the profile of f_r as a function of r. Notice that f_r is maximum at $|r| = b = 0.84 r_o$. Function f_z has the same shape as f_r, but with larger amplitude.

The flow is initialized (t=0) by the fields given in Eqs. (6.4) - (6.12), and then imposing the solid wall boundary conditions at $z = 0$ to simulate the ground.

The initial velocity vector field in the jet exit plane is shown in Figure 6.6. The figure shows that the velocity vectors are randomly distributed in the xy plane. The contour plots for the velocity components, u, v, and w, in the jet exit plane are shown in Figures 6.7, 6.8, and 6.9, respectively. The contour plots for the vorticity vectors in the $x-$, $y-$, and $z-$ directions are shown in Figures 6.10, 6.11, and 6.12, respectively. In these and subsequent contour plots, dashed lines indicate negative contour levels, while solid lines indicate positive contour levels.

6.1 Instantaneous Flow Field

6.1.1 Transition to turbulence

Figures 6.13 through 6.18 are three-dimensional perspectives for the iso-surface of the total vorticity magnitude $|\vec{\omega}|$ at a specified level. The figures show the formation of the fountain and its transition to turbulent flow.

Figures 6.13 shows the vortex rings formed by the jet shear layers which are represented by the cylindrical tubes. After impinging on the ground, each vortex ring propagates on the ground and induces a secondary vortex ring of opposite vorticity as can be seen in the figure. Each primary vortex ring expands (i.e., ring diameter increases) until it collides with the nearby primary vortex ring and rises from the ground into the fountain as shown in Figure 6.14. In the fountain region, the vortex rings continue to expand upwards and begin to twist and stretch each other until the vortical structures break down into small-scale structures as shown in Figures 6.15 through 6.17. At later times, the fountain become fully turbulent, and no distinct large-scale vortical structures can be discerned as can be seen in Figure 6.18.

From the figures, it can be seen that as the primary vortex rings are lifted off the ground and then broken into small-scale structures, the secondary vorticity associated with each ring dissipate. In addition, these figures also show the development of jet shear layers into helical shape as a result of the forcing being applied circumferentially and axially. Moreover, the vortex rings also exhibit spiral nature, i.e. they are not perfectly circular.

Figures 6.19 through 6.24 show the velocity vector field with streamlines in the plane that contains the centerlines of the jets ($y = 0$) at the six different times corresponding to Figures 6.13 through 6.18. Figure 6.19 shows that at $t = 3.5866$, the fountain is symmetric with respect to its centerline at $x = 0$. However, as time elapses, the fountain root begins to become asymmetric as shown in Figure 6.20. Once the asymmetry develops, the fountain began to flap as shown from Figure 6.21 through 6.24. Once flapping occurs, the fountain's centerline is no longer located at $x = 0$. The location of the fountain centerline changes with time.

Figures 6.25 and 6.26 are close views at the fountain root for Figures 6.19 and 6.23, respectively. The former shows that the fountain is symmetric with respect to its centerline at $x = 0$, whereas the latter shows that the fountain is asymmetric and its centerline is no longer located at $x = 0$. Figures 6.25 and 6.26 also show the existence of secondary vorticities which are of opposite sense to the primary vorticities at the fountain root. From these figures, it is evident that the generation of secondary vorticity is due to the formation of the wall boundary layer as the result of the propagation of the primary vorticity above the ground.

The corresponding velocity vector fields in the xy plane for the above-mentioned figures are plotted in Figures 6.27 through 6.32. These figures are plotted at different $z-$location in order to show the characteristic features of the flow field. The presence of vortex rings can be seen in these figures. In addition, the figures also show the development of turbulent flow in the fountain region.

6.1.2 Turbulent flow field

6.1.2.1 Velocity Field

Figures 6.33 through 6.38 are the time sequences of the velocity vector field with streamlines in the $y = 0$ when the fountain flow is fully turbulent. The first time frame is obtained at t=104.3092, which is approximately 90 time units after the large vortical structure in the fountain has broken down into small-scale structures (see Fig 6.17). The time interval between two consecutive time frames is $\Delta t = 1.4$.

Due to the growth of the unstable waves at the jet shear layers, one can see in these figures that the shear layers of the two impinging jets are undergoing rollup. The main influence of the fountain on the impinging jets is due to the lateral interaction between the fountain and the jets. This interaction occurs at $z \leq 2$. This lateral interaction between the fountain and the jets is quite strong and can modify the jet spreading characteristics. As the activities of the fountain is confined in the region between the impinging jets and $z \leq 2$, it can be said that the influence of the fountain on the upper wall is weak for the present case understudy ($H^*/D^* = 4$).

Figures 6.39, 6.40 and 6.41 are close views at the fountain root for Figures 6.34, 6.36 and 6.38, respectively. These figures show that the location of the stagnation line on the ground varies with time.

The flapping behavior of the fountain as discussed in the previous section is also observed here. Therefore, it is clear that the flapping of the fountain is a periodic behavior. In order to determine the frequency of the flapping, a Fourier analysis was performed on the time history of u at the point $(0, 0, 0.5012)$, as shown in Figures 6.42. The power spectral density of u obtained from the discrete Fourier transform (DFT) is presented in Figure 6.43. The

frequency at which the peak is the highest in this figure gives the frequency of flapping. From this figure, it can be determined that the frequency of flapping is 0.14 which means that the period of flapping is approximately $7D^*/W_o^*$. From the animation of fountain flow, the period of flapping is confirmed. In addition, the animation also shows the physics of flapping and its relation to the impingement of the large-scale vortical structures of the jet shear layers on the ground.

The corresponding time sequences of the velocity field in the $x = 0$ plane, which passes through the fountain region, are shown in Figures 6.44 through 6.49. In these figures one can see that the flow fans out rapidly from the fountain in the $y-$direction. The magnitude of the velocities above $z = 2.0$ is very small and the effect of the fountain on the upper wall is weak.

Figures 6.50, 6.51 and 6.52, are close views at the fountain root for Figures 6.45, 6.47 and 6.49, respectively. From these figures, one can see that the location of the stagnation line in the fountain varies with time. Figures 6.51 and 6.52 show the existence of a "node" in the fountain at $(x, y, z) \approx (0, 0.1, 0.15)$ and at $(x, y, z) \approx (0, -0.08, 0.11)$, respectively. However, no such point is observed in Figure 6.50. Hence, the occurrence of the "node" is varying with time.

Figures 6.53 through 6.58 are the corresponding velocity field in the xy plane at $z = 0.536607$. This is the plane which cuts through the fountain upwash where the maximum mean upward velocity is recorded. It is evident from these figures that the collision of two opposing wall jets on the ground produces a flow that is biased towards the fountain plane, which is perpendicular to the plane containing the jet axes. The figures also show that there is a strong lateral interaction between the fountain and the impinging jets.

The modification of the jet velocity profile due to the entrainment of the fountain flow into the jets can be seen clearly in Figure 6.59 which shows the variation of w-velocity as a function of x in the $y = 0$ plane at $t = 108.5092$. Figure 6.59(a) is the w-velocity profile for the left jet, whereas Figure 6.59(b) is the w-velocity profile for right jet. Due to the random forcing, these two jets do not have similar instantaneous velocity profiles.

The corresponding spreading characteristics of the fountain is shown in Figure 6.60. Figure 6.60(a) shows the increase of maximaum w from the loaction at $z = 0.005745$ to $z = 0.652032$, whereas Figure 6.60(b) shows the decay of maximaum w from $z = 0.652032$ to $z = 4.0$. Notice that w-velocity reaches its maximum over a very short z-distance and diffuses very rapidly before reaching the top wall, an indication of a high spreading rate.

Figures 6.61 and 6.62 show the u-velocity and v-velocity, respectively, for the jets at three different instants of time. From these figures, it can be seen that u and v have high values in the region where $z \leq 2$. This is the region where strong lateral interaction occurs between the jets and the fountain, as observed previously. Figure 6.63(a) and 6.63(b) show the variation of the w-velocity with z for the centerlines of the left jet and right jet, respectively, at three different times during which the fountain flaps. The magnitude of w decreases as the

impingement region is approached. The large velocity gradient between $z = 0$ and $z = 1.0$ indicates the formation of shock waves. From the figures, it can be seen that the stand-off distance of the shock wave varies with time, around $z \approx 0.4$ (or $z^* \approx 0.4D^*$). The existence of the unsteady shock waves in the simulation is an indication of the ability of the WENO scheme to capture moving shock waves.

The u-velocity and v-velocity profiles in the fountain plane at $y = 0$ are shown, respectively, in Figures 6.64 and 6.65. It can be seen in these figures that u and v have large magnitudes in the region $0 \leq z \leq 2$, This indicates that the interaction of the fountain with the jets is confined within this region as the value of u beyond this region is very small. Figure 6.66 shows the variation of the w-velocity with z in the fountain region at $x = 0$ in the $y = 0$ plane. Positive value of w indicates upward flow. It can be seen from this figure that the upwash flow loses its positive z-momentum at about $z = 2.0$.

Figure 6.67 shows the u-velocity profile as a function of z at various x-locations between the jets in the $y = 0$ plane at $t = 108.5092$. The velocity profiles show that the wall jet on the ground speeds up towards the fountain and then slows down as the collision zone is approached. There are local regions of reverse flow just outside the wall jet region. This reverse flow is due to the recirculation and entrainment of the fluid. The velocity profiles also show that there is no formation of wall jet on the top wall as the the fountain spreads very rapidly in the x-directions and weakens as it moves upward. The magnitude of u is almost zero at about $z \approx 3$. The velocity profiles for the locations between $x = -0.25$ and $x = 0.25$ indicate the occurrence of the separation of the wall boundary layer. This region of adverse pressure gradient on the ground is associated with the formation of secondary vorticity described above. The reverse flow at $x = -1$ and $x = 1$, which are the shear layers of the left and right jets respectively, is the evidence that some of the fluid in the recirculation region of the fountain is entrained into the impinging jets, thereby modifying the spreading characteristics of the jets.

Figures 6.68 shows the u-velocity profiles as a function of z at various x-locations between the left jet and the left boundary in the $y = 0$ plane at $t = 108.5092$. The growth of wall boundary layer on the ground, i.e., the wall jet, is clearly visible. Some regions of reverse flow are seen at $x = -2$, indicating the entrainment of flow by the impinging jets.

Figure 6.69 shows the u-velocity profile as a function of z at various x-locations between the right jet and the right boundary in the $y = 0$ plane at $t = 108.5092$. Again, the growth of wall boundary layer on the ground is evident. The shear layer of the right jet at $x = 2$ also shows signs of entrainment of the fluid from the surrounding.

Figure 6.70 shows the v-velocity profile as a function of z at various y- locations in the $x = 0$ plane. This plane falls within the fountain region. The velocity profiles show a large region of reverse flow above the wall jets, indicative of the recirculation of flow in this region. At $y = -0.1$, the flow direction near the wall which is opposite to the outflow direction (towards the negative y direction) indicates that separation of boundary layer has occurred. Similarly, the separation of boundary layer has also occurred at the wall at $y = 0.1$ as the flow here is

opposite to the outflow direction (towards the positive y direction).

Figure 6.71 shows the v-velocity profile as a function of z at various y-locations in the $x = -1.5$ plane, the plane which passes through the left jet axis. Figure 6.72 shows the v-velocity profile as a function of z at various y-locations in the $x = 1.5$ plane, the plane which passes through the right jet axis. The velocity profiles at $y = -0.5$ and $y = 0.5$ are those of the shear layers for left and right jets respectively. Some regions of reverse flow are also seen near the boundary at $y = -0.27158$ and $y = 0.27158$, indicating the entrainment of the fluid from outside the boundary. There is also a very small region of reverse flow near the top wall.

6.1.2.2 Vorticity Field

The y-vorticity contours in the $y = 0$ plane at $t = 104.3092$, 105.7092, 107.1092, 108.5092, 109.9092, and 111.3092 are shown in Figures 6.73 through 6.78, respectively. Only vorticity in the range between -5 and 5, inclusive, are shown in these figures as vorticity of higher levels are concentrated on the ground plane.

From these figures, the formation of large-scale structures as a result of instabilities at the jet shear layers can be seen propagating from each of the jet exit planes to the ground plane. It is observed that the fountain is the region of high vorticity. The structures in the fountain region, which are the cross-sections of the vortical tubes are seen to exhibit flapping behavior. However, it does not seem to have a well-defined shape. No symmetry is observed in the fountain structure.

From the figures, it can be seen that there is a strong lateral interaction between the fountain and the impinging jets, indicating strong lateral spreading of the fountain. However, the fountain loses its momentum before reaching the upper wall and its influence on the upper wall is very weak. The vorticity level is practically zero at the top wall. The interaction of the fountain and the jets has significance only when $z \leq 3$. In contrast, the wall jets on the ground plane has high level of vorticity. The vortical structures of the wall jet on the ground are quite coherent.

Figures 6.79 and 6.80 show the details of the fountain flapping in the $y = 0$ plane. When the large-scale vortical structures from the jets impinge on the ground plane, they propagate away from their respective jet axis and induce secondary vorticities of opposite sense on that plane. Figures 6.79(a) and 6.79(b) show how a left primary vortex tube originating from the left jet comes into contact with a right secondary vortex tube of the same sign and merges with it to form a left-inclining vortical structure. This newly formed vortical structure has opposite sense to the left secondary vortex tube on the ground and is thus being raised up by it from the ground. The left-inclining vortical structure eventually breaks up and gives the opportunity for the left secondary vortex tube to come into contact with the right primary vortex tube of the same sign, as can be seen in Figure 6.79(c). The left secondary vortex tube

then merges with the right primary vortex tube to form a right-inclining vortical structure, as shown in Figure 6.80. The right-inclining vortical structure will also break up eventually after being raised up by the right secondary vortex tube on the ground. This alternating merging of the primary vortex tube with the secondary vortex tube from the neighboring jet to form a new vortical structure that rises into the fountain region creates an impression that the fountain is flapping.

The x-vorticity contours in the $x = 0$ plane at six different times are shown in Figures 6.81 through 6.86. This is the plane that passes through the fountain region. From these figures, it can be seen that the fountain and the ground plane are regions of high vorticity. These figures also show that the vortical structures of the wall jet on the ground in this plane are not as coherent as those in the $y = 0$ plane.

The x-vorticity contours in the midplanes ($x = \pm 1.5$) of the two jets at six different times are shown in Figures 6.87 through 6.92. The large vortical structures in the jet shear layers are seen to propagate from the jet exit planes to the ground. The frequency at which these vortical structures impinge on the ground affects the flapping frequency of the fountain. From the animation of the simulation data, it was found that this frequency is two times the fountain flapping frequency, viz., 0.28. Since the forcing is applied randomly, the vortical structures of the two jets are not identical. Vortical structures are also observed in the wall jet region on the ground.

Figures 6.93 through 6.98 show the z-vorticity contour in the $z = 0.005745$ plane at six different times corresponding to the figures described previously. This is the plane just above the ground. As can can be seen from these figures, no vortex ring is observed. The structures in the wall jet region consists of vortical tubes.

Figure 6.99 shows three-dimensional perspectives of iso-surface of the vorticity magnitude at the level $|\omega| = 6.0$ for $t = 111.3092$. The region outside this surface are of lower vorticity magnitude. The figure implies that complex interactions, such as distortion, merging and breaking of vortex tubes occur in the fountain region.

6.1.2.3 Pressure Field

Figures 6.100 through 6.105 are contour plots for pressure coefficient, C_p, in the $y = 0$ plane at six different times. The high concentration of contour lines in the impingement regions is an indication of the formation of shock waves. As can be seen from these figures, the shock wave fronts change with time. The stand-off distances of the two shock waves vary between 0.3 and 0.4. Therefore, it is clear that the shock waves are oscillating. From these figures, it can also be seen that the upper part of the fountain and the region below the top plane are regions of negative C_p. These are the regions where suction force occurs.

The pressure coefficient contours corresponding to the previous figures in the $x = 0$ plane are shown in Figures 6.106 through 6.111. These figure show the presence of high pressure

gradient at the fountain base. This is the region where two opposing wall jets collide with each other. As a result of collision, the pressure increases rapidly and thus produces a high pressure gradient. The location of this high pressure region varies with time.

Figures 6.112 through 6.117 show the contour plots of the pressure coefficient, C_p, in the $z = 0.005745$ plane at six different times. This the plane just above the ground. The pressure coefficient at the fountain base which is relatively higher than the neigboring region indicates that the fountain flow is mostly spreading towards the positive and negative y-directions.

The details of shock wave can be seen clearer in Figure 6.118 which shows the distribution of pressure coefficient, C_p, with respect to z along the centerline of the two jets at three different times. For both the left and the right jets, one can see the formation of "nominally normal" shock waves near the ground in the region defined by $0.2 \leq z \leq 0.4$. Notice that at $t = 105.7092$, there is a sharp discontinuity at $z \approx 2.8$ for the left jet and at $z \approx 0.7$ for the right jet. These discontinuities indicate the formation of weak oblique shock waves. The location of these weak oblique shock waves varies with time. The sharpness of the discontinuities in these figures shows that the fifth-order WENO scheme used in the present simulation is capable of capturing the shock very well.

Figure 6.119 shows the distribution of pressure coefficient, C_p, with respect to z at $x = 0$ in the $y = 0$ plane, which is within the fountain region. As expected, one can see a sudden increase in the value of C_p at $z = 0$ where the two opposing wall jet collide. The C_p near the wall is positive nearly at all times.

Figure 6.120 shows the distribution of C_p as a function of x for $-1.0 < x < 1.0$ at $y = 0$ in the $z = 4$ plane. The curves are obtained at four different times. The corresponding distribution of C_p as a function of y at $x = 0$ in the $z = 4$ plane is shown in Figure 6.121. These figures show that the pressure on the top plane changes with time. The pressure is sometimes slightly higher than the ambient pressure (i.e., C_p is positive) but mostly lower than the ambient pressure (i.e., C_p is negative). This shows that a V/STOL aircraft in hovering mode will certainly experience downward force as the pressure coefficient under it has negative value.

6.2 Mean Flow Field

In this section, the mean velocity field with components in x, y and z directions represented by U, V and W, respectively, the mean pressure coefficient by $\bar{C}_p$, and the mean vorticity by Ω, are presented. These mean flow variables are obtained over a nondimensional time interval of 403.3827.

6.2.1 Velocity Field

Figure 6.122 shows the mean velocity vector field in the $y = 0$ plane. The mean fountain flow appears to be symmetric with respect to the two jets. However, a closer look at the mean fountain base as shown in Figure 6.123 reveals that the streamlines of the mean fountain flow is inclined slightly towards the right jet. In addition, the mean stagnation line is not located at $x = 0$ but is shifted to $x \approx -0.05$. Therefore, there is a slight asymmetry in the fountain. This asymmetry is much larger for smaller averaging time and when the seeding for the random number generator is fixed. Our study shows that the asymmetry is most likely due to the averaging time is not long enough. The asymmetry of the fountain was also observed by Elavarasan and *et al.* [23] in their experiment and no explanation was given. From Figure 6.123, the counter-rotating secondary vortices on the ground plane are also clearly visible.

Figure 6.124 shows the mean velocity vector field in the $x = 0$ plane. The fountain looks symmetrical in this plane. A closer look at the fountain root as shown in Figure 6.125 indicate the existence of a "node" at $(x, z) \approx (0.02, 0.003)$. The streamlines are seen to be originated from this point and extend to the boundary.

Figure 6.126 shows the mean velocity vector field in the $z = 0.005745$ plane, the plane just above the ground. As can be seen in this figure, the flow field is symmetric.

Figure 6.127 shows the mean velocity vector field in the $z = 0.5366$ plane, the plane at which the peak of W-velocity is maximum. From this figure, it can be seen that the fountain flow is biased towards the y direction.

Figures 6.128 and 6.129 are the contour plots for mean velocities U and W, respectively, corresponding to Figure 6.122. Figure 6.128 shows that U is anti-symmetric with respect to the $x = 0$ axis. Figure 6.129 shows that the fountain flow is slightly biased towards the right jet. However, W is in general quite symmetric with respect to $x = 0$ plane.

Figures 6.130 and 6.131 are the contour plots for mean velocities V and W, respectively, corresponding to Figure 6.124. Figure 6.130 shows that V is almost anti-symmetric with respect to $y = 0$, whereas Figure 6.131 shows that W is almost symmetric with respect to $y = 0$.

The symmetry and asymmetry of the velocity fields can be seen clearer in Figures 6.132 through 6.137 which show the one-dimensional distribution of the mean velocity components, viz., U, V and W at $z = 0.5366$ in the $y = 0$ plane, the location where the peak of W is maximum.

Figures 6.132 shows the variation of U along the x direction. From this figure, it can be seen that the U-velocity profile is almost anti-symmetric about the centerline passing through zero and has almost the same magnitude on either side. The reason why the profile is not perfectly anti-symmetric may be due to the following two factors : (1) the averaging time is not long enough, and (2) the random number used in the random forcing may have some

bias, i.e., the random number generator does not generate the random number in a fully random manner.

Figure 6.133 is the distribution of V as a function of x. We have seen in Figure 6.130 that V is antisymmetric with respect to the $y = 0$ plane. Hence, it is expected that V should be zero in the $y = 0$ plane. This is confirmed by the result shown in Figure 6.133. Therefore, this is a good indication that the flow is moving towards stationary state.

Figure 6.134 shows the distribution of W as a function of x. From the figure, it is evident that the maximum value of W in the $x = 0$ plane is 0.40406 and it occurs at $z = 0.536607$. Elavarasan and *et al.* [23] reported that the peak velocity in the fountain is 0.4261 and is reached at about 0.7692 from the ground plane for all H^*/D^* in the range from 1 to 4. An experimental study using water as a working medium by El-Okda [21] found that the peak velocity in the fountain is 0.45 and it occurs at about 0.6 from the ground plane.

Figure 6.135 shows the distribution of U as a function of y at $z = 0.5366$ in the $x = 0$ plane. It has been seen in Figure 6.128 that U is almost anti-symmetric with respect to the $x = 0$ axis. Hence, U should be zero in the $x = 0$ plane. This explains why U is nearly zero in Figure 6.135. It is reasonable to believe that U will be zero if averaging is done over a longer period of time. Figure 6.136 shows the distribution of V as a function of y at $z = 0.5366$ in the $x = 0$ plane. It is evident in this figure that V is anti-symmetric with respect to the line which passes through $x = 0$, as has been observed earlier in Figure 6.130. Figure 6.137 shows the distribution of W as a function of y at $z = 0.5366$ in the $x = 0$ plane. It is clear that W is symmetric with respect to the line passing through $x = 0$.

Visualization experiments by Saripalli ([63, 64]) indicate that the jets and the fountain region are highly unsteady. In order to show the level of unsteadiness in comparison with the mean flow, we plotted together the instantaneous velocities and mean velocity as functions of z in Figures 6.138 and 6.139. Figure 6.138 shows the variations of the instantaneous centerline velocity, w, at two different instants as well as the variation of mean centerline velocity, W, along the left jet centerline. The unsteady nature of the jet can be clearly seen in this figure. Figure 6.139 shows the variation of the instantaneous centerline velocity, w, at two different instants as well as the variation of the mean centerline velocity, W, along the z direction at $y = 0$ in the $x = 0$ plane (the fountain plane). As can be seen in this figure, high unsteadiness of the fountain is confined in the region $z \leq 3$, the region where complex interactions occur in the fountain.

Figures 6.140 shows the variation of U along the x-direction at various z-positions in the $y = 0$ plane within the fountain region $(-1 \leq x \leq 1)$. Notice that at $z = 0.005745$, there is a change of sign in U between $x = -1$ and $x = 0$, and between $x = 0$ and $x = 1$. This is due to the presence of seondary vorticity which is of opposite sense to the primary vorticity. The figure shows that U decays very rapidly as the fountain rises from the ground. This indicates that the mean lateral spreading rate in the x direction decreases with height.

Figure 6.141 shows the variation of W along the x-direction at various z-positions in the

$y = 0$ plane. As can be seen from this figure, W increases as the fountain rises from the ground plane until $z = 0.536607$. Thereafter, W decays rapidly as z increases and the fountain loses its z-momentum before reaching the top plane at $z = 4$.

Figures 6.142 shows the variation of V along the y-direction at various z-positions in the $x = 0$ plane. Comparing this figure with Figure 6.140, it can be seen that the diffusion of V in the y-direction is not as rapid as the diffusion of U in the x-direction.

Figures 6.143 shows the variation of W along the y-direction at various z-positions in the $x = 0$ plane. The figure shows that W increases as the fountain rises from the ground to $z = 0.536607$ and then decreases beyond $z = 0.536607$. Comparing this figure with Figure 6.141, it can be concluded that the mean lateral spreading rate of W in the fountain is higher in the y direction.

Figure 6.144 shows the variation of the W-velocity profile of the jets in the $y = 0$ plane. The similarity of the profiles for the two jets indicates that both the jets have the same mean characteristics. From the figure, it can be seen that the end of the core region occurs at $z = 0.501221$.

Figure 6.145 shows the U-velocity profile as a function of z at various x-locations between the jets in the $y = 0$ plane. Due to the curvature effects during impingement, the walls jet leaving the impingement regions at $x = \pm 1$ are accelerating initially. They begin to slow down as the collision zone is approached. It can also be seen from this figure that the peak velocity of the wall jets decreases and the boundary layers grow thicker as the wall jets approach the collision region.

Figures 6.146 shows the U-velocity profile as a function of z at various x-locations between the left jet and the left boundary in the $y = 0$ plane. Figures 6.147 shows the U-velocity profile as a function of z at various x-locations between the right jet and the right boundary in the $y = 0$ plane. From these figures, it can be seen that the wall jet is speeding up initially due to the curvature effects but slowing down as the boundaries are approached.

Figures 6.148 shows the V-velocity profile as a function of z at various y-locations in the $x = 0$ plane, which is within the fountain region. It can be seen that the peak velocity of the wall jet increases and the boundary layer becomes thinner as the boundary is approached.

Figures 6.149 and 6.150 show the V-velocity profile as a function of z at various y-locations in the plane which passes through the axes of the left and right jets respectively. Here $x = \pm 0.5$ are the shear layers of the impinging jets. From the figures, it can be seen that the wall jet speeds up initially due the curvature effect and then slows down as the boundary is approached.

6.2.2 Vorticity Field

Figures 6.151 shows the mean y-vorticity contours in the $y = 0$ plane. Vortical structures of the jet layers in the impinging regions of the two jets are clearly visible. The secondary vorticities induced by the primary vorticities are also visible in the collision region. These secondary vorticities are of opposite sense to the primary vorticities that produce them.

Figures 6.152 is the contour plot for the mean x-vorticity contours in the $x = 0$ plane, which is located in the fountain region. From this figure, it is evident that the x-vorticity in this plane is concentrated in the wall jet region. In addition, it can also be seen that the x-vorticity in the wall jet region is anti-symmetric with respect to the $y = 0$ axis.

The x-vorticity contours in the midplanes of the two jets are shown in Figure 6.153 . It is evident from the figure that the two jets have identical vortical structures. The anti-symmetry of the wall jet region can also be seen from the figure.

Figures 6.154 shows the z-vorticity contours in the $z = 0.005745$ plane, the plane just above the ground. As shown in this figure, the vortical structures in this plane is anti-symmetric with respect to the centerlines of the plane.

Figures 6.155 shows the z-vorticity contour in the $z = 0.005745$ plane, the plane at which the peak of W is maximum. It can be seen that the vortical structures in this plane are also anti-symmetric with respect to the centerlines of the plane.

Figure 6.156 shows the three-dimensional iso-surface of the mean total vorticity magnitude at the level $|\bar{\omega}| = 2.0$. As can be seen from this figure, large vortical structures are confined in the region between the jets. However, no dominant large-scale vortical structure can be discerned in this region.

6.2.3 Pressure Field

Figure 6.157 shows the contour plot of the mean pressure coefficient, $\bar{C}_p$, in the $y = 0$ plane. The figure indicates that the pressure field is symmetric with respect to the $x = 0$ axis. The formation of shock waves can be seen at the impingement zone where the contour lines are concentrated. The stand-off distance for the two shock waves in the mean flow is approximately $0.4D^*$ above the ground. From the figure, it can also be seen that the fountain region has the lowest mean pressure. In addition, one can also see that the region below the top plane has negative values of $\bar{C}_p$, an indication that this region is experiencing suction force due to entrainment of flow into the jets.

Figure 6.158 is the contour plot for the mean pressure coefficient in the $x = 0$, the plane passing through the fountain region. One can see in this figure that the fountain region has the lowest value of $\bar{C}_p$ and the region below the top plane has negative $\bar{C}_p$. The region with highest value of $\bar{C}_p$ is found to be located at $y = 0$ just above the ground, which is the

collision region where opposite wall jets of high velocities collide with each other and give rise to a high increase in pressure.

Figure 6.159 shows the mean pressure coefficient contours of the top plane. From this figure, it is evident that the top plane has negative values of $\bar{C}_p$ (white level is in the range between -0.009 and -0.014). This is an indication that the undersurface of an aircraft is experiencing a suction force.

A clearer view of the mean pressure coefficient distribution underneath the top plane is given by Figures 6.160 and 6.161 which show the distribution of the mean pressure coefficient along the x- and y- directions, respectively. In Figure 6.160, the mean pressure coefficient distribution of the jets is not shown. Figure 6.160 shows that $\bar{C}_p$ varies between -0.010 and -0.013, whereas Figure 6.161 shows that $\bar{C}_p$ varies between -0.008 and -0.013. From these two figures, one can conclude that the value of $\bar{C}_p$ underneath the top plane is always negative.

Figure 6.162 show the variation of the mean pressure coefficient as a function of z along the jet centerlines. The shock wave is observed at $z \approx 0.4$ as seen earlier in Figure 6.157. Since the mean characteristics of the two jets are identical, there is no difference in the distribution of mean pressure coefficients between the jets.

Figure 6.163 shows the variation of mean pressure coefficient ($\bar{C}_p$), as well as instantaneous pressure coefficient (C_p) at three different instants of time, as a function of z at $x = 0$ in the $y = 0$ plane. This figure shows that the pressure is highly unsteady in the collison region and in the fountain region where $z \leq 2$.

6.2.4 Grid Resolution Near the Wall

For turbulent boundary layer, there exists a dimensionless distance from the surface, z^+, such that the velocity varies approximately linearly with z^+ close to the surface, and gradually asymptotes to the law of the wall for large values of z^+ [82]. The dimensionless normal distance z^+ is defined by

$$z^+ = z^* \, u^*_\tau / \nu^*. \tag{6.13}$$

The term u^*_τ in the above equation is known as the friction velocity and is defined by

$$u^*_\tau = \sqrt{\tau^*_w / \rho^*}. \tag{6.14}$$

The shear stress at the wall τ^*_w is given by

$$\tau^*_w = \mu^* \frac{\partial u^*_{x^*y^*}}{\partial z^*}. \tag{6.15}$$

where $u^*_{x^*y^*}$ is the velocity magnitude in the x^*y^* plane.

Using Eqs. (6.14) and (6.15) in Eq. (6.13) and expressing the resulting equation in terms of the nondimensional variables defined in Chapter 2, we have

$$z^+ = z\,\sqrt{Re\,\frac{\partial u_{xy}}{\partial z}}. \tag{6.16}$$

The impingement region is not a boundary-layer type flow, and hence z^+ may be irrelevant here. Nevertheless, for reference purpose, the contour plot which shows the distribution of z^+ in the mean flow in the $z = 0.00574535$ plane, the plane next to the ground, is presented in Figure 6.164. From this figure, it can be seen that the impingement regions have high values of mean z^+, whereas the collision region has low values of mean z^+. The maximum value of mean z^+ is 48 and it occurs at the jet shear layers. The minimum value of z^+ is 5.3 and it occurs, approximately, at $(-1.5,\ 0,\ 0.0057435)$ and $(1.5,\ 0,\ 0.0057435)$, i.e., at the centers of the jets.

6.3 Reynolds Stress Field

In this section, we present the Reynolds stress field obtained over a nondimensional time interval of 198.8000. This averaging time is shorter than that used to obtain the mean flow field, and therefore, may not be long enough for the Reynolds stresses to reach the steady state.

Figures 6.165 through 6.170 show, respectively, the contour plots for the six Reynolds stress components, $\overline{u'u'}$, $\overline{u'v'}$, $\overline{u'w'}$, $\overline{v'v'}$, $\overline{v'w'}$ and $\overline{w'w'}$ in the $y = 0$ plane, which passes through the jet centerlines. The Reynolds normal stress in the x-direction, $\overline{u'u'}$, is symmetric with respect to the $x = 0$ axis as can be seen in Figures 6.165. The maximum value of $\overline{u'u'}$ is approximately 0.3078 and it occurs at $z = 0.1$, the location where high speed wall jets originating from two impinging jet collide and rise from the ground. As the flow moves upward from the collision region, the value of $\overline{u'u'}$ decreases. Neither symmetry nor anti-symmetry is observed in the Reynolds shear stress $\overline{u'v'}$ shown in Figure 6.166. As can be seen in the figure, the magnitude of $\overline{u'v'}$ is very small. It is believed that $\overline{u'v'}$ may converge to zero if the averaging period is long enough. The Reynolds shear stress $\overline{u'w'}$ shown in Figure 6.167 is anti-symmetric with respect the $x = 0$ axis. High levels of $\overline{u'w'}$ are found in the impinging jet shear layers just above the impingement regions and in the collision zone. The high level of $\overline{u'w'}$ in the impinging jet shear layers is due to the sudden reversal of flow direction during impingement. The magnitude of the highest level of $\overline{u'w'}$ is 0.025. The Reynolds normal stress in the y-direction, $\overline{v'v'}$, shown in Figure 6.168 is also symmetric with respect to the $x = 0$ axis. The impingement region is the region of high $\overline{v'v'}$. The curvature effects due to the sudden turning of the flow direction during impingement contributes to the high level of $\overline{v'v'}$ in this region. The stress reaches its maximum value of 0.05 at $(-0.95,\ 0,\ 0.25)$ and $(0.95,\ 0,\ 0.25)$. The contour plot in Figure 6.169 shows that neither symmetry nor anti-symmetry can be discerned in the Reynolds shear stress $\overline{v'w'}$. Notice that the magnitude of

this stress is very small. This indicates that $\overline{v'w'}$ may also converge to zero if the averaging period is long enough. The Reynolds normal stress in the z-direction, $\overline{w'w'}$ also exhibits symmetry with respect to the $x = 0$ axis, as can be seen from Figure 6.170. The impinging jet shear layers and the fountain have high values of $\overline{w'w'}$. The Reynolds stress $\overline{w'w'}$ is maximum in the inner jet shear layers (i.e., at $x = \pm - 1$) at $z \approx 0.4$. This position almost coincides with the location of the shock wave in the mean flow. The relatively high levels on the centerlines of the two jets are caused by the unsteady location of the shocks, and therefore may not represent true turbulence fluctuations. From the above six figures, it is obvious that the Reynolds normal stress in the x-direction, $\overline{u'u'}$, is dominant in the plane which passes through the jet centerlines ($y = 0$ plane).

The contour plots for the Reynolds stress components, $\overline{u'u'}$, $\overline{u'v'}$, $\overline{u'w'}$, $\overline{v'v'}$, $\overline{v'w'}$ and $\overline{w'w'}$ in the $x = 0$ plane are shown in Figures 6.171 through 6.176 respectively. The Reynolds normal stress in the x-direction, $\overline{u'u'}$, is also symmetric in the $y = 0$ plane with respect to the plane centerline, as can be seen from 6.171. The region of high level of $\overline{u'u'}$ is located above the collision zone at the fountain base. The maximum value of $\overline{u'u'}$ occurs at $(0,\ 0,\ 0.1)$ and it is equal to 0.3012 . The Reynolds shear stress $\overline{u'v'}$ does not exhibit any symmetry or anti-symmetry in the $x = 0$ plane, as one can see from Figure 6.172. Since $\overline{u'v'}$ should be zero at $y = 0$, it can be concluded that this stress has not converged to steady state yet, and hence longer averaging period is needed. The Reynolds shear stress, $\overline{u'w'}$, shown in Figure 6.173 is not symmetric with respect to $y = 0$ axis. However, it seems to have a tendency to exhibit some degree of symmetry. Therefore, it is believed that with longer period of averaging, $\overline{u'w'}$ will be symmetric in this plane. It can be seen from this figure that $\overline{u'w'}$ reaches its maximum magnitude of 0.018 in the fountain region at $(0,\ -0.22,\ 0.4)$. The Reynolds normal stress in the y-direction, $\overline{v'v'}$, is symmetric with respect to the $y = 0$ axis, as can be seen from Figure 6.174. The maximum value of $\overline{v'v'}$ in this plane is 0.04 and it occurs at $(0,\ 1.7,\ 0.3)$. The Reynolds shear stress $\overline{v'w'}$ shown in Figure 6.175 is quite anti-symmetric with respect to $y = 0$ axis for $z \leq 2.0$. The small regions in the neighborhood of the points $(0,\ -1.1,\ 0.4)$ and $(0,\ 1.25,\ 0.4)$ have highest values of $\overline{v'w'}$ which is equal to 0.021. The Reynolds normal stress in the z-direction, $\overline{w'w'}$, also looks somewhat symmetric in the $x = 0$ plane, except in the lower region just above the wall jets where the stress level on the negative side of the y axis is higher. This indicates that more averaging time is required in order for $\overline{w'w'}$ to become perfectly symmetric. The Reynolds normal stress $\overline{w'w'}$ reaches its maximum value of 0.047 at $(0,\ -0.2,\ 0.4)$.

The contour plots for the six Reynolds stress components, $\overline{u'u'}$, $\overline{u'v'}$, $\overline{u'w'}$, $\overline{v'v'}$, $\overline{v'w'}$ and $\overline{w'w'}$ in the $z = 0.005745$ plane, the plane just above the ground are shown, respectively, in Figures 6.177 through 6.182. From these figures, it can be seen clearly that in this plane the Reynolds shear stresses, $\overline{u'v'}$, $\overline{u'w'}$ and $\overline{v'w'}$ are anti-symmetric with respect to the centerlines of the plane. On the other hand, the normal Reynolds stresses $\overline{u'u'}$, $\overline{v'v'}$ and $\overline{w'w'}$ are more or less symmetric with respect to the centerlines of the plane. From these six figures, it is evident that $\overline{u'u'}$ is dominant in the region between the jets.

Figures 6.183 through 6.188 show the distribution of the Reynolds stresses in the x-direction

in the $y = 0$ plane at $z = 0.536607$, the elevation where the fountain peak velocity reaches its maximum. It is evident from Figure 6.183 that $\overline{u'u'}$ is symmetric with respect to the $x = 0$ axis. The stress component reaches its peak of 0.067 at $x = 0$. Figures 6.184, 6.185 and 6.187 show, respectively, that $\overline{u'v'}$, $\overline{u'w'}$ and $\overline{v'w'}$ exhibit some degrees of anti-symmetry with respect to the $x = 0$ axis. It is possible that these stress components will be anti-symmetric with respect to the $x = 0$ axis if averaging of these stresses is taken over a longer period of time. In addition, the low levels of $\overline{u'v'}$ and $\overline{v'w'}$ indicate that these two stress components will eventually converge to zero. With longer period of averaging, it may also be possible for the Reynolds stresses $\overline{v'v'}$ and $\overline{w'w'}$, which are shown in Figure 6.186 and Figure 6.188, respectively, to become symmetric with respect to the $x = 0$ axis. Due to the interaction of the jets and the fountain, the distribution of normal stresses in the impinging jets is not symmetric with respect to the jet axes. The stress levels of $\overline{u'u'}$, $\overline{v'v'}$, and $\overline{w'w'}$ are higher in the inner jet shear layers at $x = 1$ and $x = -1$ than in the outer jet shear layers at $x = 2$ and $x = -2$ as shown in Figures 6.183, 6.186 and 6.188, respectively.

Figures 6.189 through 6.194 show the distribution of the Reynolds stresses in the y-direction in the $x = 0$ plane at $z = 0.536607$. The Reynolds normal stress $\overline{u'u'}$, shown in Figure 6.189, looks quite symmetric with respect to the $x = 0$ axis, with a slight bias towards the positive y-direction. The Reynolds shear stress $\overline{u'v'}$ is somewhat anti-symmetric with respect to the $y = 0$ axis, as can be seen from Figure 6.190. The Reynolds shear stress $\overline{u'w'}$, shown in Figure 6.191 is seen to exhibit some degree of symmetry with respect to the line passing through $x = -0.5$. The Reynolds normal stresses $\overline{v'v'}$ and $\overline{w'w'}$, shown respectively in Figures 6.192 and 6.194 are seen to be somewhat symmetric with respect to the $y = 0$ axis. The Reynolds shear stress $\overline{v'w'}$ is clearly seen to be anti-symmetric with respect to the $y = 0$ axis in Figure 6.193. The above figures indicates that longer averaging time may be needed to see if the Reynolds stress components will become perfectly symmetric or anti-symmetric with respect to the centerlines of the plane under consideration.

Figures 6.195 through 6.200 show, respectively, the variation of Reynolds stresses, $\overline{u'u'}$, $\overline{u'v'}$, $\overline{u'w'}$, $\overline{v'v'}$, $\overline{v'w'}$ and $\overline{w'w'}$ as a function of z at various x locations between the impinging jets in the $y = 0$ plane. The upper profiles in these figures show the changes of the Reynolds stresses from the shear layer of the left jet at $x = -1$ towards the vicinity of collision zone at $x = -0.05$, whereas the lower profiles in the figures show the changes of the Reynolds stresses between the shear layer of the right jet at $x = 1$ and the vicinity of collision zone at $x = 0.05$. These figures show that the effect of the Reynolds stresses is more or less confined in the region $0 \leq z \leq 3$. From Figure 6.195, it can be seen that the effect of $\overline{u'u'}$ is only significant in the wall jet region. The evolution of the profiles of $\overline{u'u'}$ clearly show that $\overline{u'u'}$ is increasing as the collision region is approached. From Figure 6.195, one can also see that at $x = 0.05$, $\overline{u'u'}$ reaches its maximum value of 0.32 at $z = 0.1$. The profiles in Figures 6.198 and 6.200 show that $\overline{v'v'}$ and $\overline{w'w'}$ are somewhat symmetric with respect to $x = 0$ plane. However, there is no symmetry in $\overline{u'v'}$, $\overline{u'w'}$ and $\overline{v'w'}$ as shown in Figures 6.196, 6.197, and 6.199, respectively. From Figure 6.198, it can be seen that $\overline{v'v'}$ is maximum at $x = \pm 1$ where the flow undergoes turning. These are also the locations where $\overline{w'w'}$ is maximum as can be

seen from Figure Figure 6.200. From these six figures, it is clear that in the $y = 0$ plane, the Reynolds normal stress $\overline{u'u'}$ is dominant in the vicinity of the collision region, i.e., at $x = \pm 0.05$.

Figures 6.201 through 6.206 show the variation of the six Reynolds stress components as a function of z at various y locations in the $x = 0$ plane. The Reynolds stresses are also seen to be confined within the region $0 \leq z \leq 3$. However, $\overline{u'u'}$ is only significant in the wall jet region. The normal stress in the x-direction, $\overline{u'u'}$, is seen to be symmetric with respect to the $y = 0$ axis in Figure 6.201, whereas the normal stresses in the y- and z- directions, $\overline{v'v'}$ and $\overline{w'w'}$, are seen to be only somewhat symmetric with respect to the $y = 0$ axis in Figures 6.204 and 6.206, respectively. The Reynolds shear stress $\overline{u'w'}$ exhibits neither symmetry nor anti-symmetry according to Figures 6.203, whereas the Reynolds shear stress $\overline{v'w'}$ is seen to be anti-symmetric with respect to $y = 0$ axis from Figures 6.205. From these profiles in the $x = 0$ plane, it is also observed that the six Reynolds stress components are more or less of the same order of magnitude.

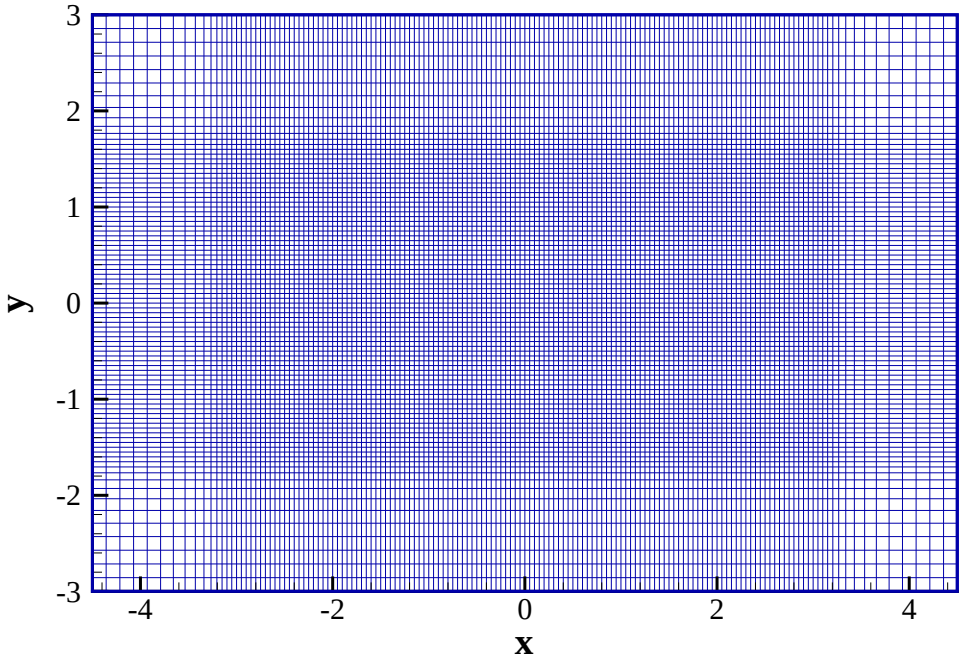

Figure 6.1: A xy-plane of computational grid

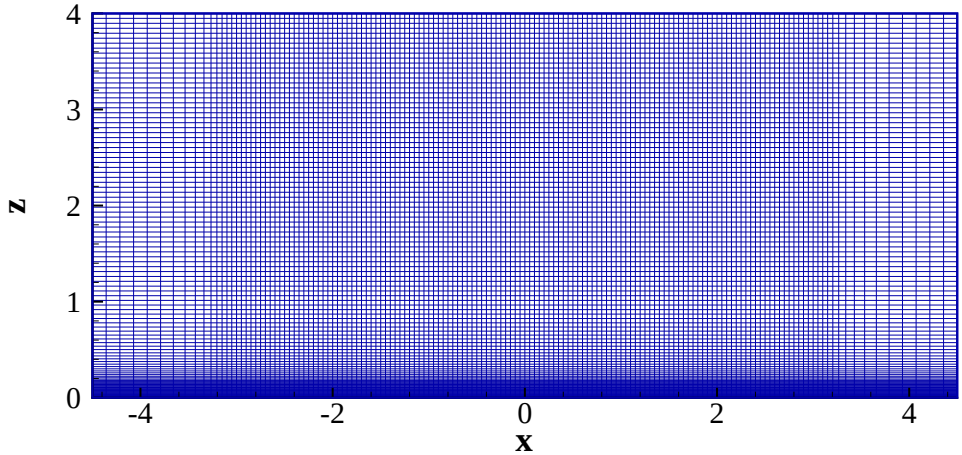

Figure 6.2: A xz-plane of computational grid

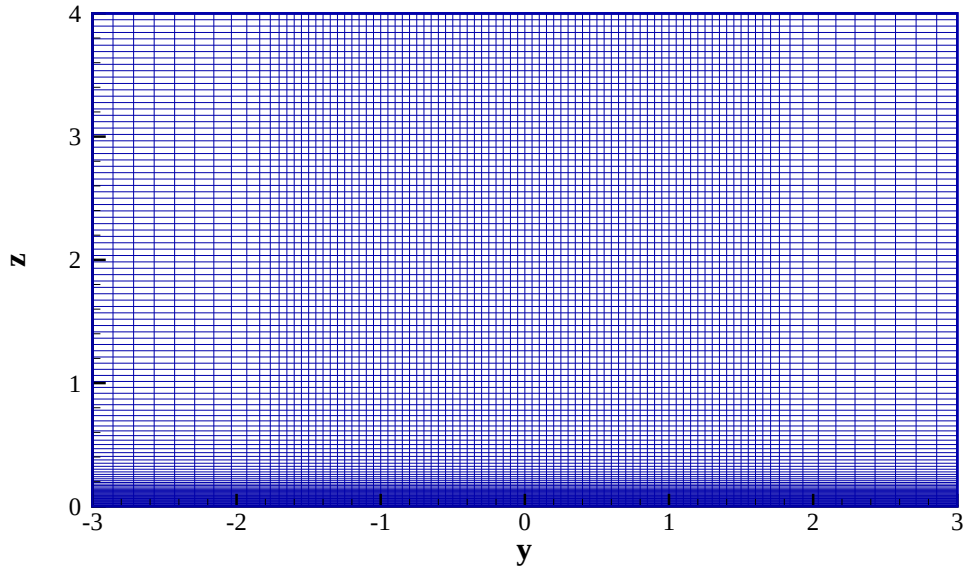

Figure 6.3: A yz-plane of computational grid

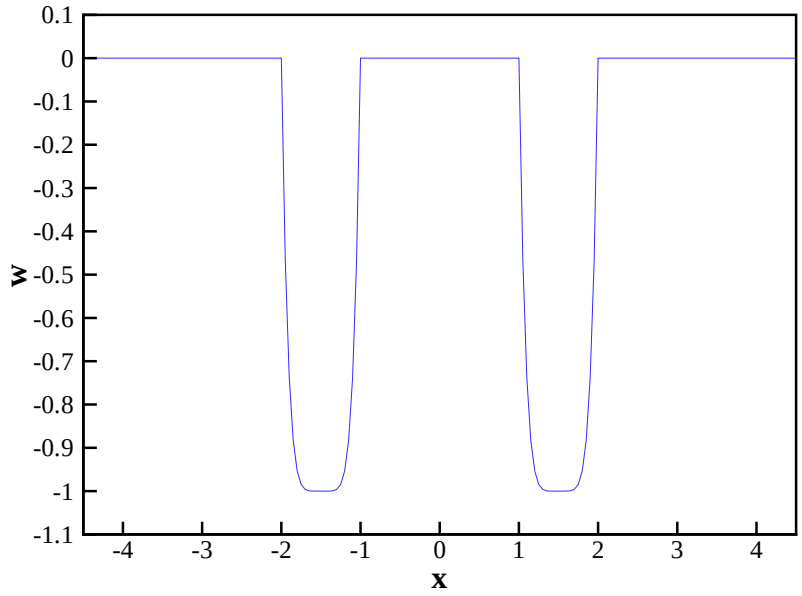

Figure 6.4: w-velocity at $z = 4$ (jet exit plane)

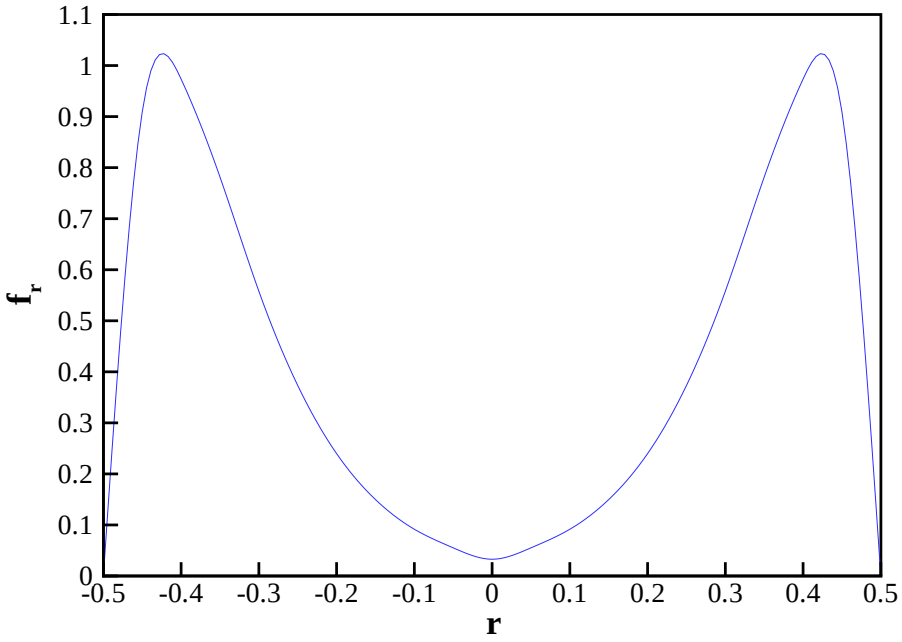

Figure 6.5: Forcing function f_r

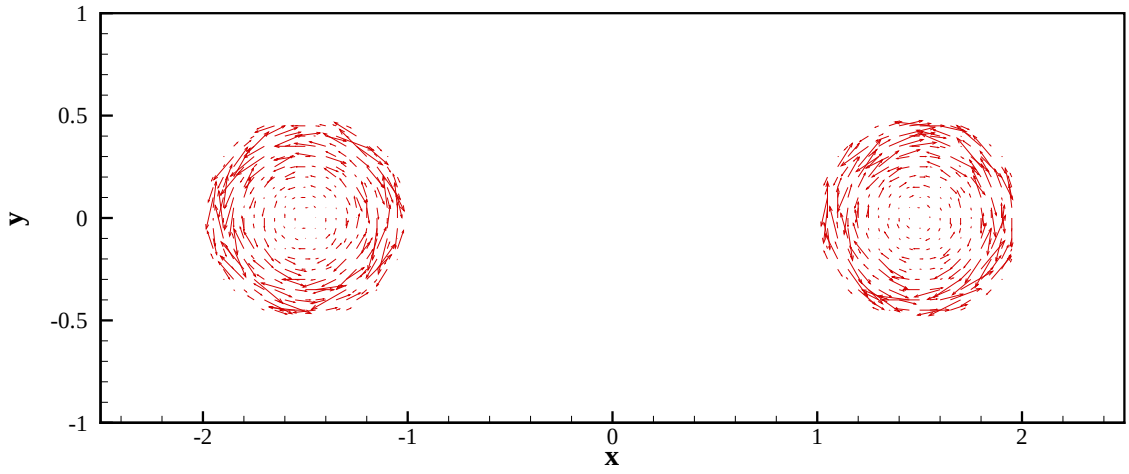

Figure 6.6: Initial velocity vector field in the jet exit plane

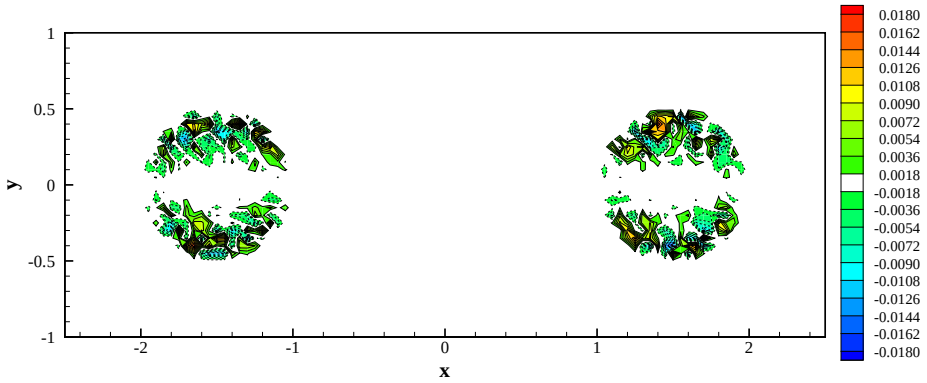

Figure 6.7: Contour plot for u in the jet exit plane.

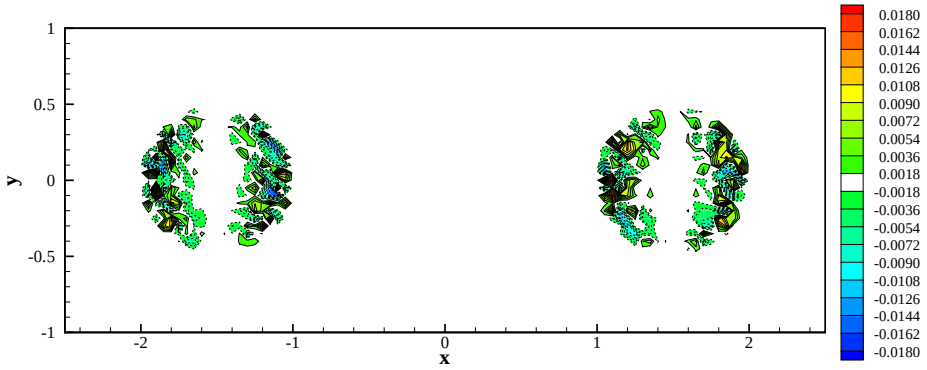

Figure 6.8: Contour plot for v in the jet exit plane.

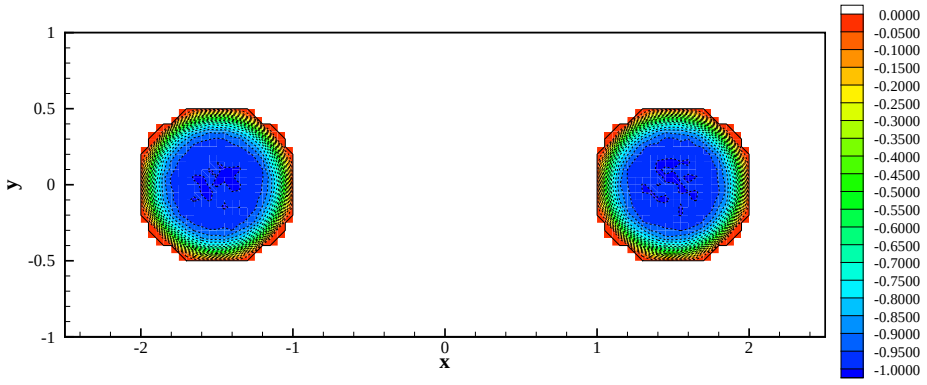

Figure 6.9: Contour plot for w in the jet exit plane.

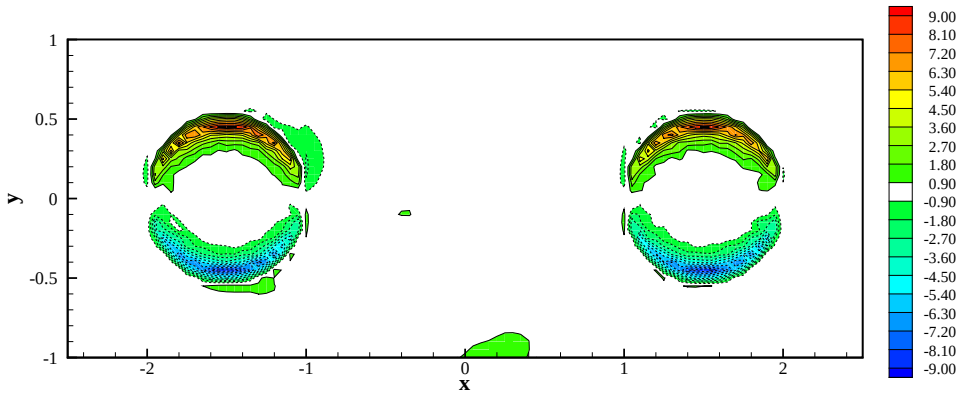

Figure 6.10: The x-vorticity contour in the jet exit plane

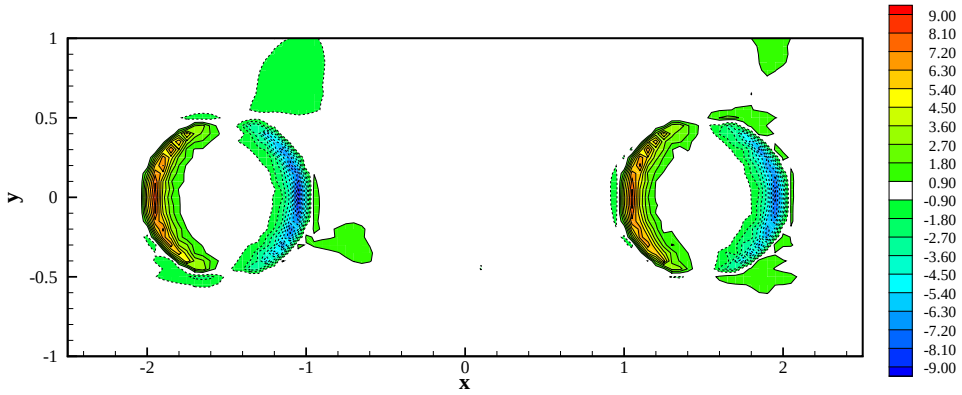

Figure 6.11: The y-vorticity contour in the jet exit plane

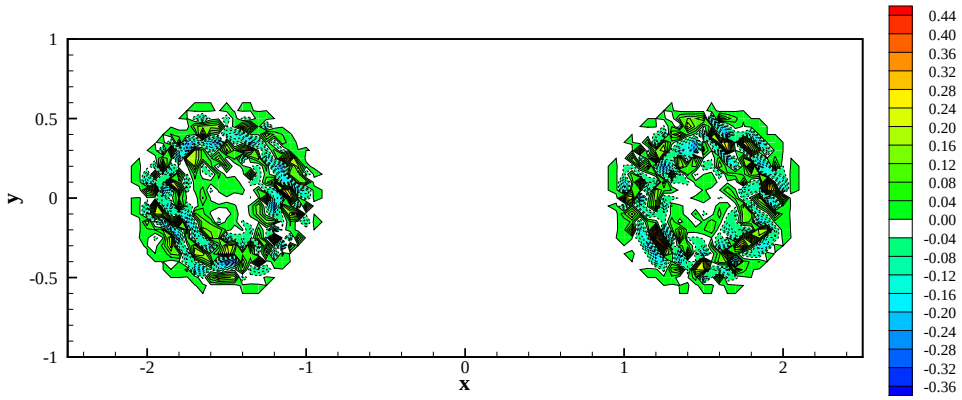

Figure 6.12: The z-vorticity contour in the jet exit plane

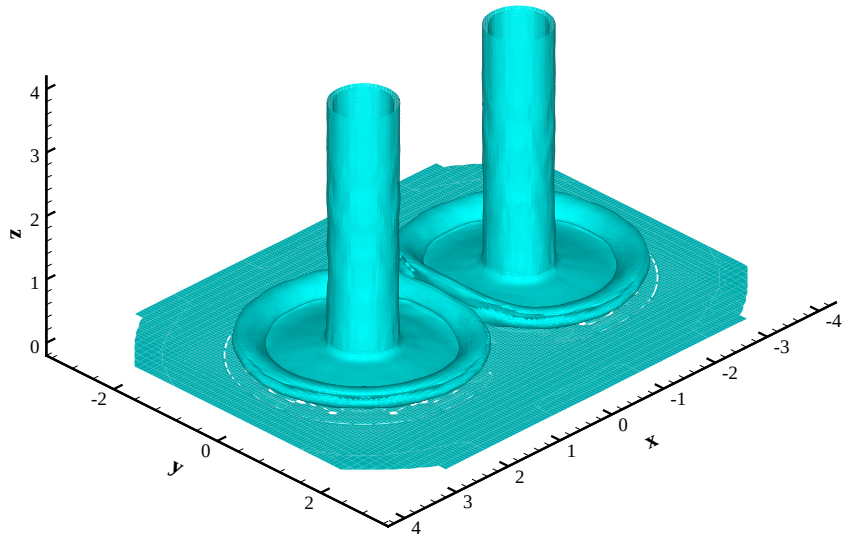

Figure 6.13: Iso-surface of vorticity magnitude at the level $|\vec{\omega}| = 5.0$ at $t = 3.5866$

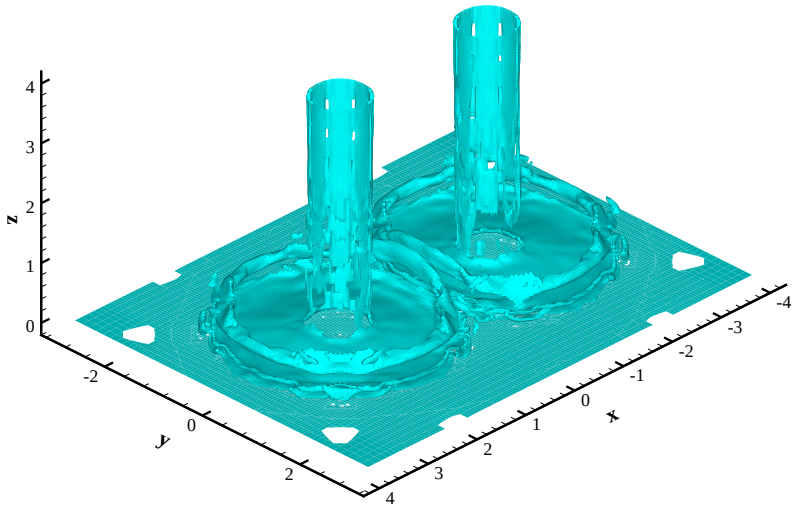

Figure 6.14: Iso-surface of vorticity magnitude at the level $|\vec{\omega}| = 6.5$ at $t = 5.3276$

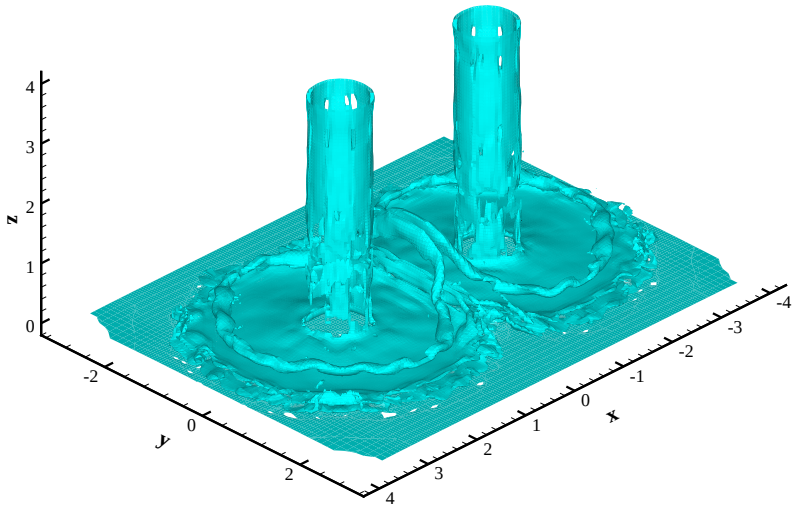

Figure 6.15: Iso-surface of vorticity magnitude at the level $|\vec{\omega}| = 6.0$ at $t = 7.0391$

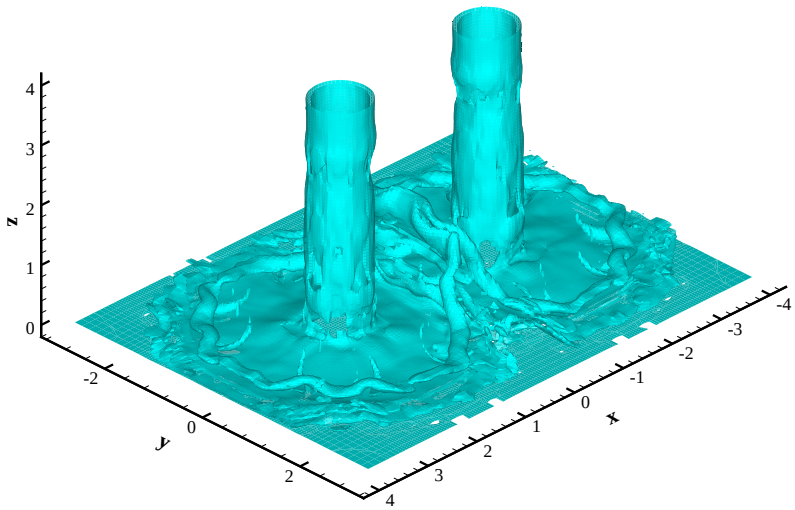

Figure 6.16: Iso-surface of vorticity magnitude at the level $|\vec{\omega}| = 6.0$ at $t = 8.7412$

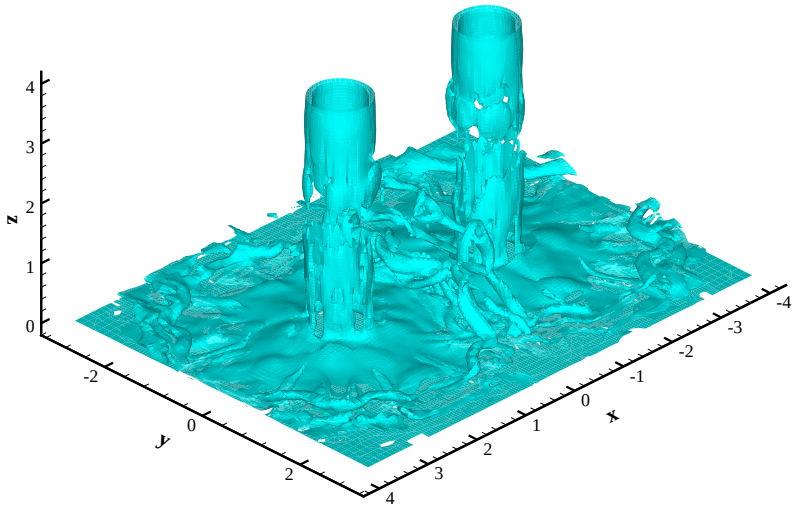

Figure 6.17: Iso-surface of vorticity magnitude at the level $|\vec{\omega}| = 6.0$ at $t = 10.4343$

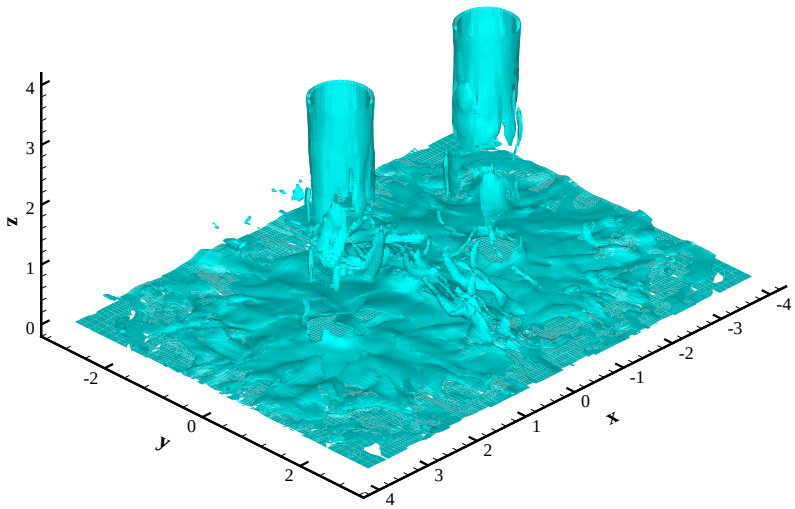

Figure 6.18: Iso-surface of vorticity magnitude at the level $|\vec{\omega}| = 6.0$ at $t = 13.0124$

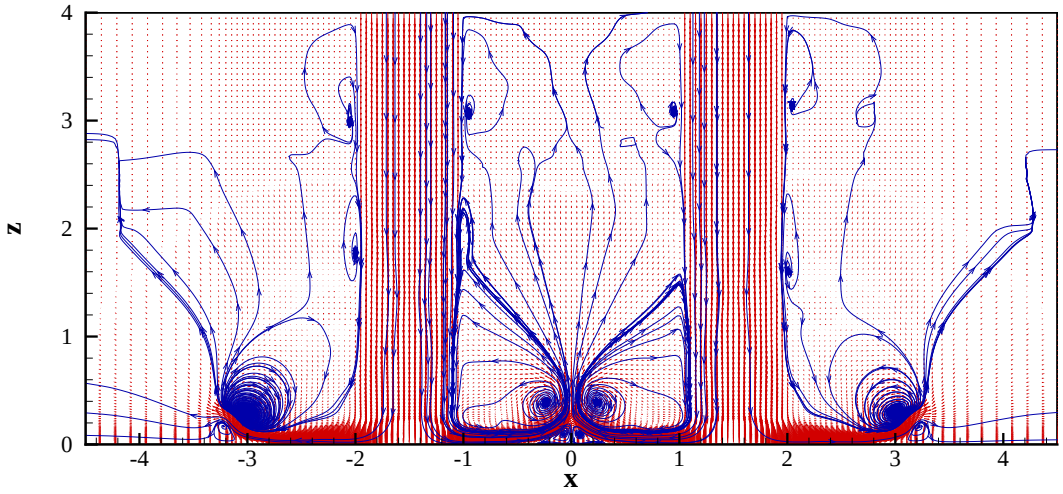

Figure 6.19: The velocity field in the $y = 0$ plane at $t = 3.5866$

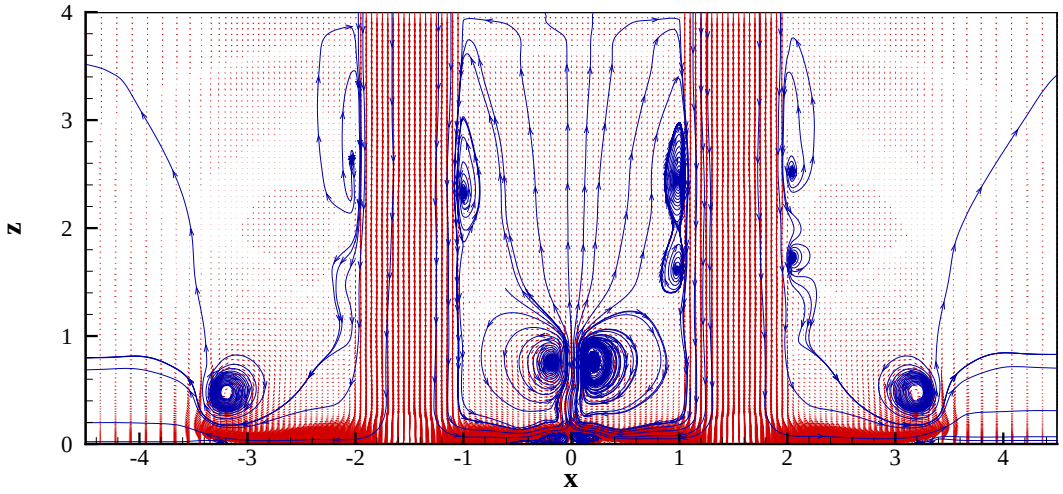

Figure 6.20: The velocity field in the $y = 0$ plane at $t = 5.3276$

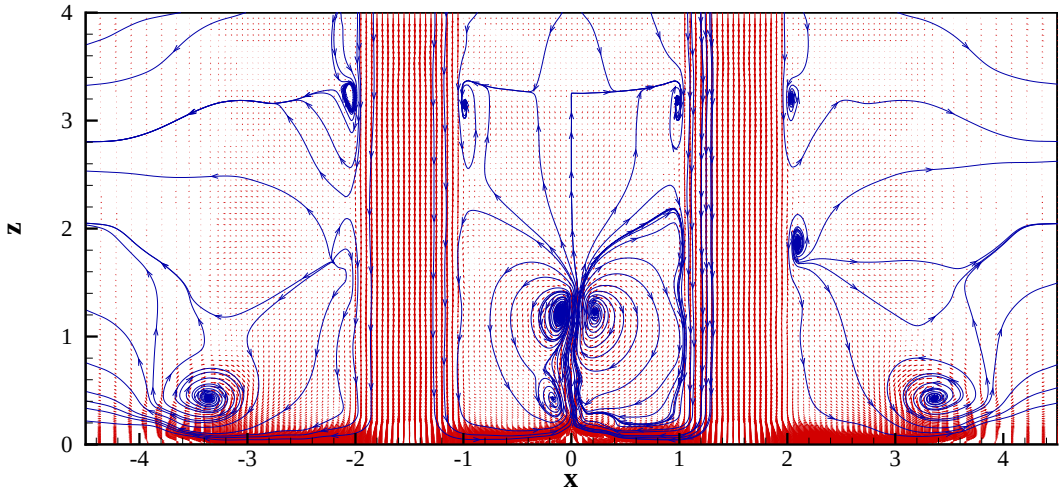

Figure 6.21: The velocity field in the $y = 0$ plane at $t = 7.0391$

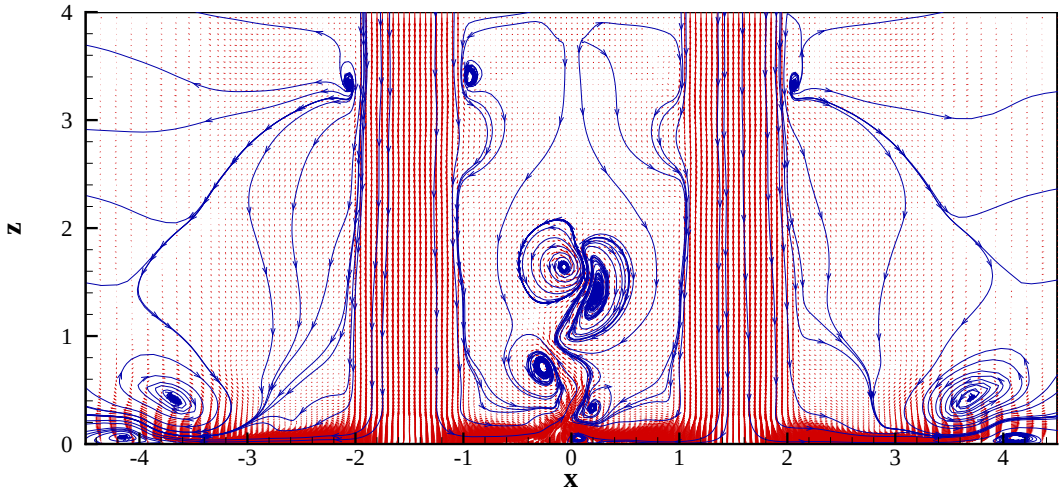

Figure 6.22: The velocity field in the $y = 0$ plane at $t = 8.74125$

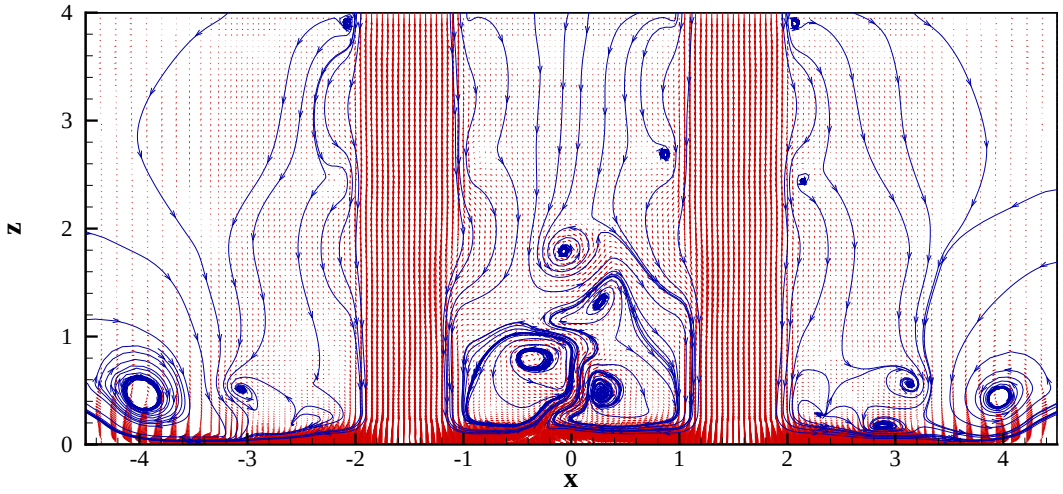

Figure 6.23: The velocity field in the $y = 0$ plane at $t = 10.4343$

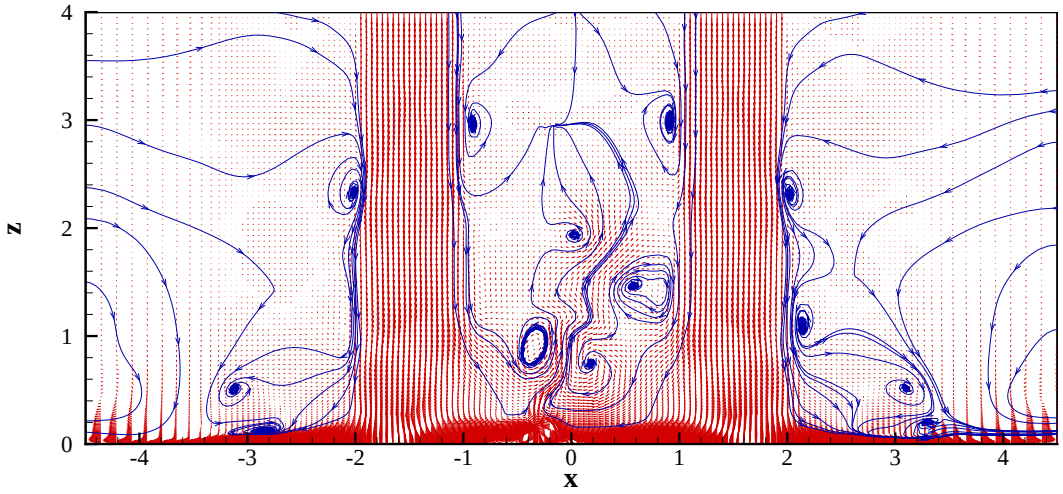

Figure 6.24: The velocity field in the $y = 0$ plane at $t = 13.0123$

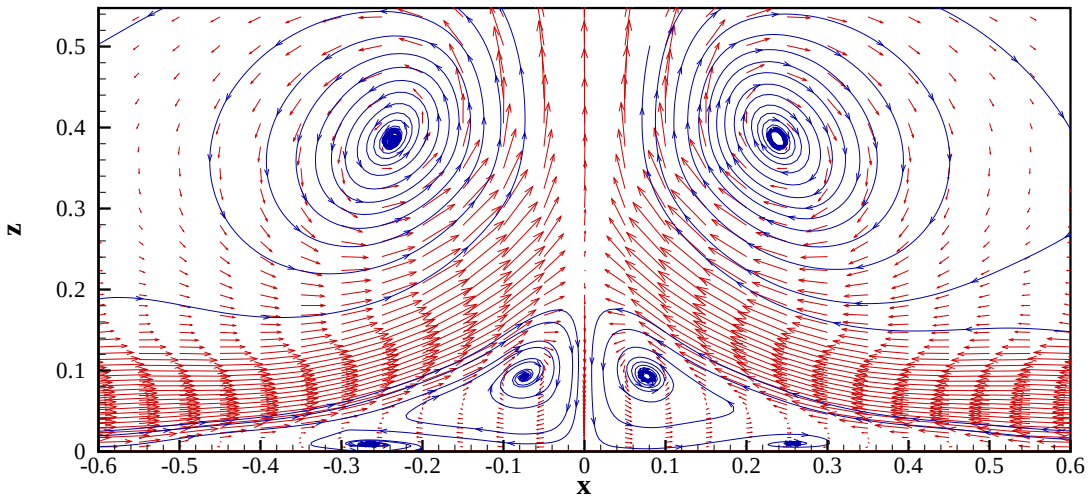

Figure 6.25: A close view of the velocity field at the fountain root in the $y = 0$ plane at $t = 3.5866$

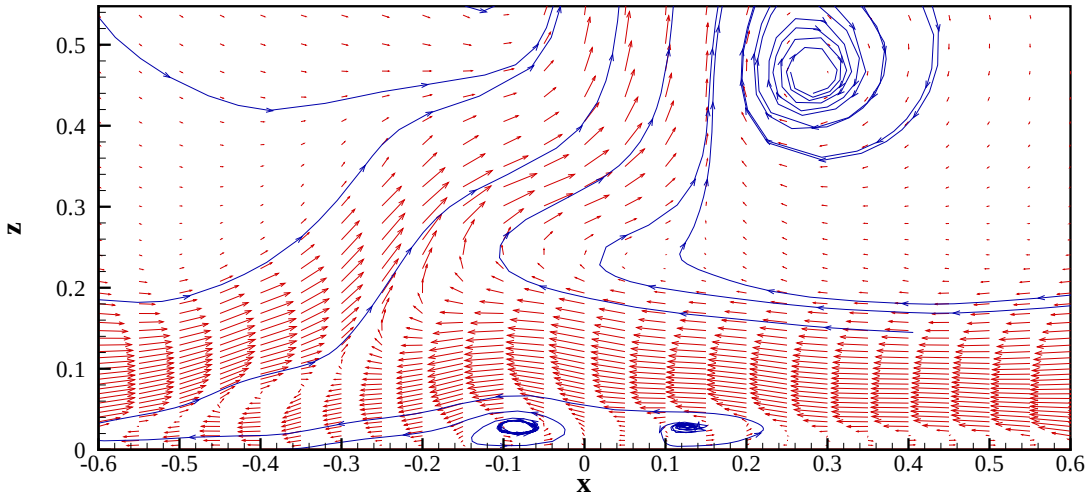

Figure 6.26: A close view of the velocity field at the fountain root in the $y = 0$ plane at $t = 10.4343$

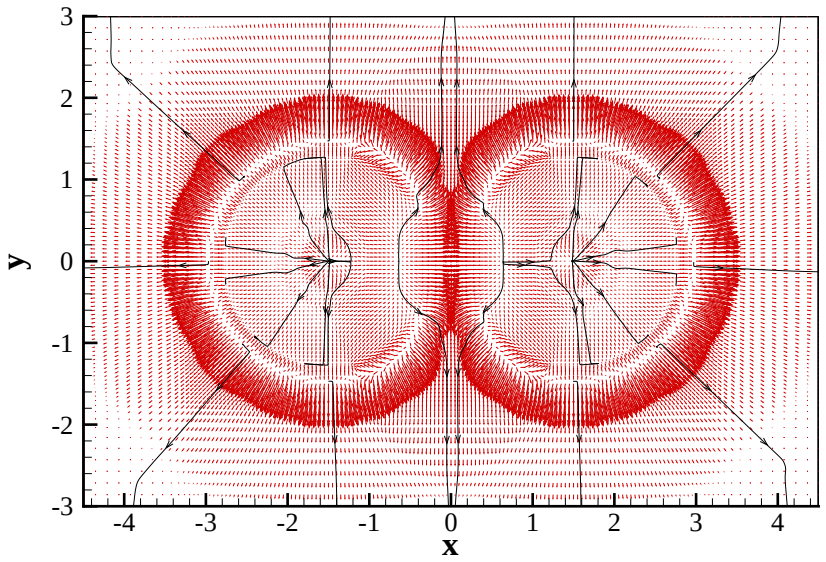

Figure 6.27: The velocity field in the $z = 0.301057$ plane at $t = 3.5866$

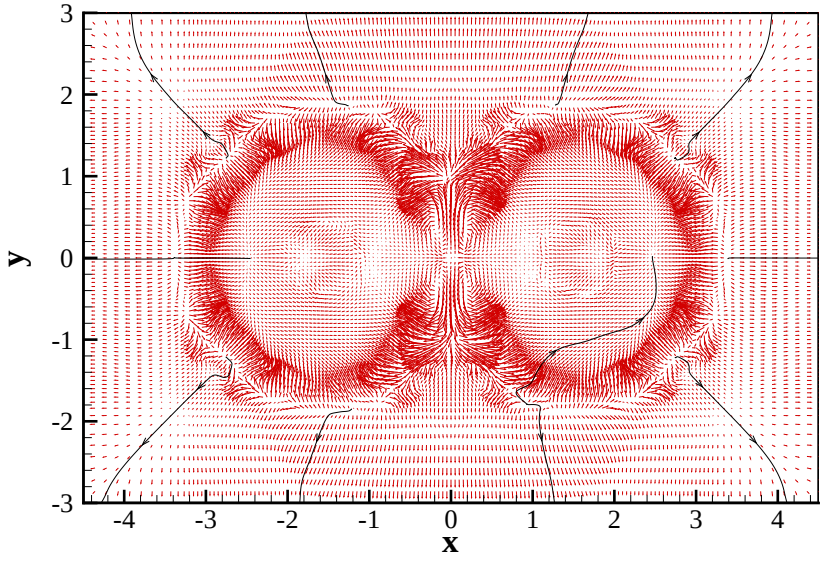

Figure 6.28: The velocity field in the $z = 0.735948$ plane at $t = 5.3276$

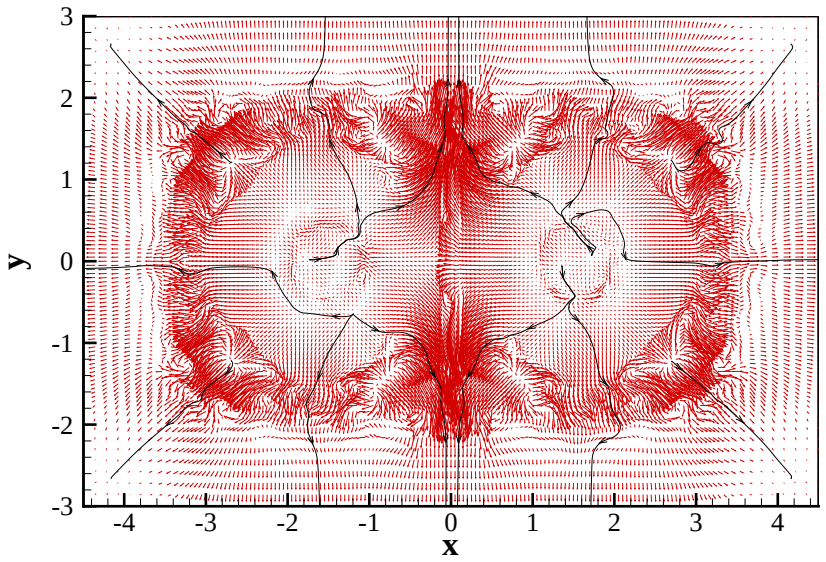

Figure 6.29: The velocity field in the $z = 0.405084$ plane at $t = 7.0391$

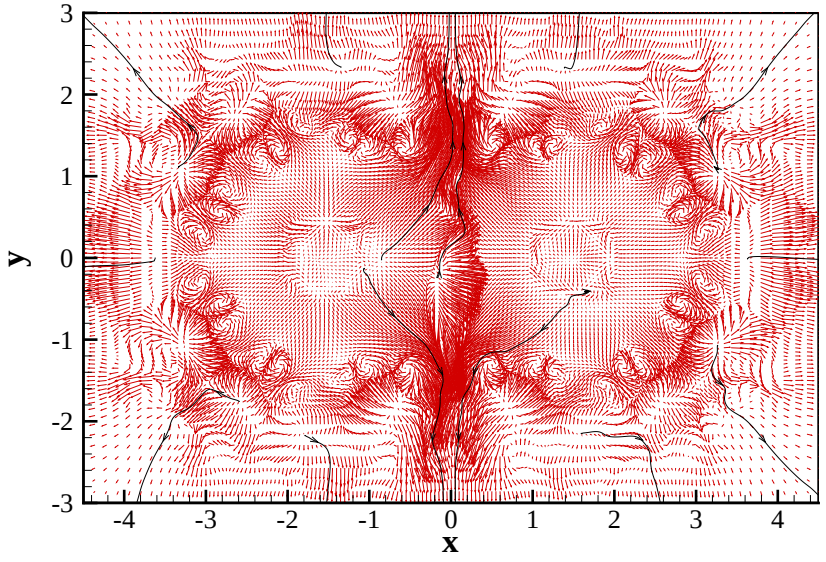

Figure 6.30: The velocity field in the $z = 0.376481$ plane at $t = 8.74125$

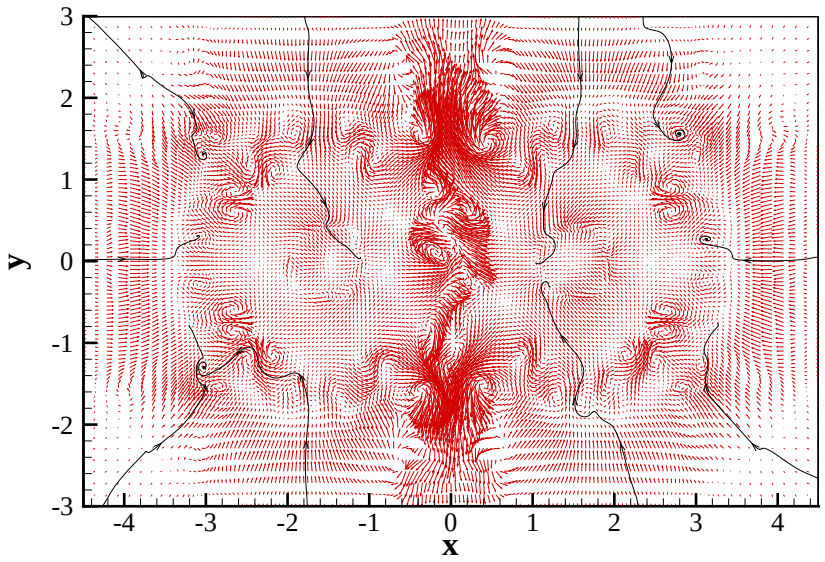

Figure 6.31: The velocity field in the $z = 0.612082$ plane at $t = 10.4343$

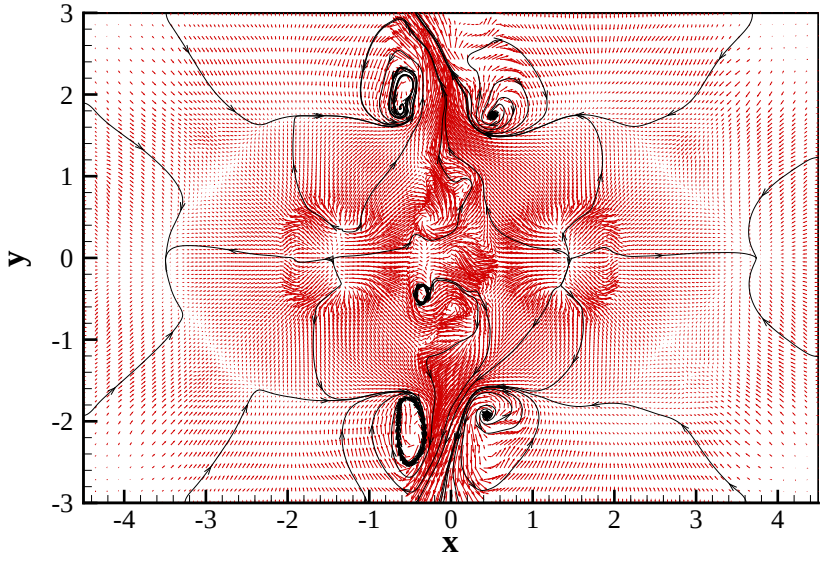

Figure 6.32: The velocity field in the $z = 0.917263$ plane at $t = 13.0123$

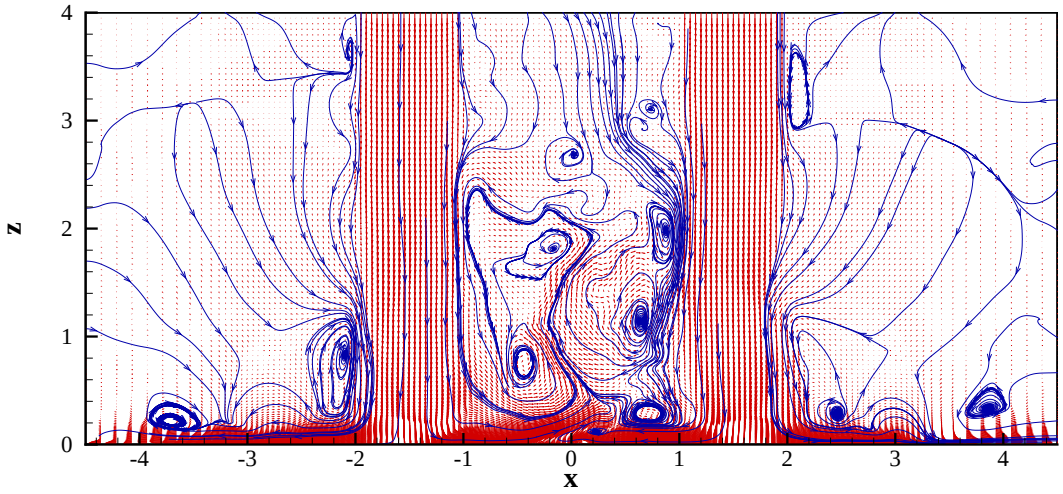

Figure 6.33: The velocity field in the $y = 0$ plane at $t = 104.3092$

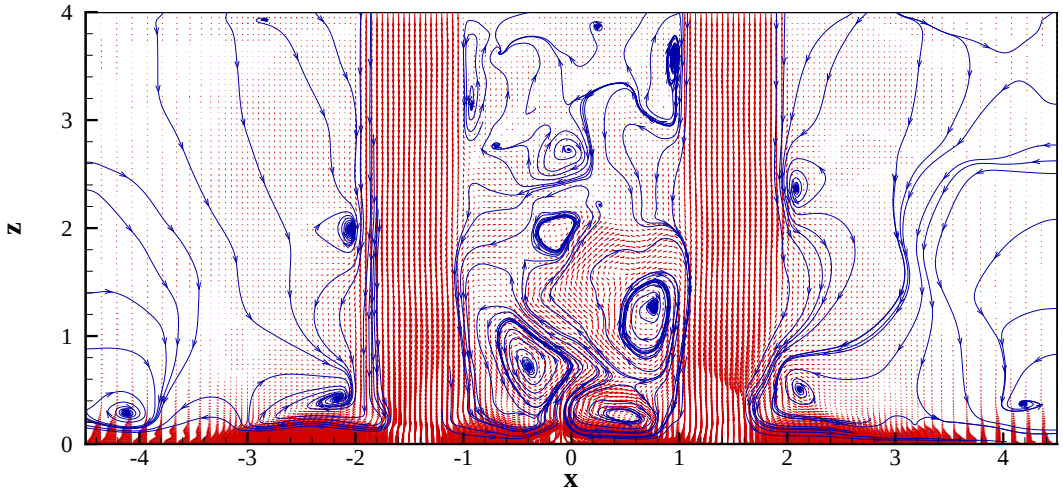

Figure 6.34: The velocity field in the $y = 0$ plane at $t = 105.7092$

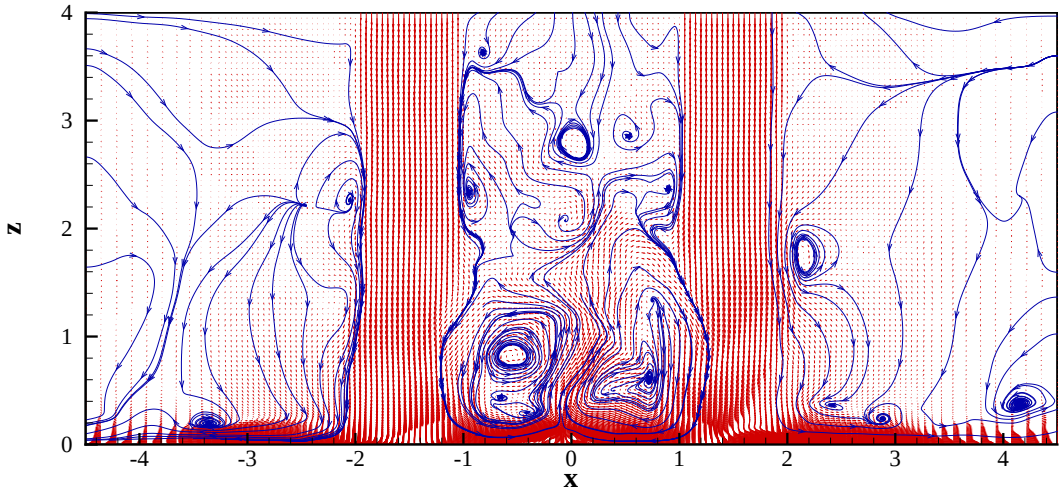

Figure 6.35: The velocity field in the $y = 0$ plane at $t = 107.1092$

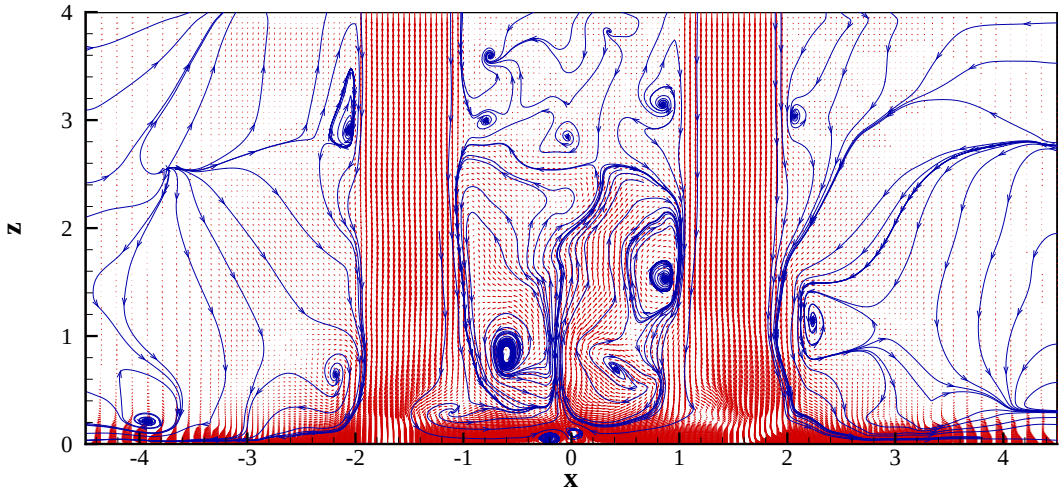

Figure 6.36: The velocity field in the $y = 0$ plane at $t = 108.5092$

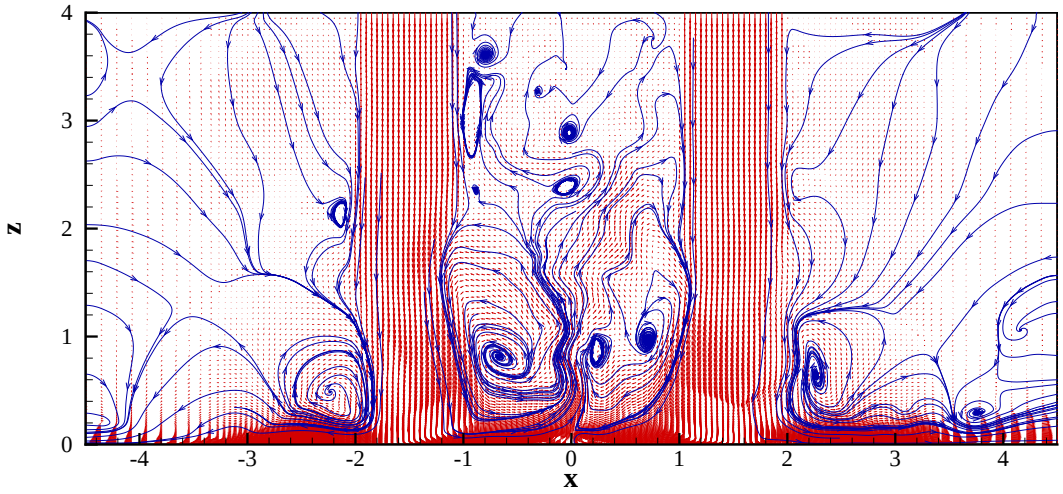

Figure 6.37: The velocity field in the $y = 0$ plane at $t = 109.9092$

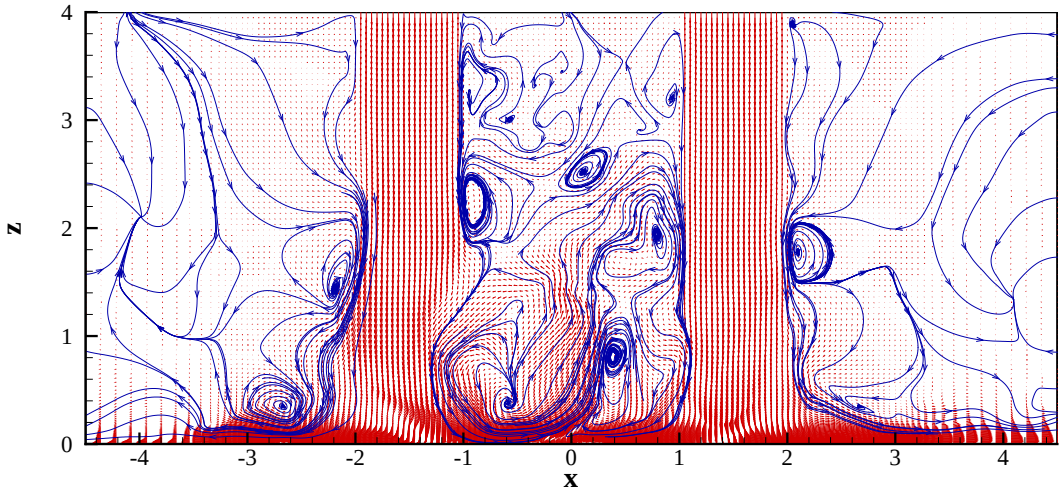

Figure 6.38: The velocity field in the $y = 0$ plane at $t = 111.3092$

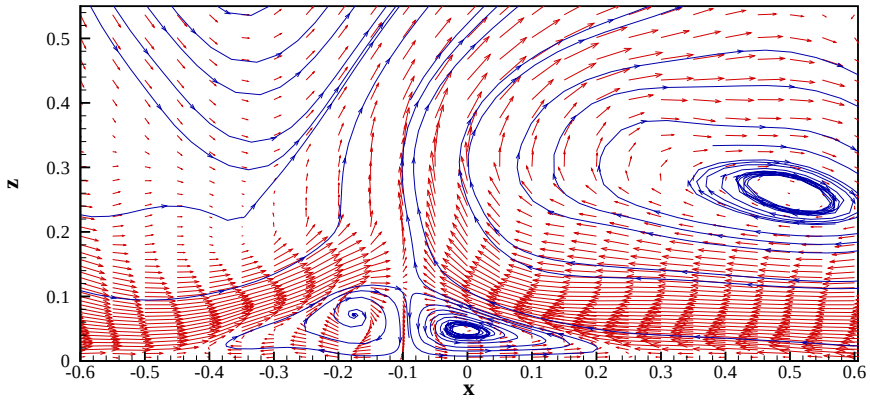

Figure 6.39: A close view of the fountain root in the $y = 0$ plane at $t = 105.7092$

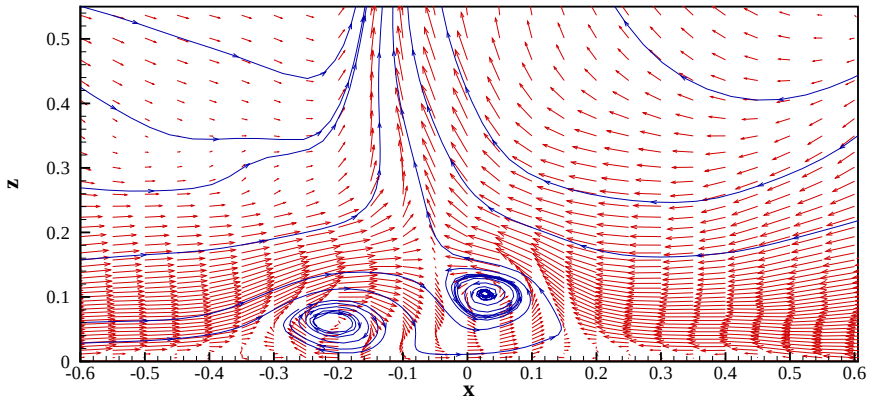

Figure 6.40: A close view of the fountain root in the $y = 0$ plane at $t = 108.5092$

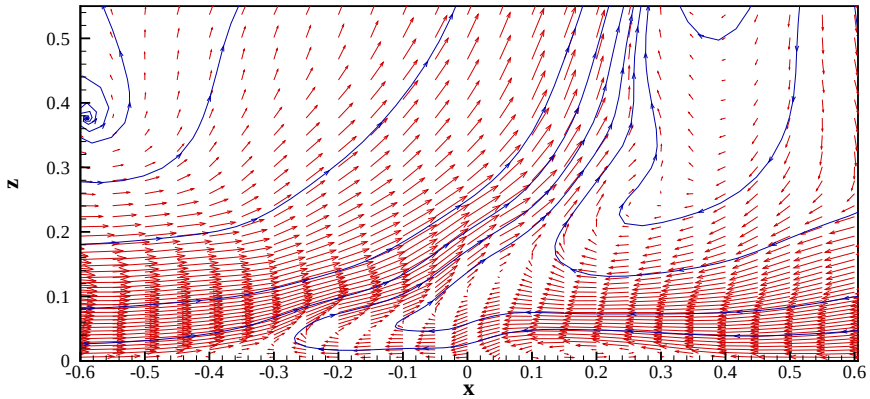

Figure 6.41: A close view of the fountain root in the $y = 0$ plane at $t = 111.3092$

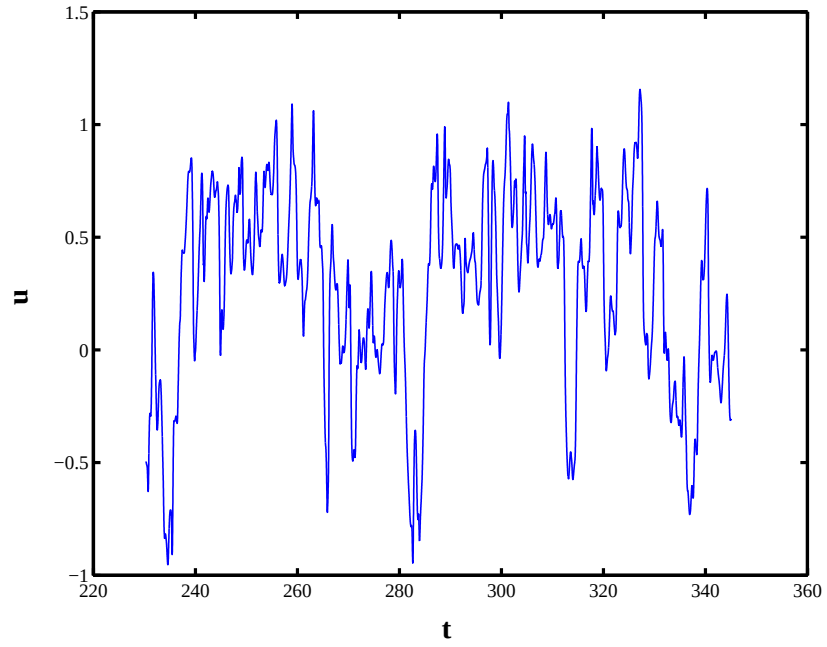

Figure 6.42: Time history of u at $(0, 0, 0.5012)$.

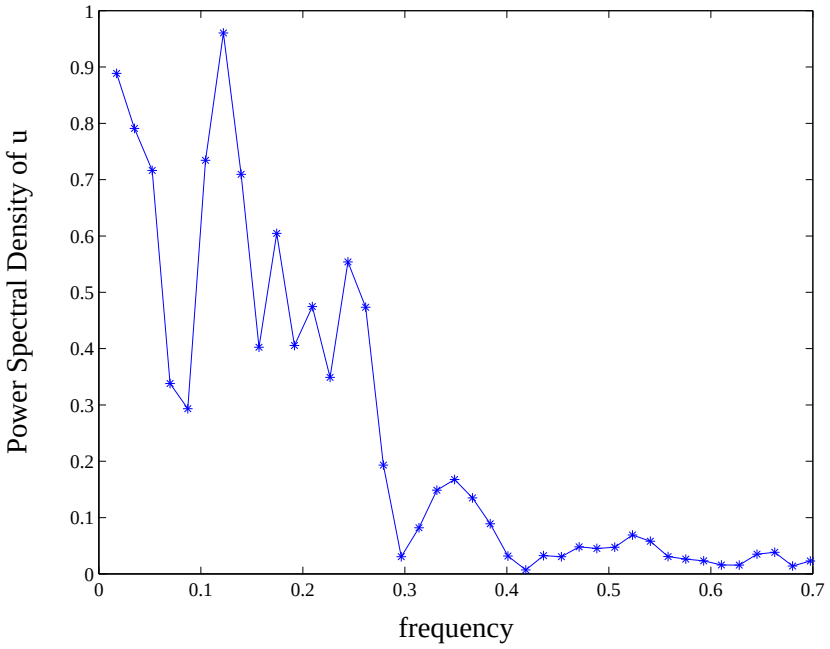

Figure 6.43: Power spectral density of u at $(0, 0, 0.5012)$.

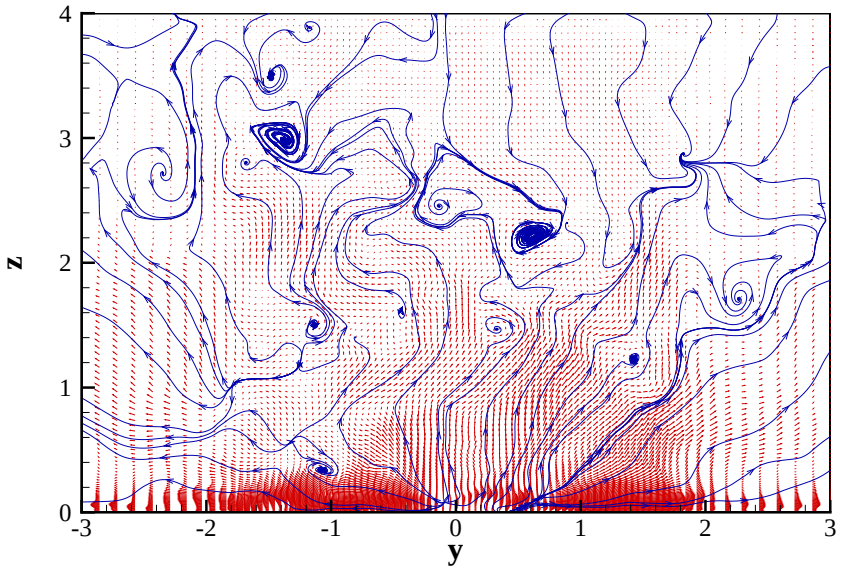

Figure 6.44: The velocity field in the $x = 0$ plane at 104.3092

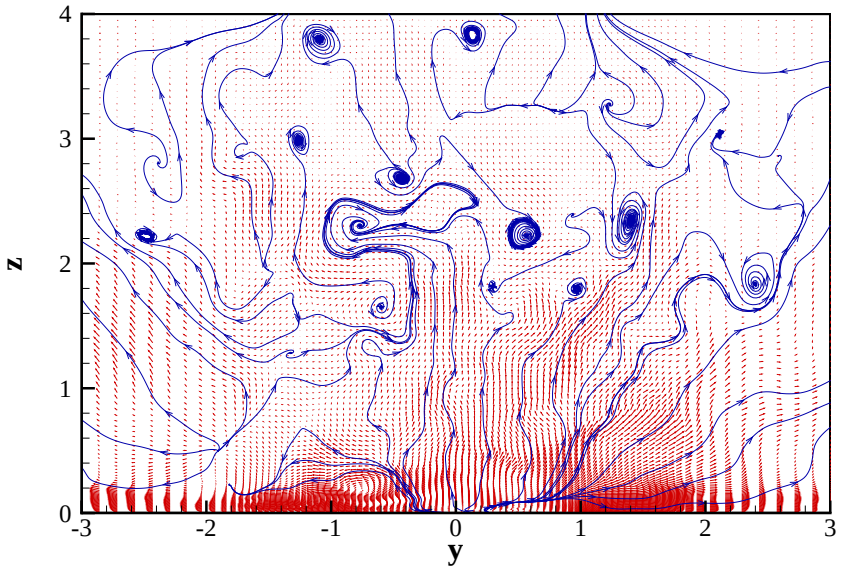

Figure 6.45: The velocity field in the $x = 0$ plane at $t = 105.7092$

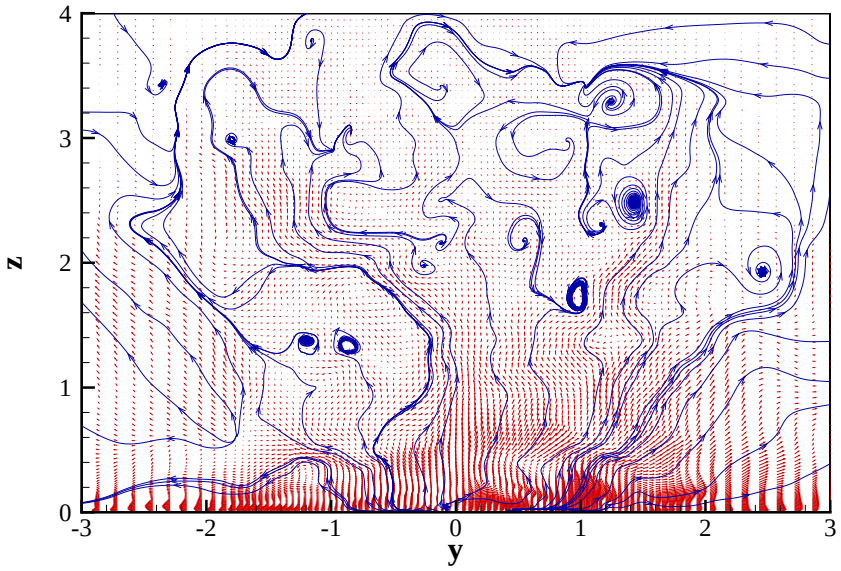

Figure 6.46: The velocity field in the $x = 0$ plane at $t = 107.1092$

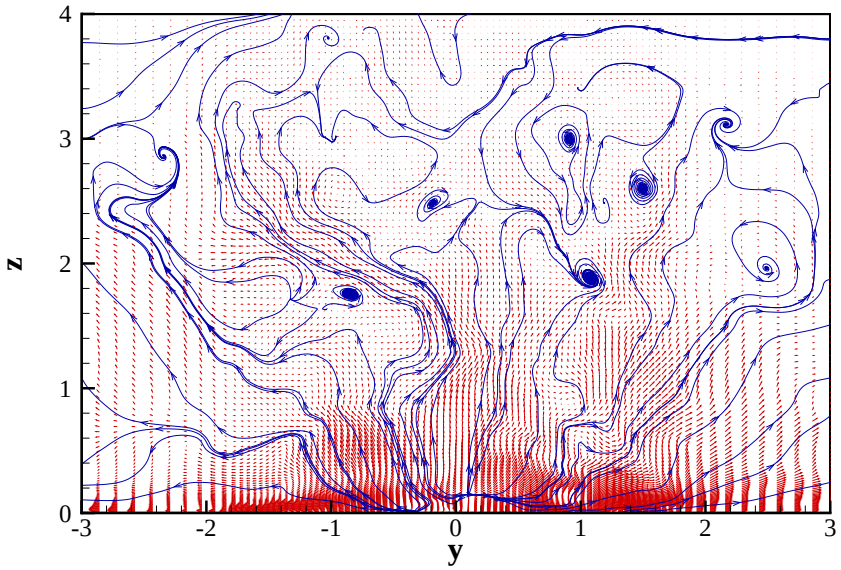

Figure 6.47: The velocity field in the $x = 0$ plane at $t = 108.5092$

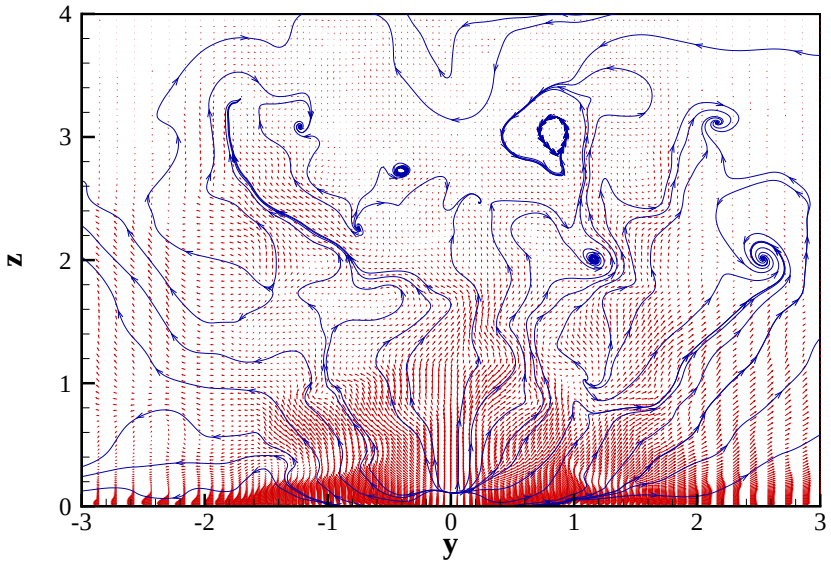

Figure 6.48: The velocity field in the $x = 0$ plane at $t = 109.9092$

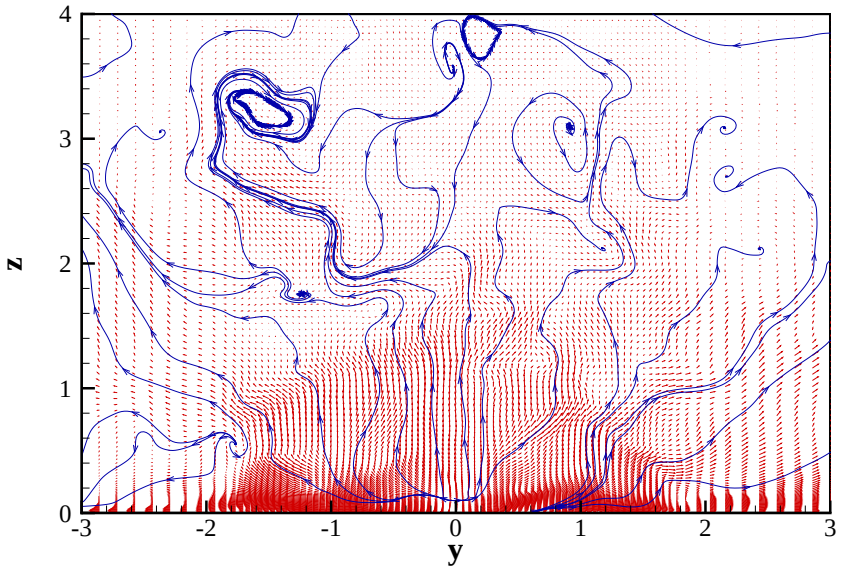

Figure 6.49: The velocity field in the $x = 0$ plane at $t = 111.3092$

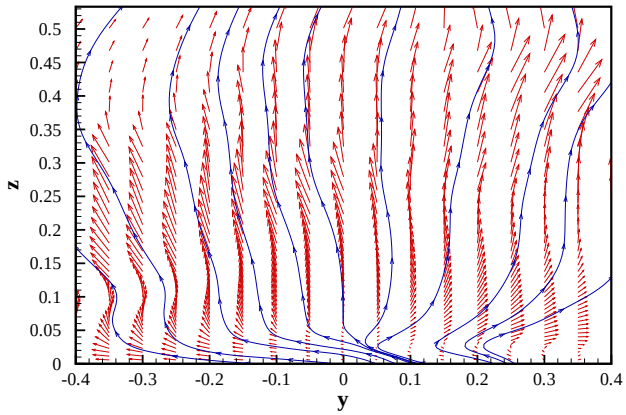

Figure 6.50: A close view of the fountain root in the $x = 0$ plane at $t = 105.7092$

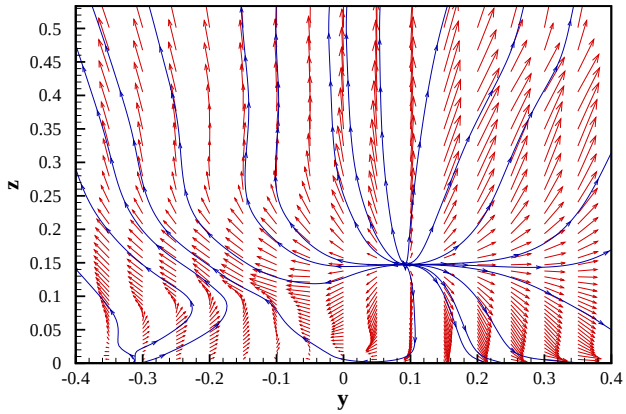

Figure 6.51: A close view of the fountain root in the $x = 0$ plane at $t = 108.5092$

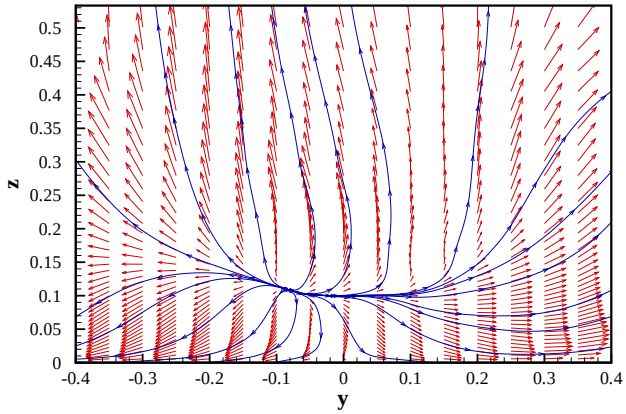

Figure 6.52: A close view of the fountain root in the $x = 0$ plane at $t = 111.3092$

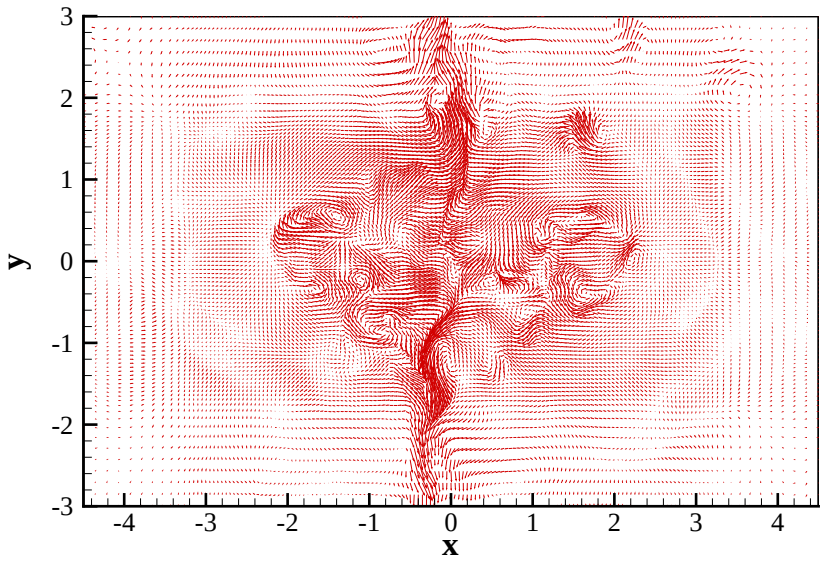

Figure 6.53: The velocity field in the $z = 0.536607$ plane at 104.3092

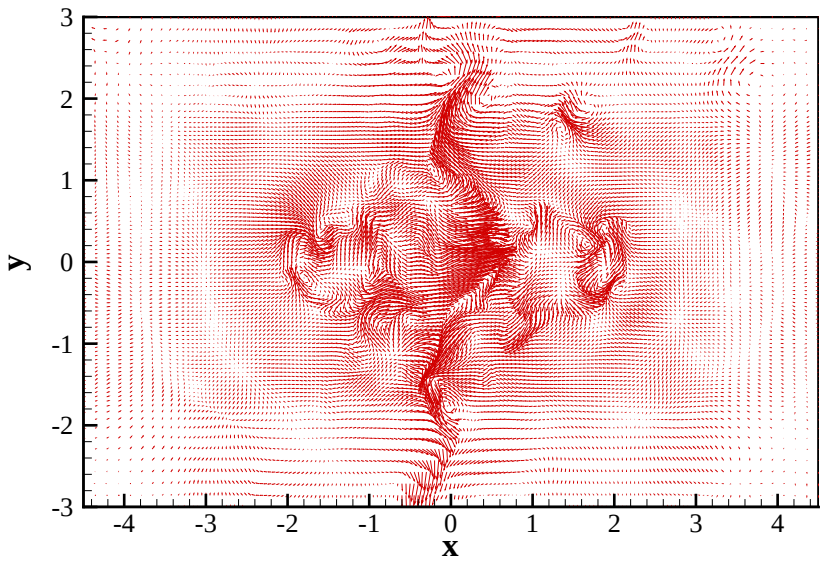

Figure 6.54: The velocity field in the $z = 0.536607$ plane at $t = 105.7092$

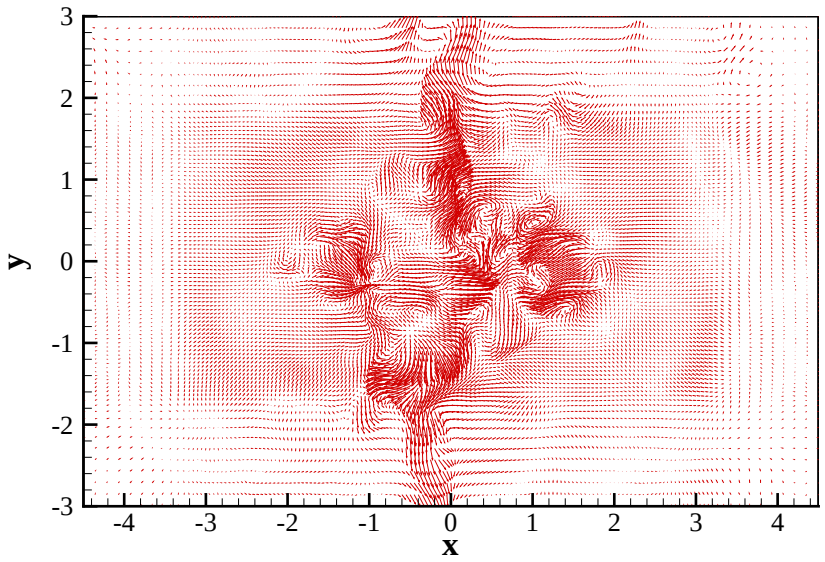

Figure 6.55: The velocity field in the $z = 0.536607$ plane at $t = 107.1092$

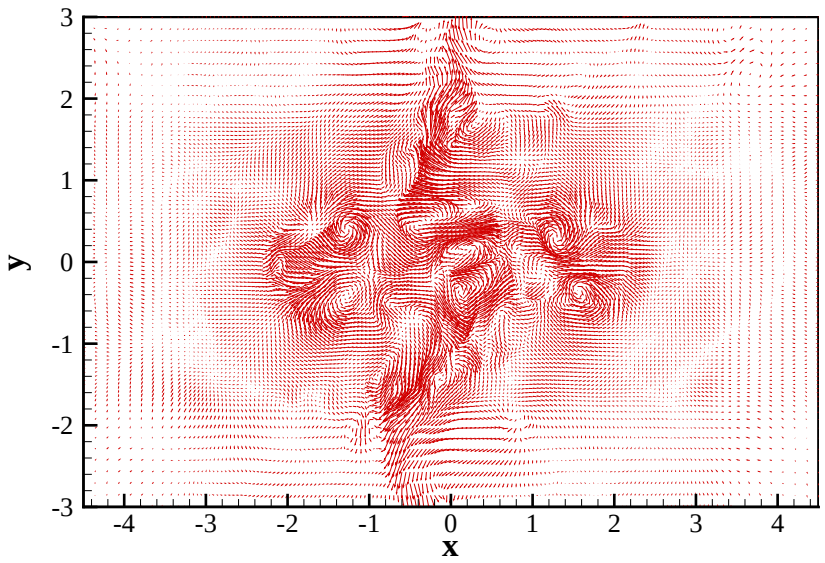

Figure 6.56: The velocity field in the $z = 0.536607$ plane at $t = 108.5092$

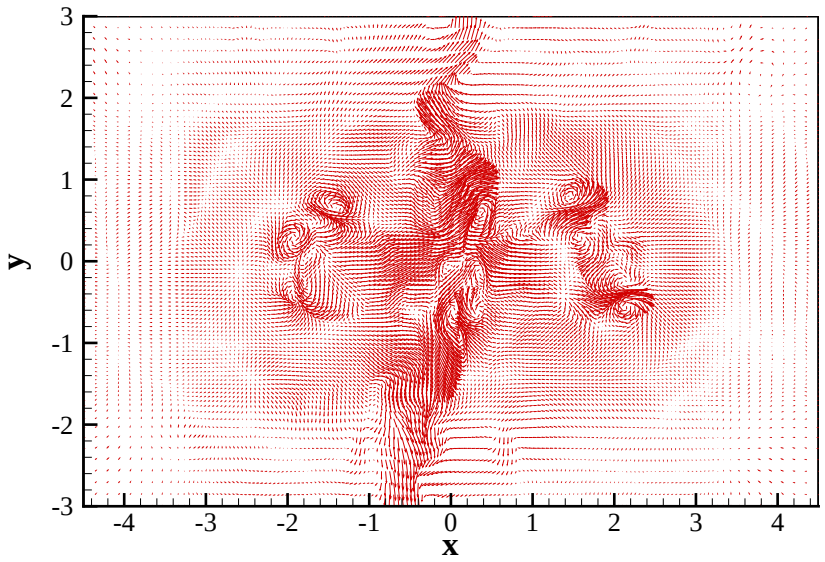

Figure 6.57: The velocity field in the $z = 0.536607$ plane at $t = 109.9092$

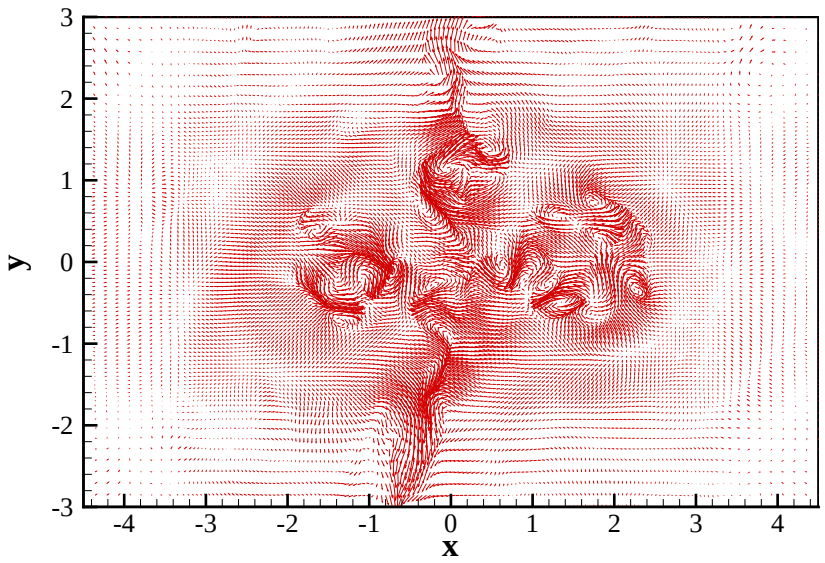

Figure 6.58: The velocity field in the $z = 0.536607$ plane at $t = 111.3092$

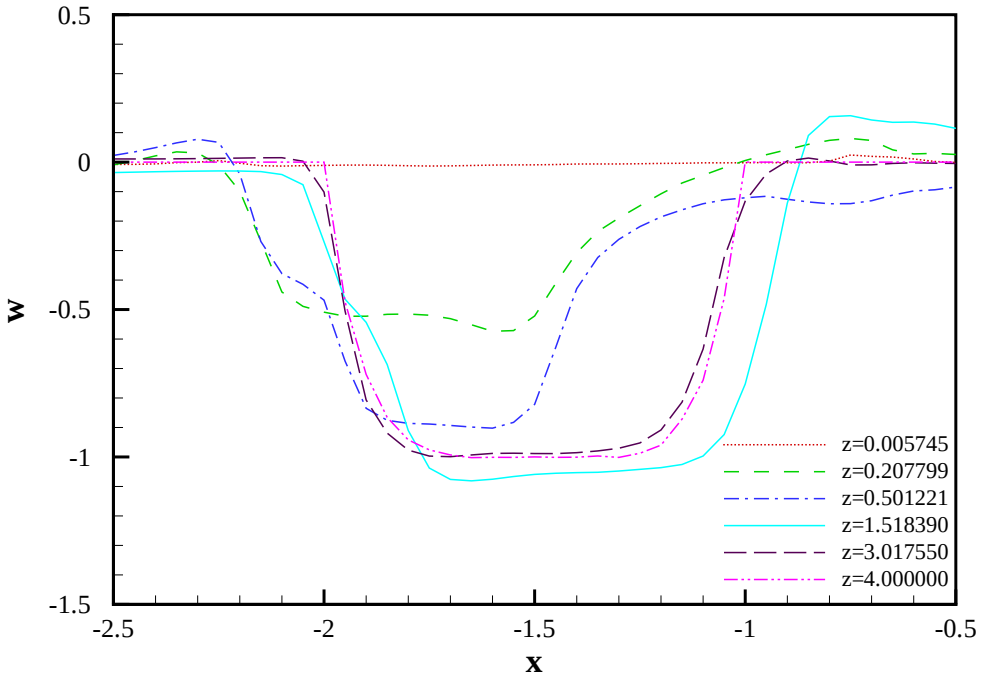

(a) Left jet

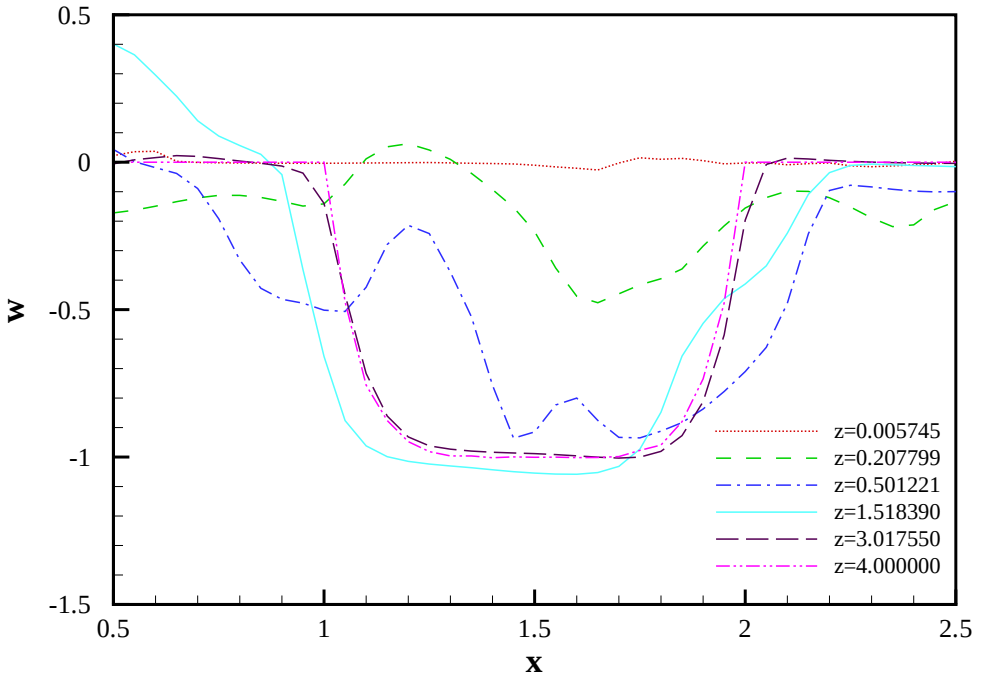

(b) Right jet

Figure 6.59: w-velocity profiles of the jets in the $y = 0$ plane at $t = 108.5092$

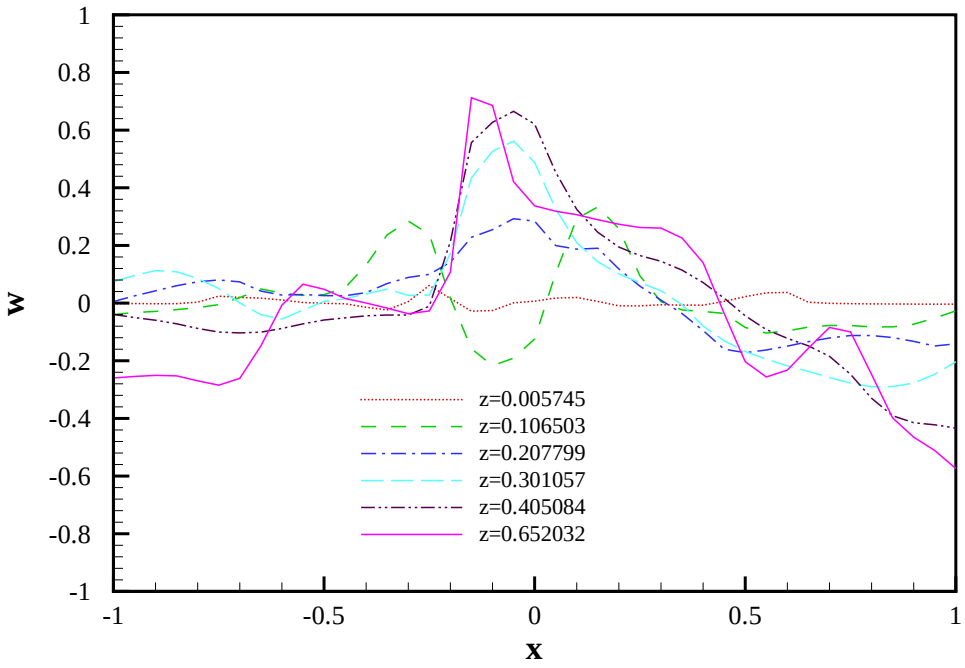

(a)

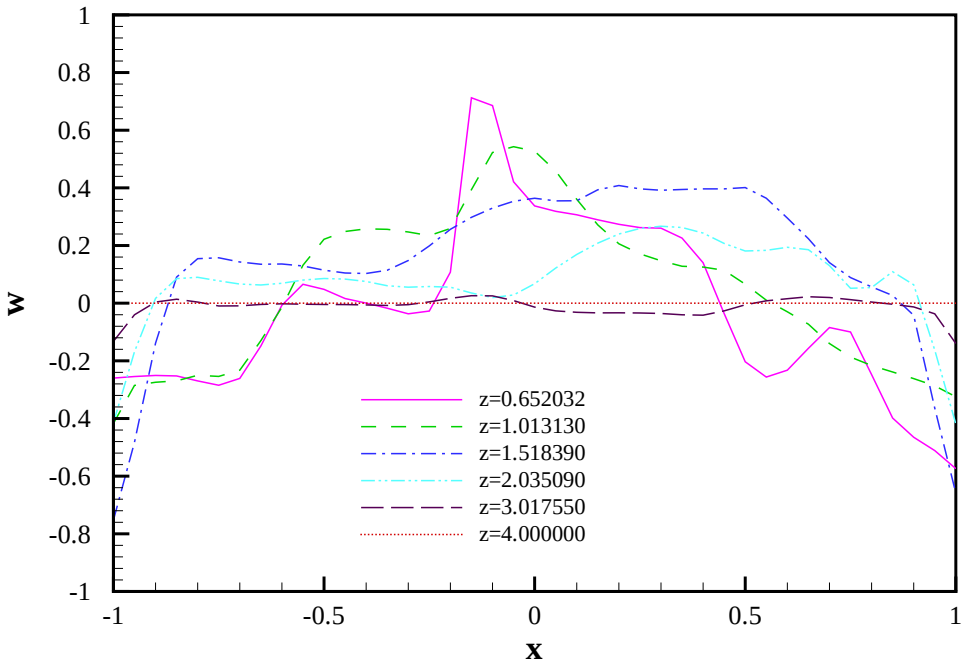

(b)

Figure 6.60: w-velocity profiles of the fountain in the $y = 0$ plane at $t = 108.5092$

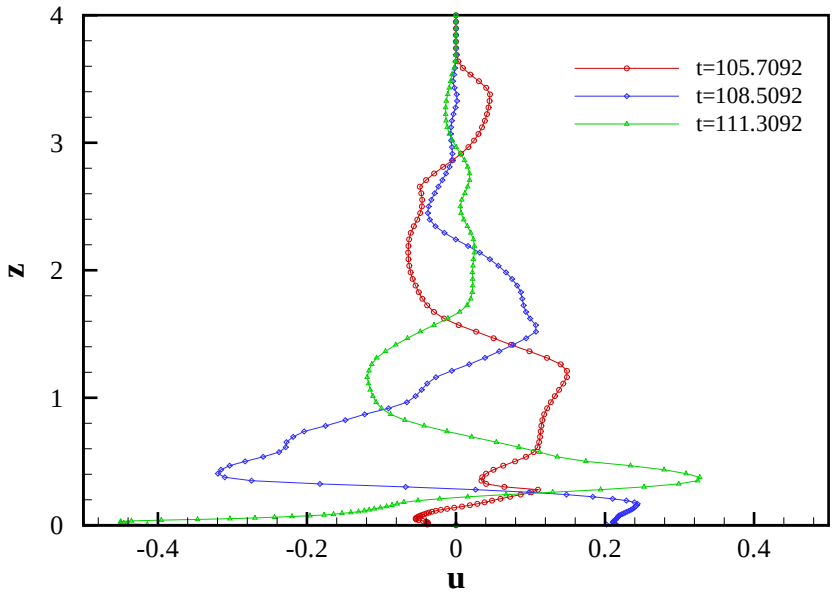

(a) along the left jet centerline

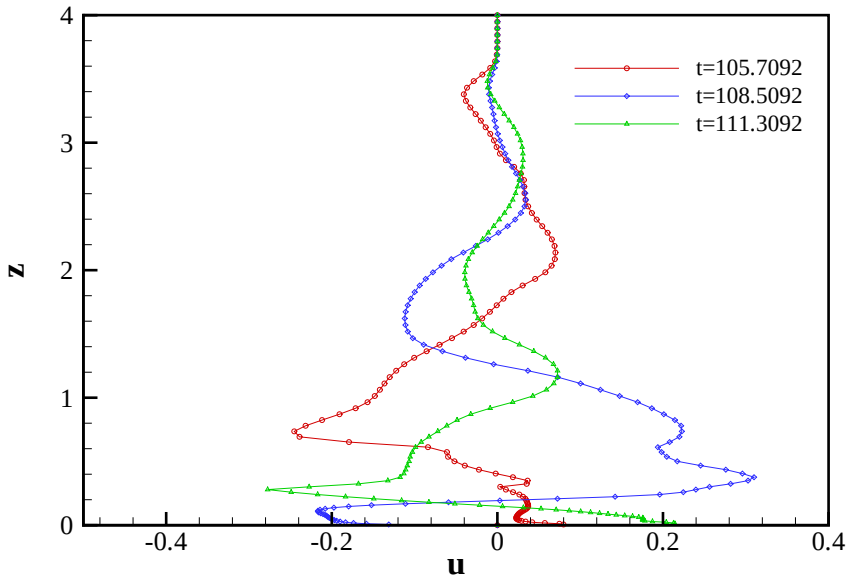

(b) along the right jet centerline

Figure 6.61: u-velocity as a function of z along the jet centerlines at three different times.

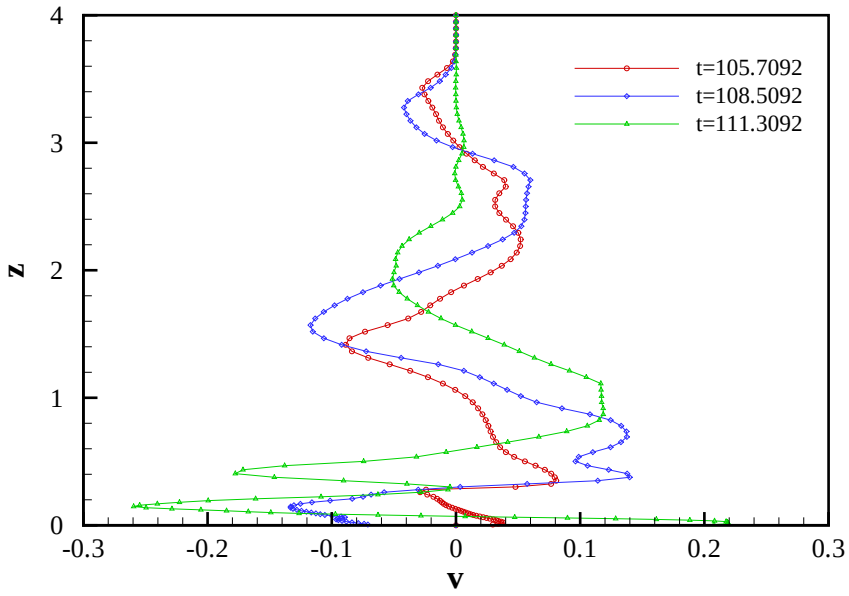

(a) along the left jet centerline

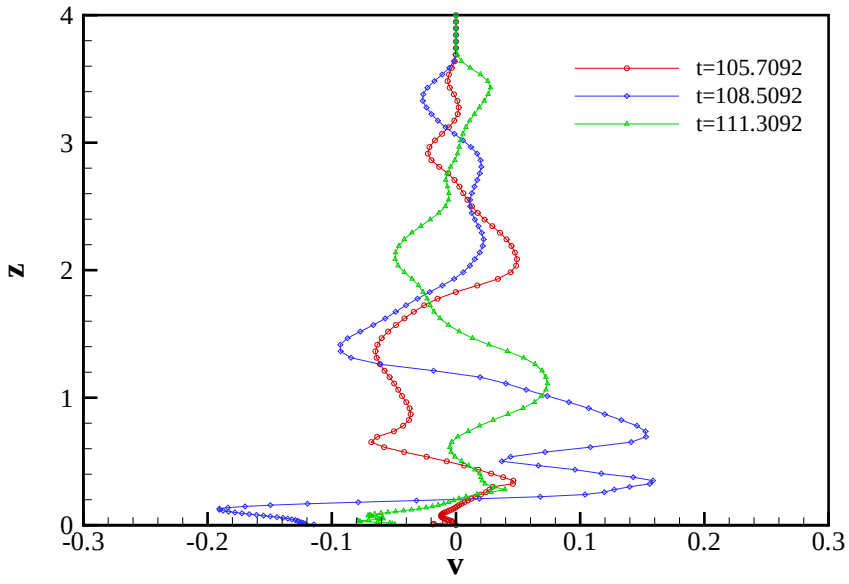

(b) along the right jet centerline

Figure 6.62: v-velocity as a function of z along the jet centerlines at three different times.

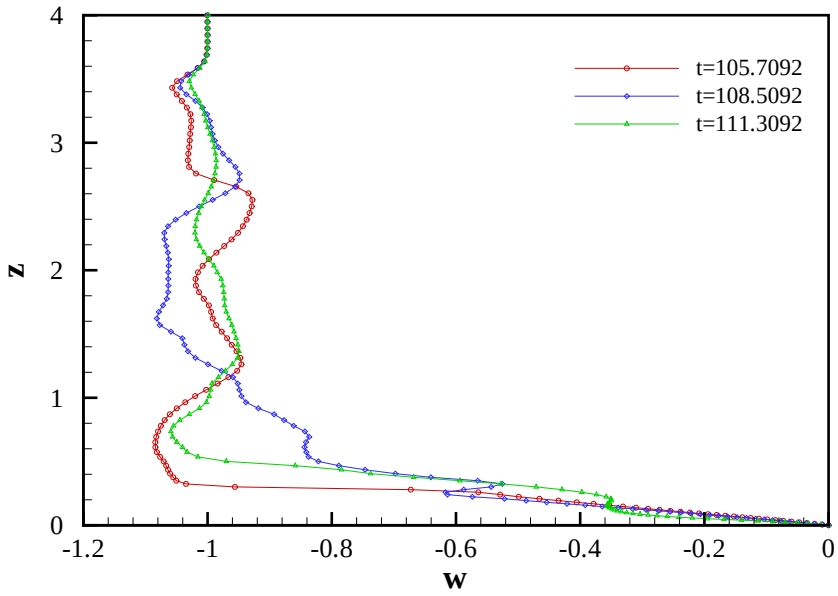

(a) along the left jet centerline

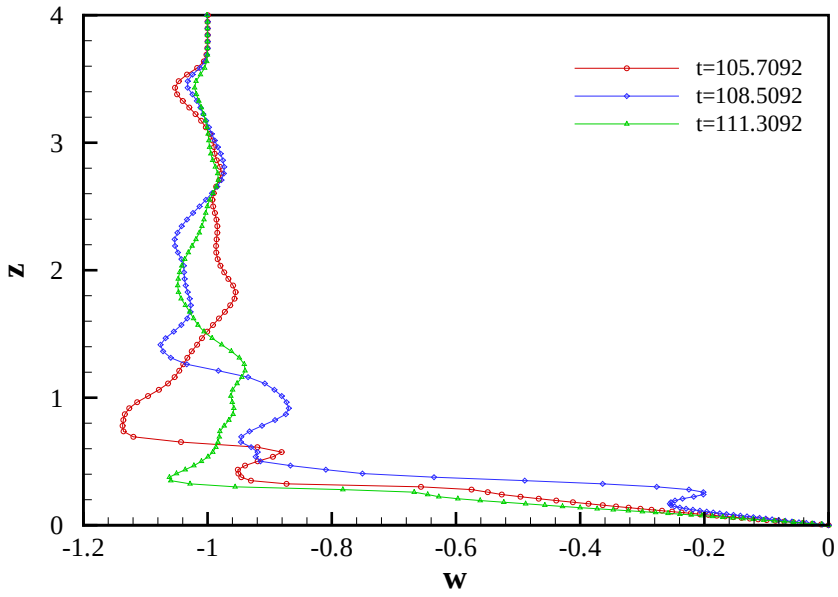

(b) along the right jet centerline

Figure 6.63: w-velocity as a function of z along the jet centerlines at three different times.

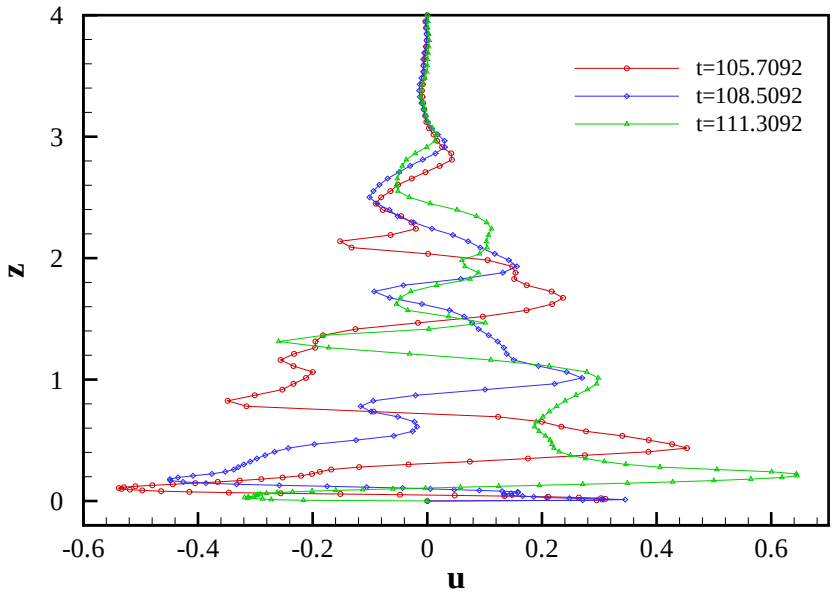

Figure 6.64: u-velocity as a function of z at $x = 0$ in the $y = 0$ plane at three different times.

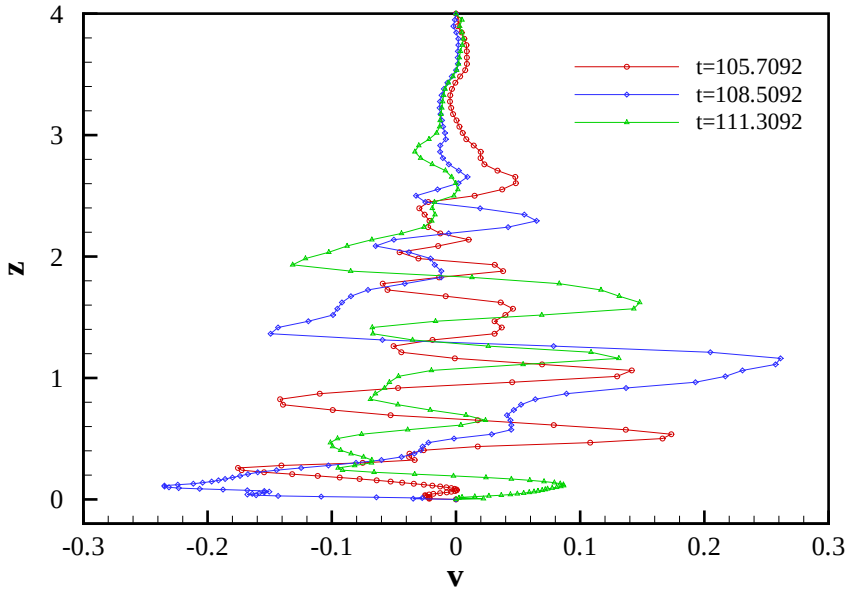

Figure 6.65: v-velocity as a function of z at $y = 0$ in the fountain plane ($x = 0$ plane) at three different times.

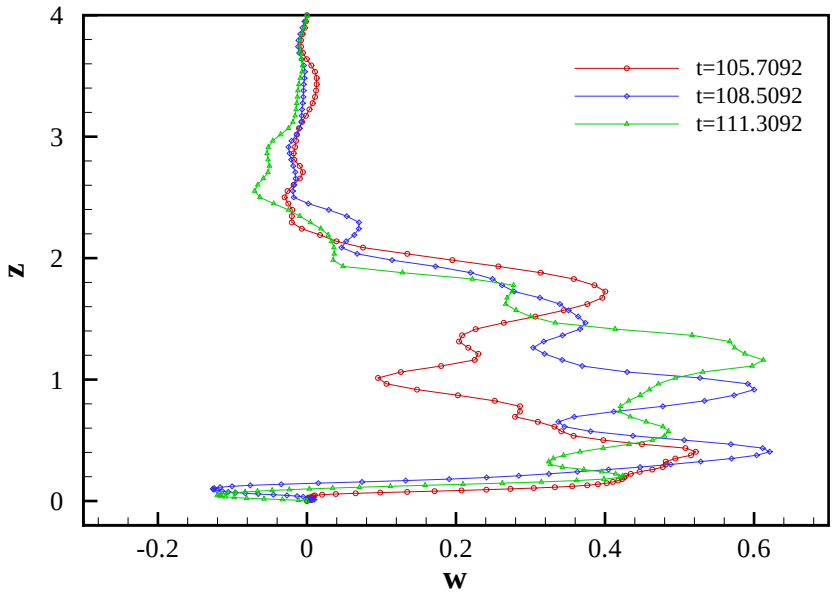

Figure 6.66: w-velocity as a function of z at $y = 0$ in the fountain plane ($x = 0$ plane) at three different times.

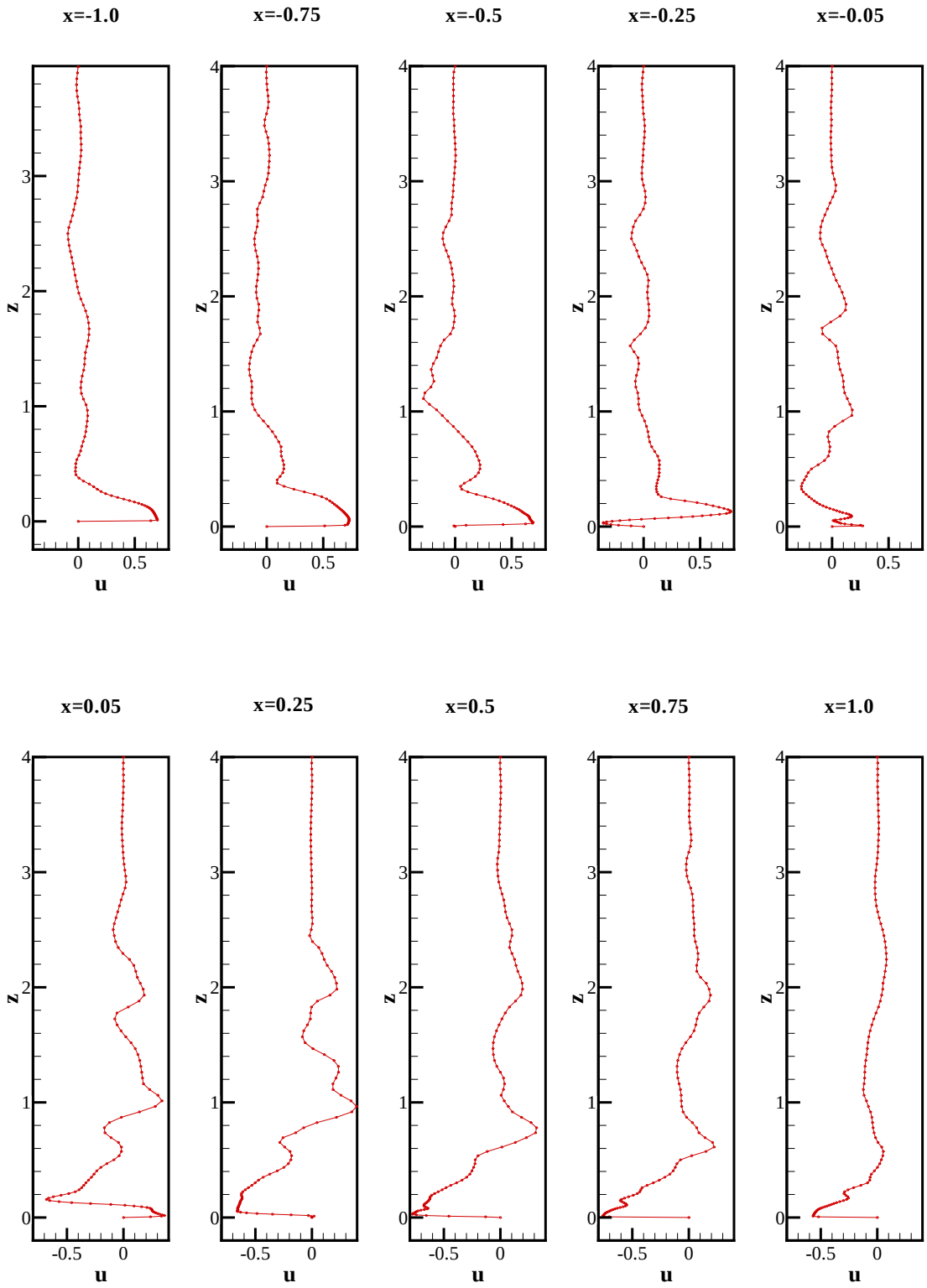

Figure 6.67: u-velocity profile as a function of z at various x-locations between the jets in the $y = 0$ plane at $t = 108.5092$.

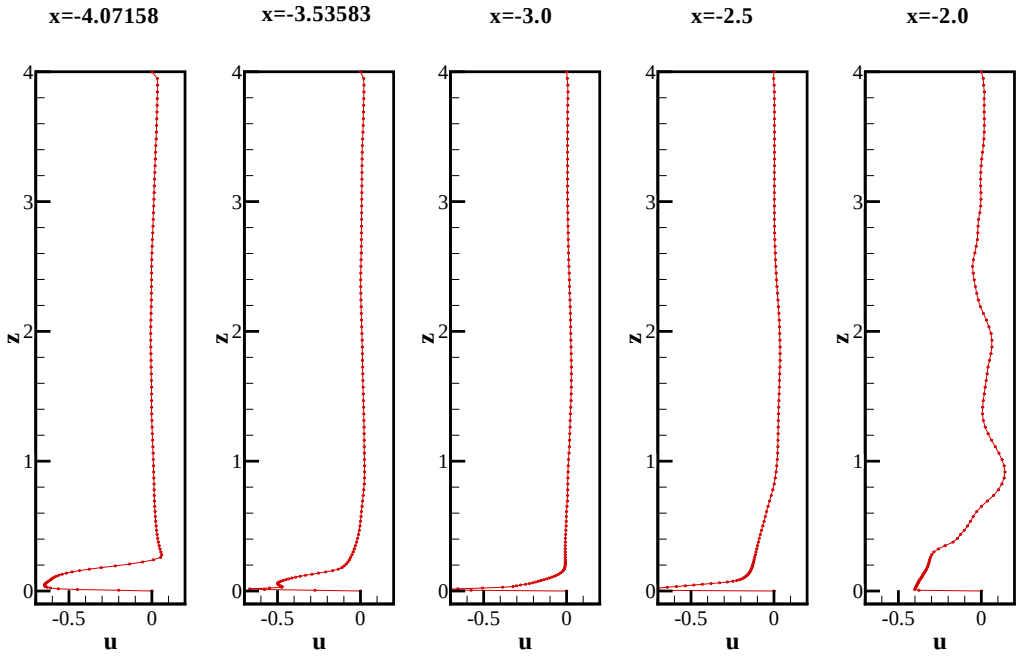

Figure 6.68: u-velocity profile as a function of z at various x-locations between the left jet and the left boundary in the $y = 0$ plane at $t = 108.5092$.

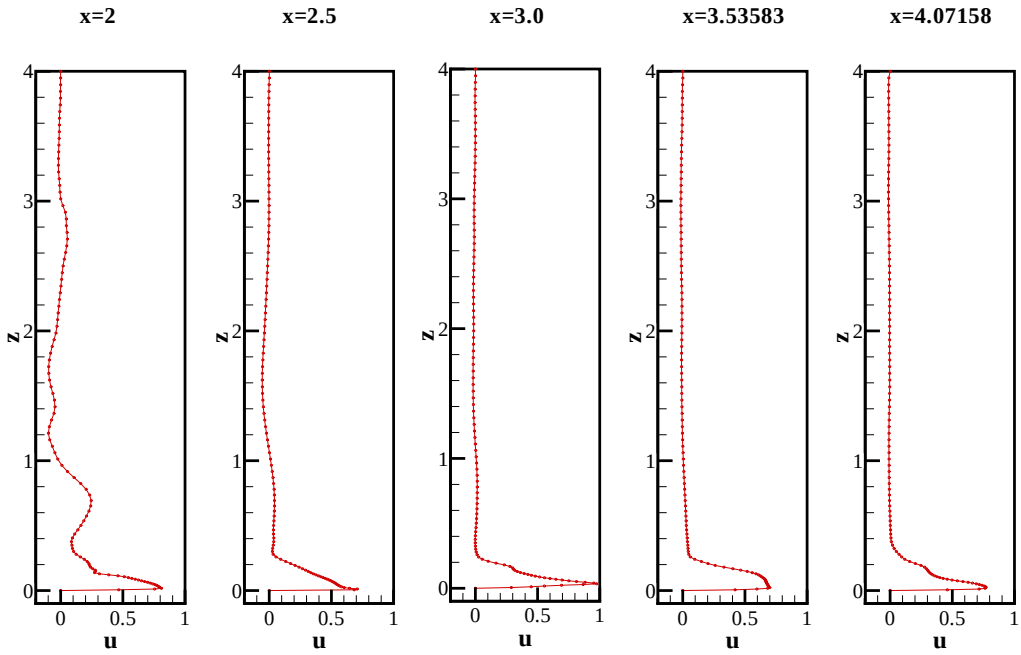

Figure 6.69: u-velocity profile as a function of z at various x-locations betwen the right jet and the right boundary in the $y = 0$ plane at $t = 108.5092$.

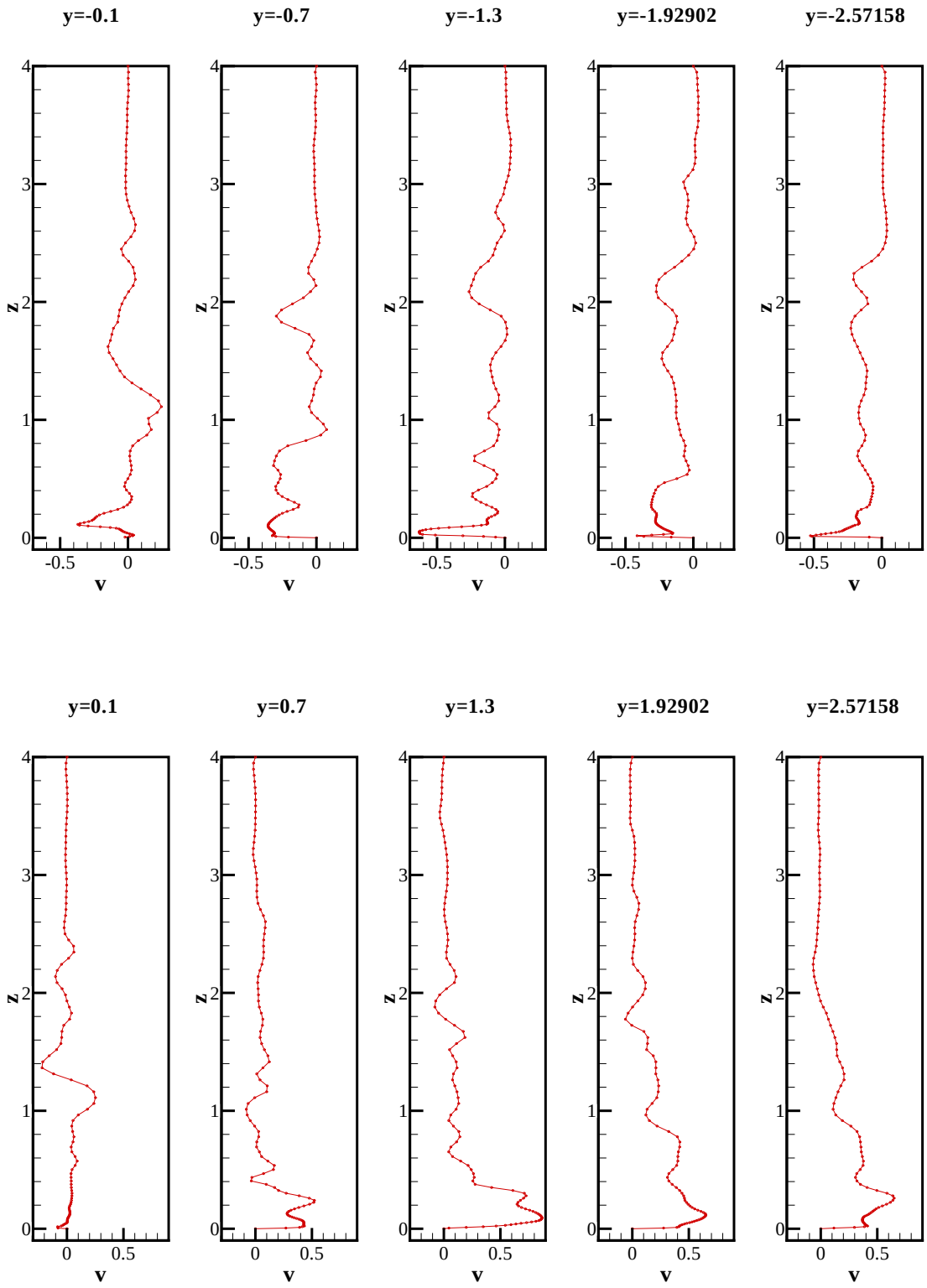

Figure 6.70: v-velocity profile as a function of z at various y-locations in the $x = 0$ plane at $t = 108.5092$.

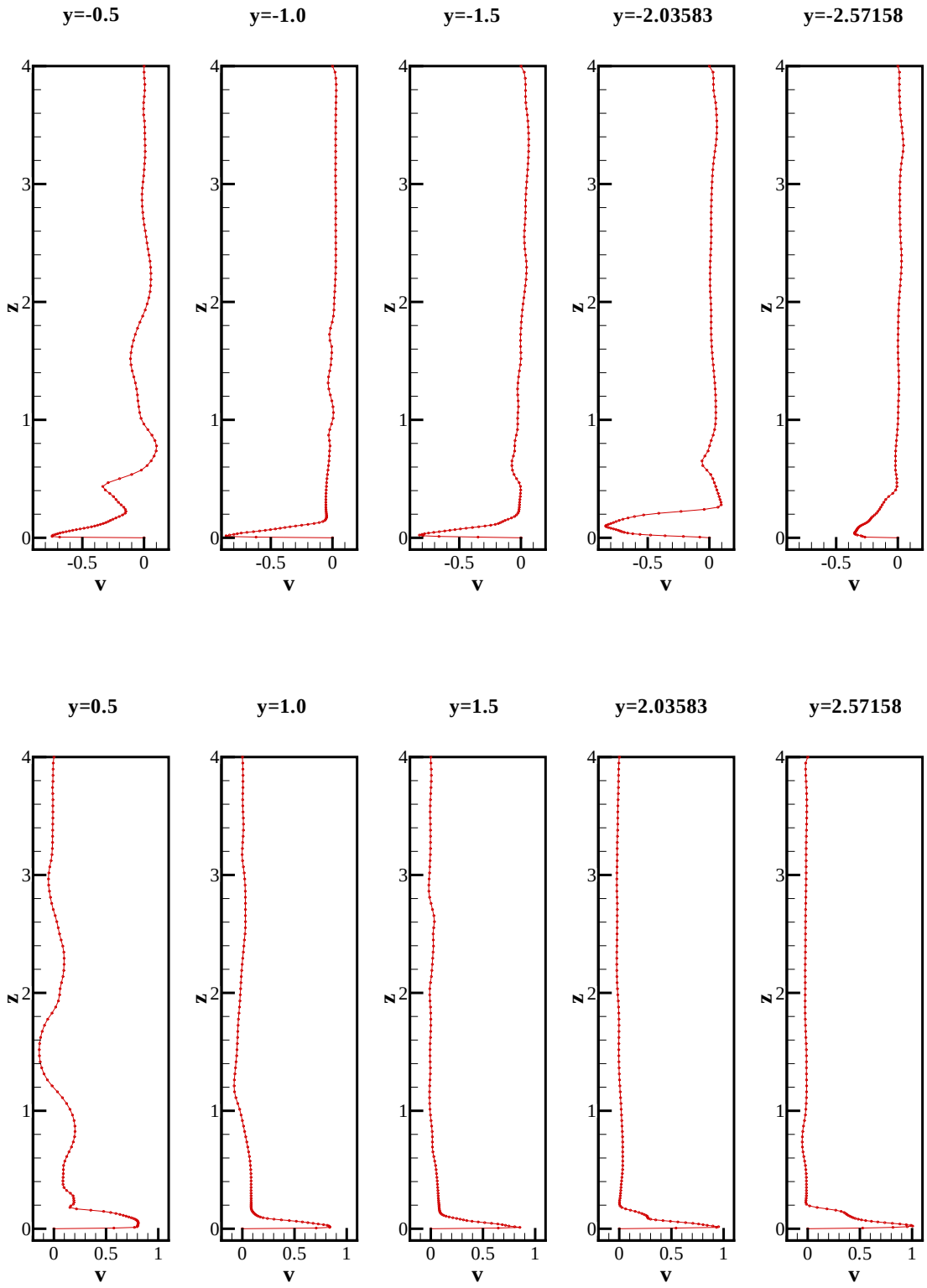

Figure 6.71: v-velocity profile as a function of z at various y-locations in the $x = -1.5$ plane (midplane of the left jet) at $t = 108.5092$.

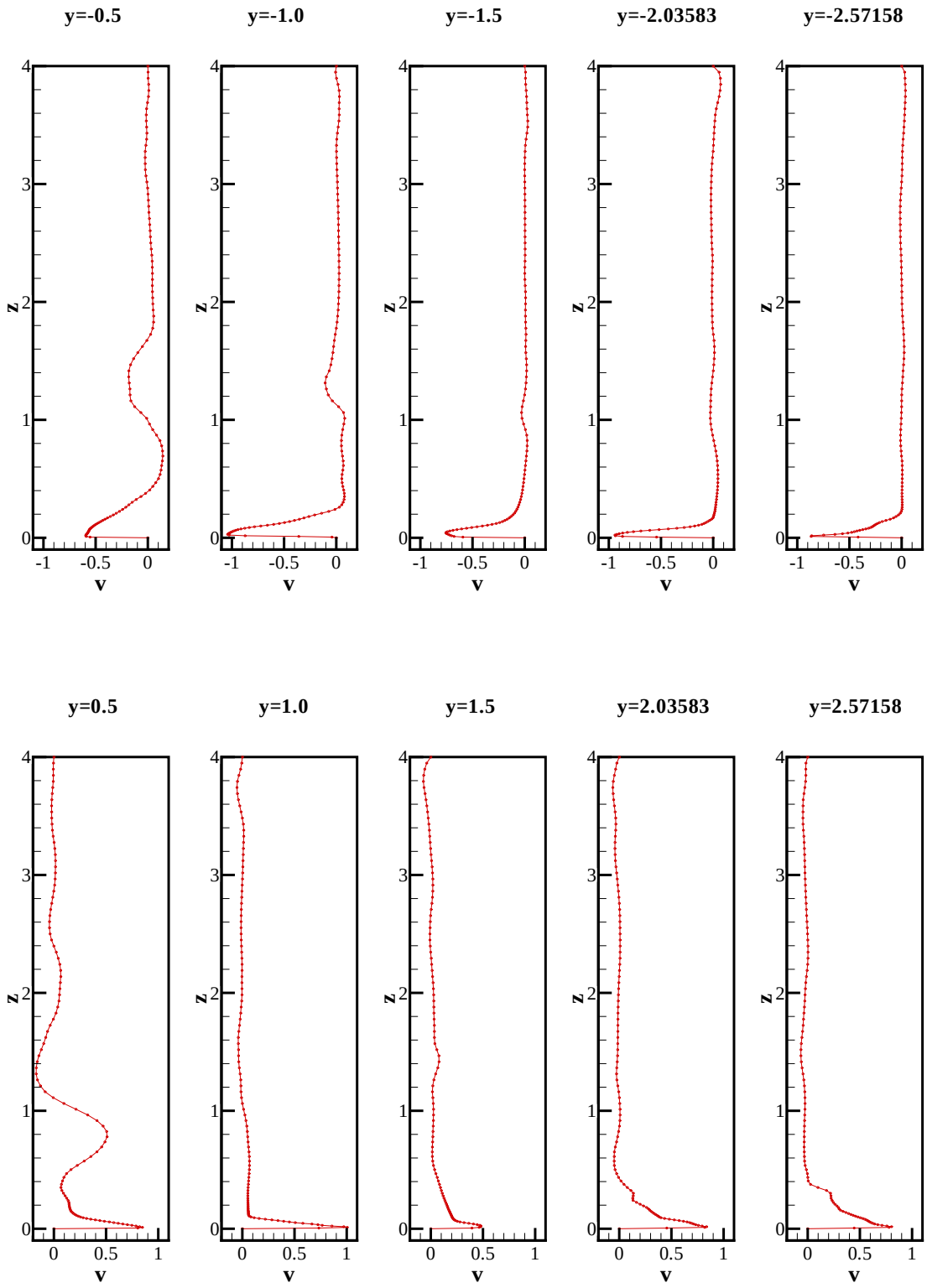

Figure 6.72: v-velocity profile as a function of z at various y-locations in the $x = 1.5$ plane (midplane of the right jet) at $t = 108.5092$.

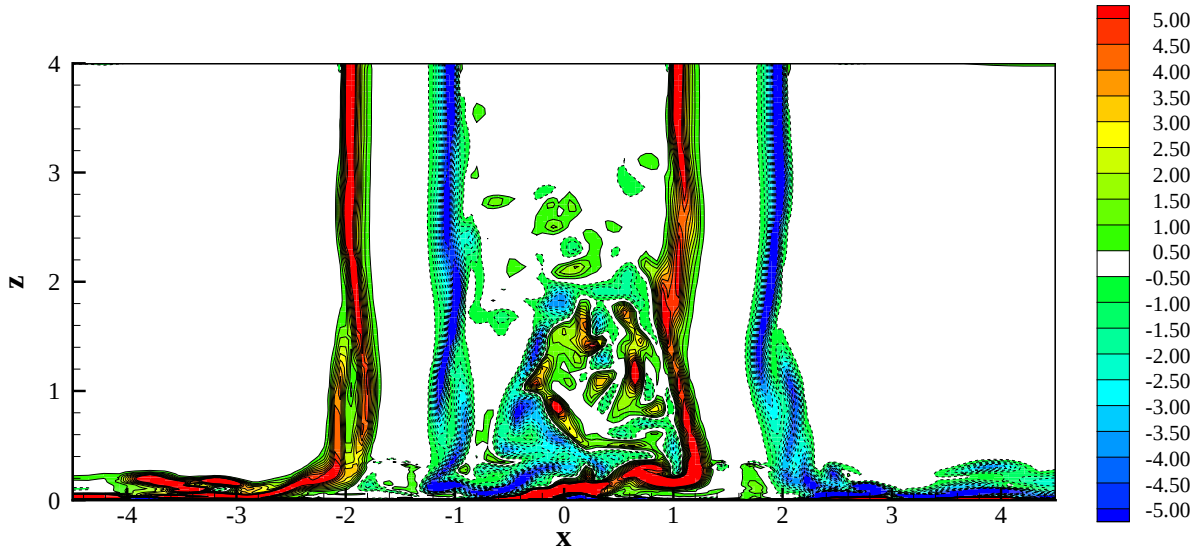

Figure 6.73: The y-vorticity contours in the $y = 0$ plane at $t = 104.3092$.

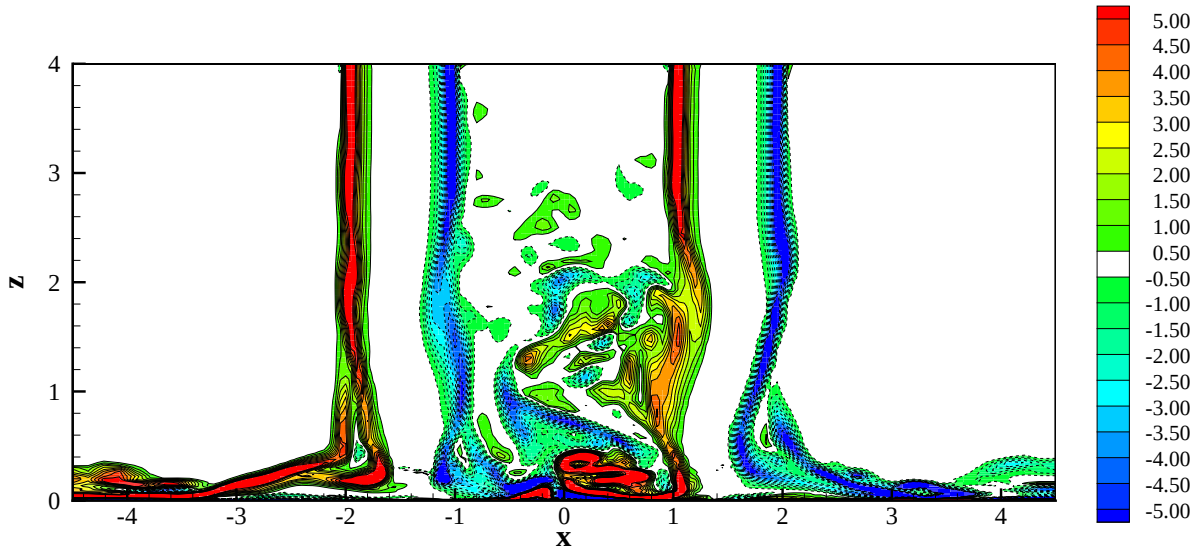

Figure 6.74: The y-vorticity contours in the $y = 0$ plane at $t = 105.7092$.

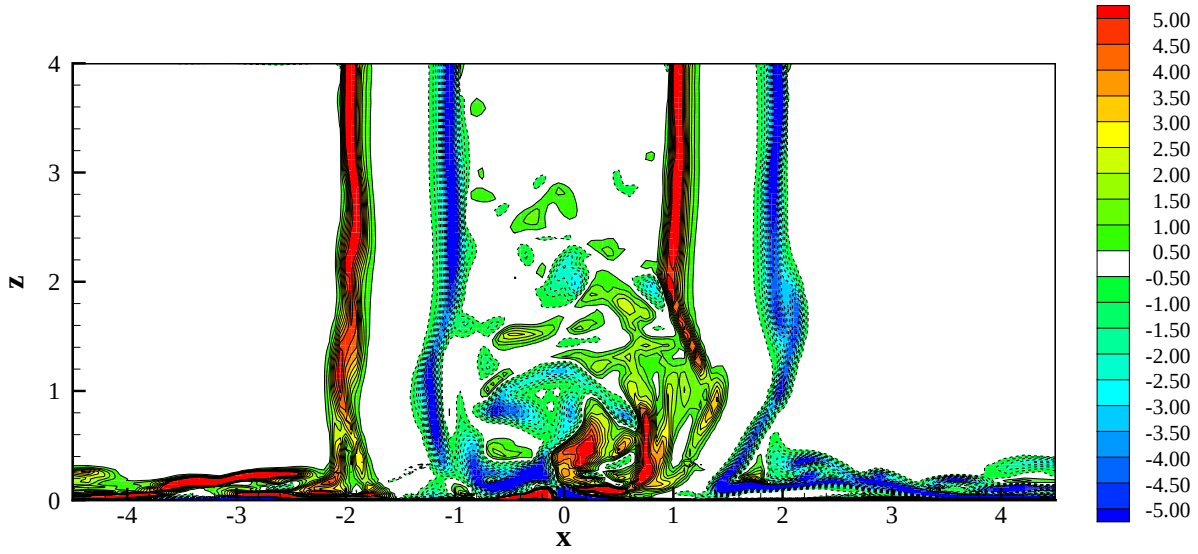

Figure 6.75: The y-vorticity contours in the $y = 0$ plane at $t = 107.1092$.

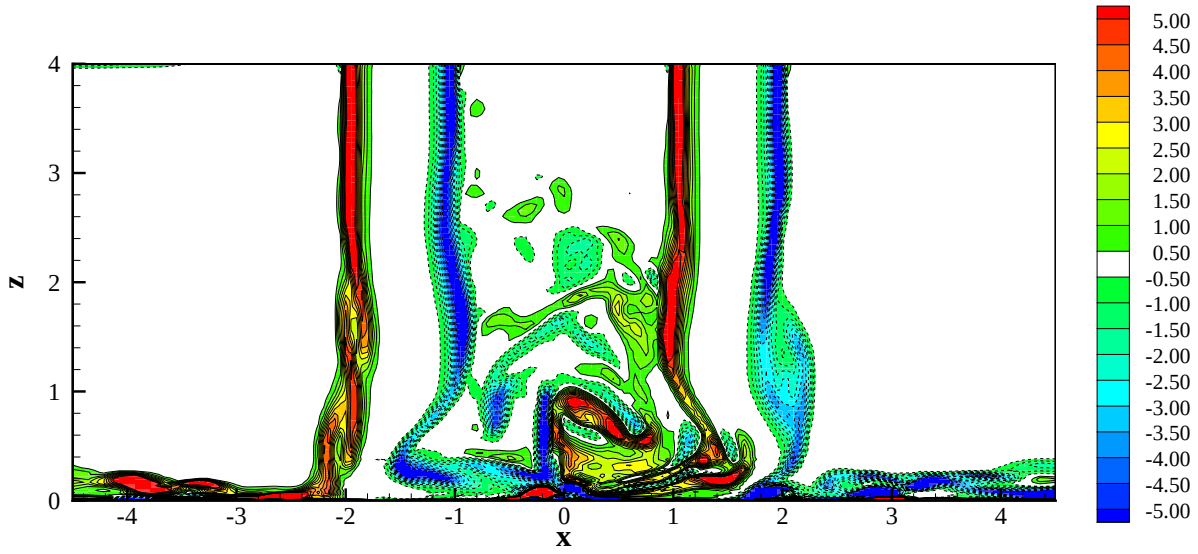

Figure 6.76: The y-vorticity contours in the $y = 0$ plane at $t = 108.5092$.

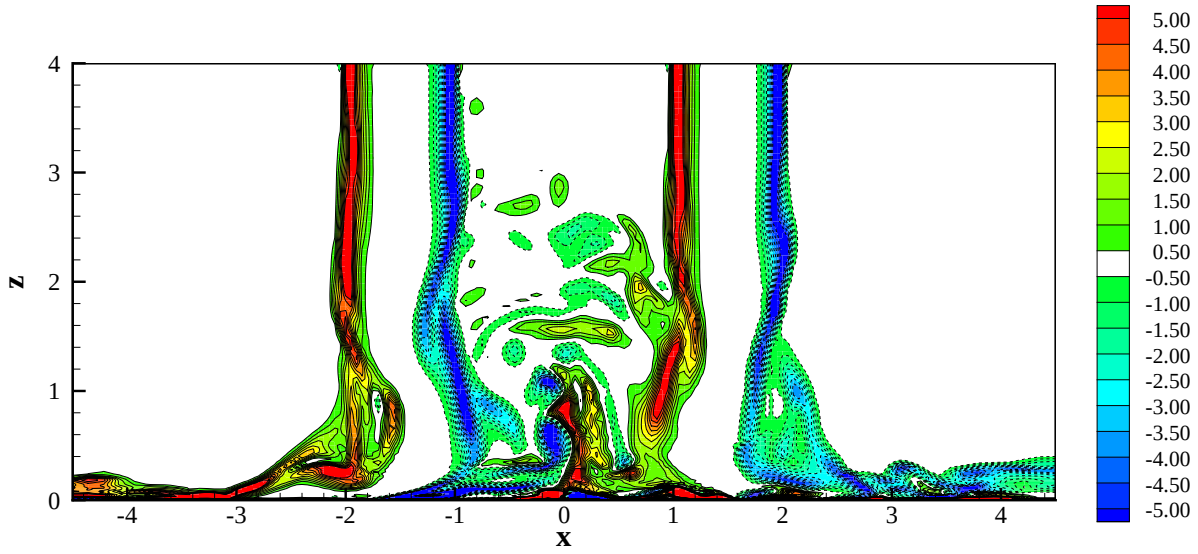

Figure 6.77: The y-vorticity contours in the $y = 0$ plane at $t = 109.9092$.

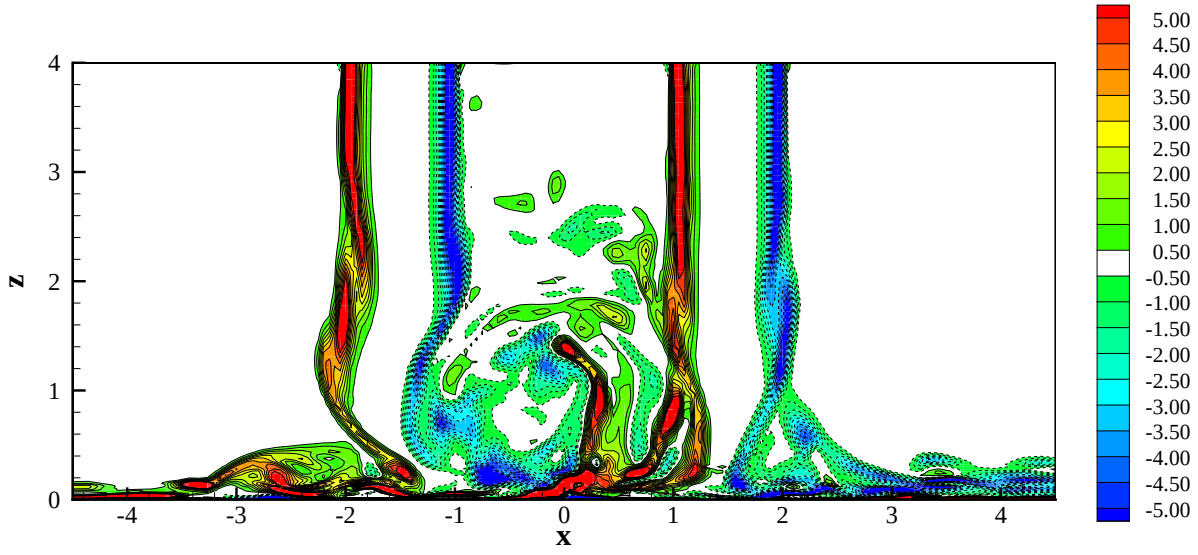

Figure 6.78: The y-vorticity contours in the $y = 0$ plane at $= 111.3092$.

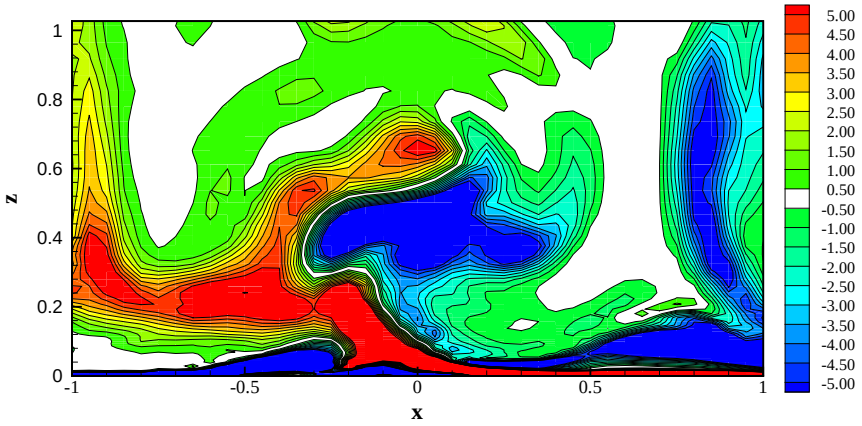

(a)

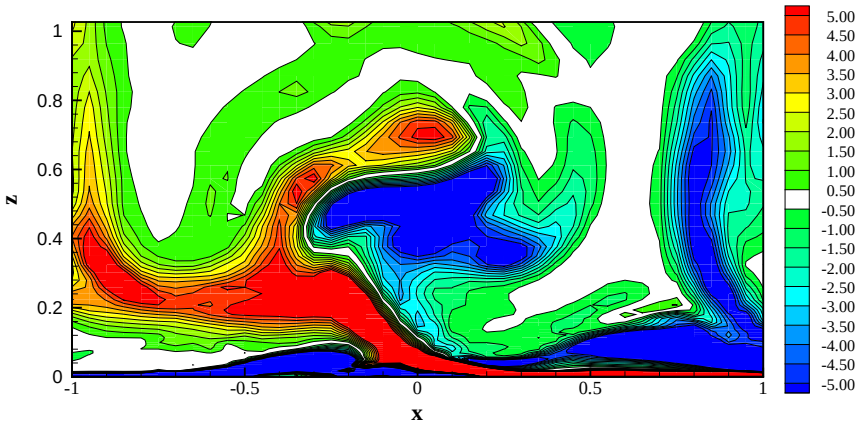

(b)

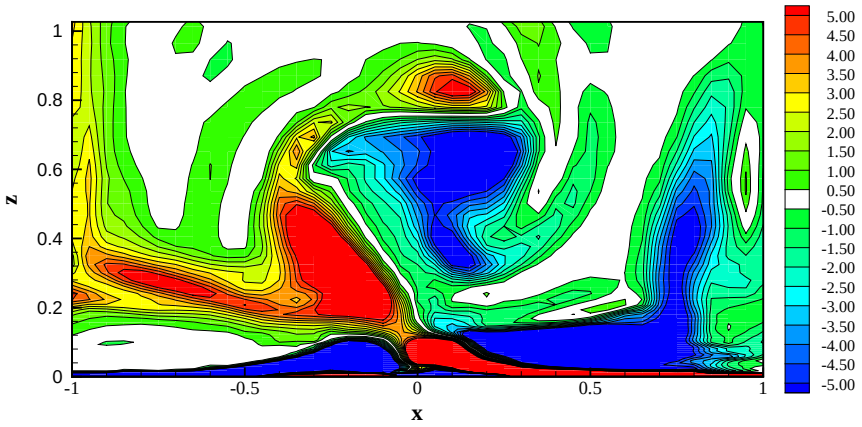

(c)

Figure 6.79: y-vorticity contours in the $y = 0$ plane in the fountain region: formation of the left-inclining vortical structure .

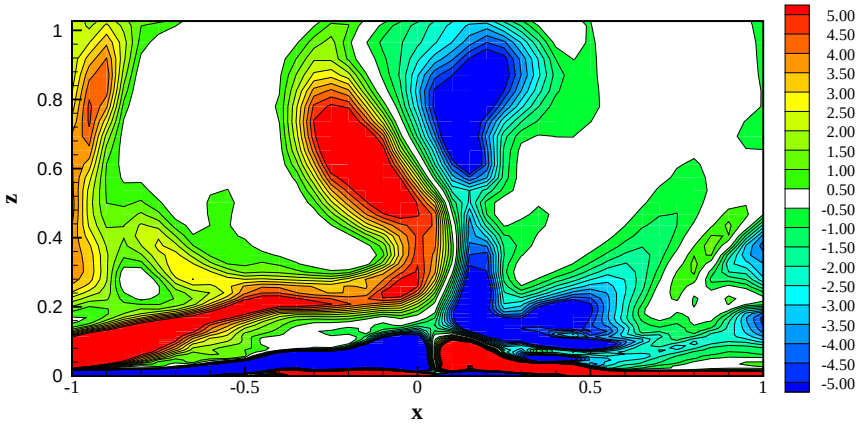

(a)

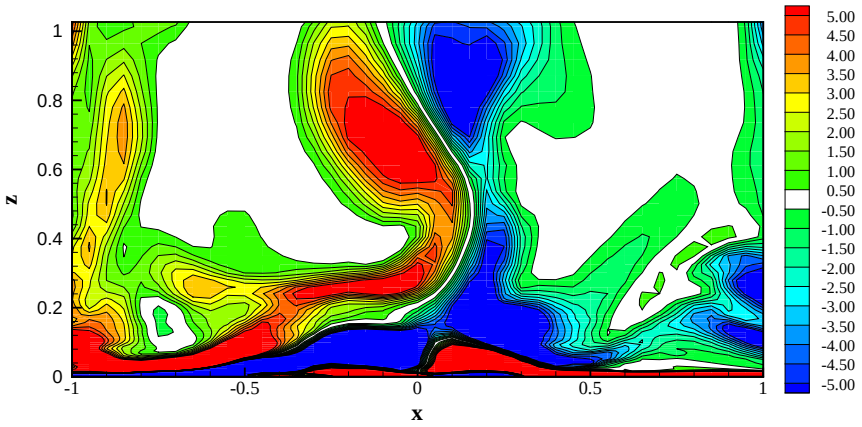

(b)

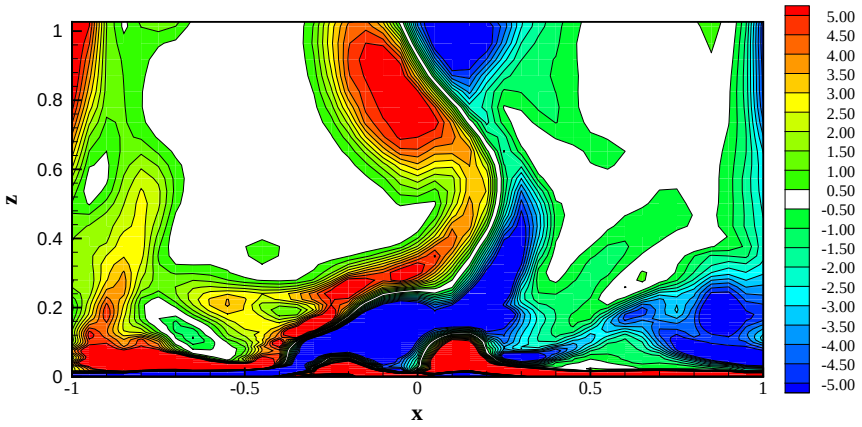

(c)

Figure 6.80: y-vorticity contours in the $y = 0$ plane in the fountain region: formation of the right-inclining vortical structure .

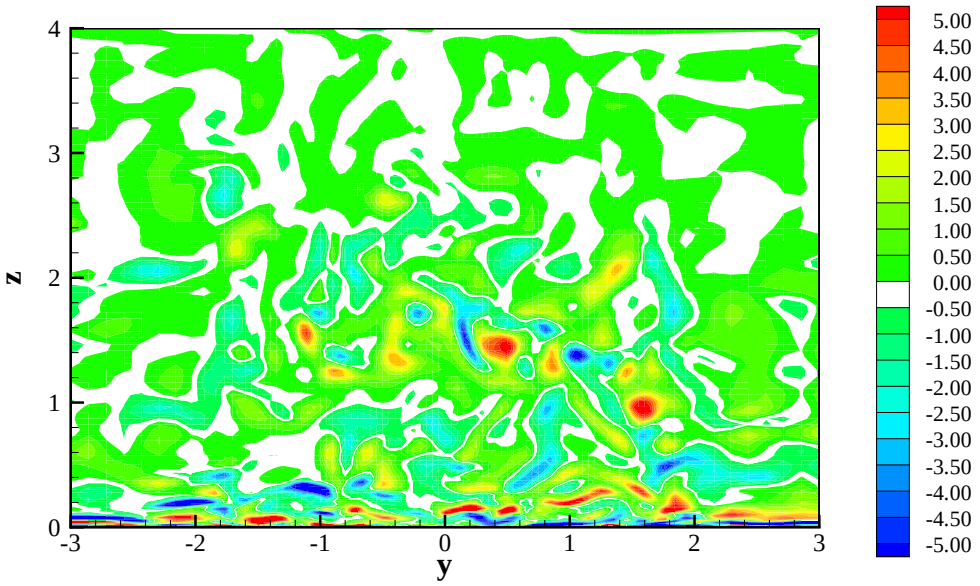

Figure 6.81: The x-vorticity contour in the $x = 0$ plane at $t = 104.3092$.

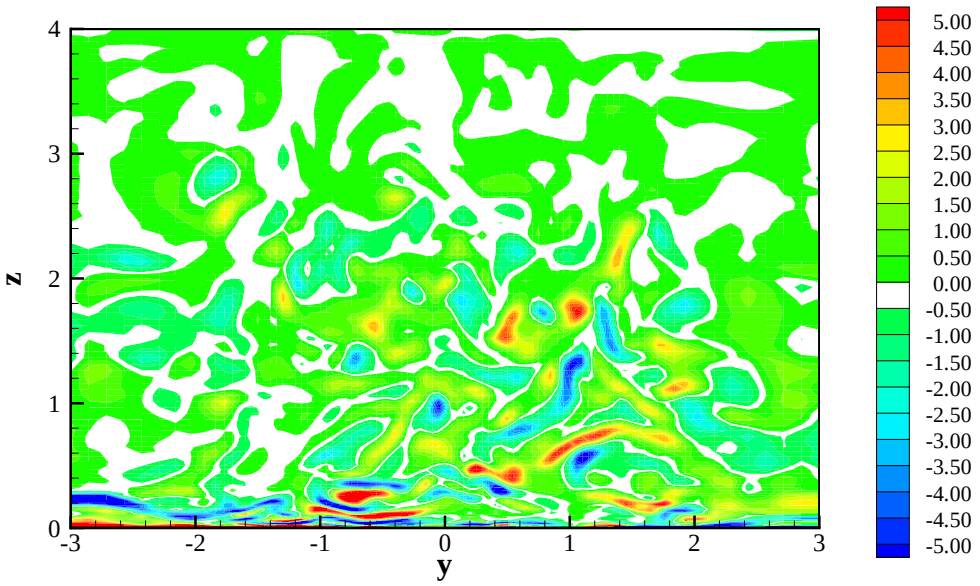

Figure 6.82: The x-vorticity contour in the $x = 0$ plane at $t = 105.7092$.

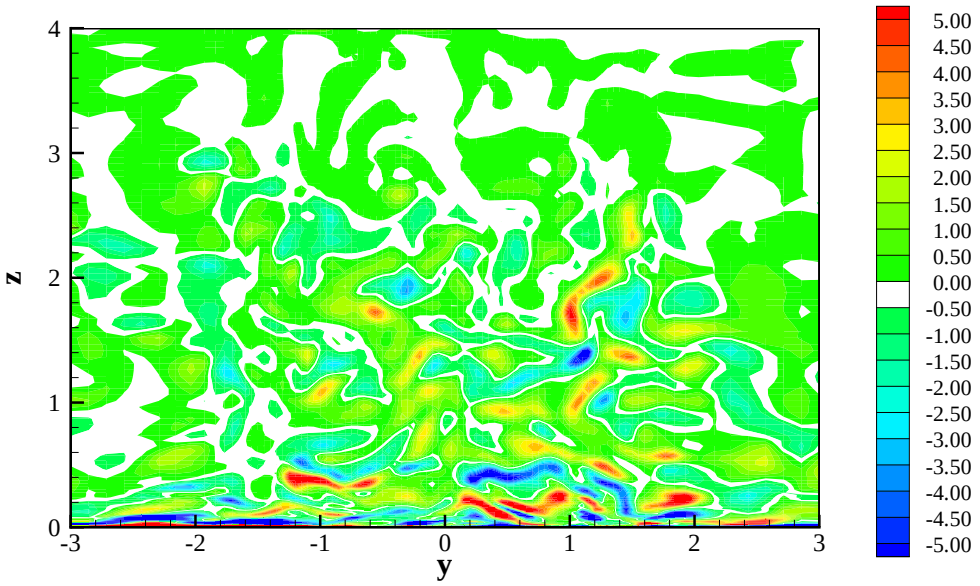

Figure 6.83: The x-vorticity contour in the $x = 0$ at $t = 107.1092$.

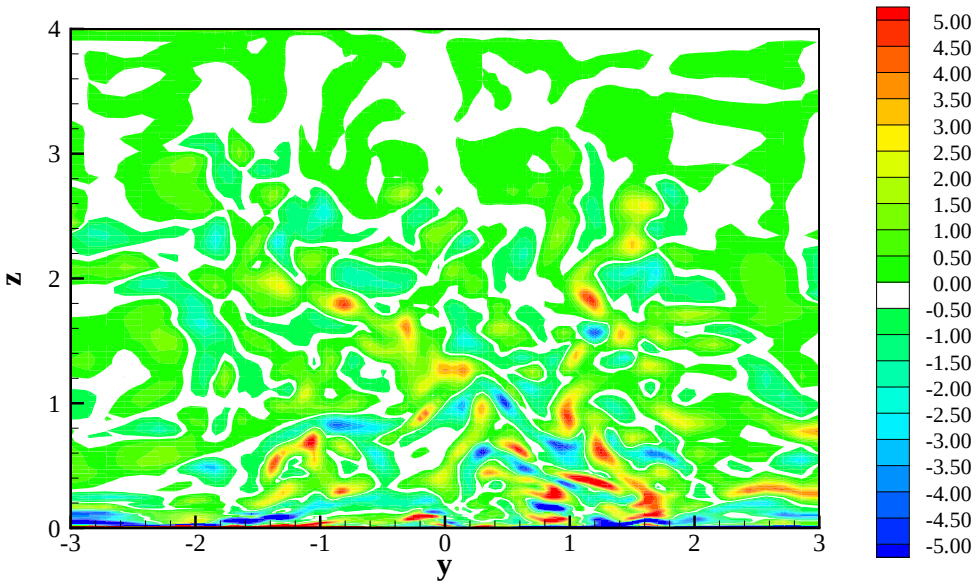

Figure 6.84: The x-vorticity contour in the $x = 0$ plane at $t = 108.5092$.

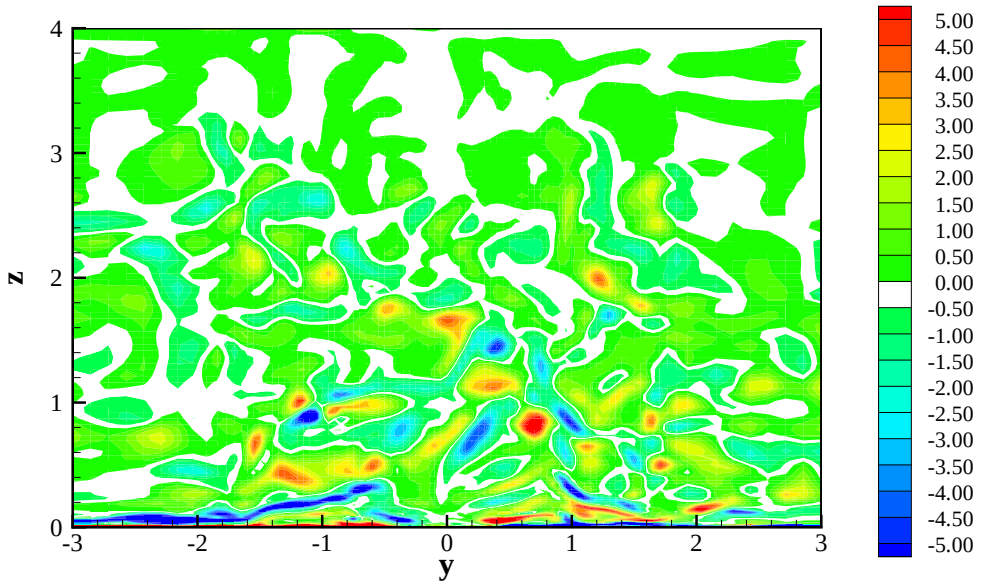

Figure 6.85: The x-vorticity contour in the $x = 0$ plane at $t = 109.9092$.

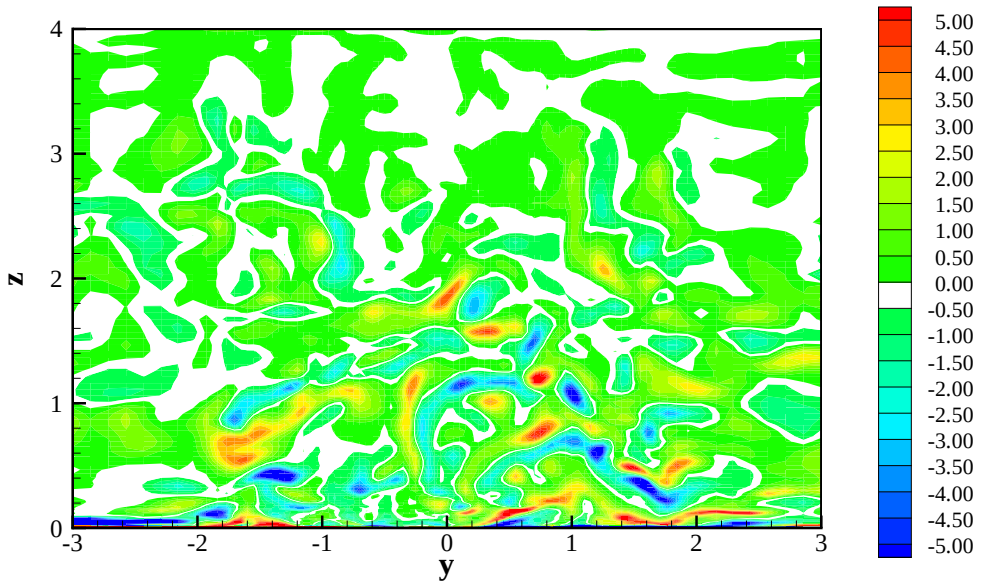

Figure 6.86: The x-vorticity contour in the $x = 0$ plane at $t = 111.3092$.

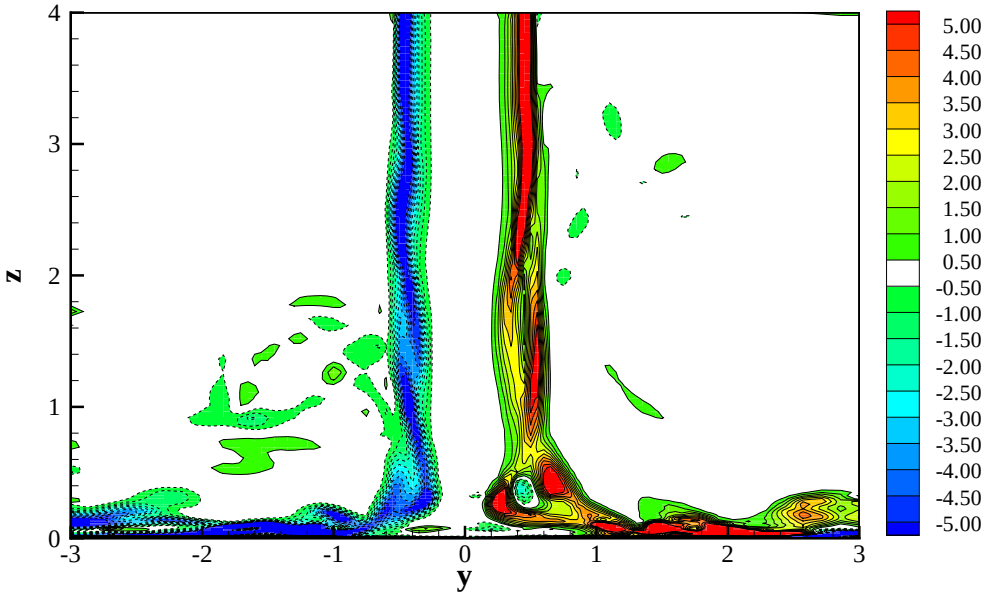

(a) left jet

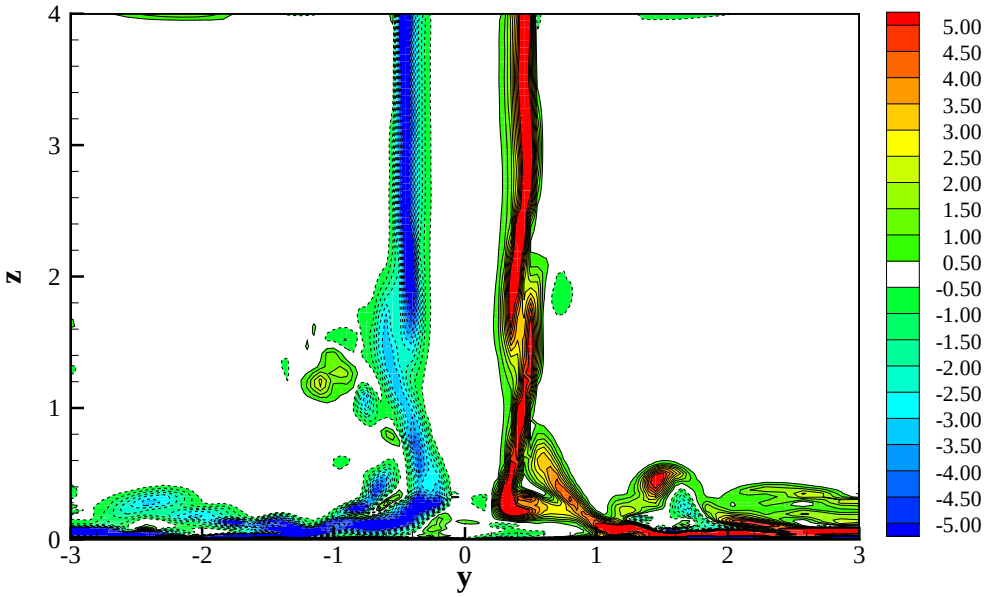

(b) right jet

Figure 6.87: The x-vorticity contour in the midplanes of the jets at $t = 104.3092$.

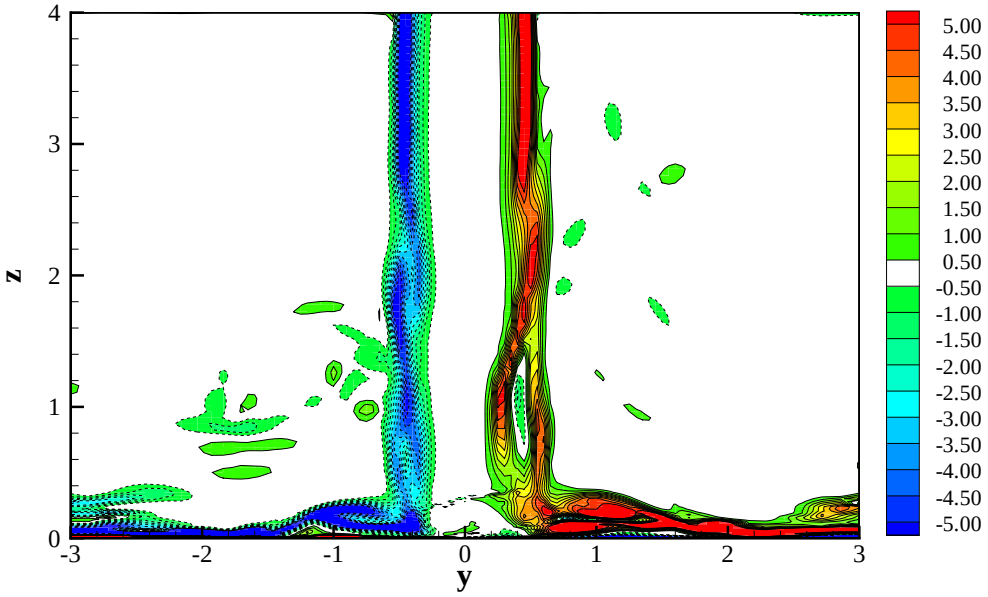

(a) left jet

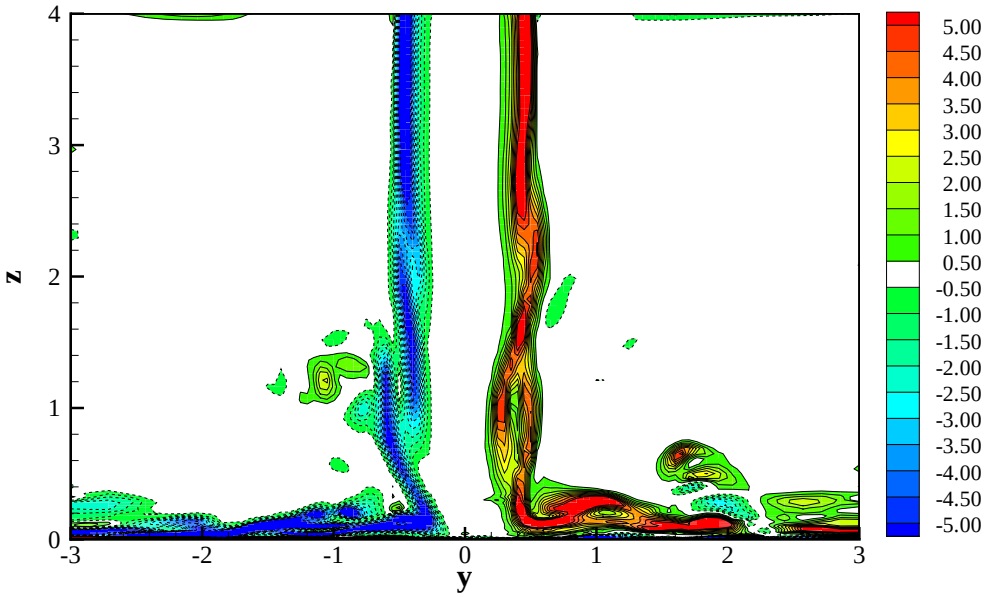

(b) right jet

Figure 6.88: The x-vorticity contour in the midplanes of the jets at $t = 105.7092$.

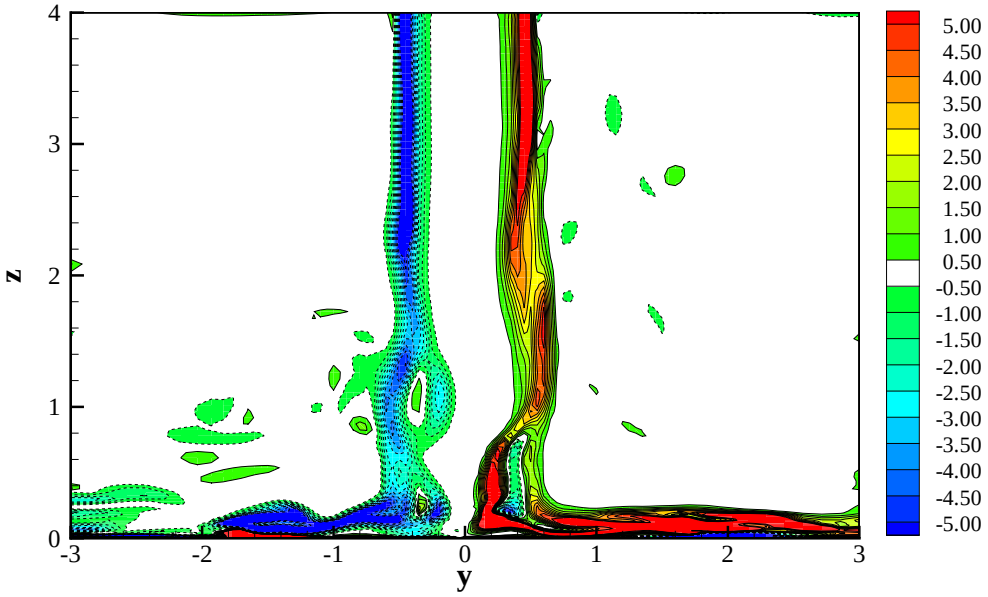

(a) left jet

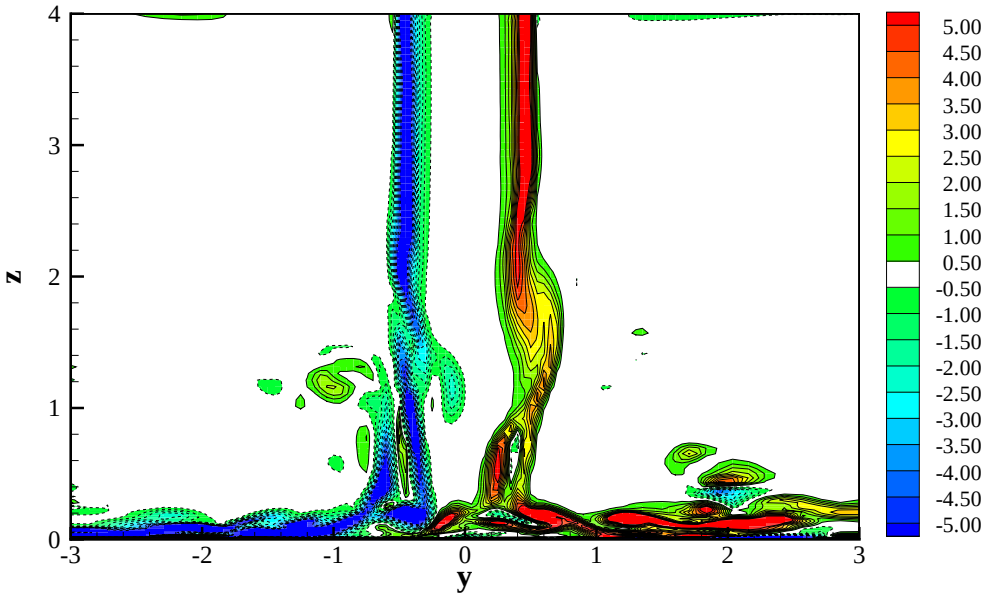

(b) right jet

Figure 6.89: The x-vorticity contour in the the midplanes of the jets at $t = 107.1092$.

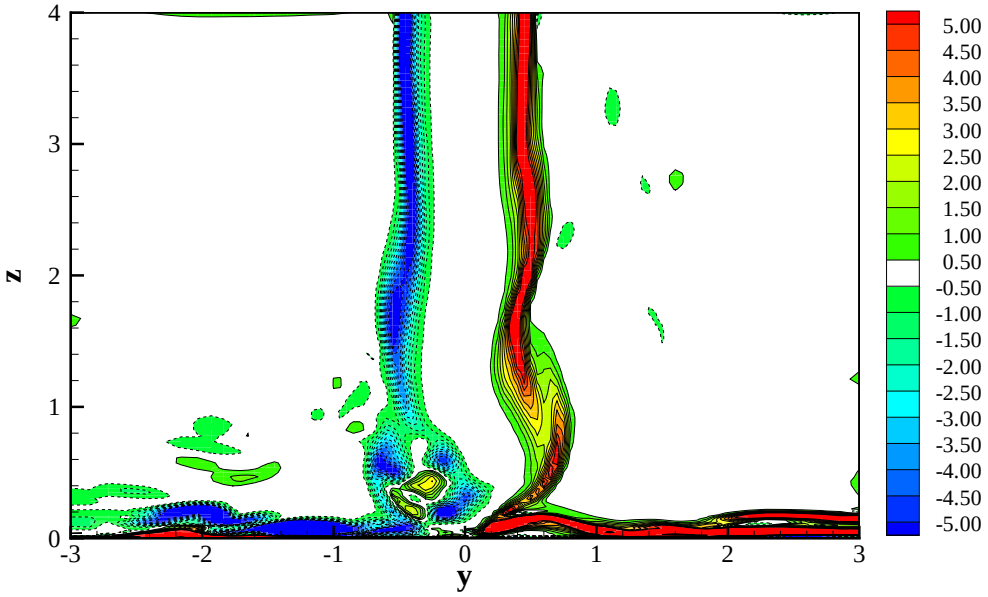

(a) left jet

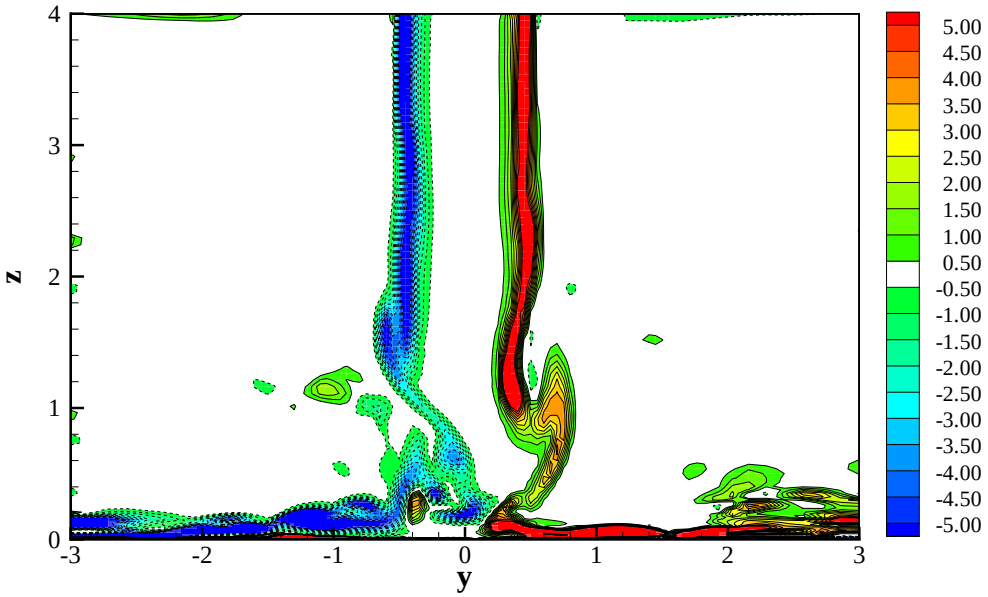

(b) right jet

Figure 6.90: The x-vorticity contour in the midplanes of the jets at $t = 108.5092$.

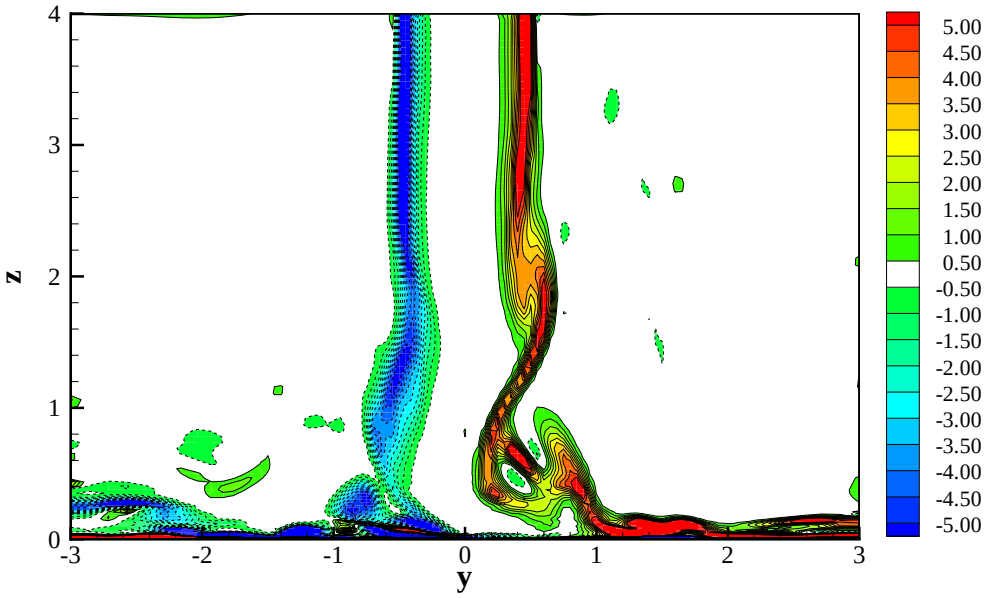

(a) left jet

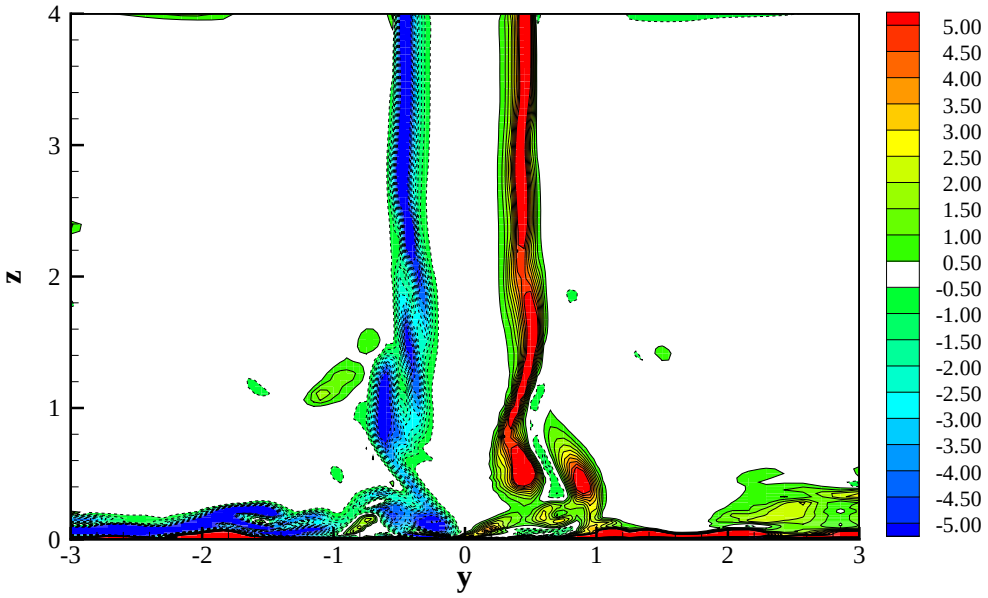

(b) right jet

Figure 6.91: The x-vorticity contour in the midplanes of the jets at $t = 109.9092$.

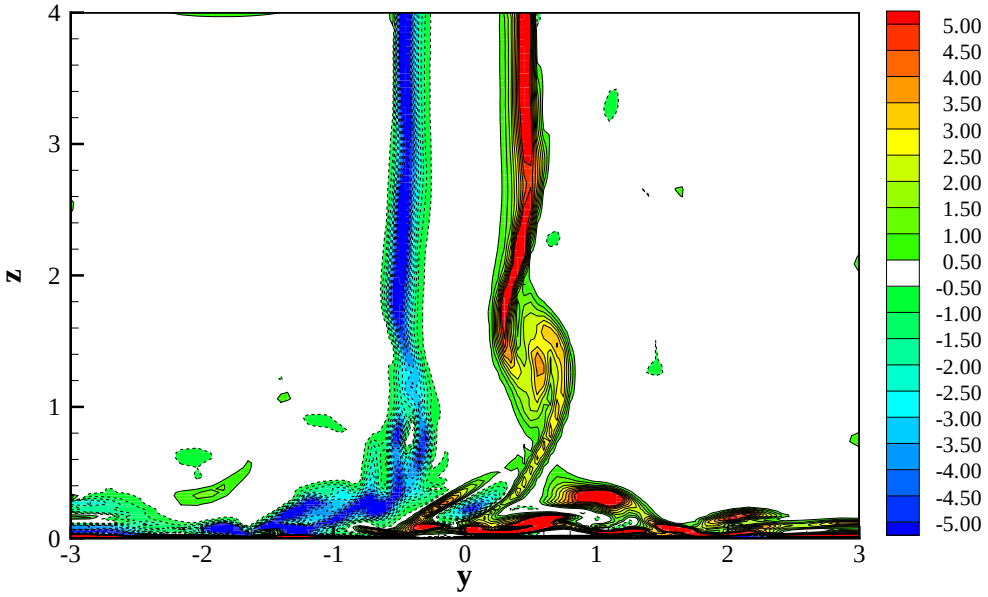

(a) left jet

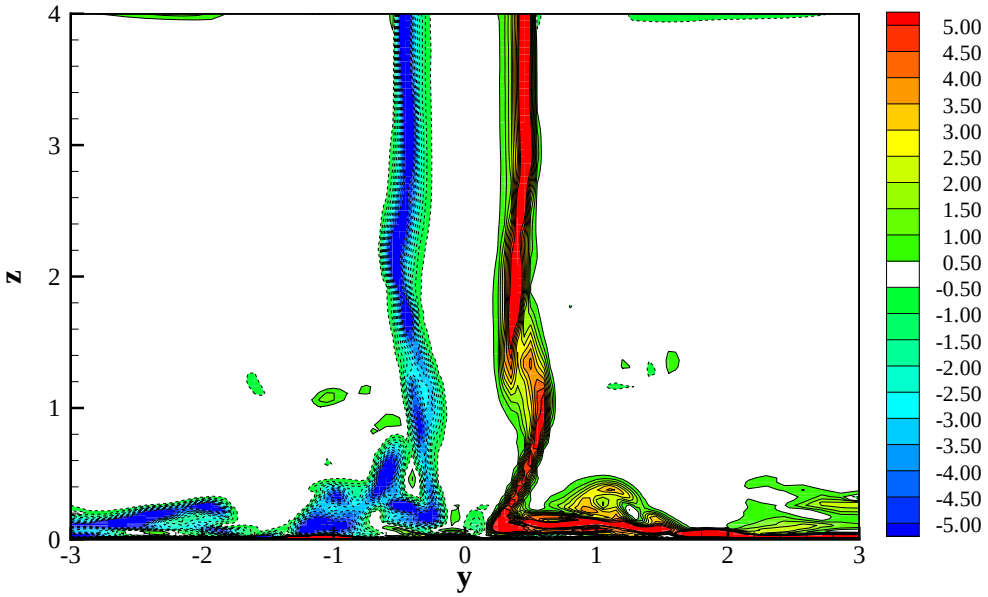

(b) right jet

Figure 6.92: The x-vorticity contour in the midplanes of the jets at $t = 111.3092$.

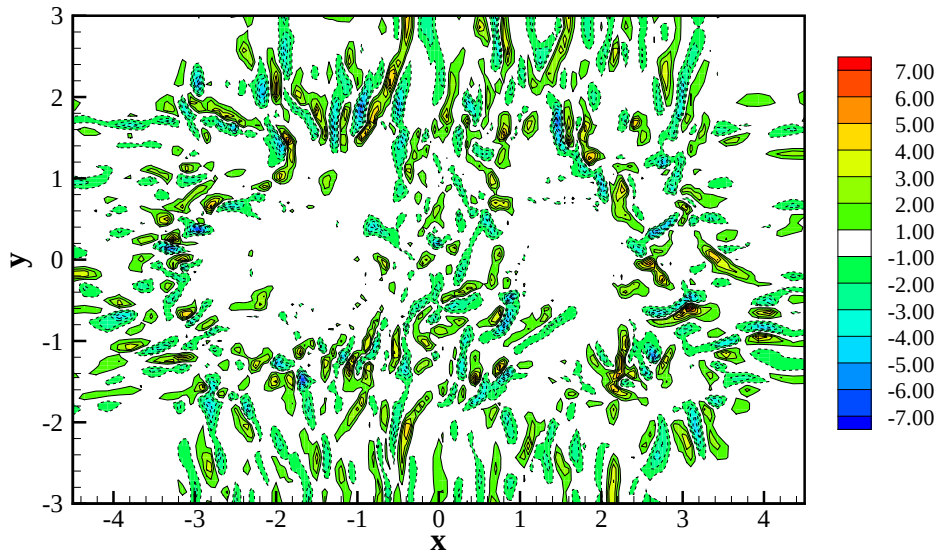

Figure 6.93: The z-vorticity contour in the $z = 0.005745$ plane at $t = 104.3092$.

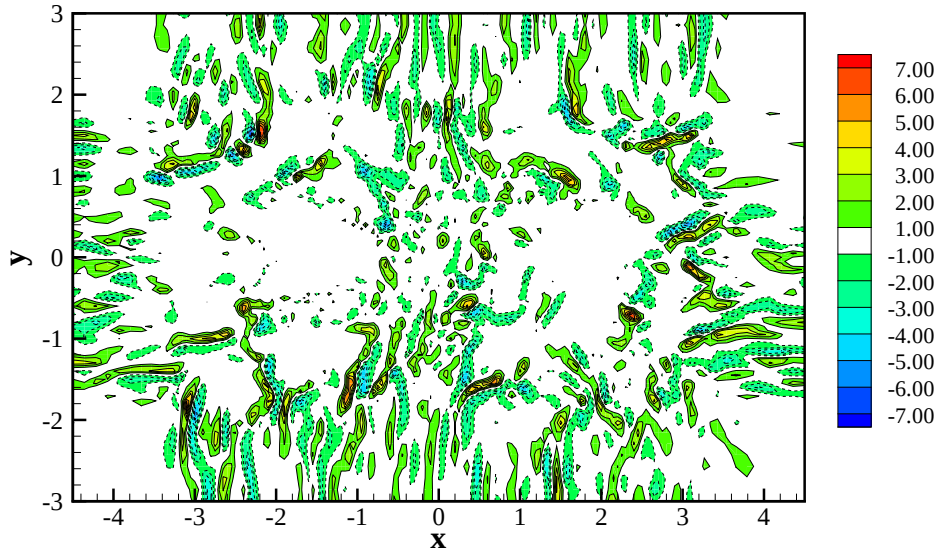

Figure 6.94: The z-vorticity contour in the $z = 0.005745$ plane at $t = 105.7092$.

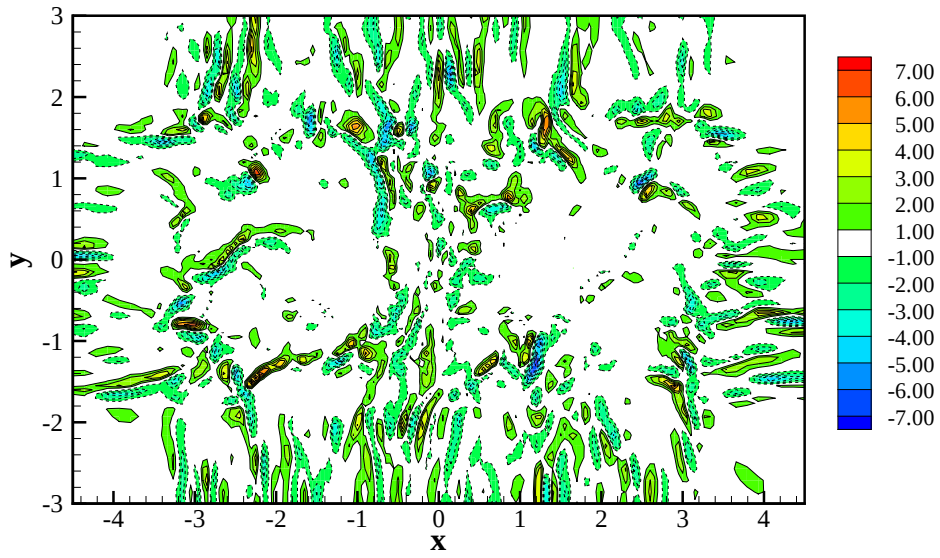

Figure 6.95: The z-vorticity contour in the $z = 0.005745$ plane at $t = 107.1092$.

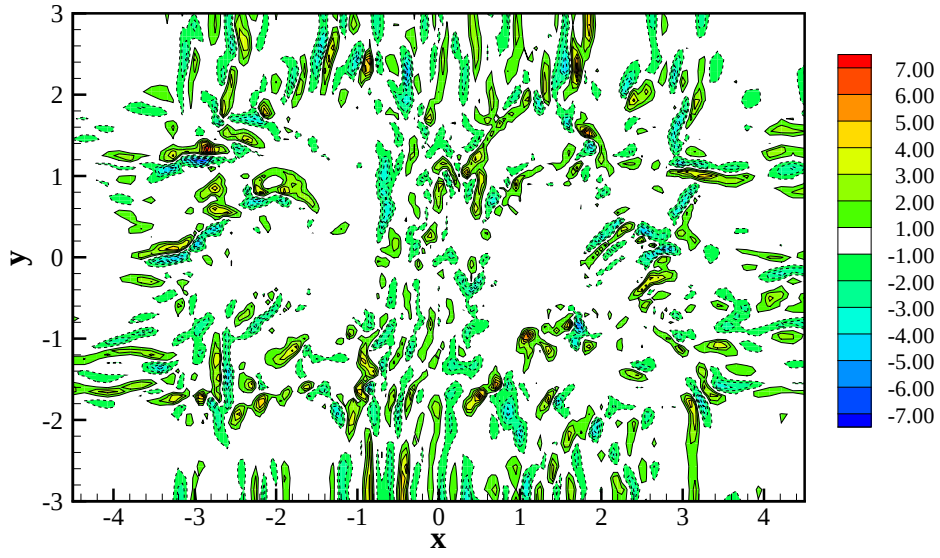

Figure 6.96: The z-vorticity contour in the $z = 0.005745$ plane at $t = 108.5092$.

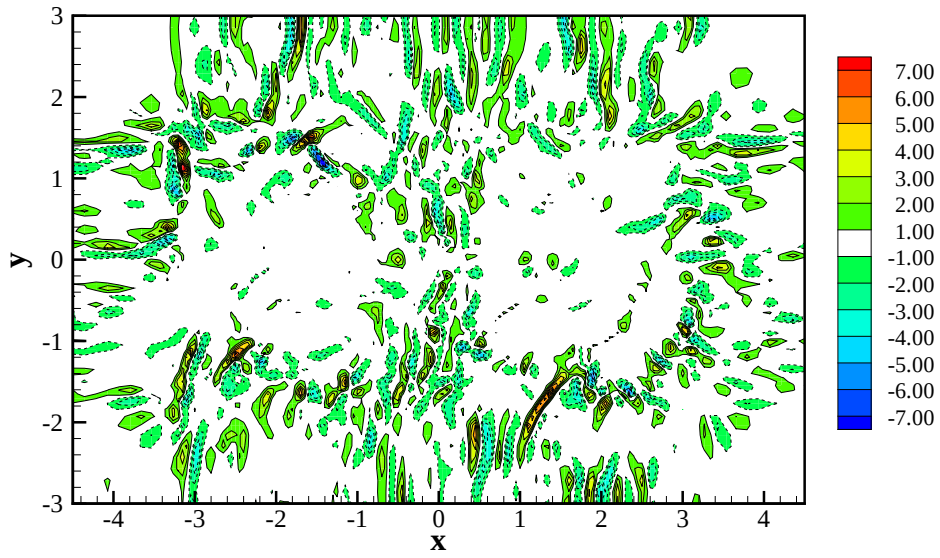

Figure 6.97: The z-vorticity contour in the $z = 0.005745$ plane at $t = 109.9092$.

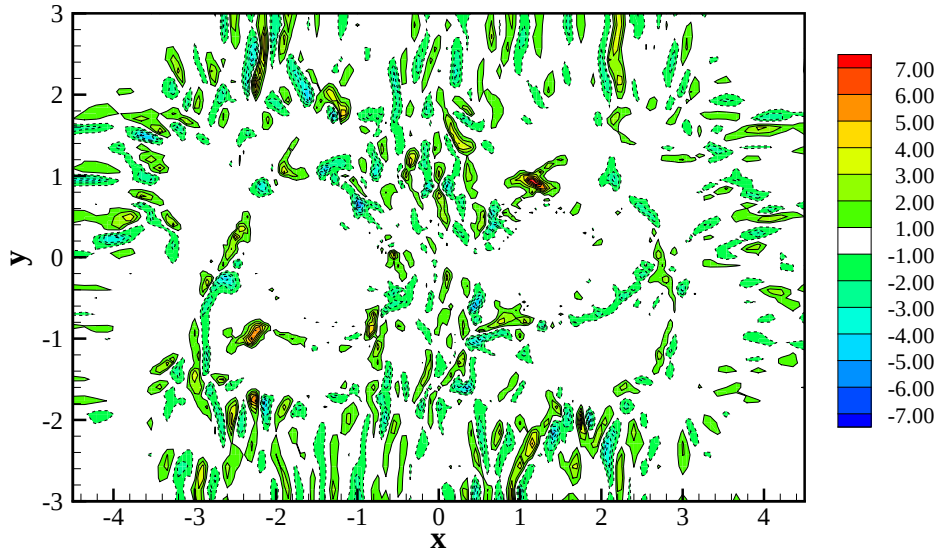

Figure 6.98: The z-vorticity contour in the $z = 0.005745$ plane at $t = 111.3092$.

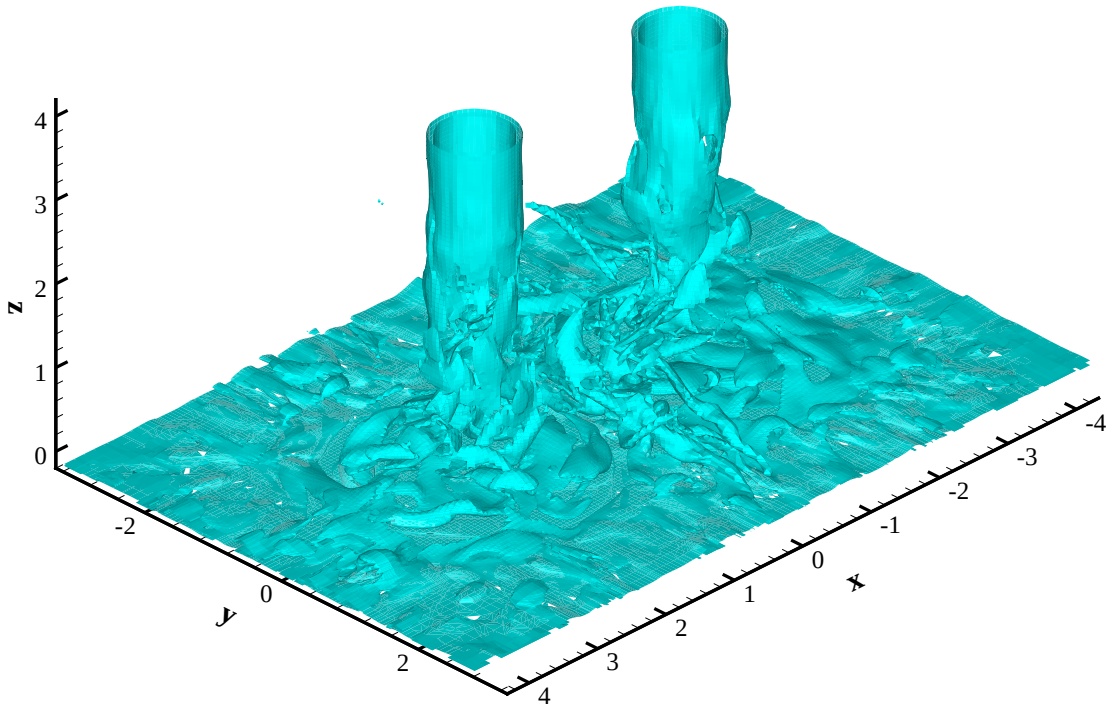

Figure 6.99: Isosurface of vorticity magnitude at the level $|\vec{\omega}| = 6.0$ at $t = 111.3092$

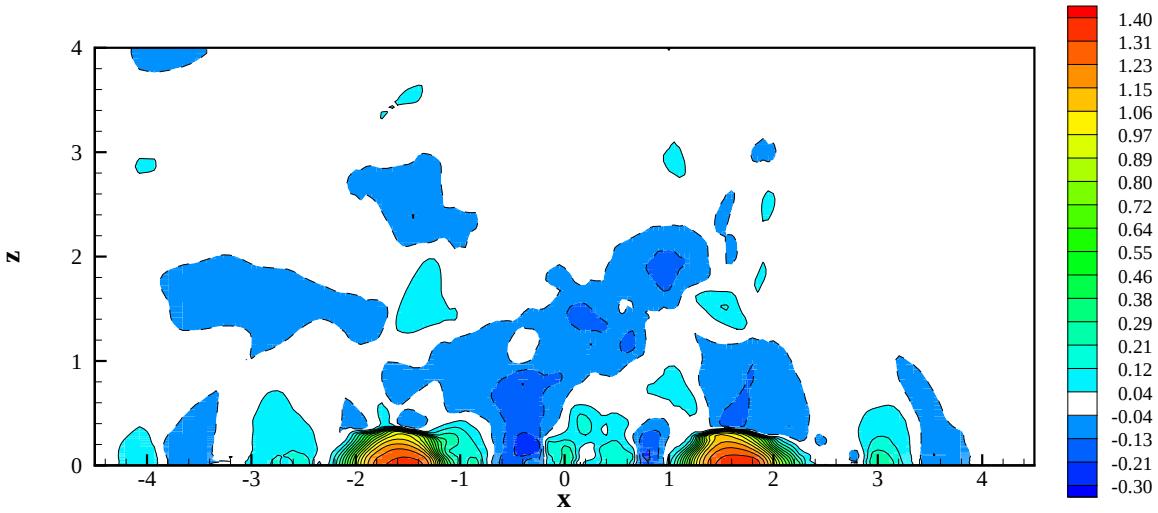

Figure 6.100: Pressure coefficient (C_p) contours in the $y = 0$ plane at $t = 104.3092$.

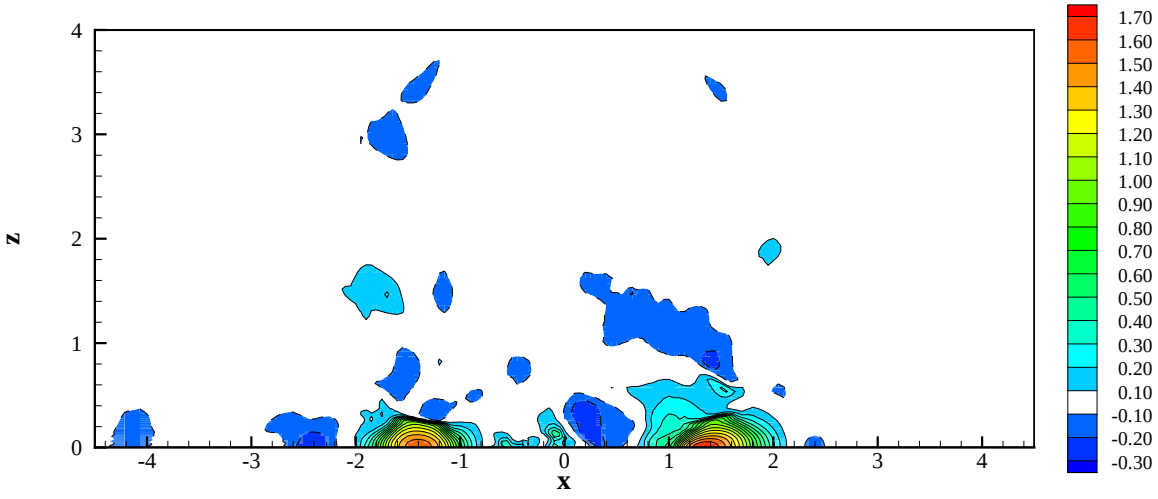

Figure 6.101: Pressure coefficient (C_p) contours in the $y = 0$ plane at $t = 105.7092$.

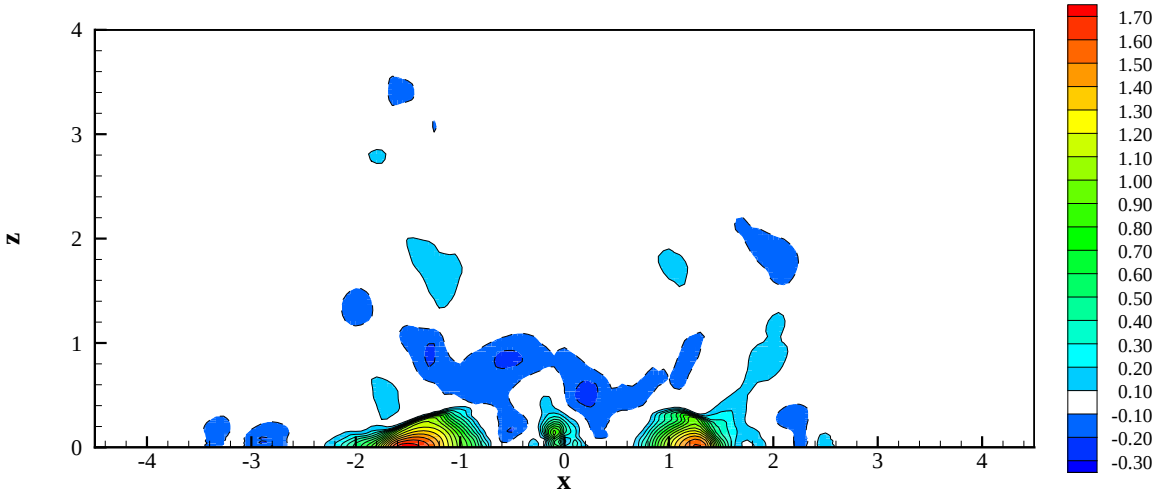

Figure 6.102: Pressure coefficient (C_p) contours in the $y = 0$ plane at $t = 107.1092$.

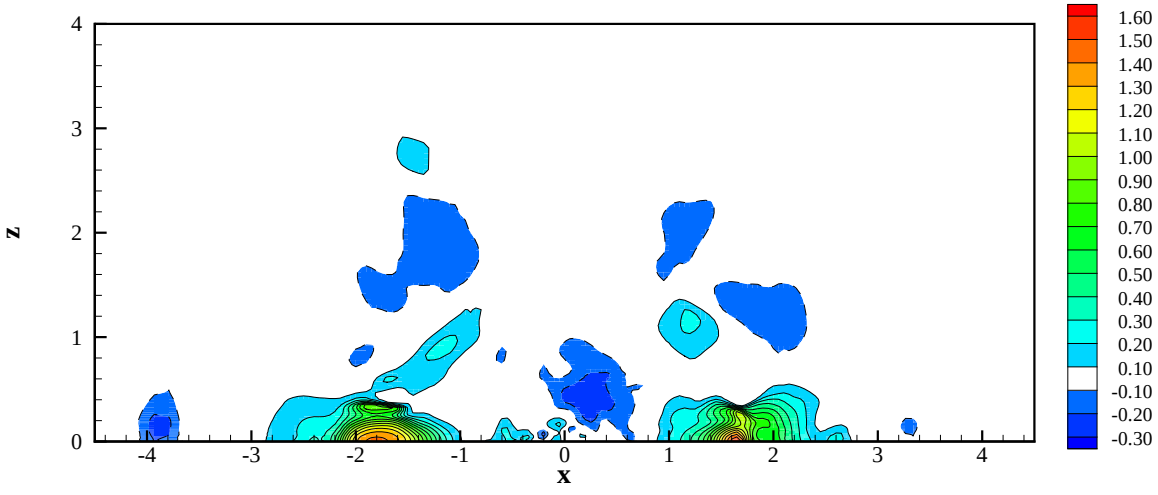

Figure 6.103: Pressure coefficient (C_p) contours in the $y = 0$ plane at $t = 108.5092$.

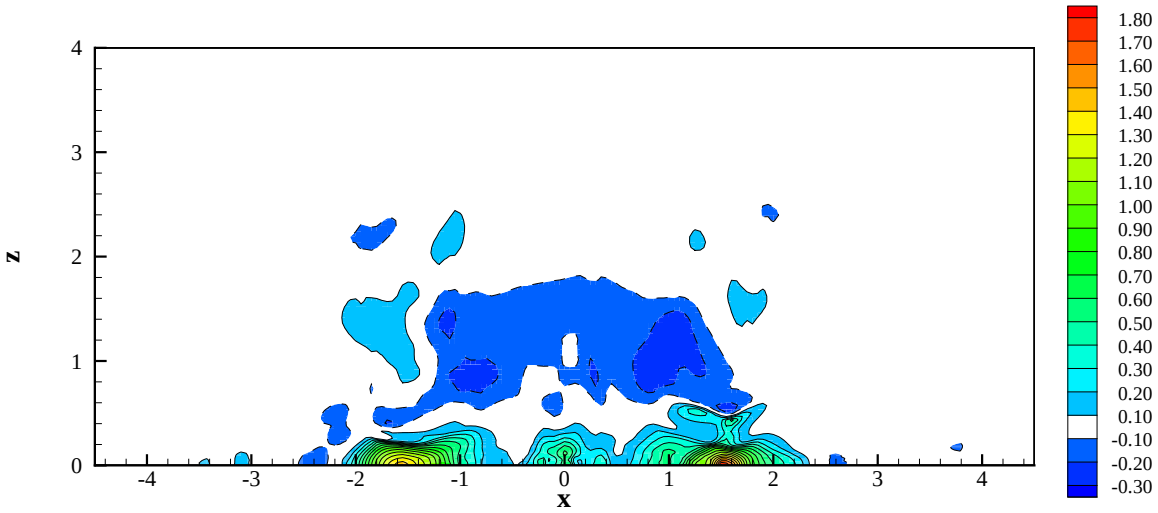

Figure 6.104: Pressure coefficient (C_p) contours in the $y = 0$ plane at $t = 109.9092$.

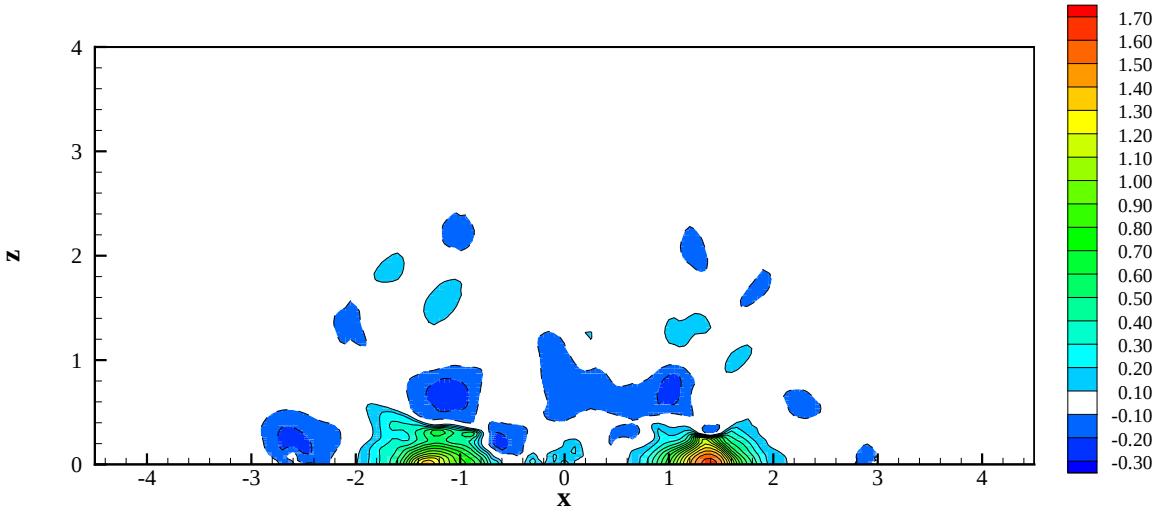

Figure 6.105: Pressure coefficient (C_p) contours in the $y = 0$ plane at $t = 111.3092$.

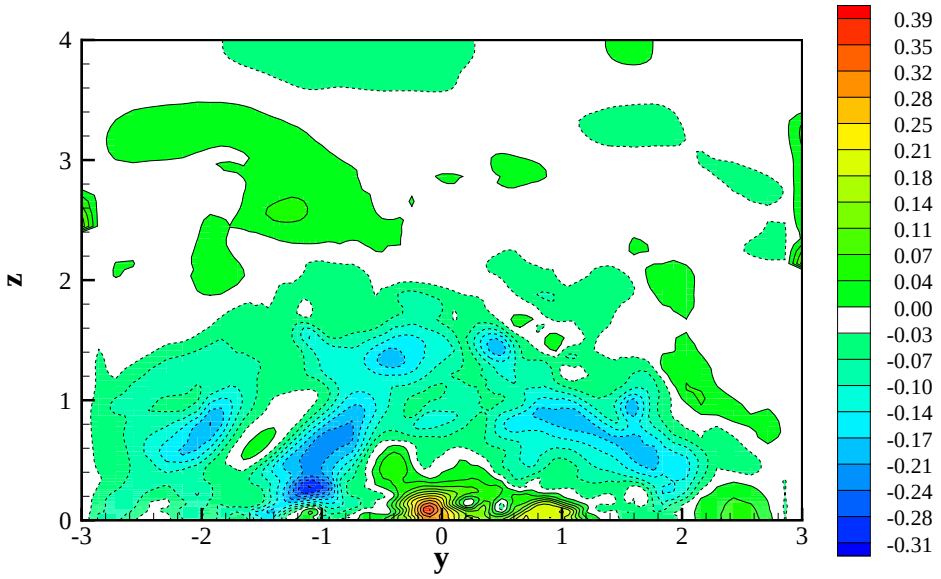

Figure 6.106: Pressure coefficient(C_p) contours in the $x = 0$ plane at $t = 104.3092$

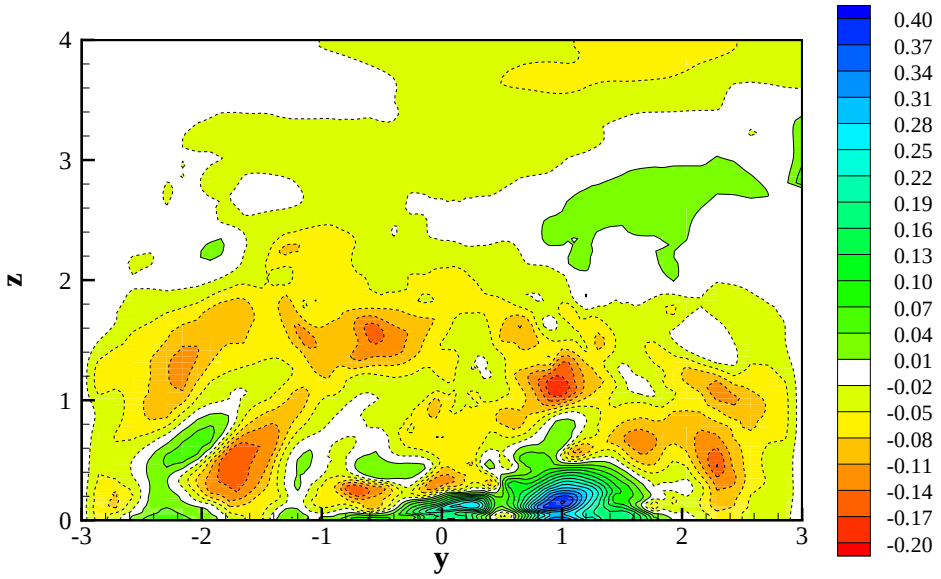

Figure 6.107: Pressure coefficient(C_p) contours in the $x = 0$ plane at $t = 105.7092$

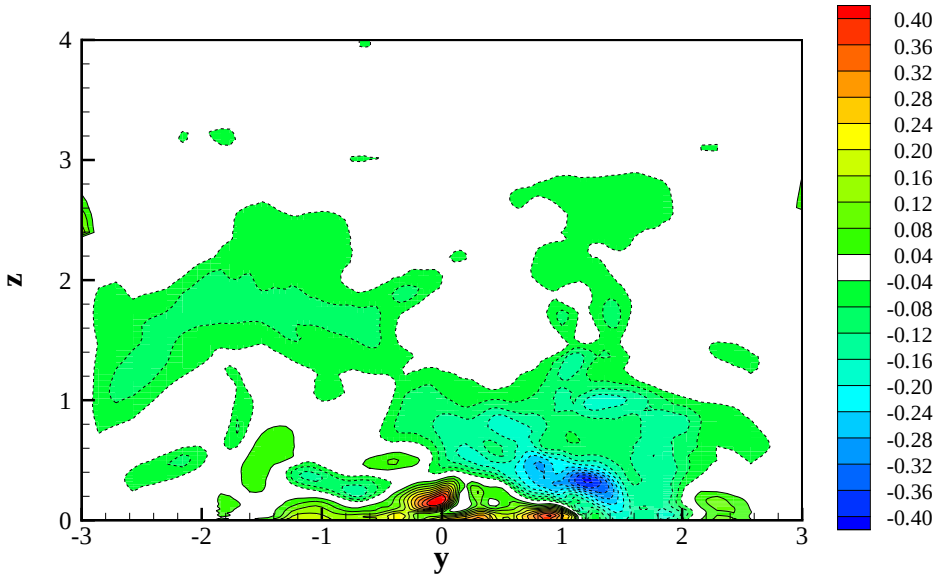

Figure 6.108: Pressure coefficient(C_p) contours in the $x = 0$ plane at $t = 107.1092$

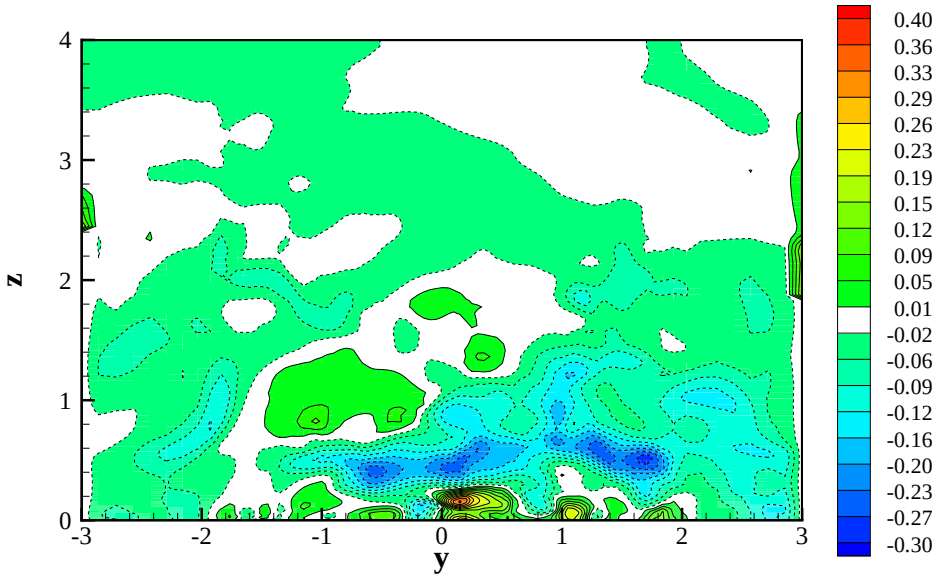

Figure 6.109: Pressure coefficient(C_p) contours in the $x = 0$ plane at $t = 108.5092$

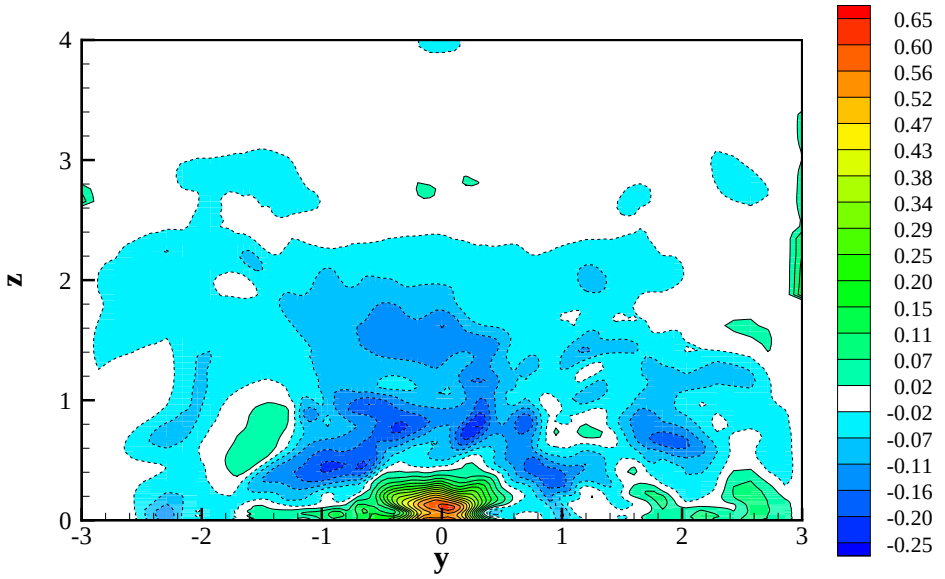

Figure 6.110: Pressure coefficient(C_p) contours in the $x = 0$ plane at $t = 109.9092$

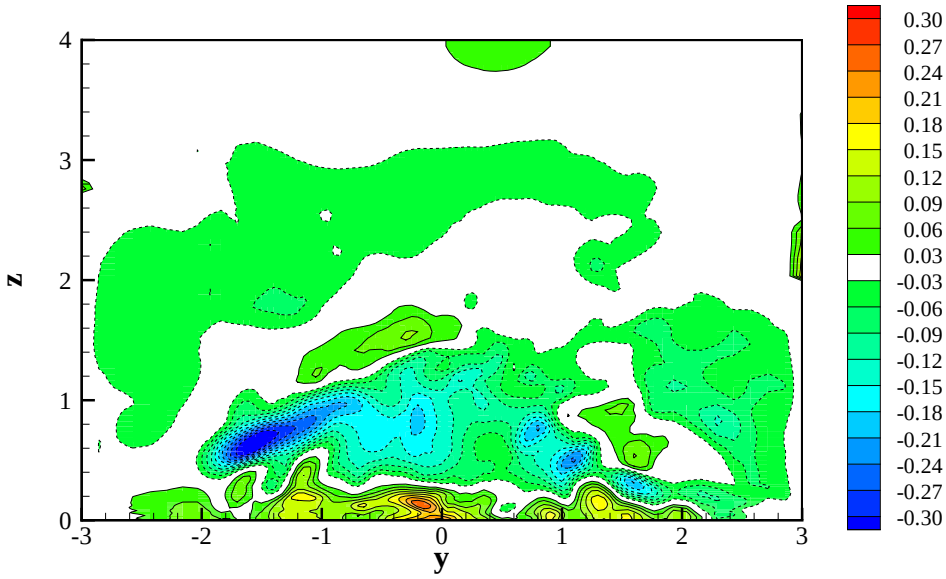

Figure 6.111: Pressure coefficient(C_p) contours in the $x = 0$ plane at $t = 111.3092$

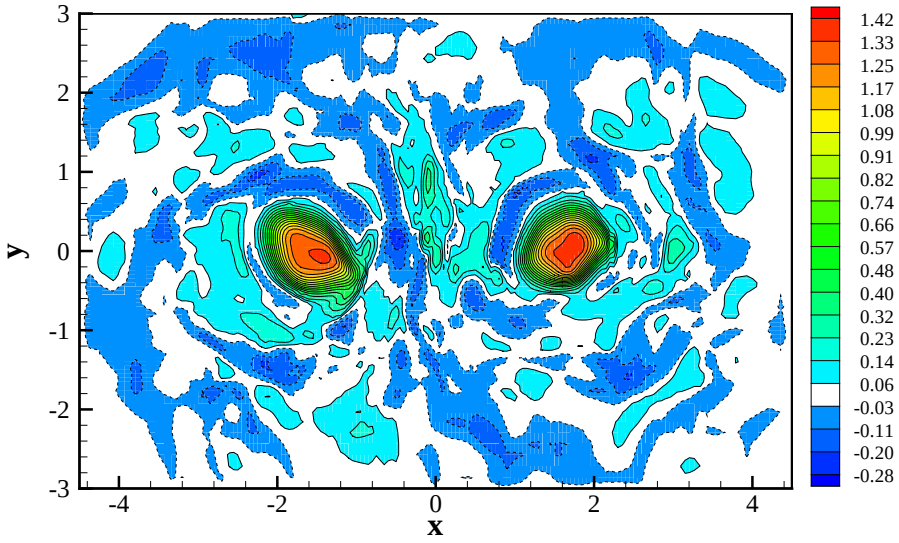

Figure 6.112: Pressure coefficient(C_p) contours in the $z = 0.005745$ plane at $t = 104.3092$.

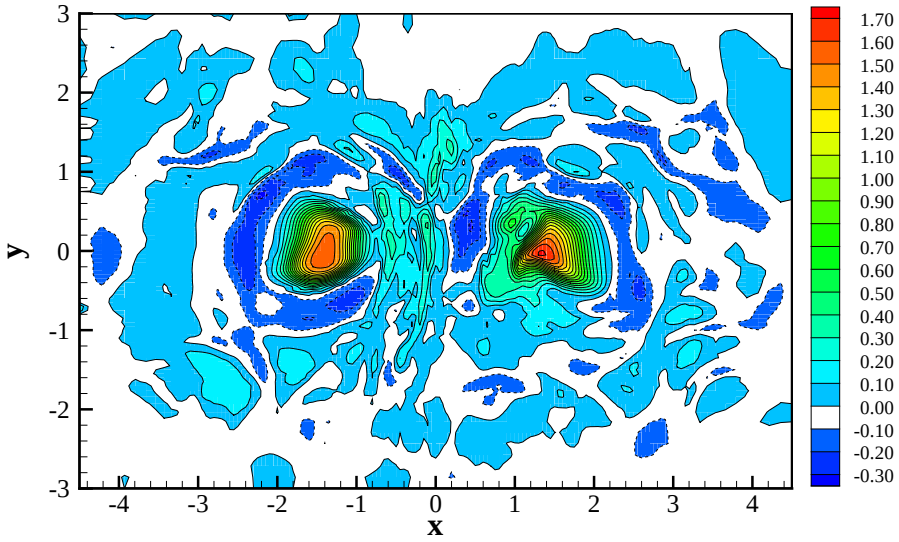

Figure 6.113: Pressure coefficient(C_p) contours in the $z = 0.005745$ plane at $t = 105.7092$.

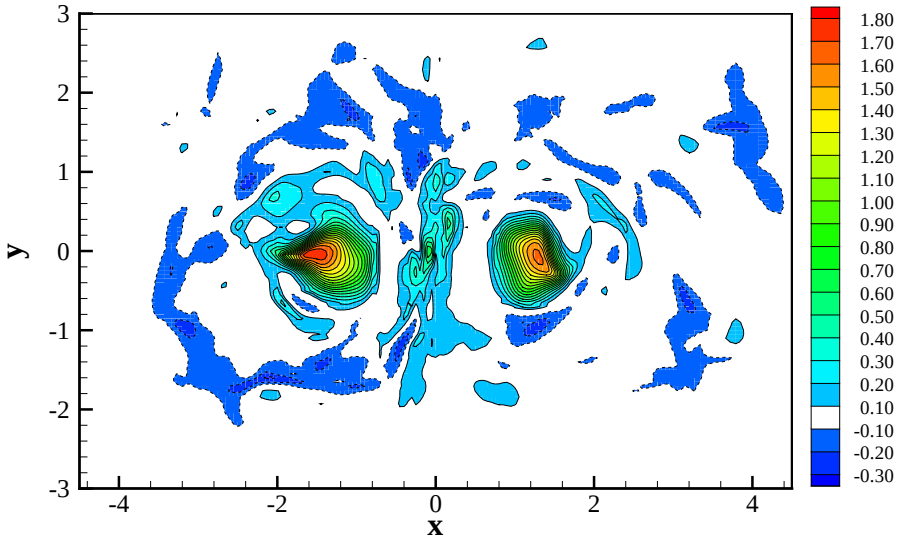

Figure 6.114: Pressure coefficient(C_p) contours in the $z = 0.005745$ plane at $t = 107.1092$.

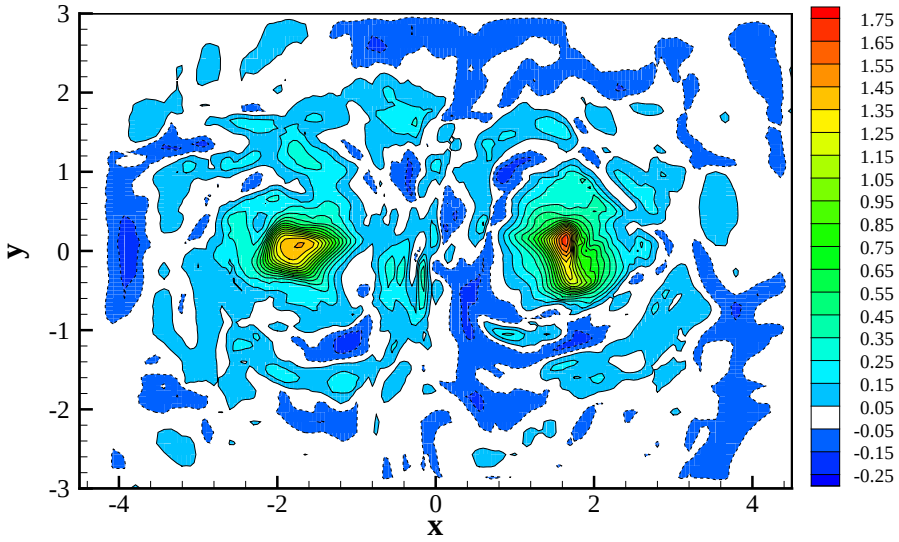

Figure 6.115: Pressure coefficient(C_p) contours in the $z = 0.005745$ plane at $t = 108.5092$.

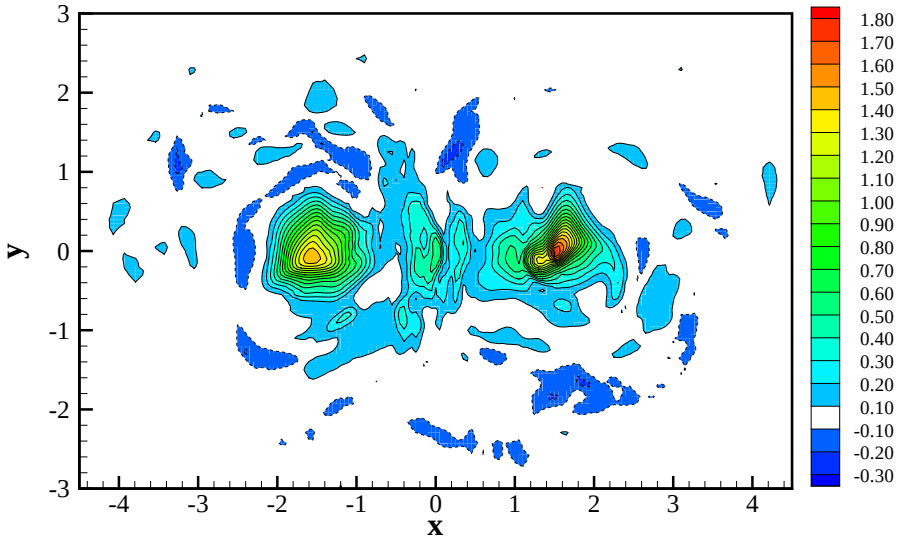

Figure 6.116: Pressure coefficient(C_p) contours in the $z = 0.005745$ plane at $t = 109.9092$.

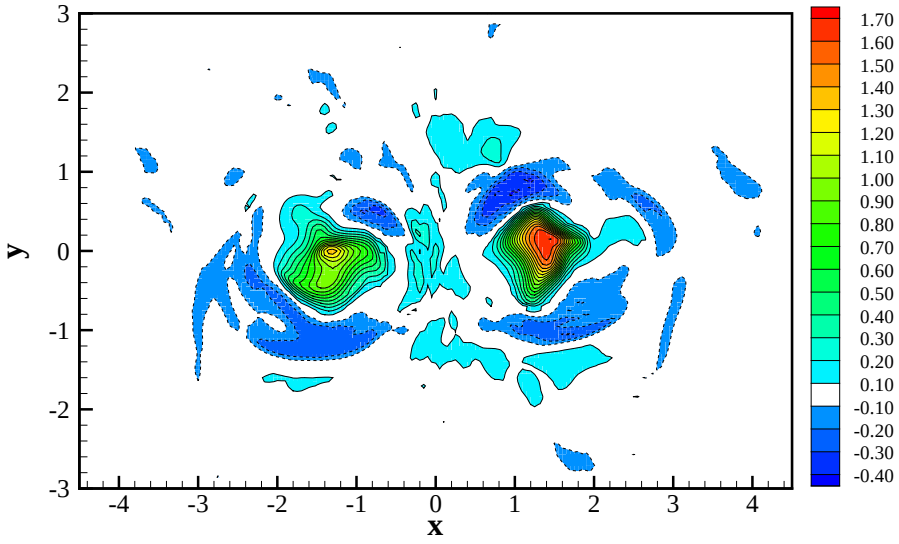

Figure 6.117: Pressure coefficient(C_p) contours in the $z = 0.005745$ plane at $t = 111.3092$.

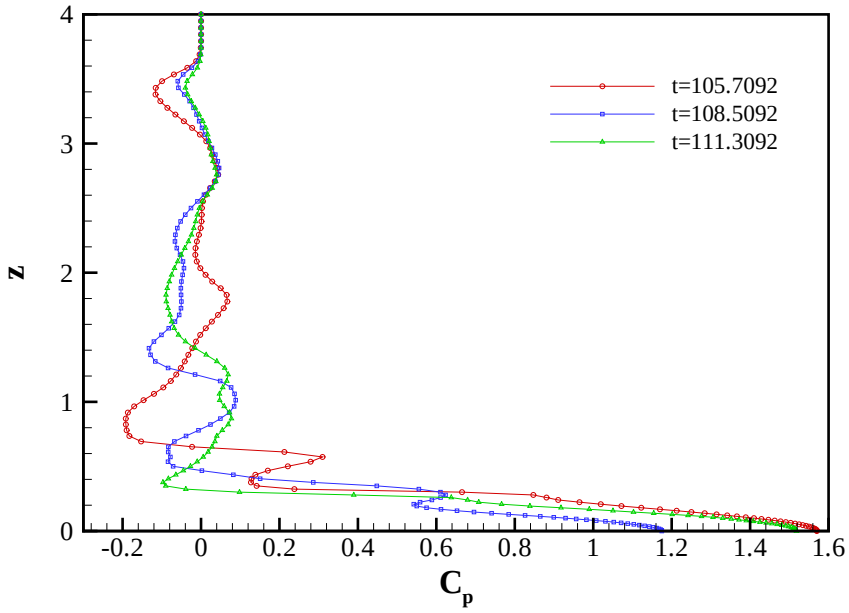

(a) left jet

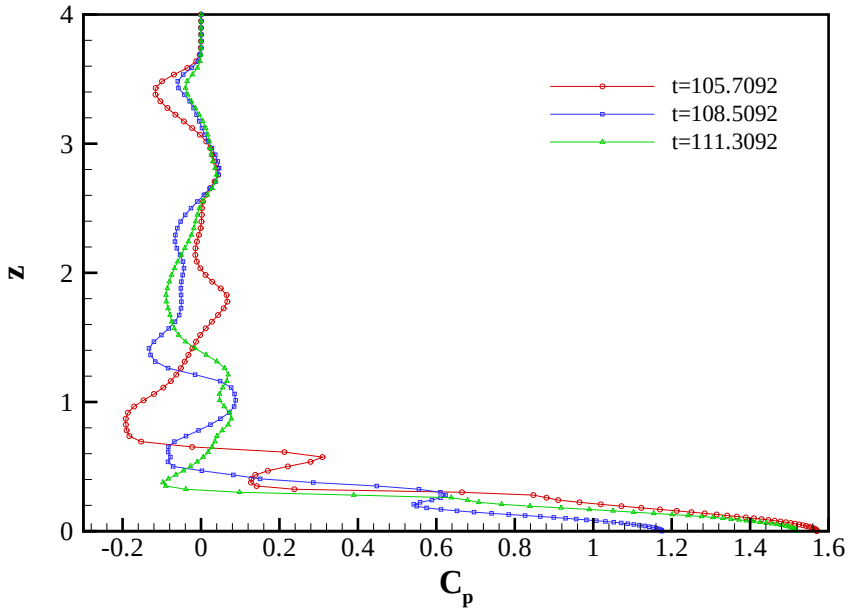

(a) right jet

Figure 6.118: Pressure coefficient, C_p, as a function of z at different times along the jet centerlines.

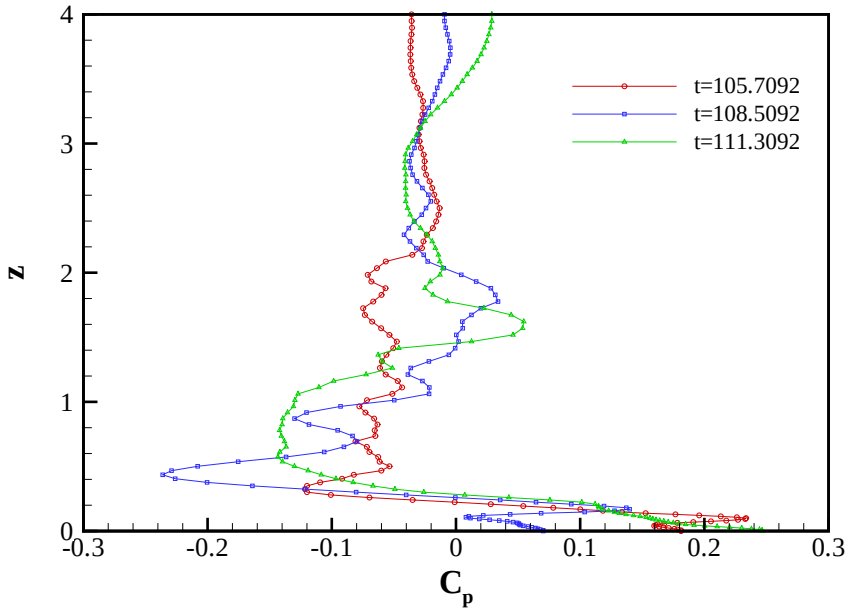

Figure 6.119: Pressure coefficient, C_p, as a function of z at different times along $x = 0$ in the $y = 0$ plane.

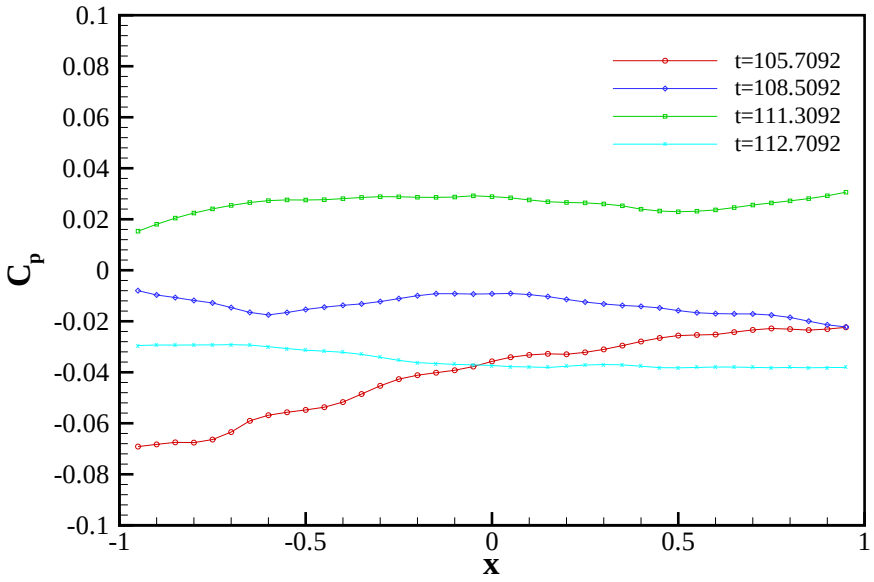

Figure 6.120: Pressure coefficient, C_p, as a function of x on the top surface at $y = 0$.

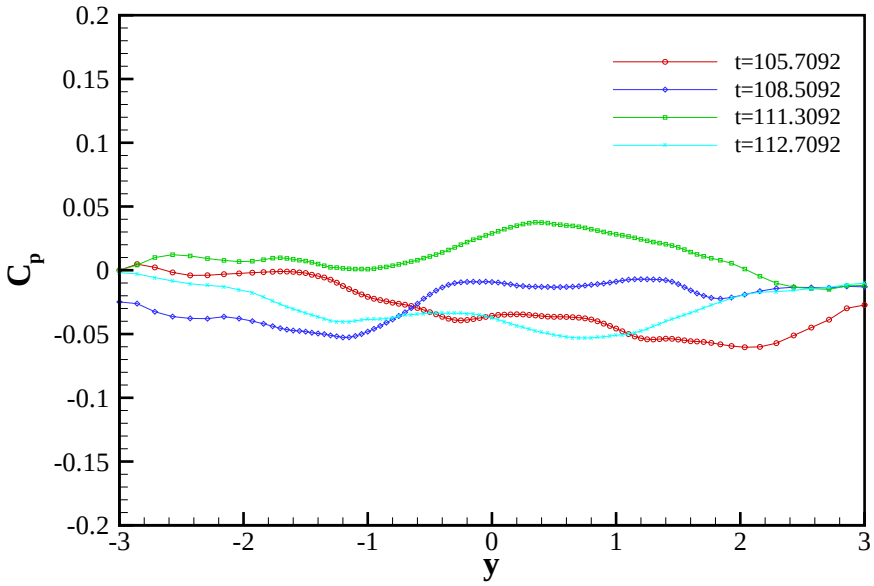

Figure 6.121: Pressure coefficient, C_p, as a function of y on the top surface at $x = 0$.

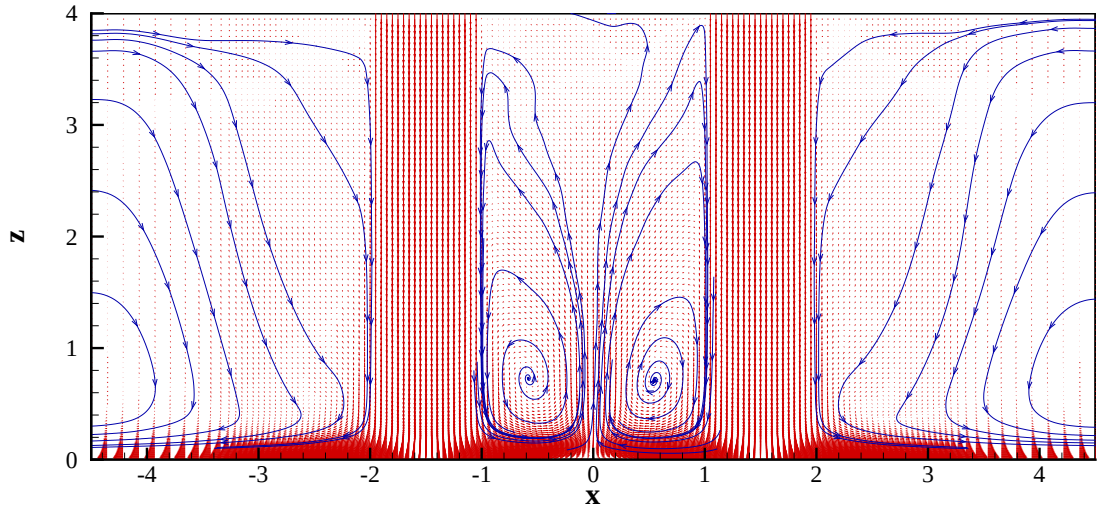

Figure 6.122: The mean velocity field in the $y = 0$ plane

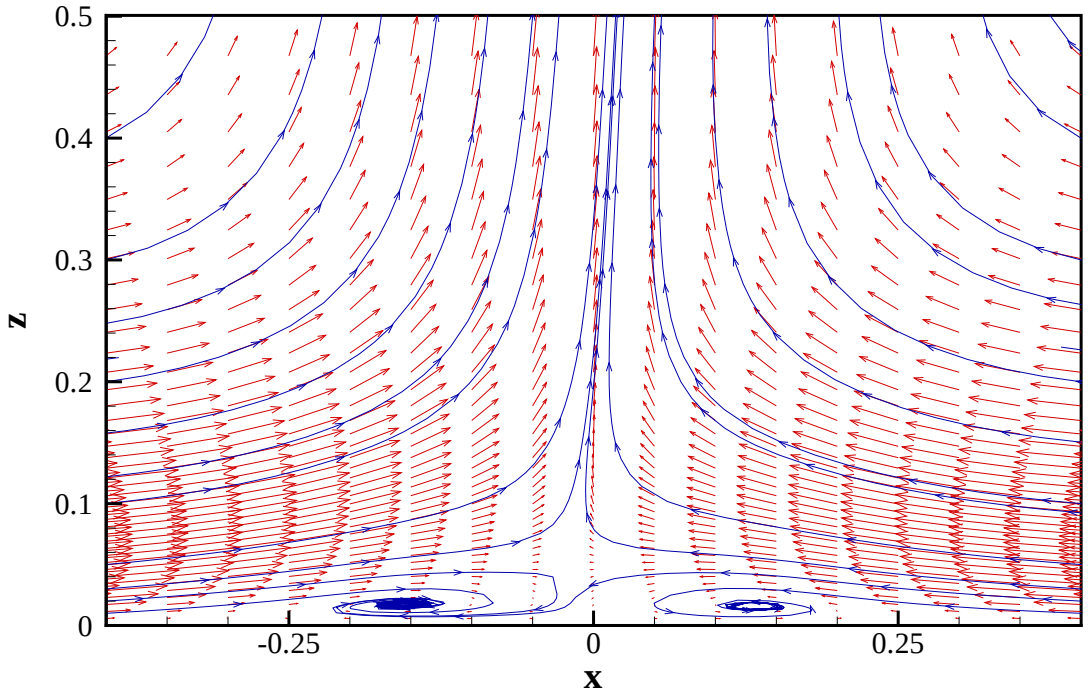

Figure 6.123: The mean velocity field in the $y = 0$ plane

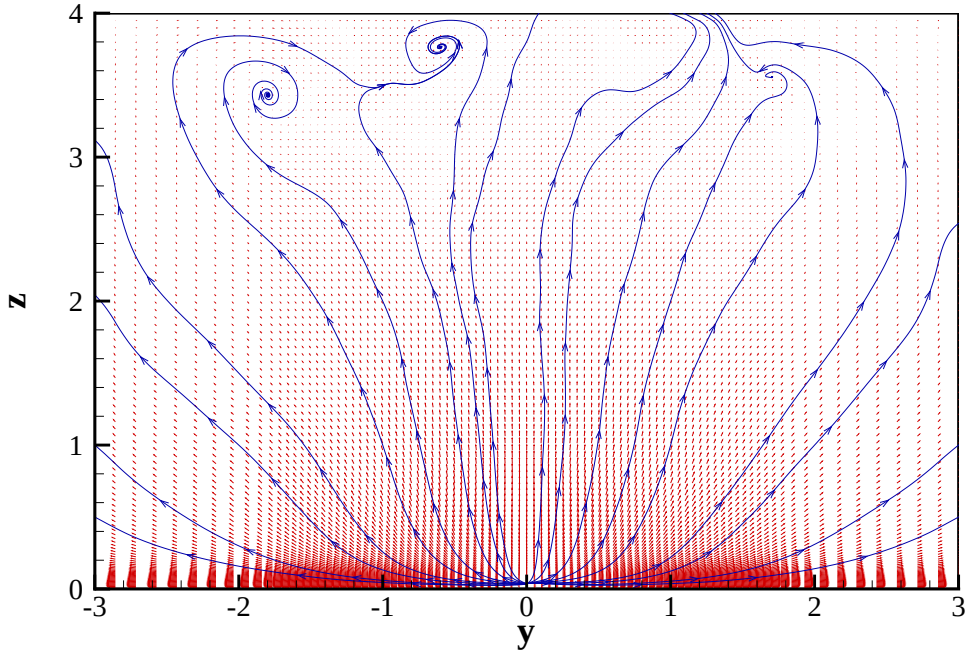

Figure 6.124: The mean velocity field in the $x = 0$ plane

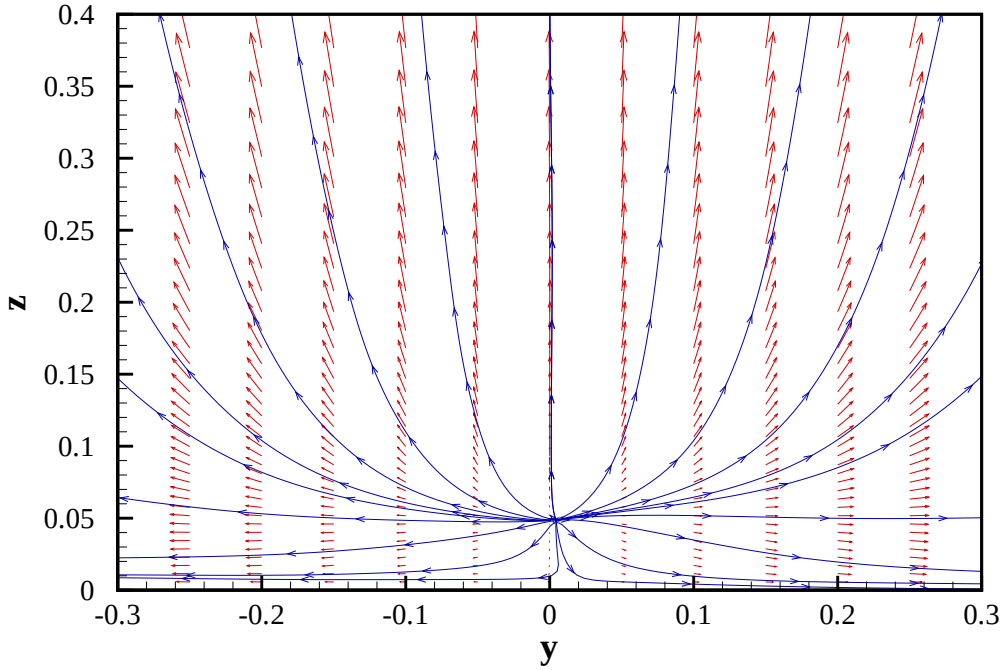

Figure 6.125: The mean velocity field in the $x = 0$ plane

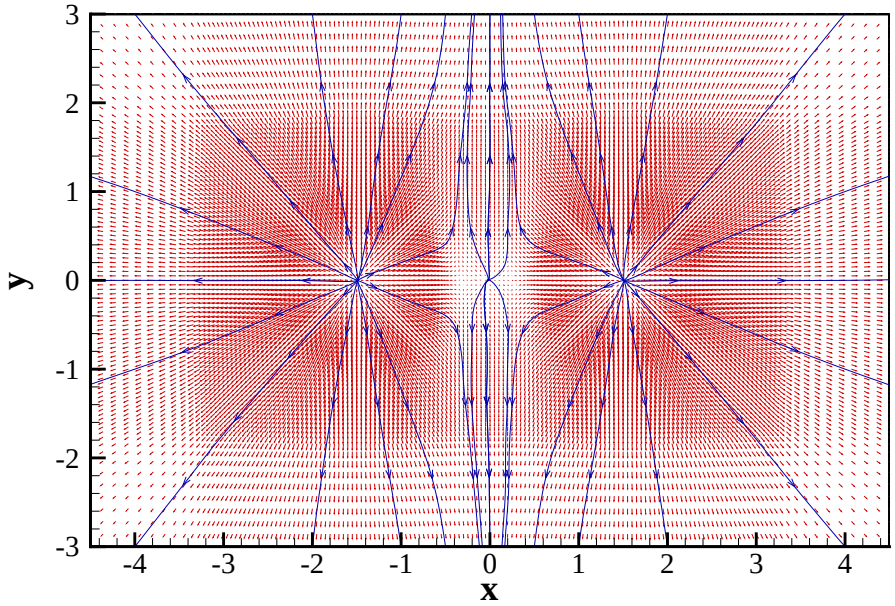

Figure 6.126: The mean velocity field in the $z = 0.005745$ plane

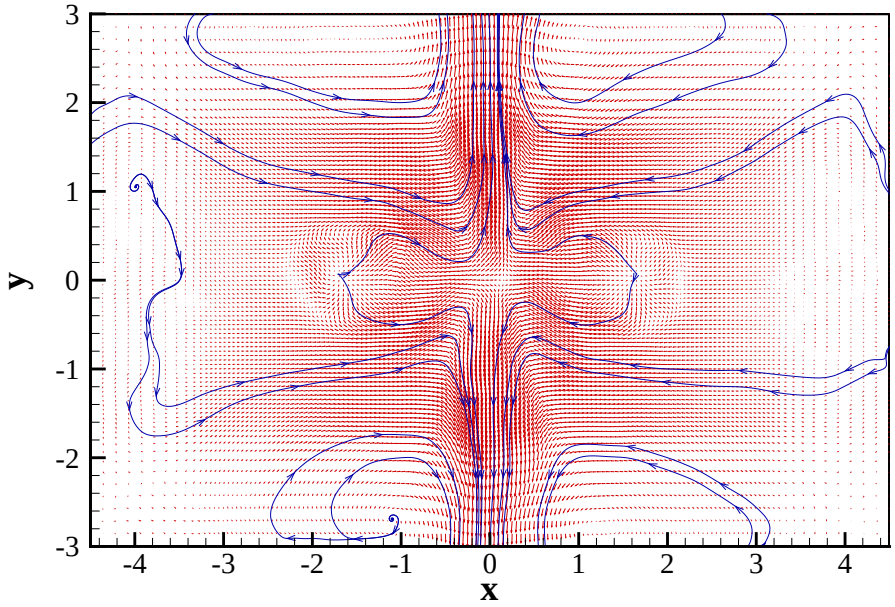

Figure 6.127: The mean velocity field in the $z = 0.5366$ plane

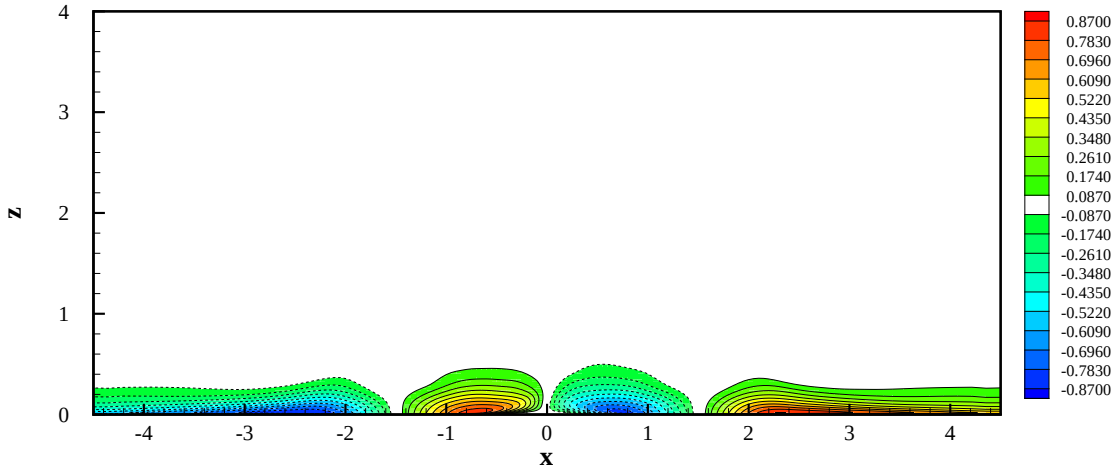

Figure 6.128: The contour plot for U in the $y = 0$ plane

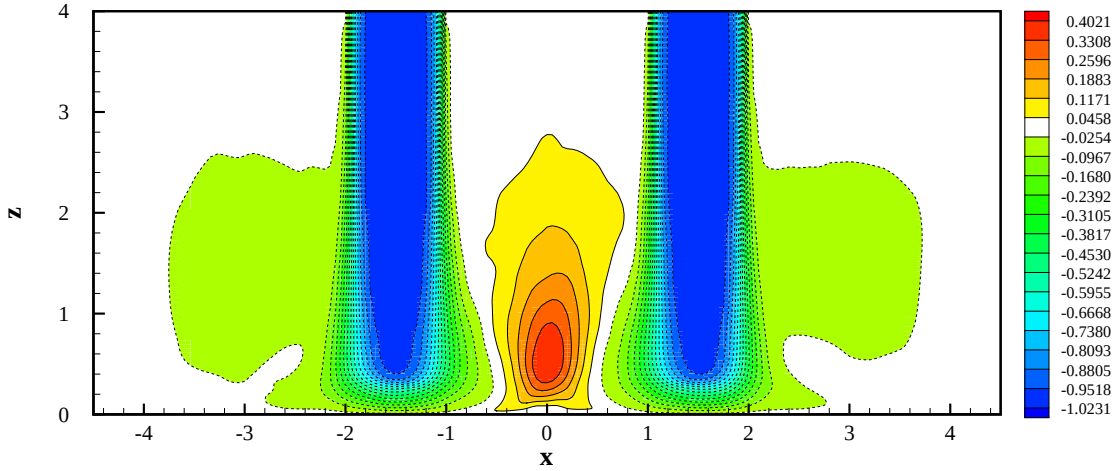

Figure 6.129: The contour plot for W in the $y = 0$ plane

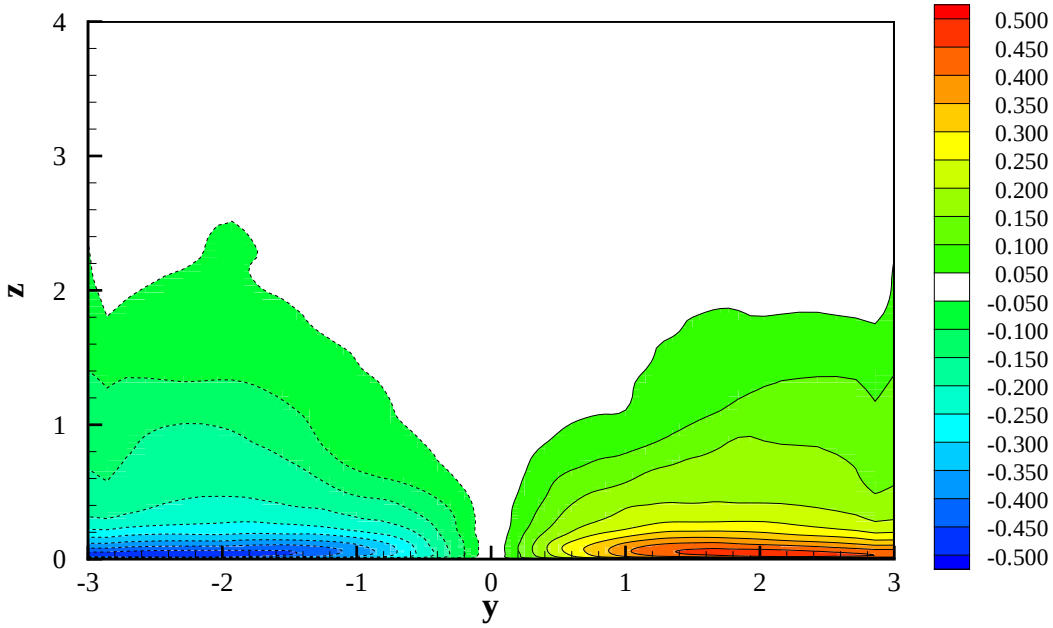

Figure 6.130: The contour plot for V in the $x = 0$ plane

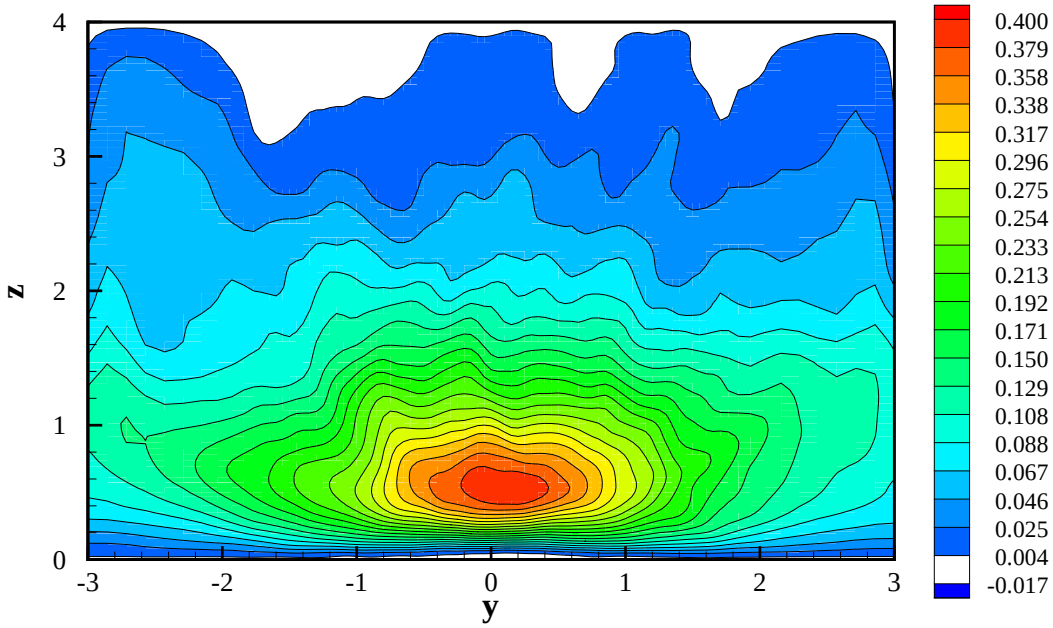

Figure 6.131: The contour plot for W in the $x = 0$ plane

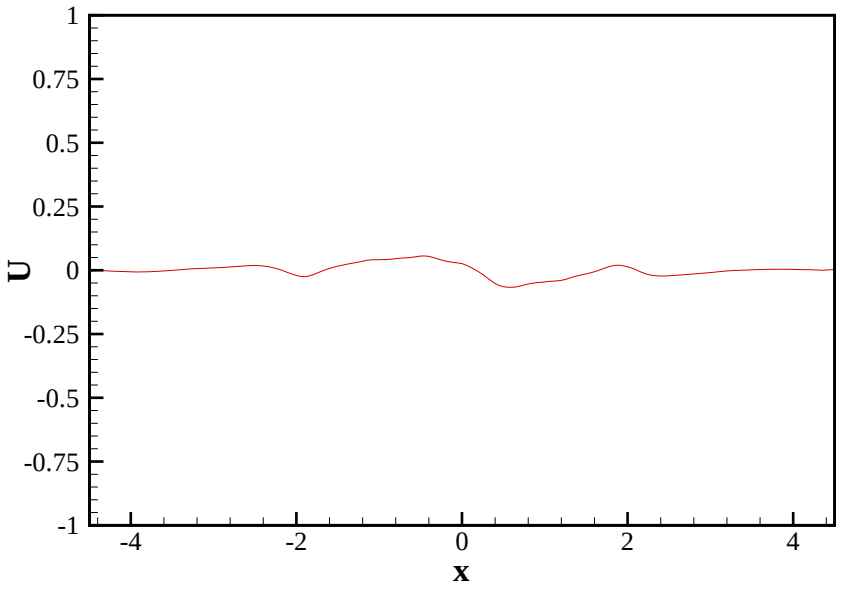

Figure 6.132: Variation of mean velocity U along the x-direction at $z = 0.536607$ in the $y = 0$ plane.

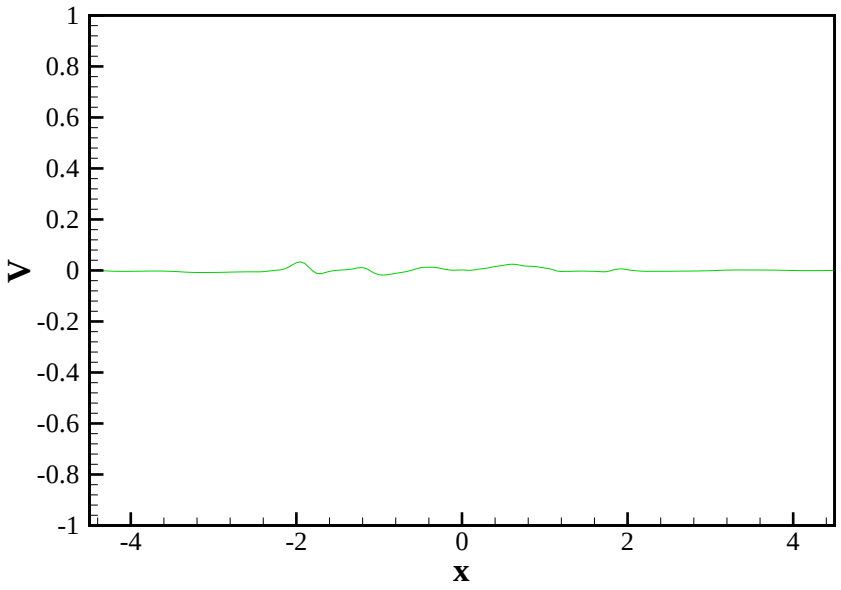

Figure 6.133: Variation of mean velocity V along the x-direction at $z = 0.536607$ in the $y = 0$ plane.

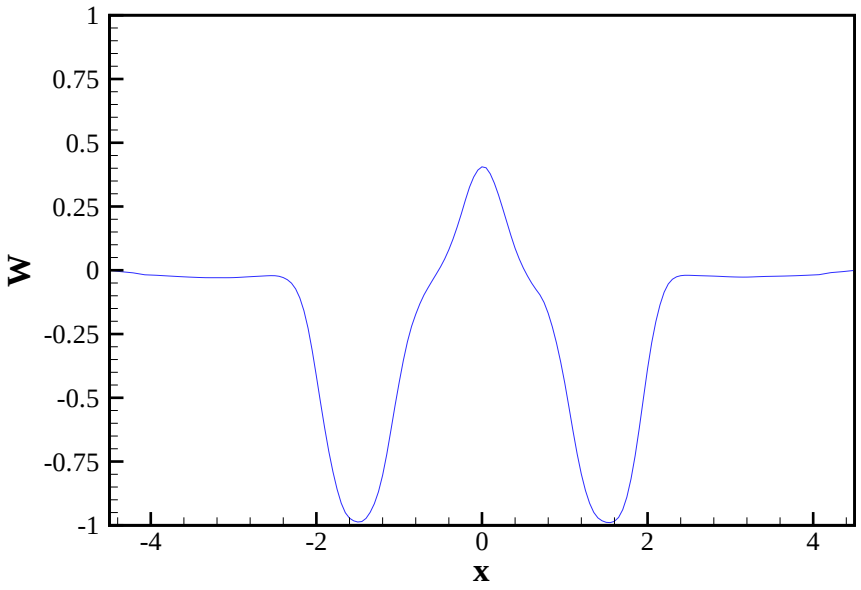

Figure 6.134: Variation of mean velocity W along the x-direction at $z = 0.536607$ in the $y = 0$ plane.

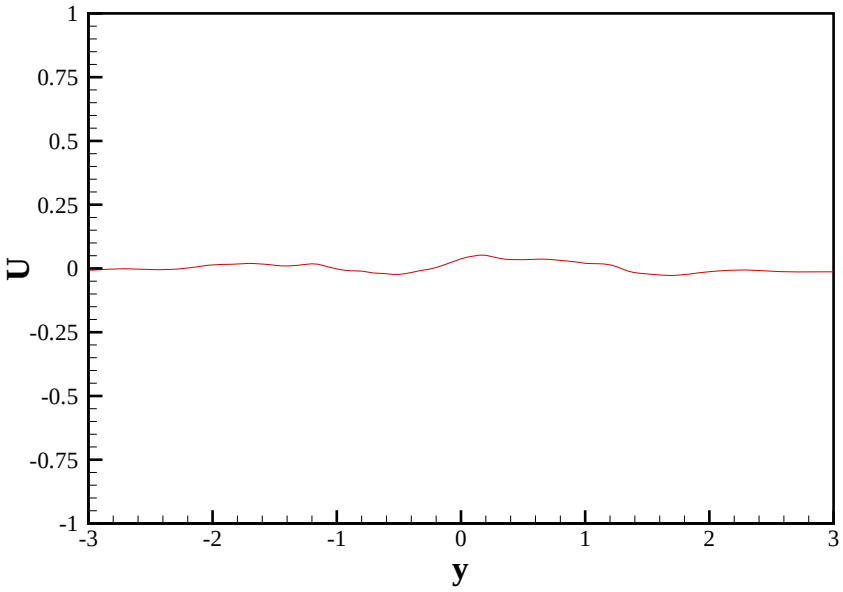

Figure 6.135: Variation of mean velocity U along the y-direction at $z = 0.536607$ in the $x = 0$ plane.

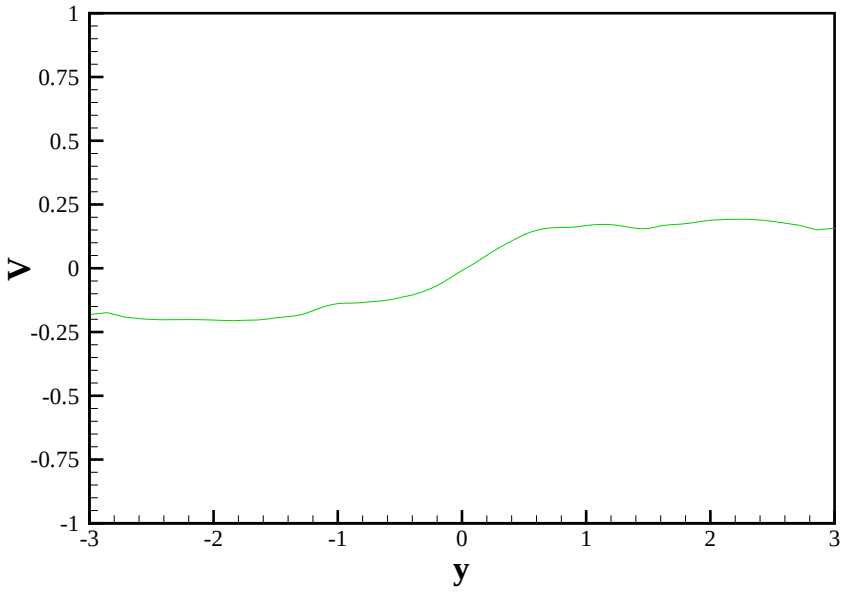

Figure 6.136: Variation of mean velocity V along the y-direction at $z = 0.536607$ in the $x = 0$ plane.

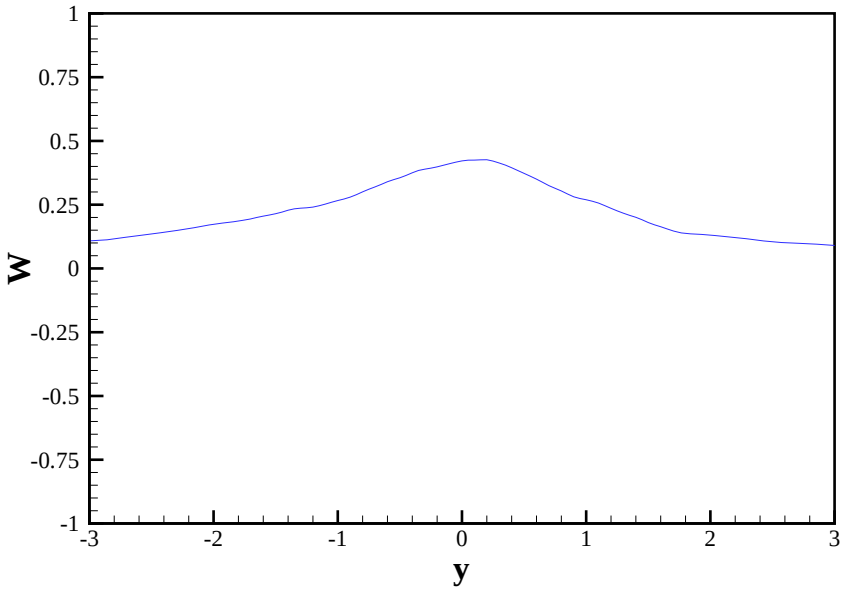

Figure 6.137: Variation of mean velocity W along the y-direction at $z = 0.536607$ in the $x = 0$ plane.

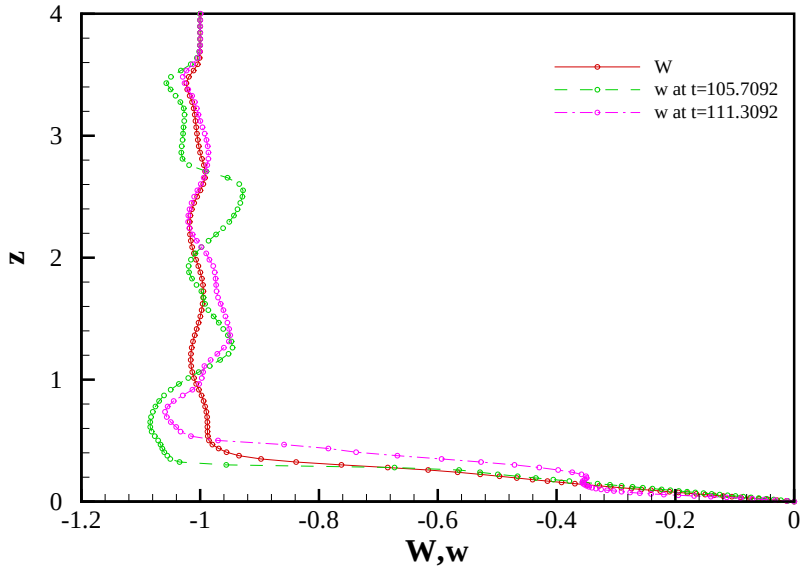

Figure 6.138: Variation of instantaneous velocity, w, and mean velocity, W, along the left jet centerline.

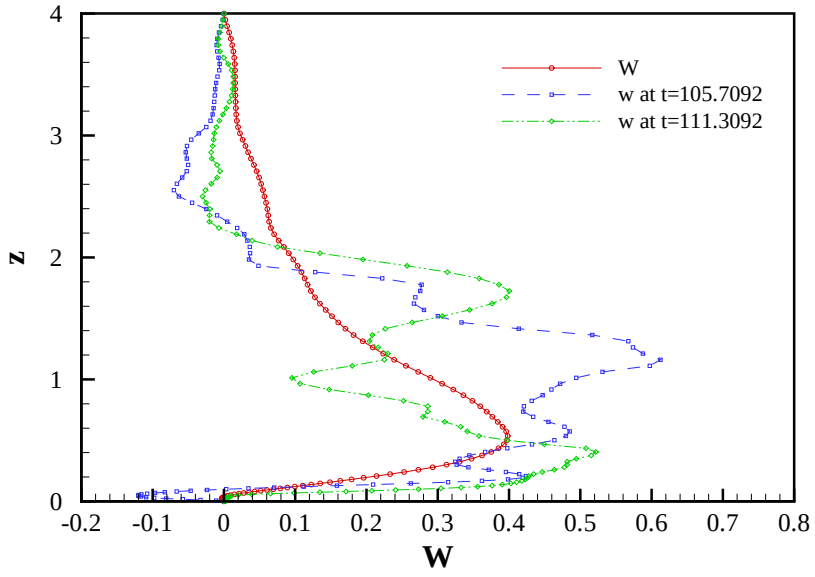

Figure 6.139: Variation of instantaneous velocity, w, and mean velocity, W, in the $y = 0$ plane at $x = 0$.

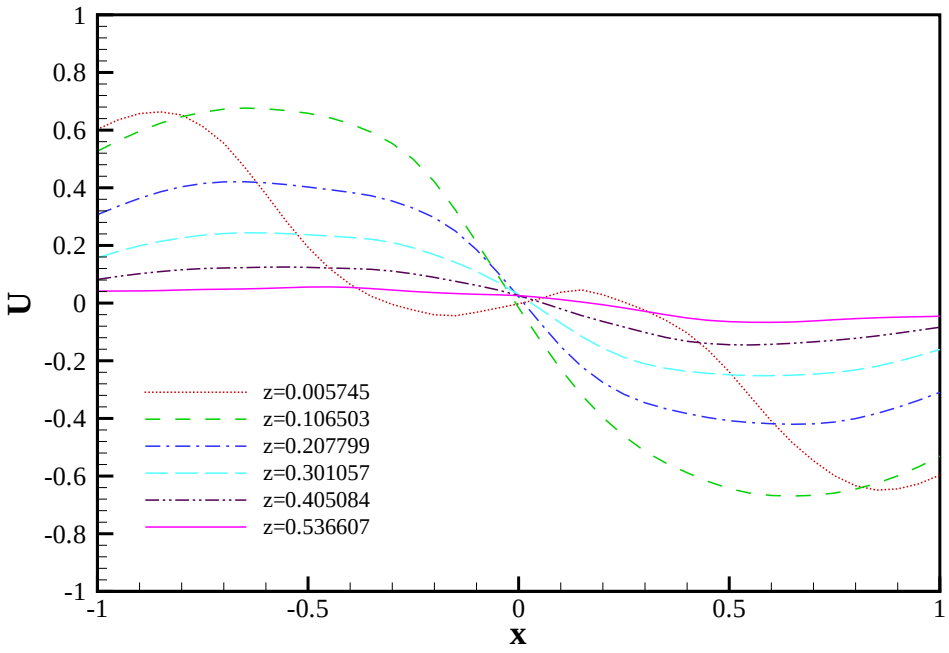

(a)

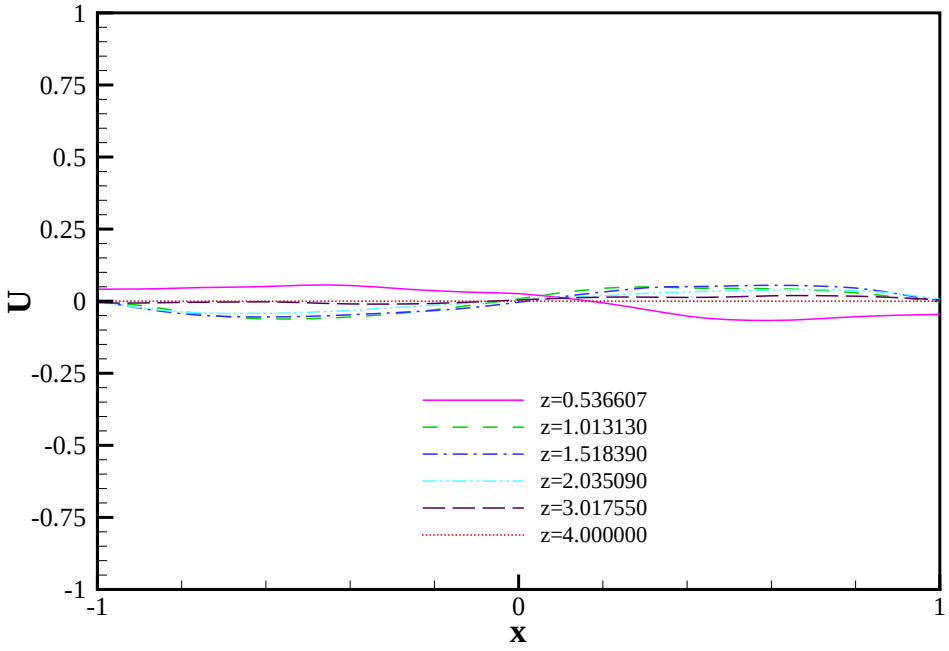

(b)

Figure 6.140: U-velocity profiles of the fountain in the $y = 0$ plane.

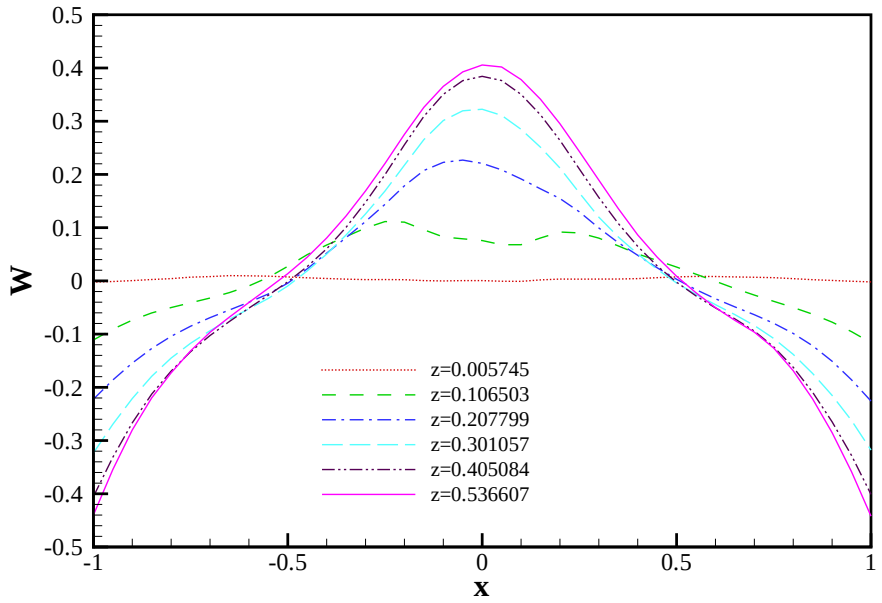

(a)

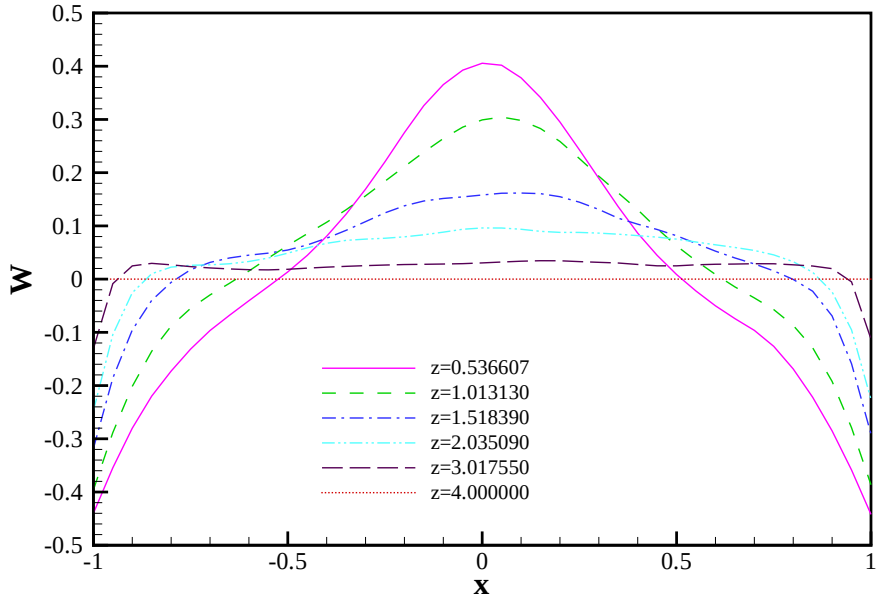

(b)

Figure 6.141: W-velocity profiles of the fountain in the $y = 0$ plane.

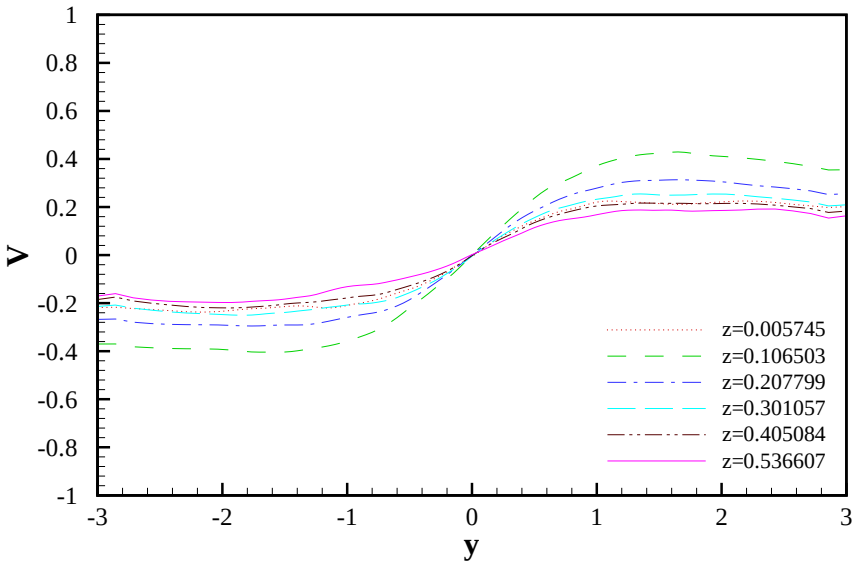

(a)

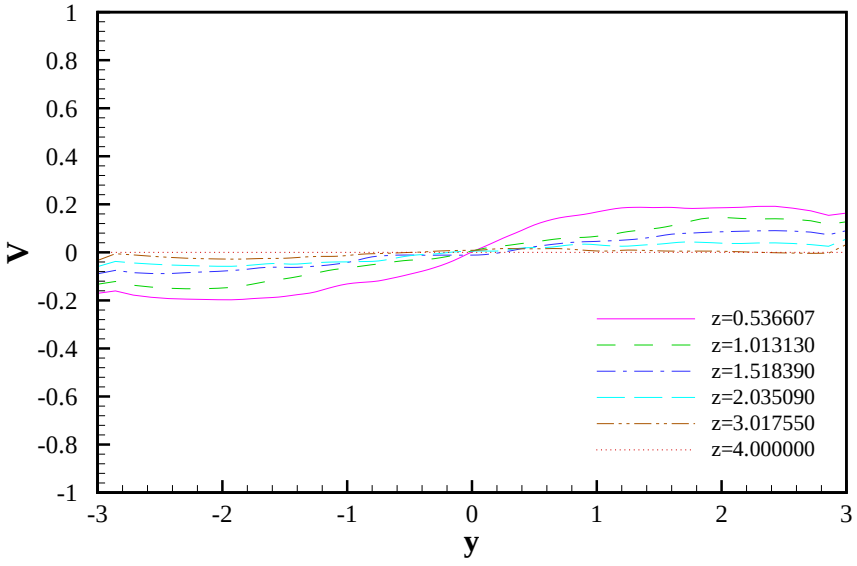

(b)

Figure 6.142: V-velocity profiles of the fountain in the $x = 0$ plane.

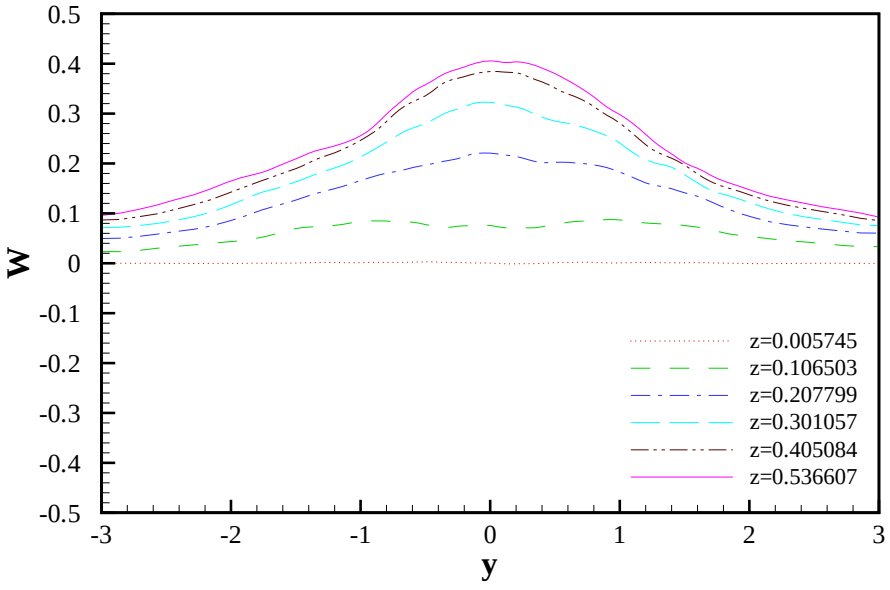

(a)

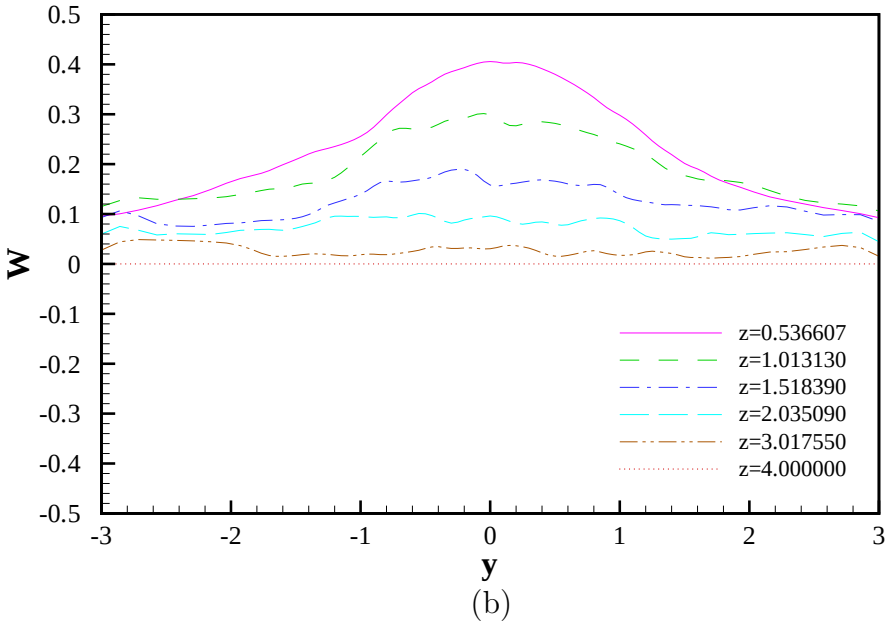

(b)

Figure 6.143: W-velocity profiles of the fountain in the $x = 0$ plane.

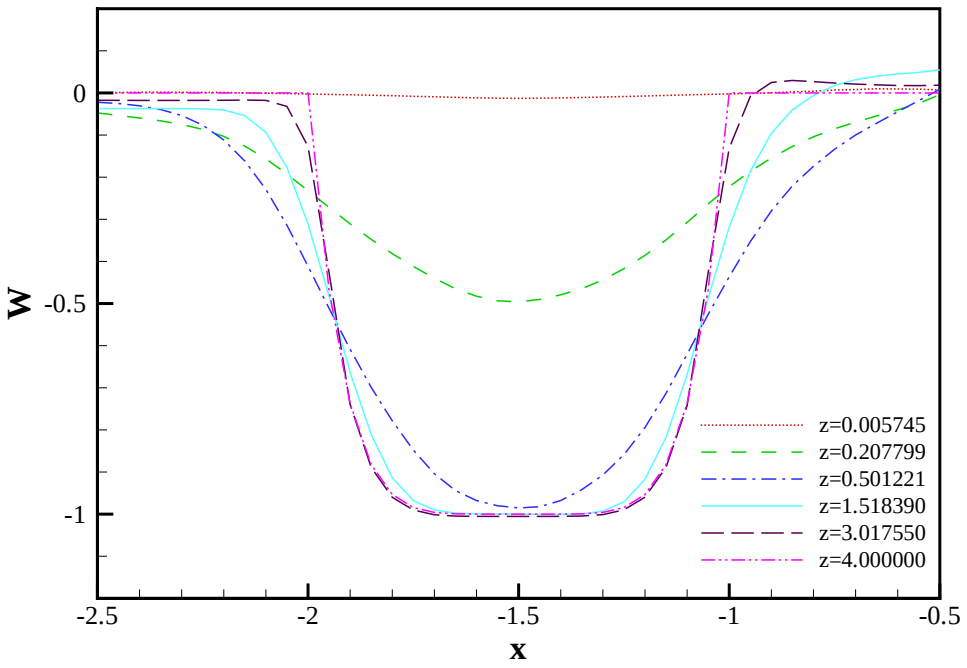

(a) Left jet

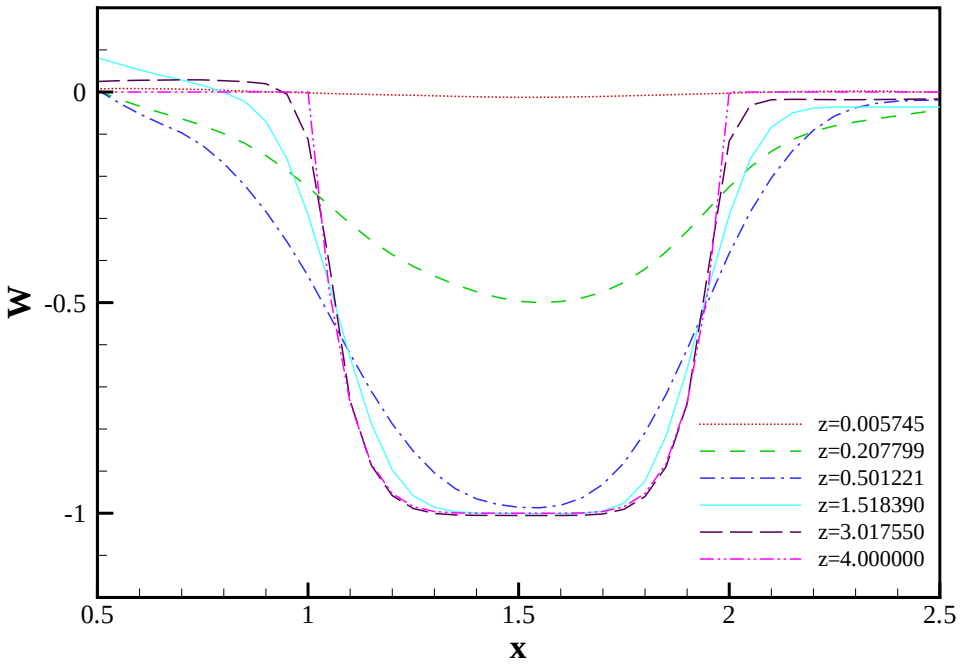

(b) Right jet

Figure 6.144: W-velocity profiles of the jets in the $y = 0$ plane.

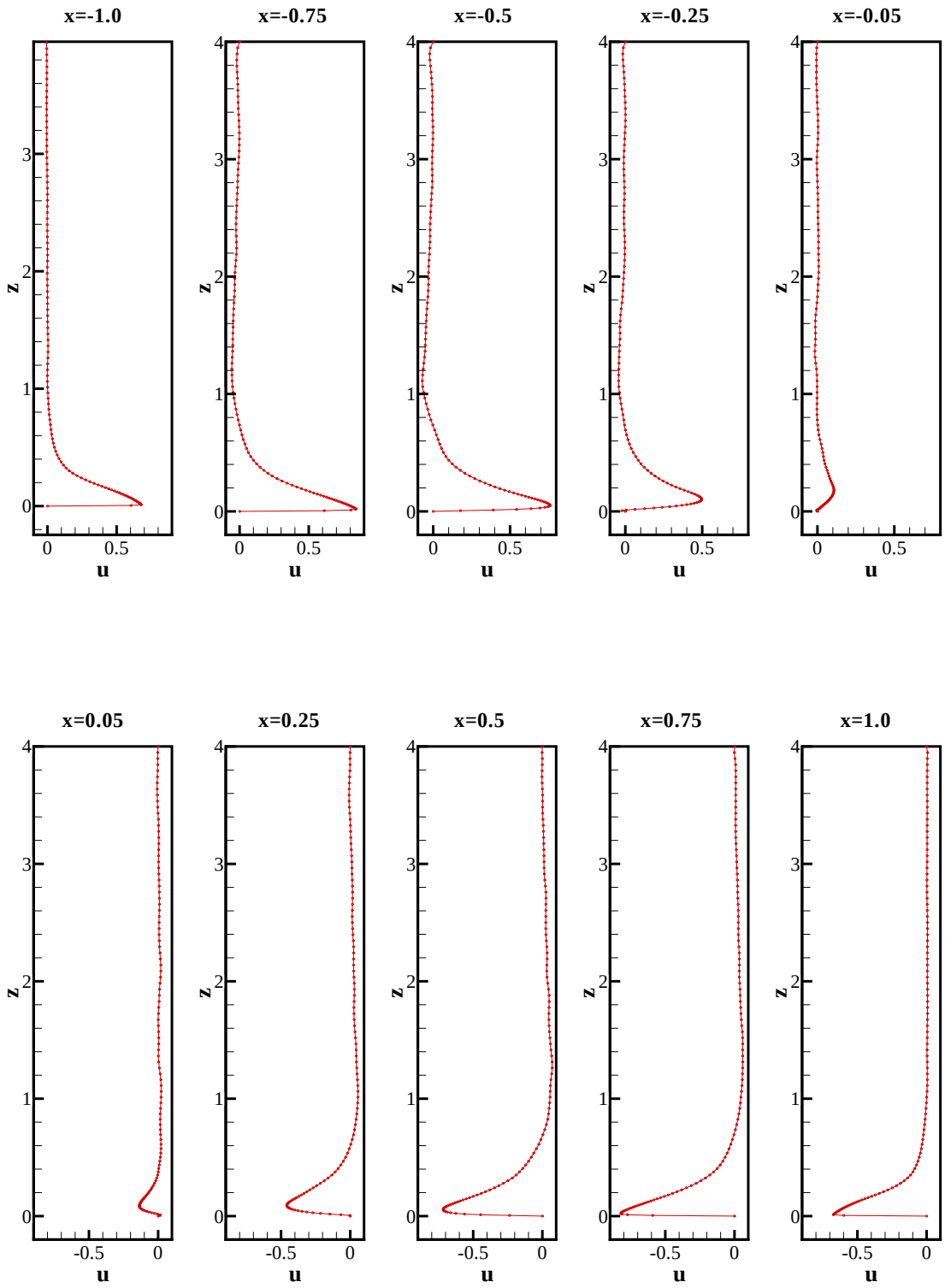

Figure 6.145: U-velocity profile as a function of z at various x-location between the jets in the $y = 0$ plane.

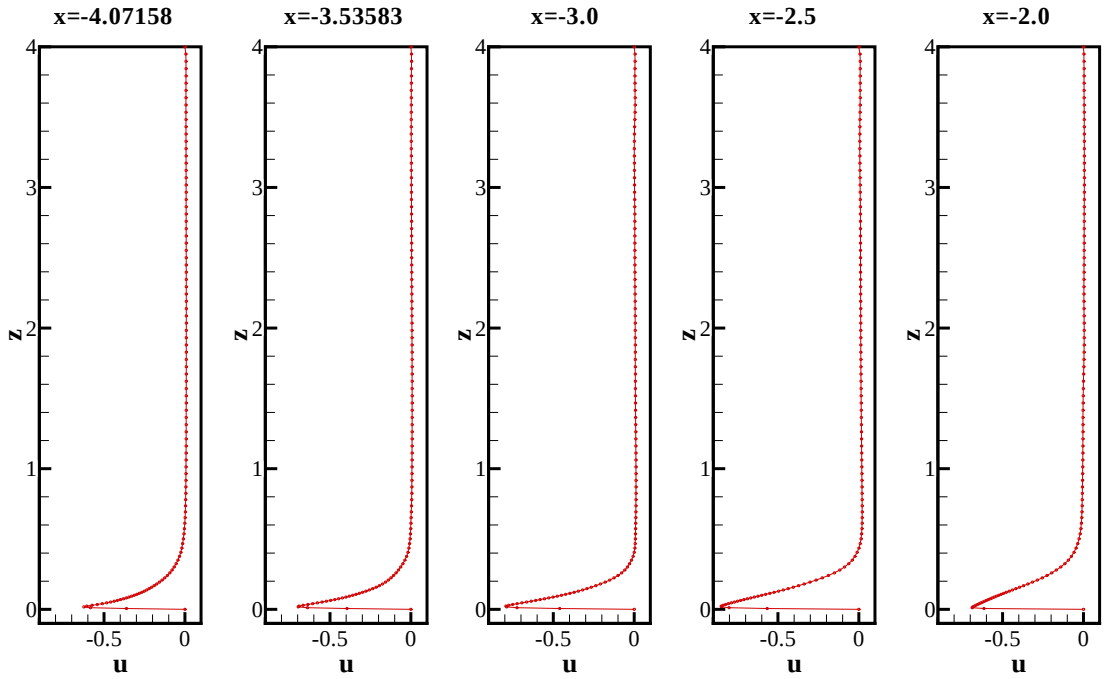

Figure 6.146: U-velocity profile as a function of z at various x-locations between the left boundary and the left jet in the $y = 0$ plane.

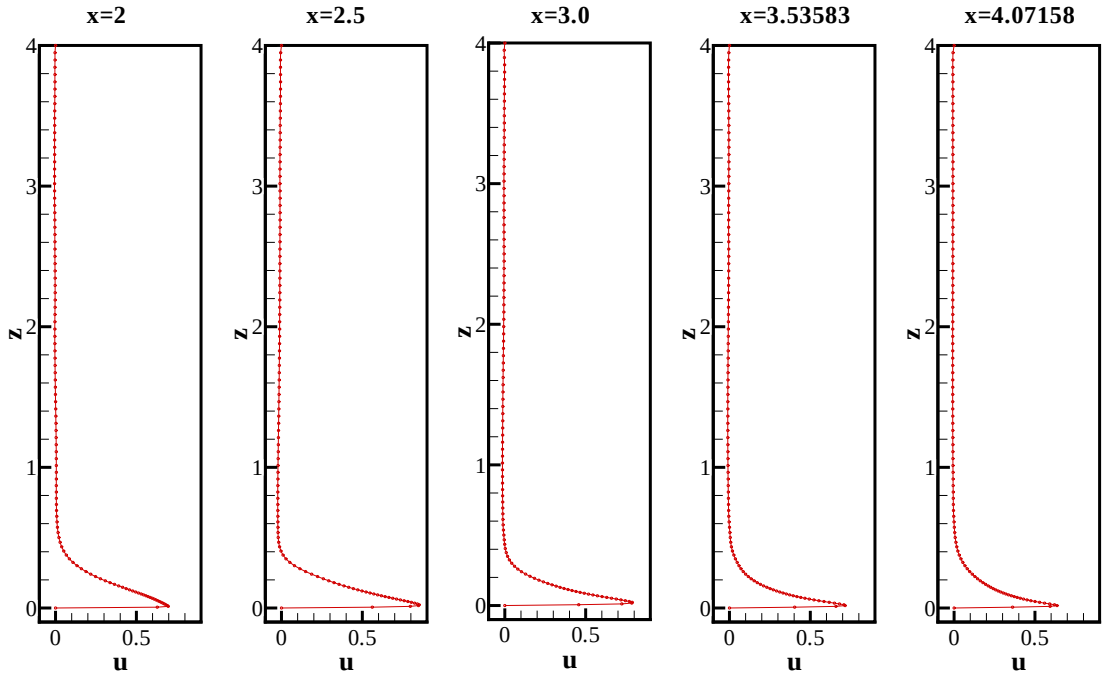

Figure 6.147: U-velocity profile as a function of z at various x-locations between the right jet and the right boundary in the $y = 0$ plane.

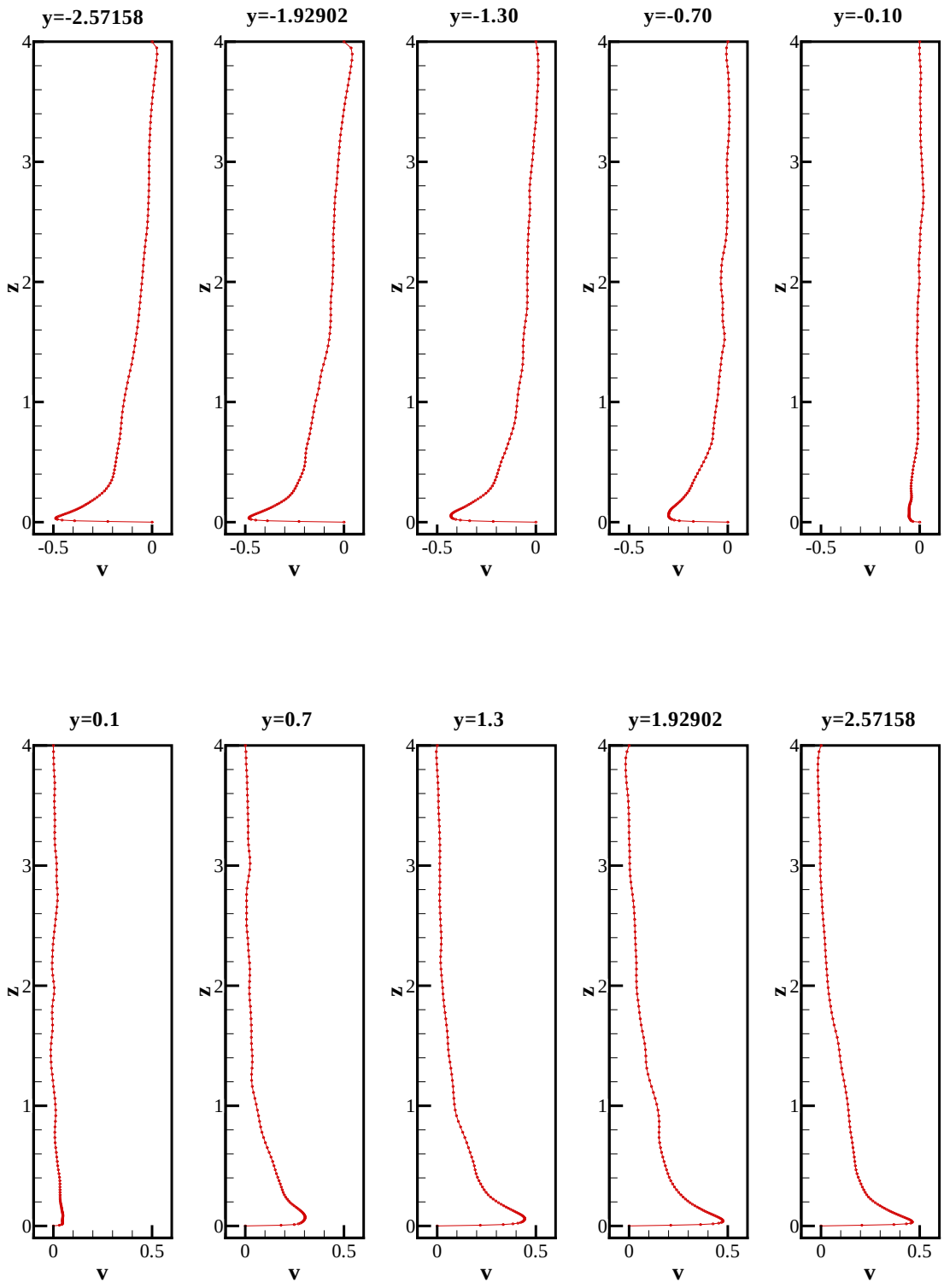

Figure 6.148: V-velocity profile as a function of z at various y-locations in the $x = 0$ plane

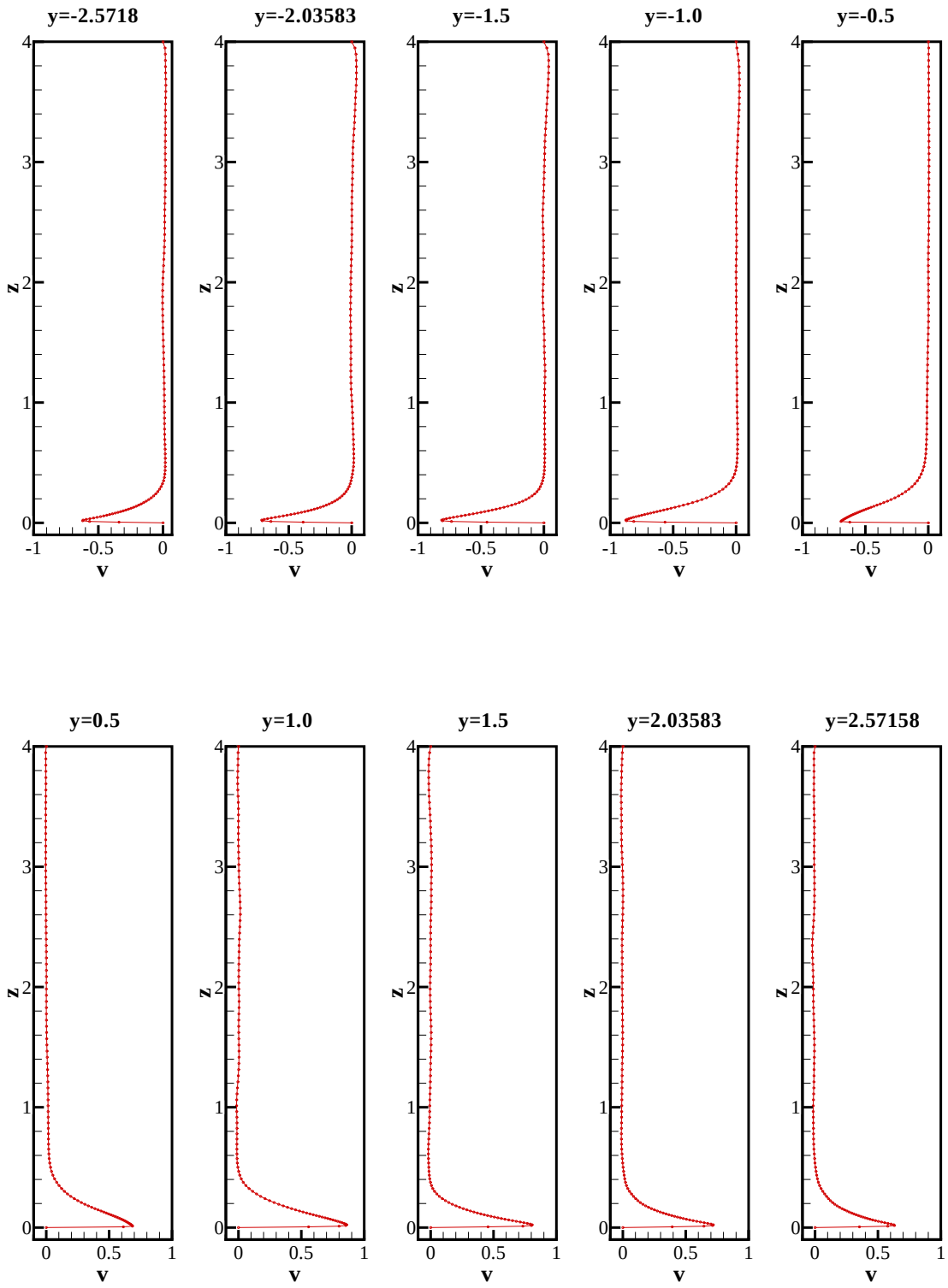

Figure 6.149: V-velocity profile as a function of z at various y-locations in the $x = -1.5$ plane (midplane of left jet)

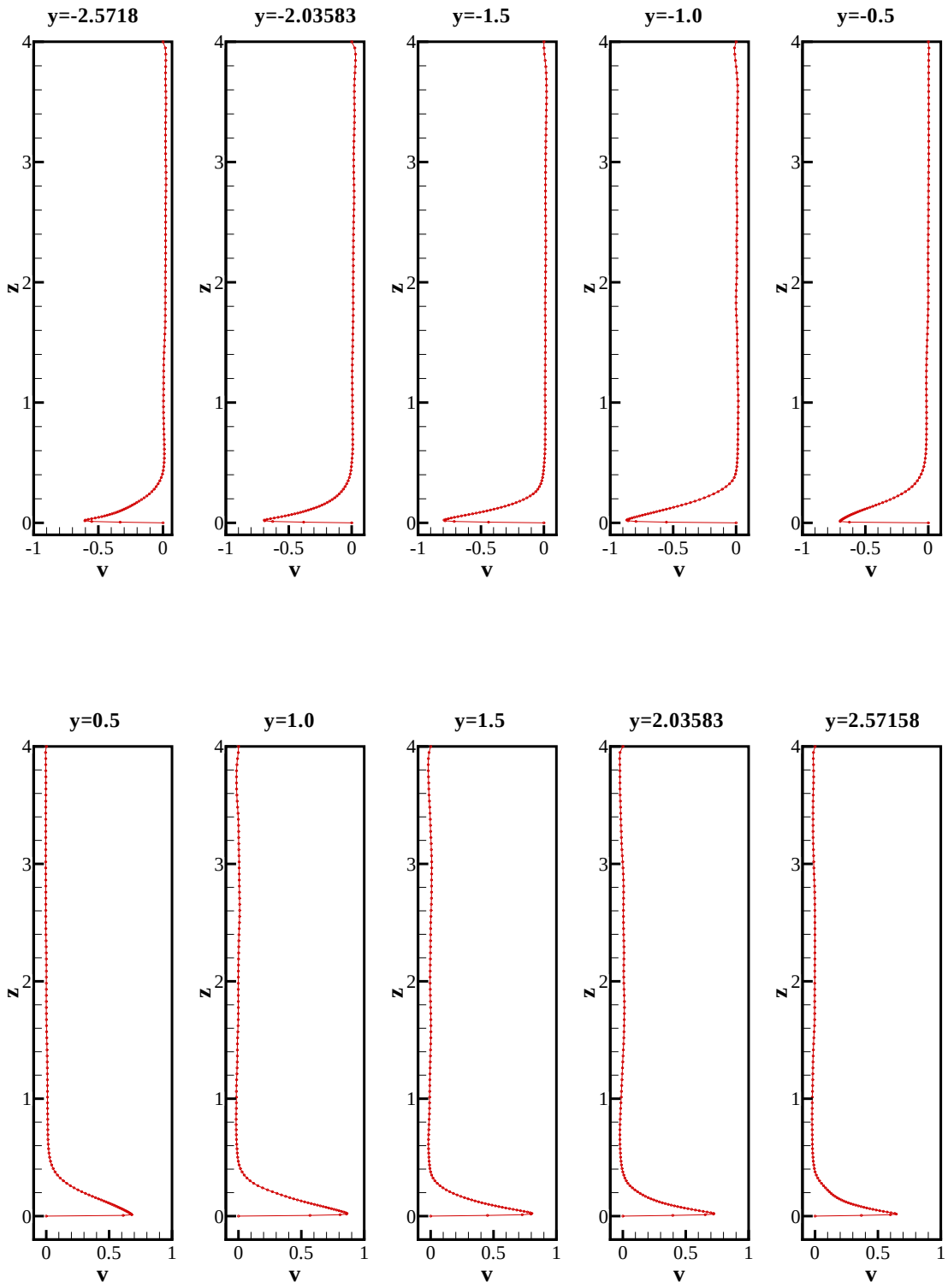

Figure 6.150: V-velocity profile as a function of z at various y-locations in the $x = 1.5$ plane (midplane of right jet)

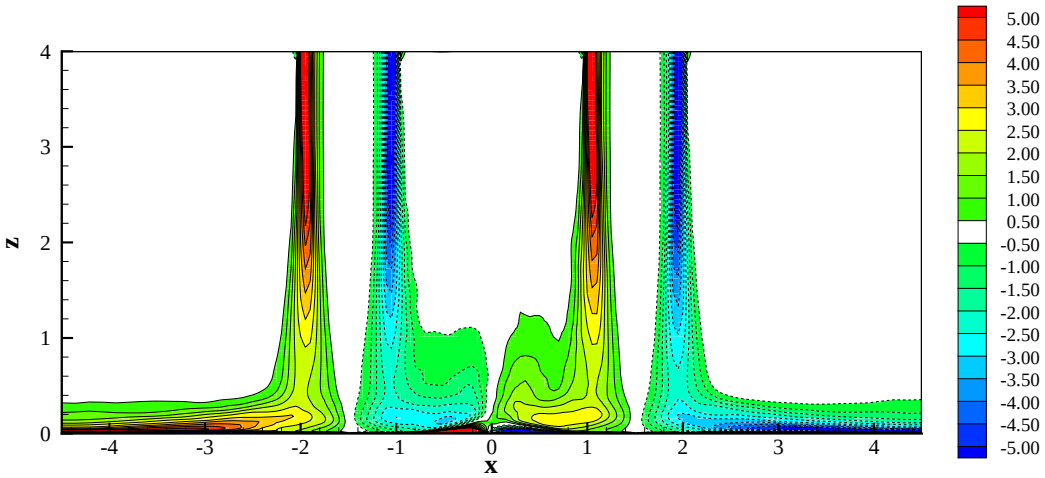

Figure 6.151: The mean y-vorticity contours, in the $y = 0$ plane

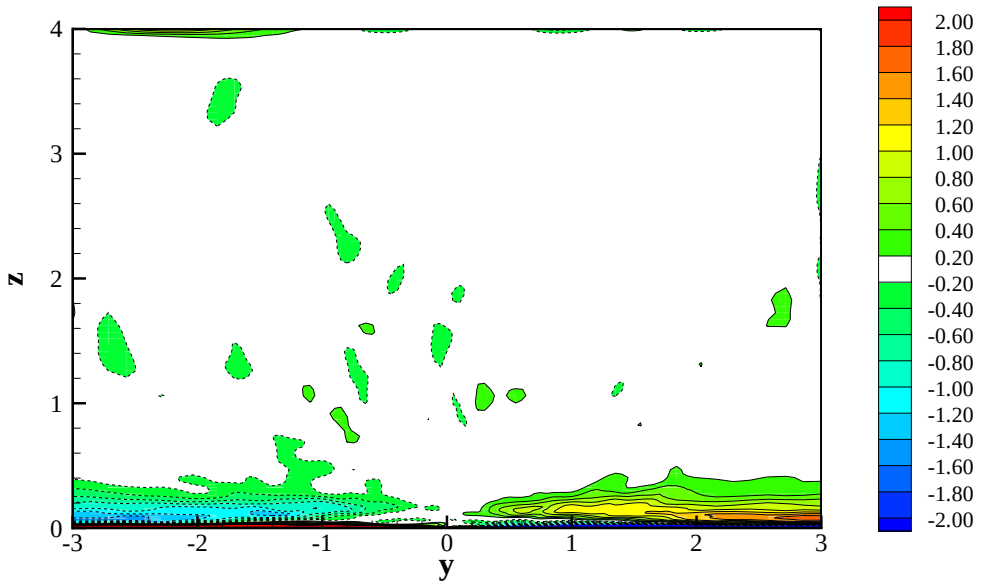

Figure 6.152: The mean x-vorticity contours in the $x = 0$ plane

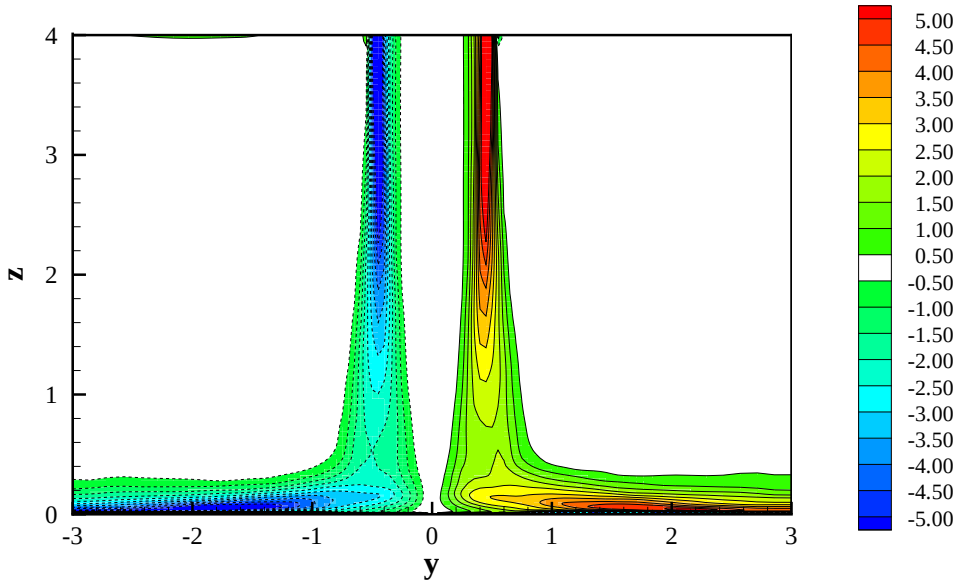

(a) left jet

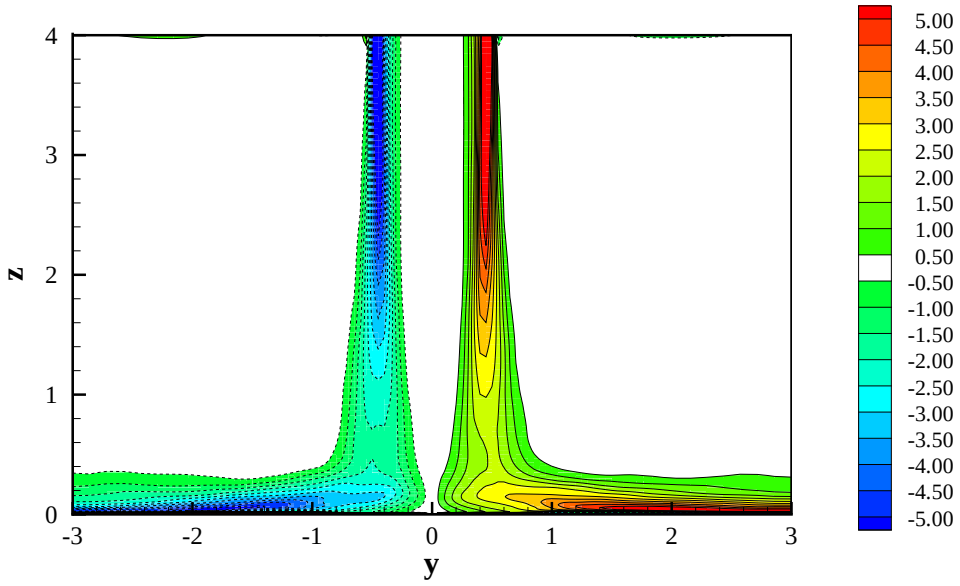

(b) right jet

Figure 6.153: The mean x-vorticity contours in the yz-plane at the center of the jets

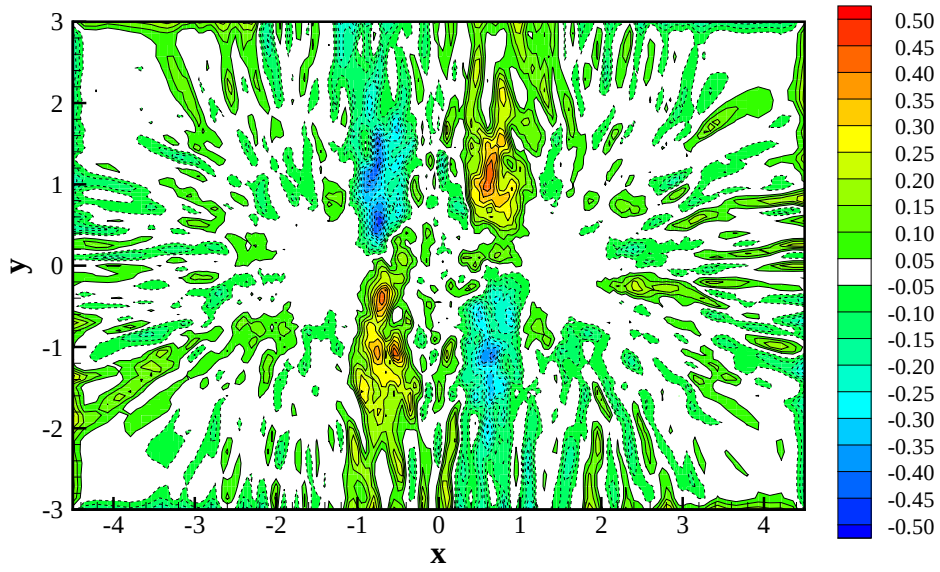

Figure 6.154: The mean z-vorticity contours in the $z = 0.005745$ plane

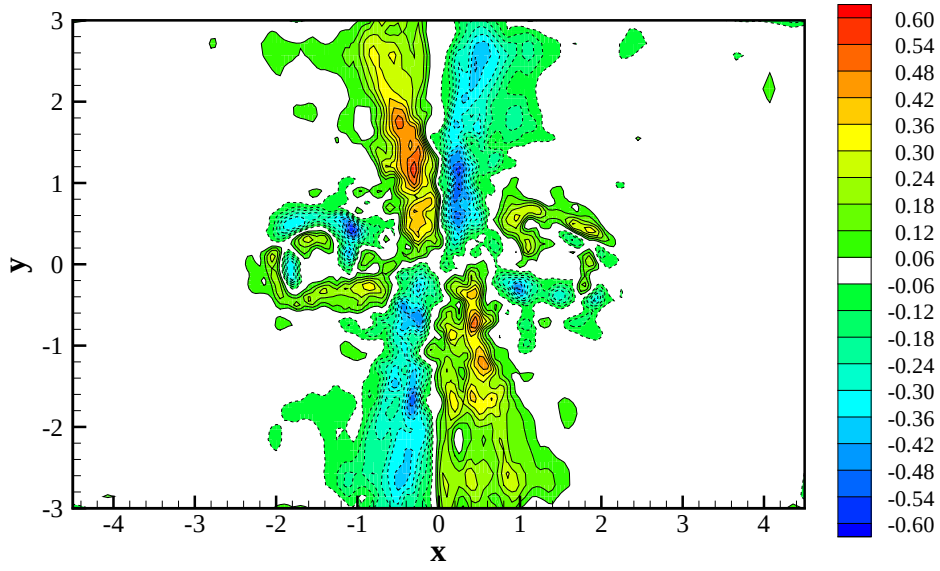

Figure 6.155: The mean z-vorticity contours in the $z = 0.5366$ plane

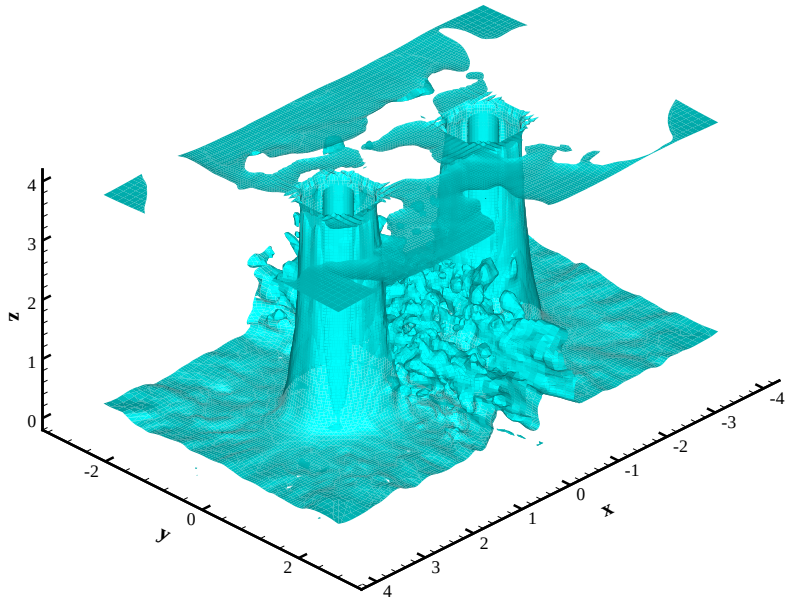

Figure 6.156: The mean vorticity magnitude contours at $|\bar{\omega}| = 0.2$

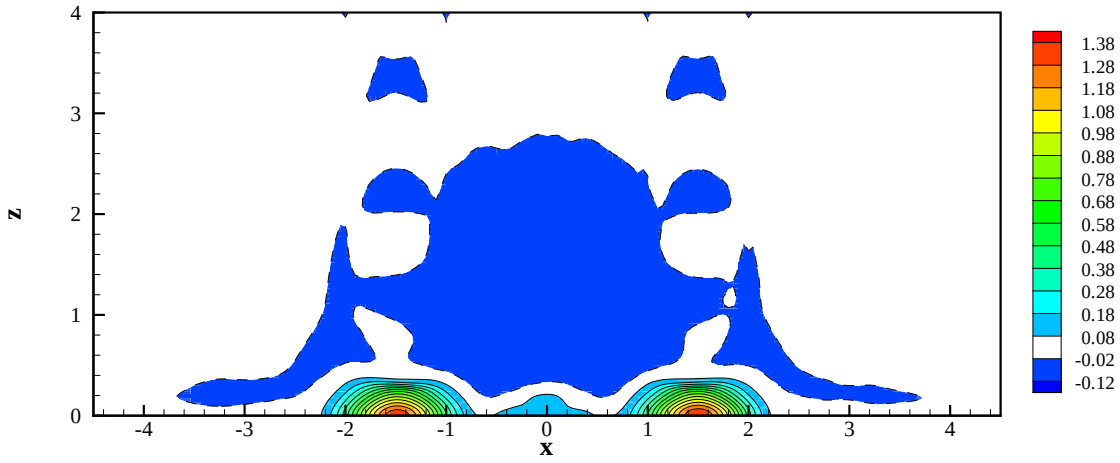

Figure 6.157: The mean pressure coefficient ($\bar{C}_p$) contours in the $y = 0$ plane

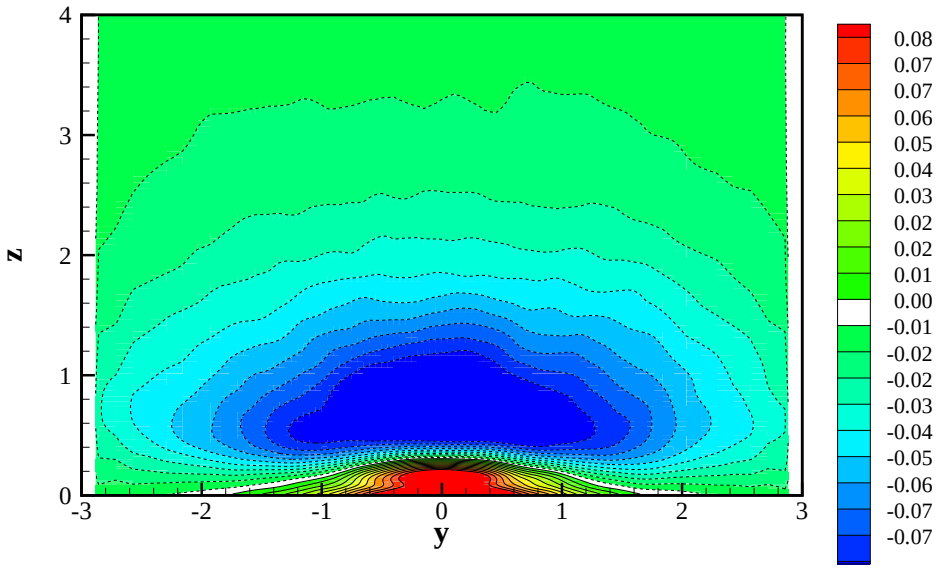

Figure 6.158: The mean pressure coefficient ($\bar{C}_p$) contours in the $x = 0$ plane

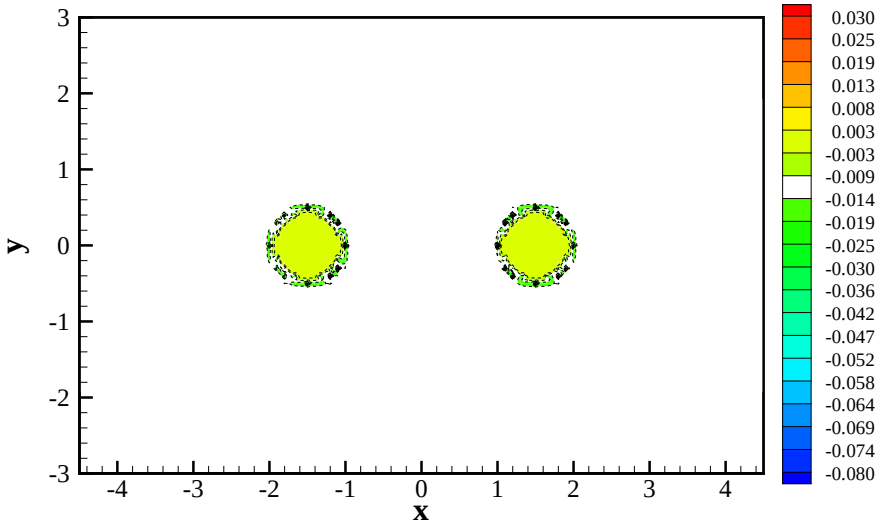

Figure 6.159: The pressure coefficient ($\bar{C}_p$) contours in the $z = 4.0$ plane

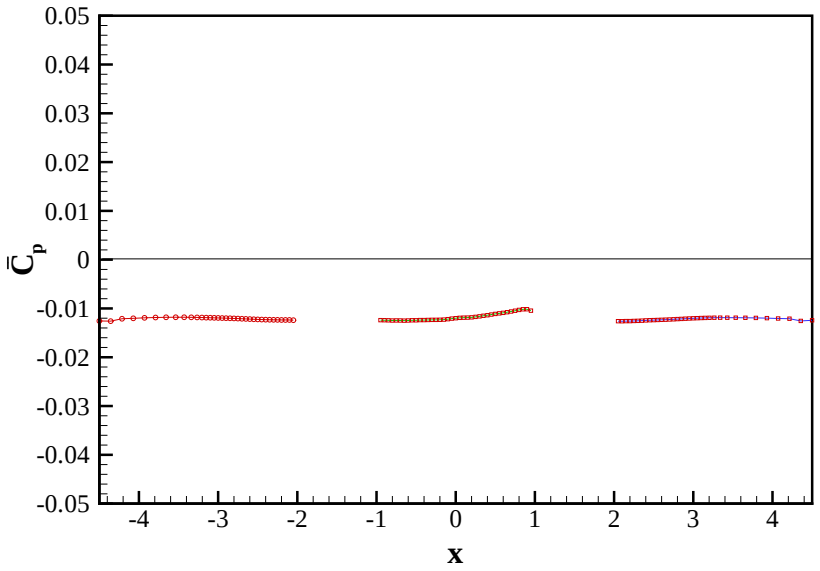

Figure 6.160: Variation of mean pressure coefficient ($\bar{C}_p$) as a function of x at $z = 4.0$ in the $y = 0$ plane.

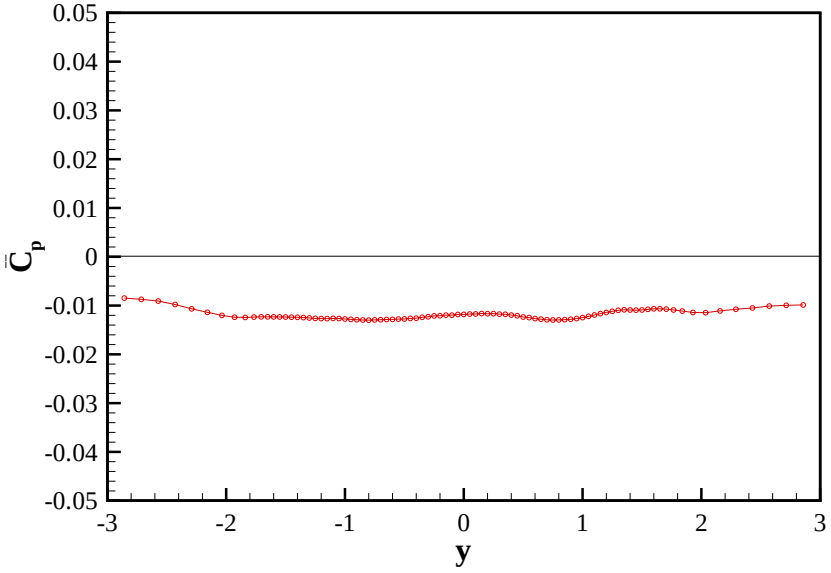

Figure 6.161: Variation of mean pressure coefficient as a function of y at $z = 4.0$ in the $x = 0$ plane.

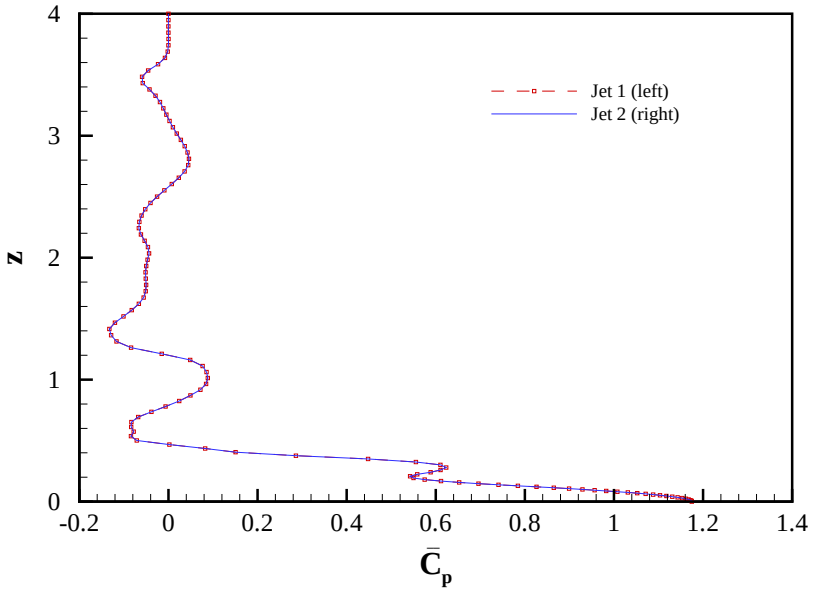

Figure 6.162: Variation of mean pressure coefficient ($\bar{C}_p$) as a function of z along the jet centerlines.

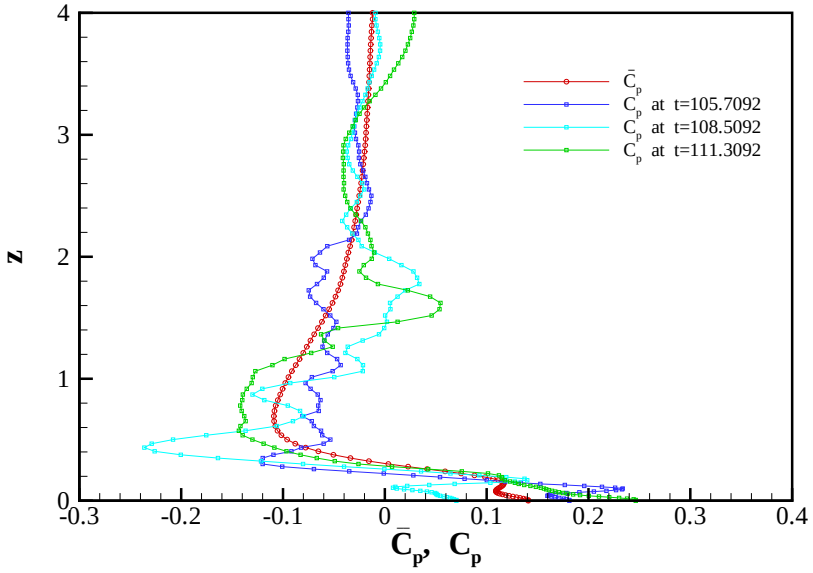

Figure 6.163: Variation of mean pressure coefficient ($\bar{C}_p$) as a function of z in the $y = 0$ plane at $x = 0$.

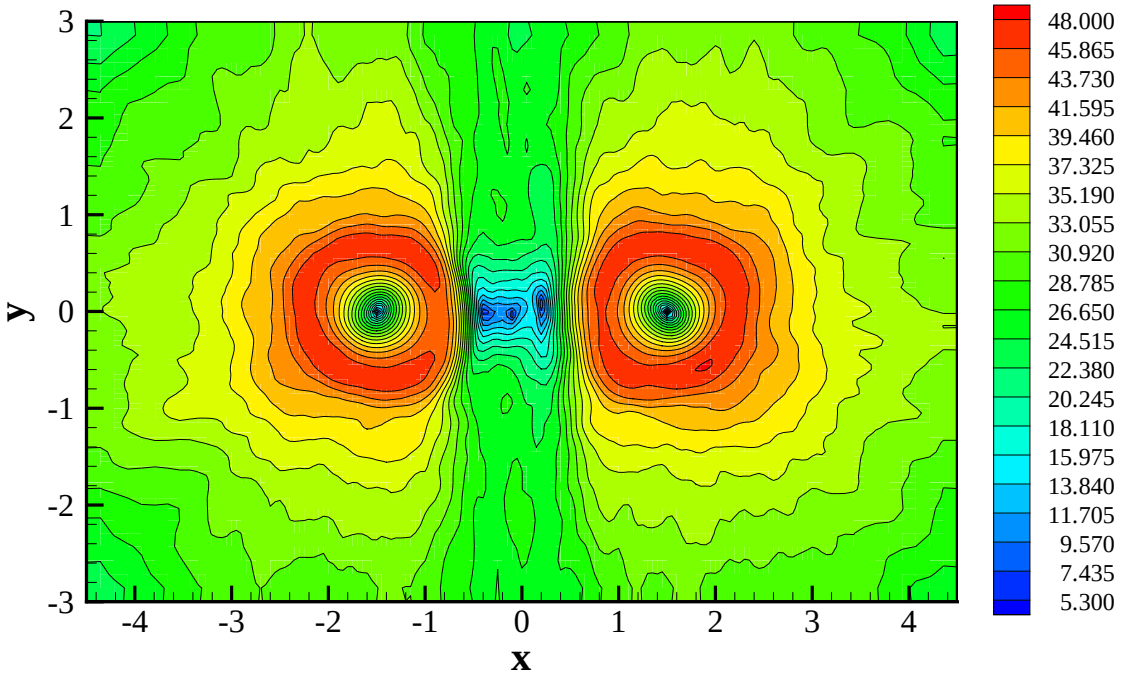

Figure 6.164: Distribution of mean z^+ at $z = 0.00574535$ plane (contour interval=2.5)

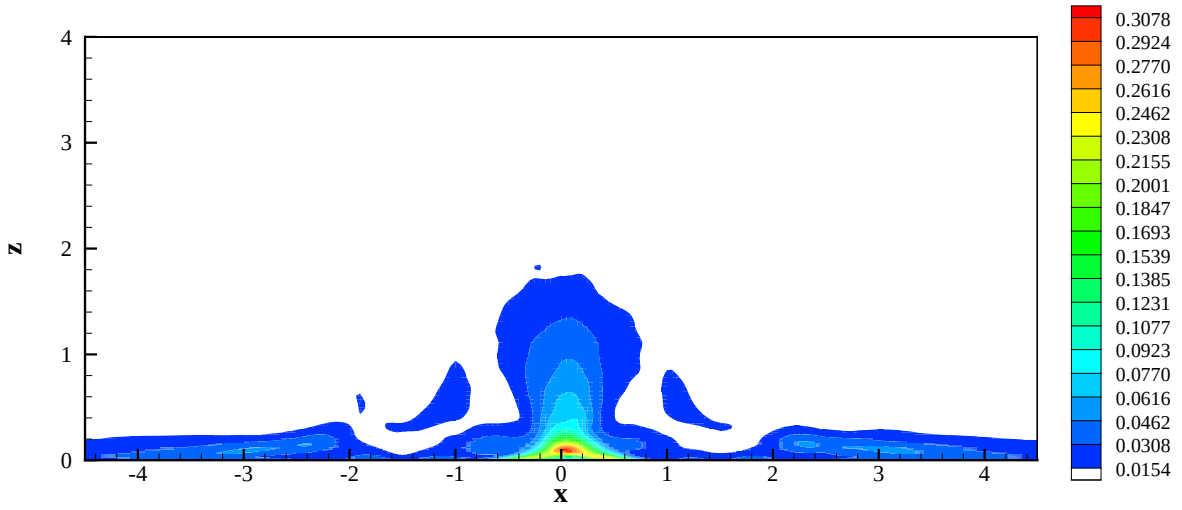

Figure 6.165: Contours of $\overline{u'u'}$ in the $y = 0$ plane.

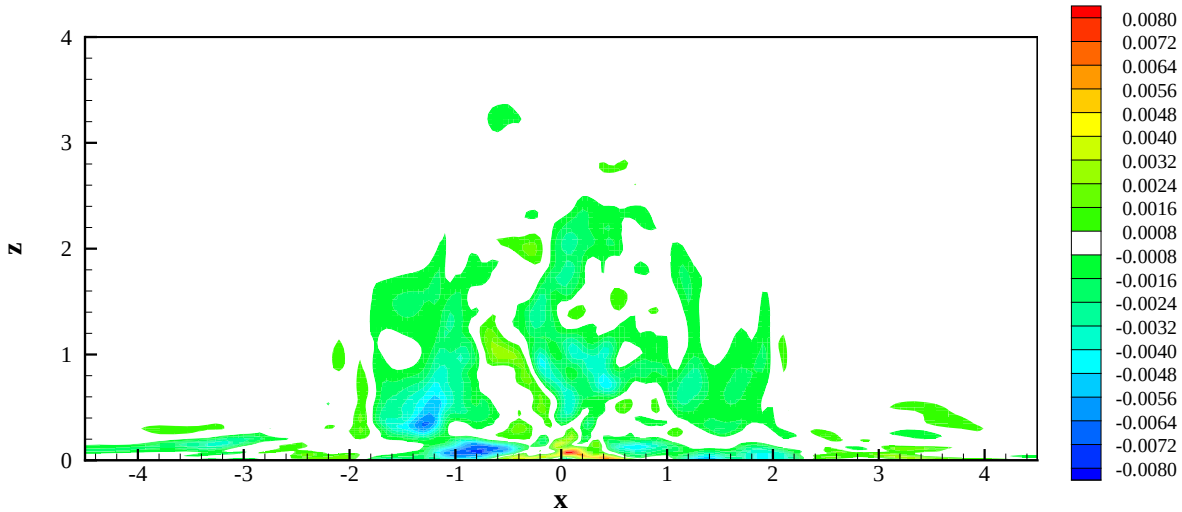

Figure 6.166: Contours of $\overline{u'v'}$ in the $y = 0$ plane.

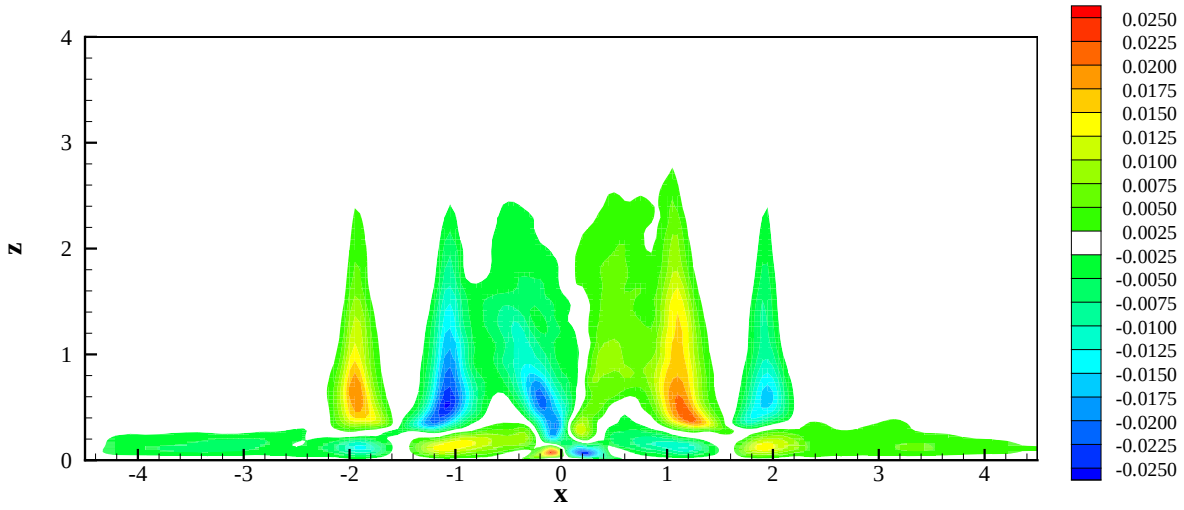

Figure 6.167: Contours of $\overline{u'w'}$ in the $y = 0$ plane.

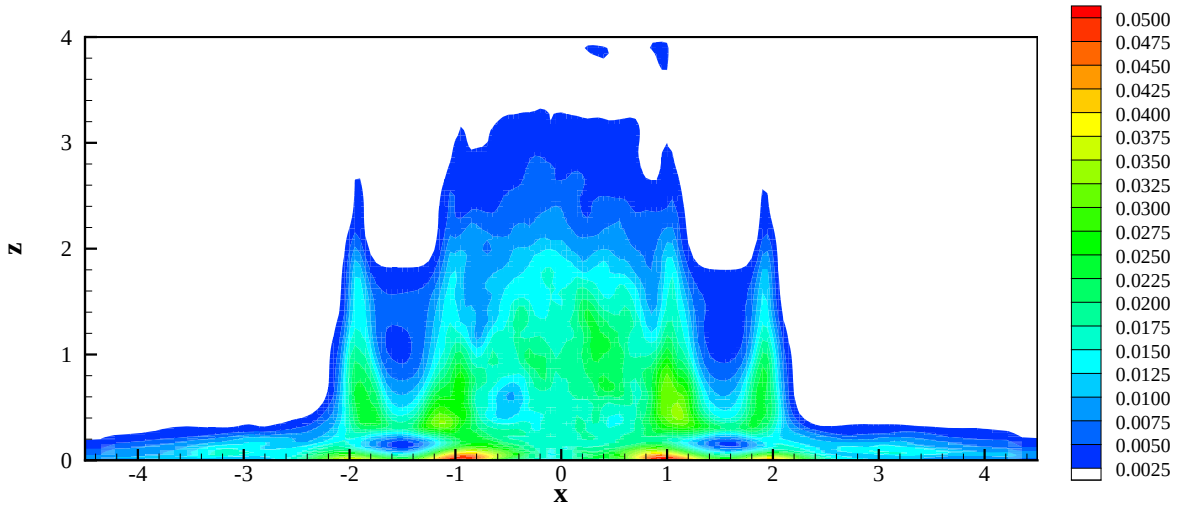

Figure 6.168: Contours of $\overline{v'v'}$ in the $y = 0$ plane.

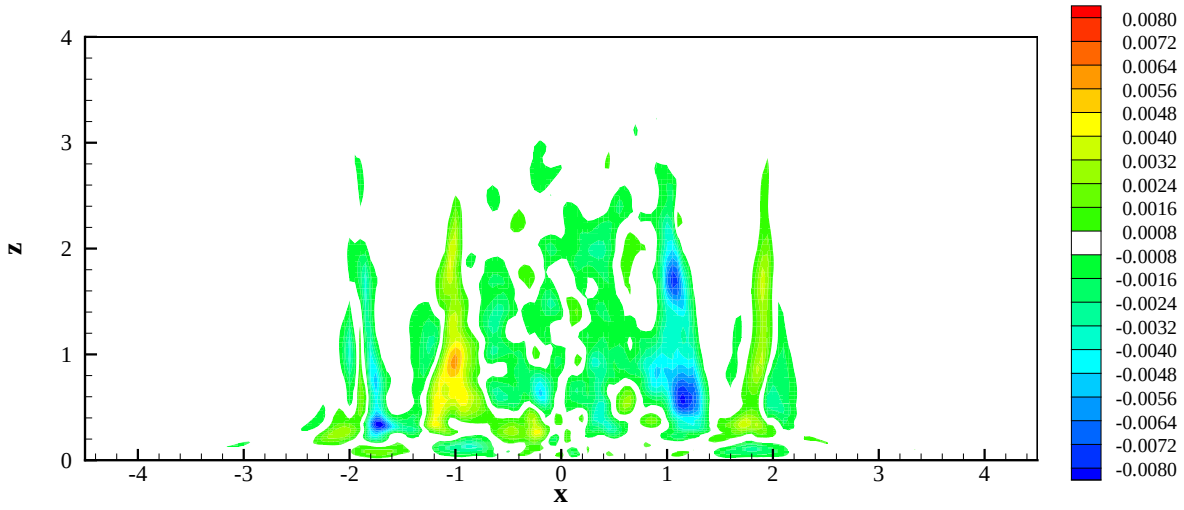

Figure 6.169: Contours of $\overline{v'w'}$ in the $y = 0$ plane.

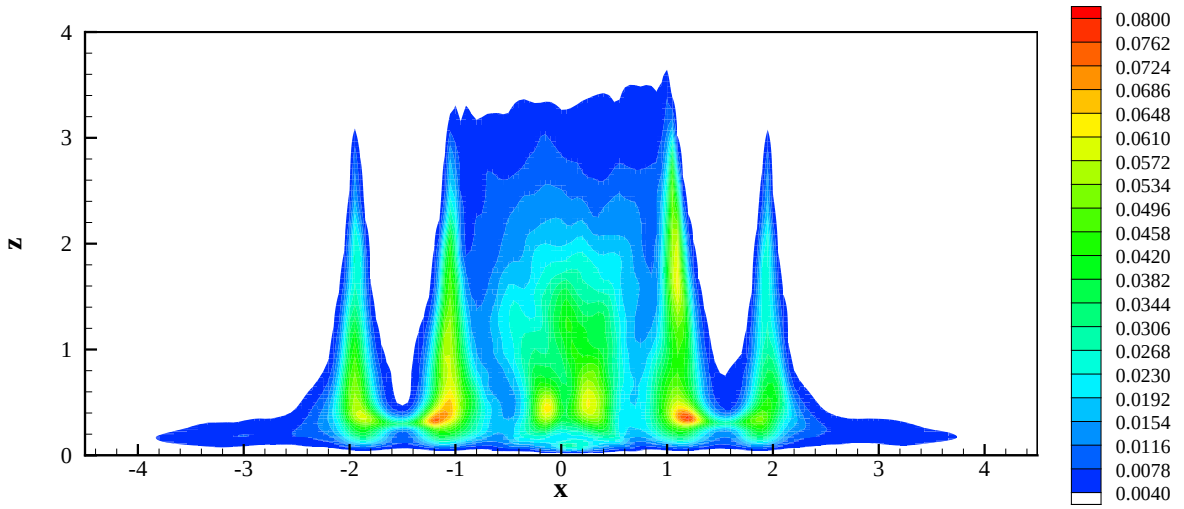

Figure 6.170: Contours of $\overline{w'w'}$ in the $y = 0$ plane.

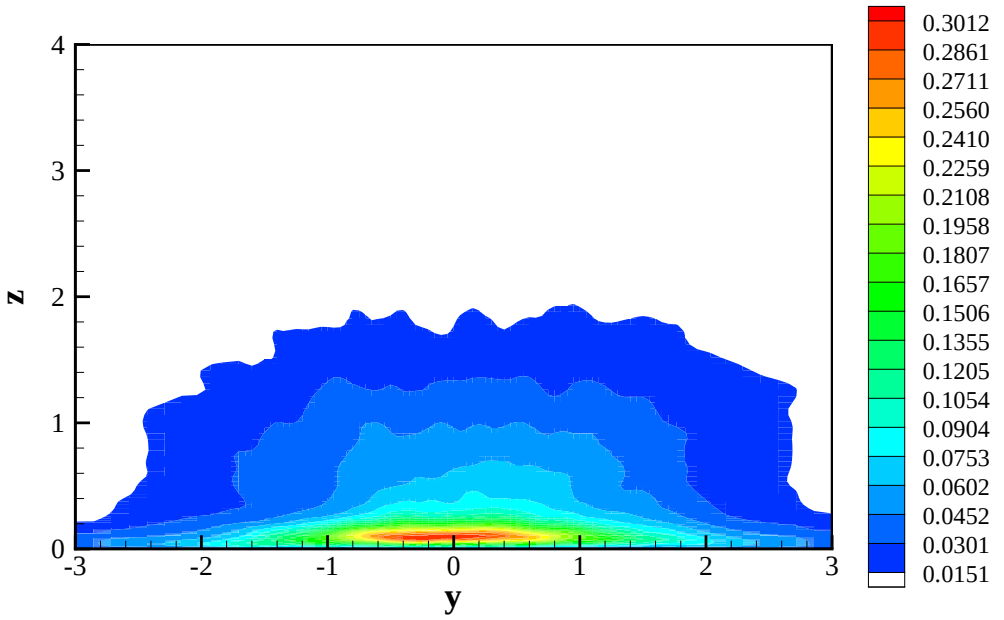

Figure 6.171: Contours of $\overline{u'u'}$ in the $x = 0$ plane.

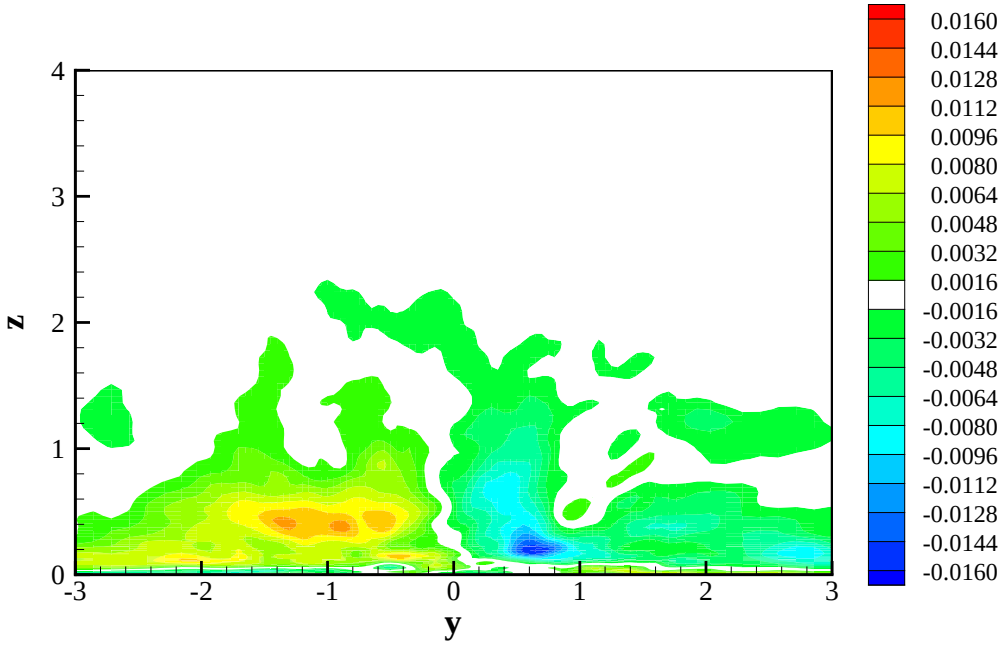

Figure 6.172: Contours of $\overline{u'v'}$ in the $x = 0$ plane.

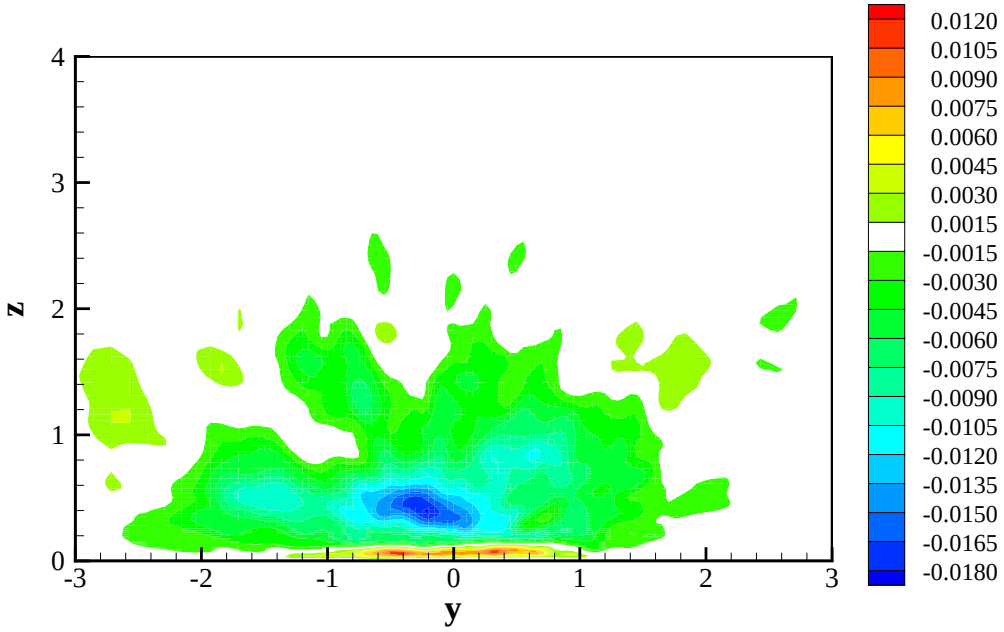

Figure 6.173: Contours of $\overline{u'w'}$ in the $x = 0$ plane.

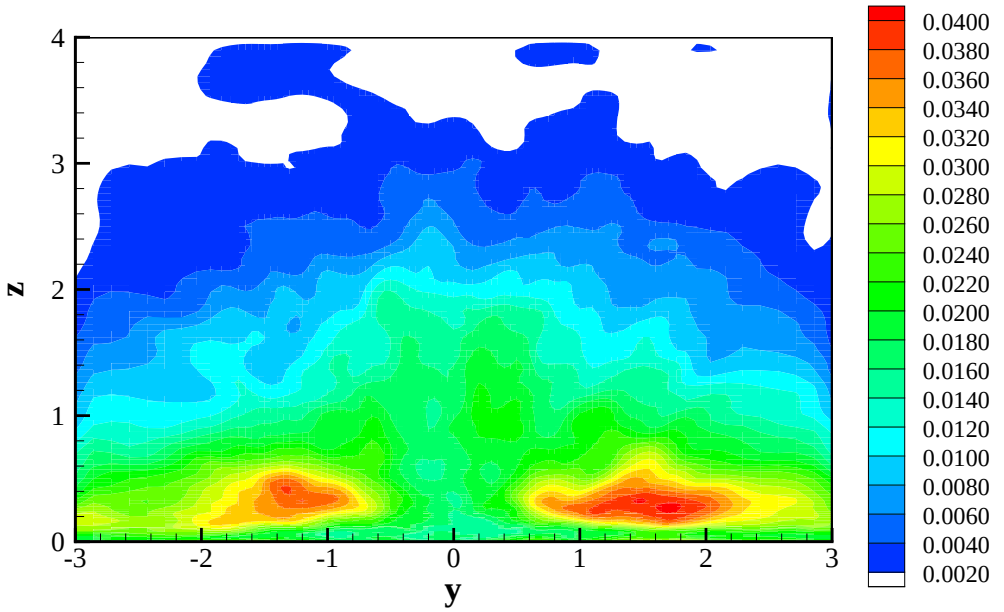

Figure 6.174: Contours of $\overline{v'v'}$ in the $x = 0$ plane.

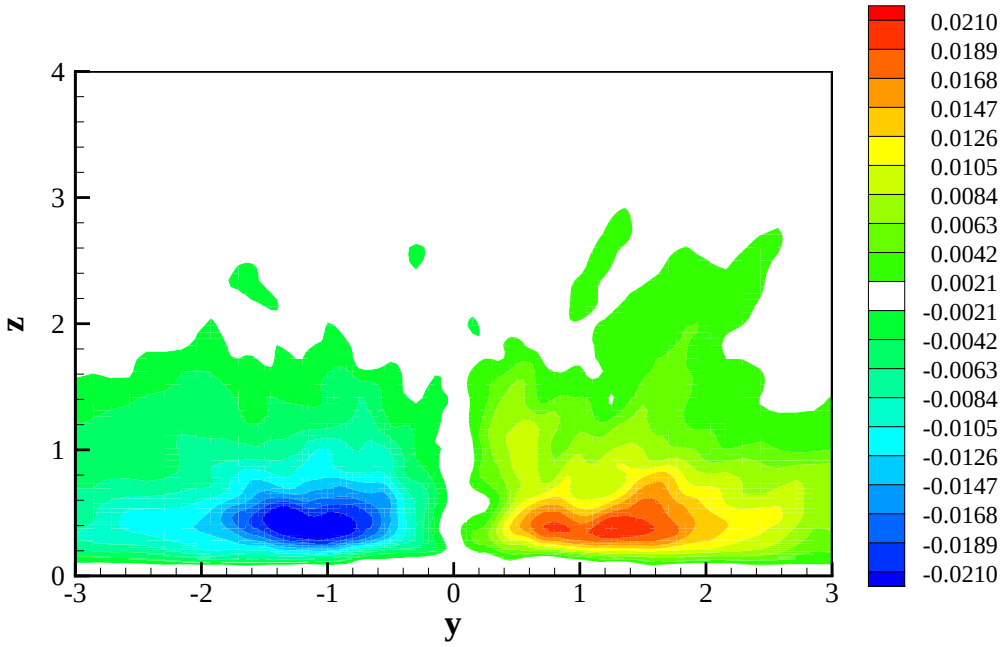

Figure 6.175: Contours of $\overline{v'w'}$ in the $x = 0$ plane.

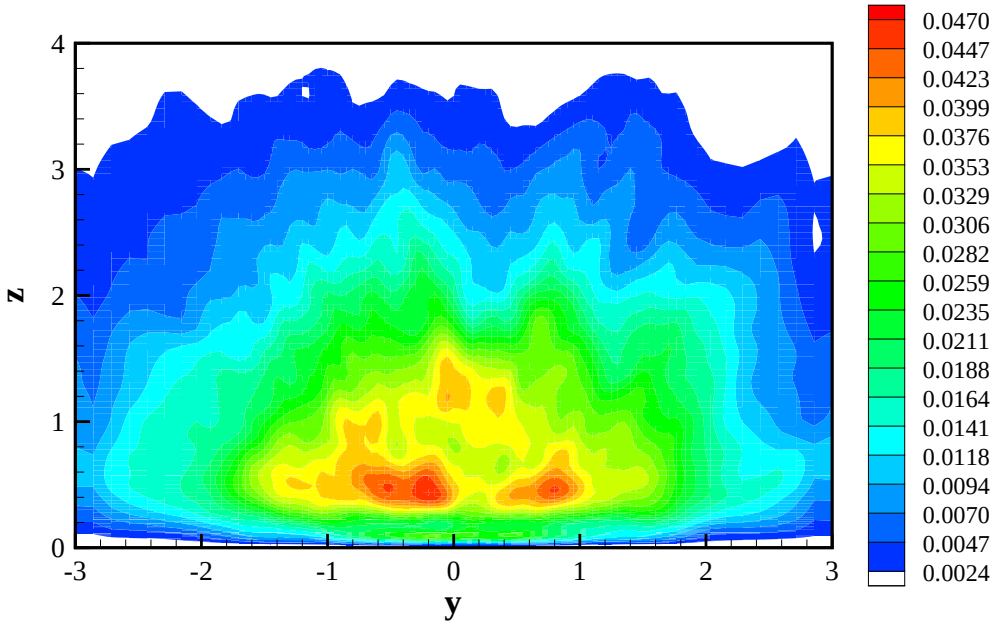

Figure 6.176: Contours of $\overline{w'w'}$ in the $x = 0$ plane.

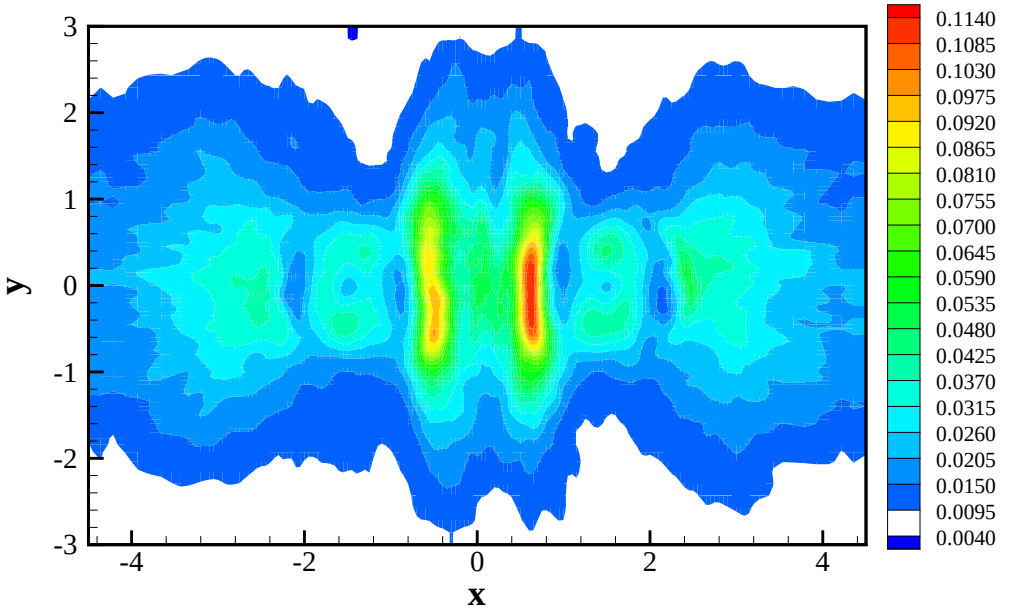

Figure 6.177: Contours of $\overline{u'u'}$ in the $z = 0.005745$ plane.

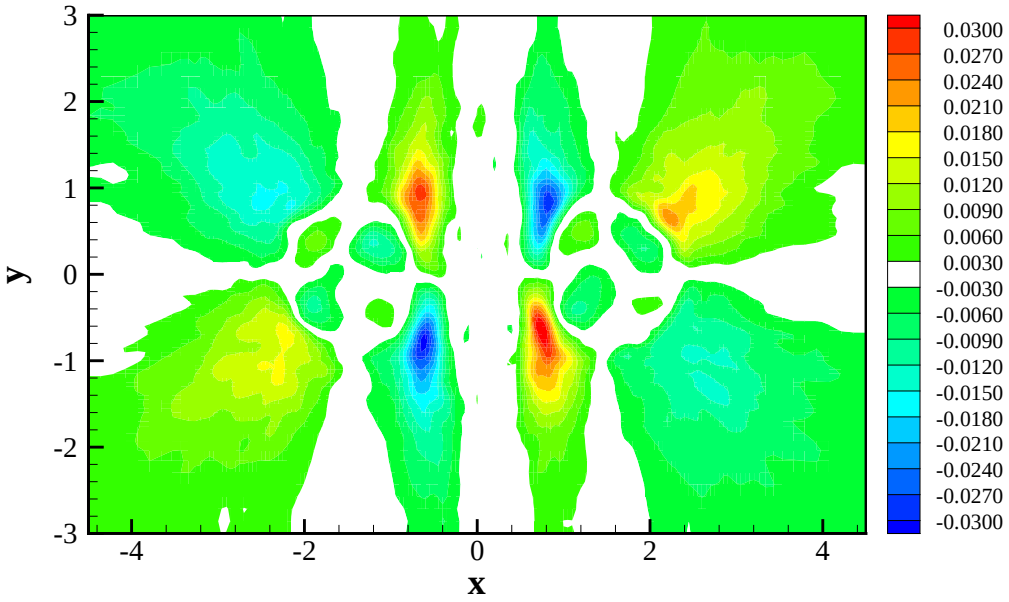

Figure 6.178: Contours of $\overline{u'v'}$ in the $z = 0.005745$ plane.

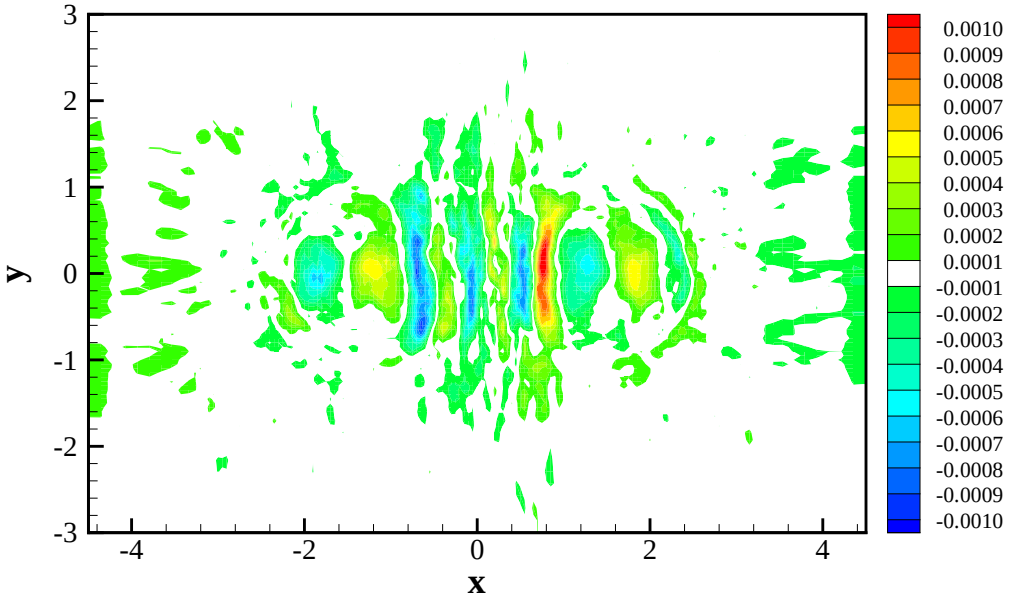

Figure 6.179: Contours of $\overline{u'w'}$ in the $z = 0.005745$ plane.

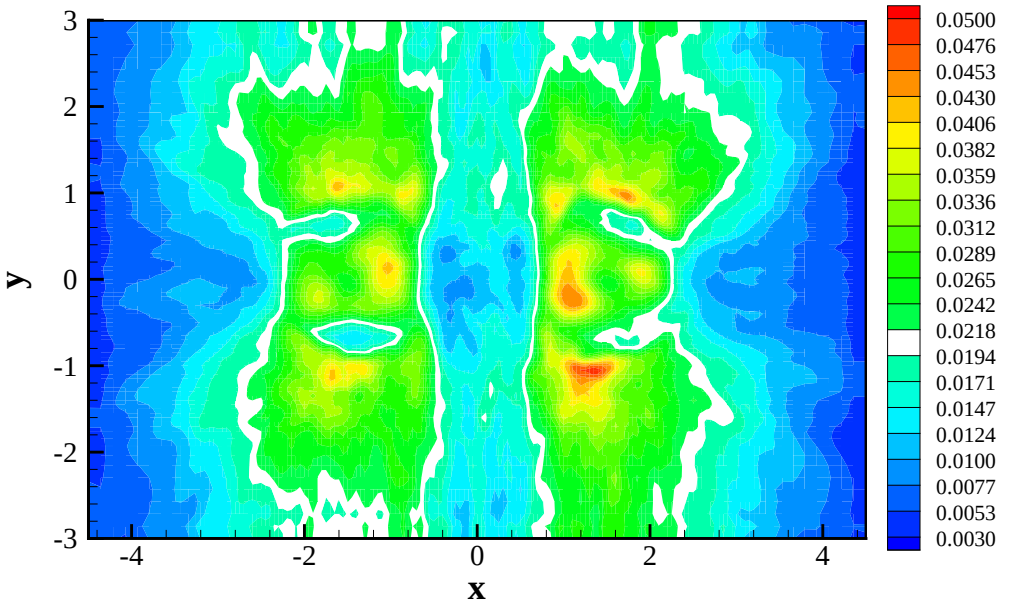

Figure 6.180: Contours of $\overline{v'v'}$ in the $z = 0.005745$ plane.

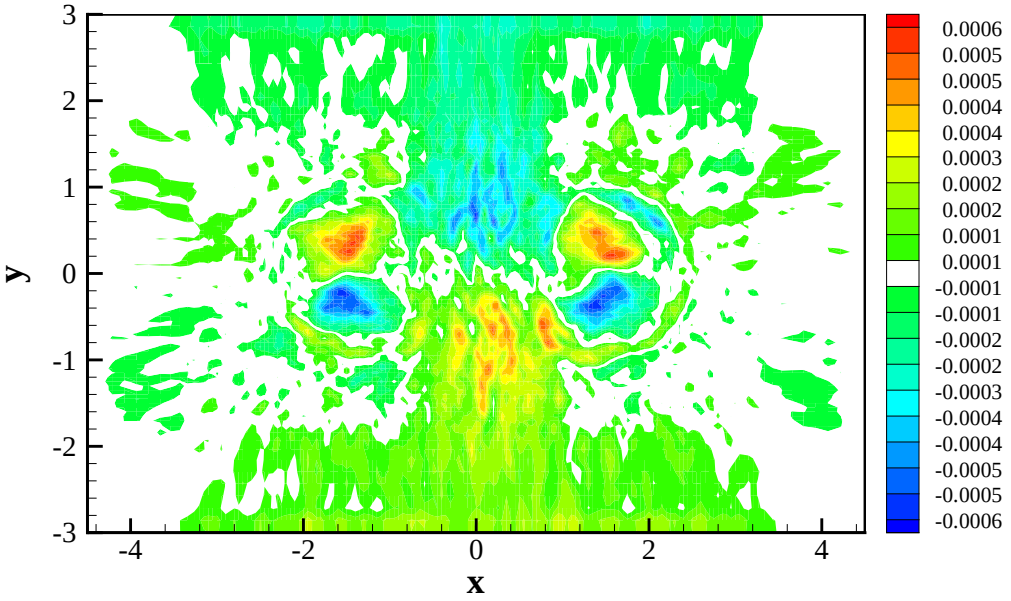

Figure 6.181: Contours of $\overline{v'w'}$ in the $z = 0.005745$ plane.

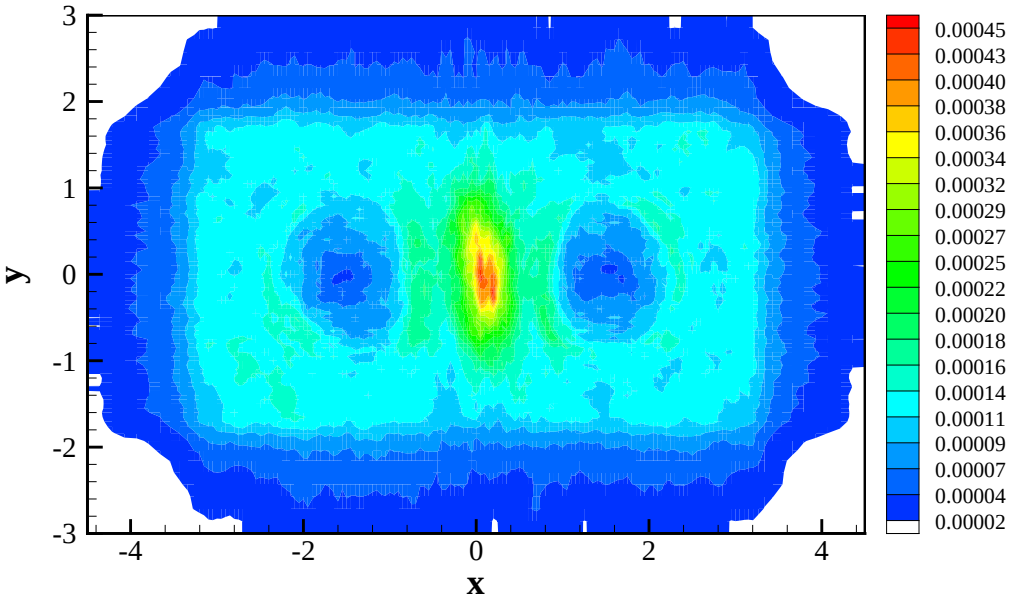

Figure 6.182: Contours of $\overline{w'w'}$ in the $z = 0.005745$ plane.

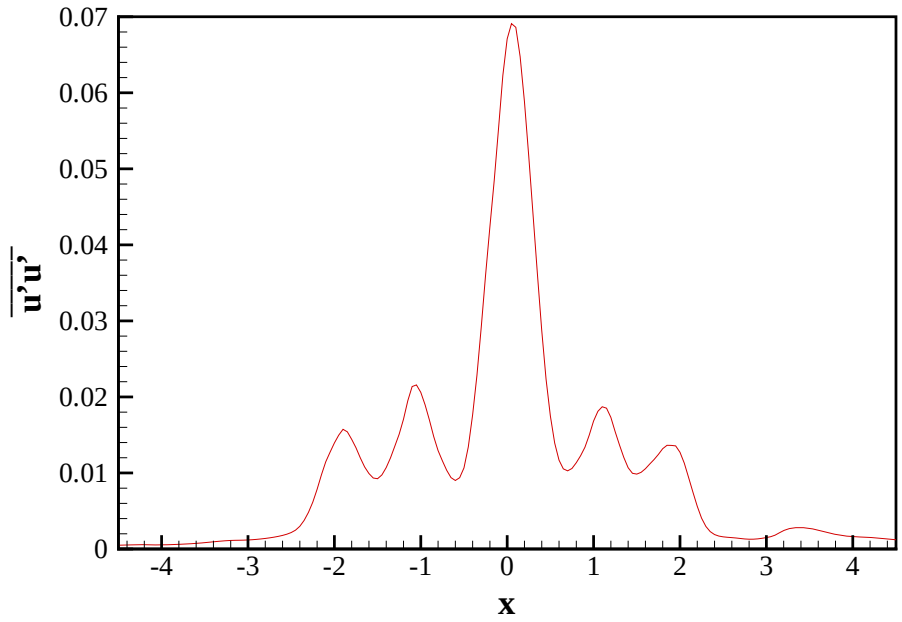

Figure 6.183: Variation of $\overline{u'u'}$ as a function of x at $z = 0.536607$ in the $y = 0$ plane.

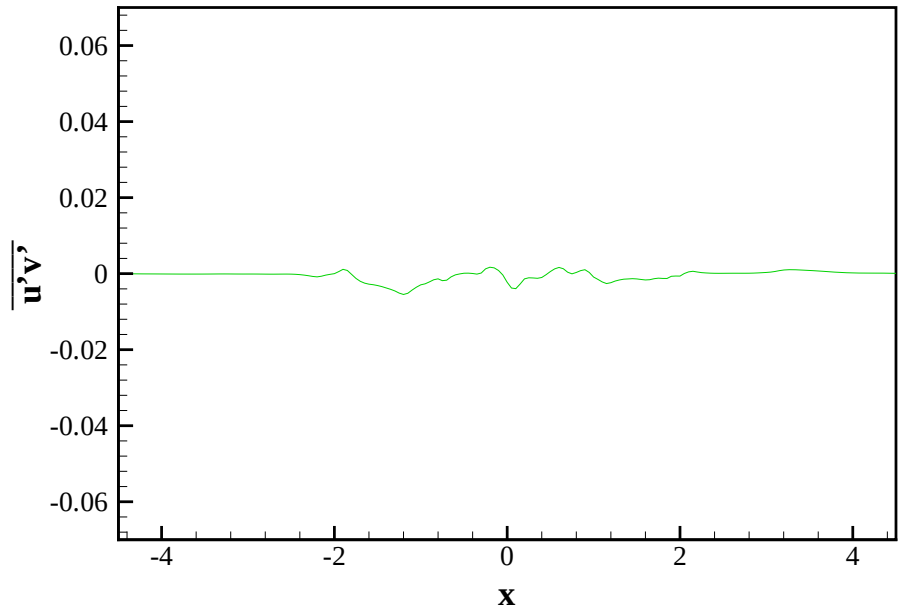

Figure 6.184: Variation of $\overline{u'v'}$ as a function of x at $z = 0.536607$ in the $y = 0$ plane.

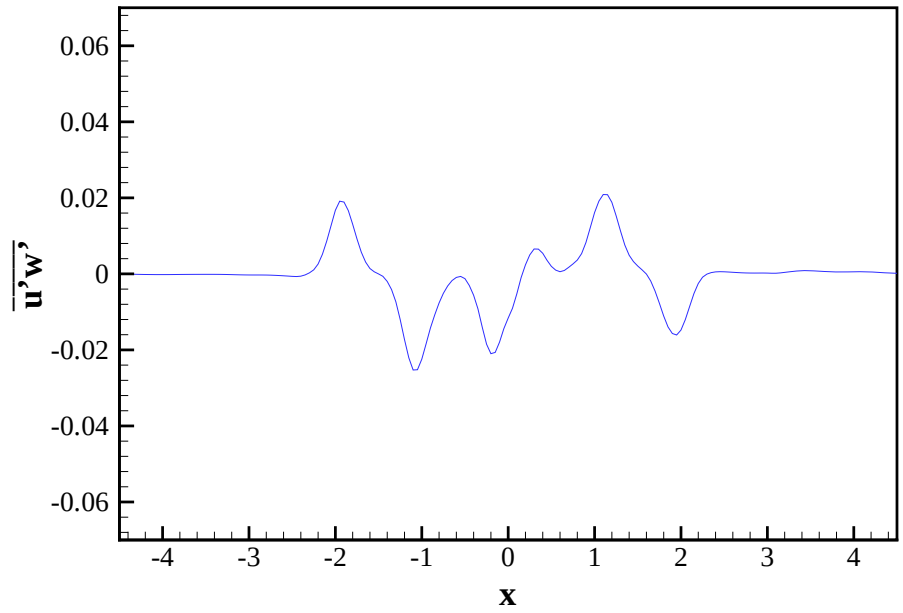

Figure 6.185: Variation of $\overline{u'w'}$ as a function of x at $z = 0.536607$ in the $y = 0$ plane.

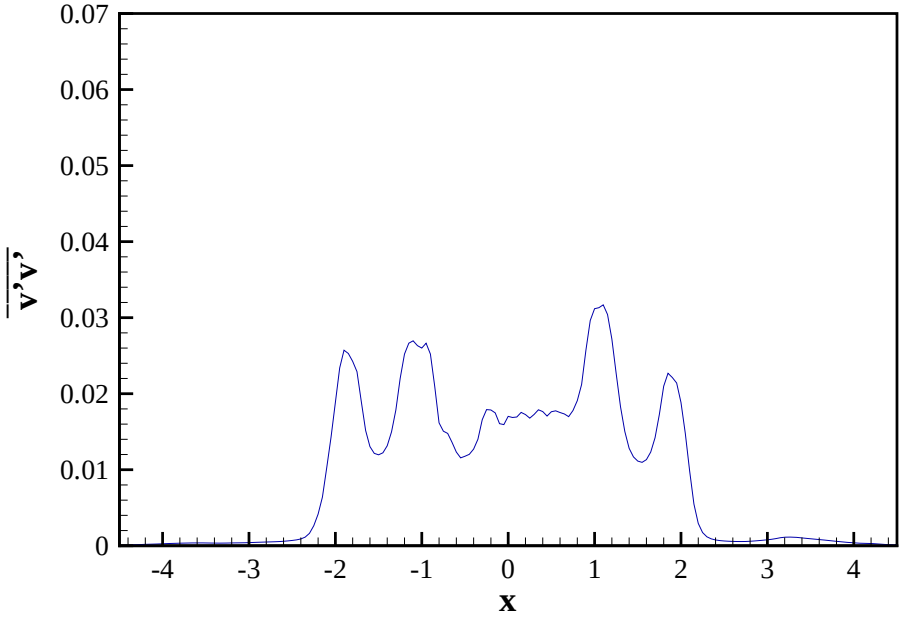

Figure 6.186: Variation of $\overline{v'v'}$ as a function of x at $z = 0.536607$ in the $y = 0$ plane.

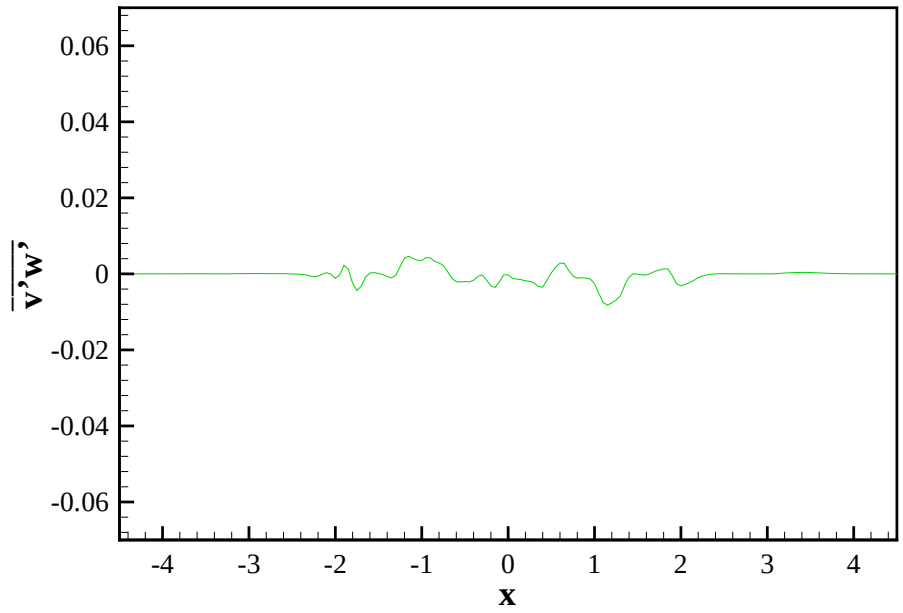

Figure 6.187: Variation of $\overline{v'w'}$ as a function of x at $z = 0.536607$ in the $y = 0$ plane.

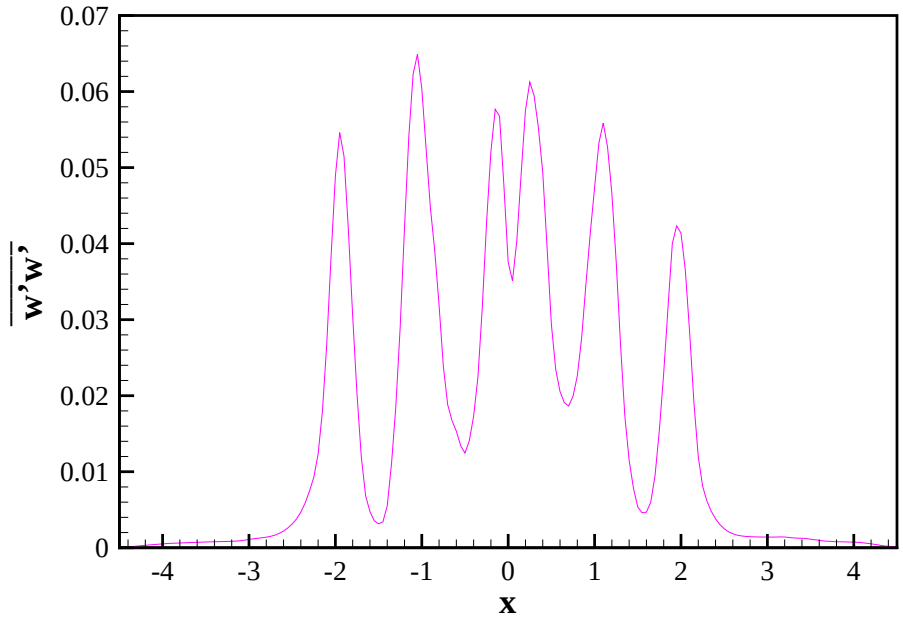

Figure 6.188: Variation of $\overline{w'w'}$ as a function of x at $z = 0.536607$ in the $y = 0$ plane.

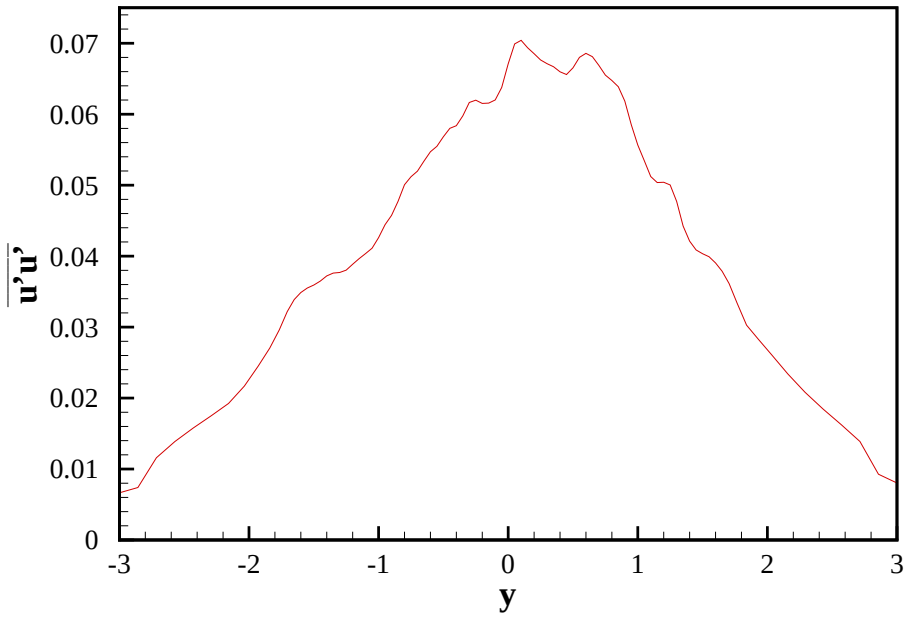

Figure 6.189: Variation of $\overline{u'u'}$ as a function of y at $z = 0.536607$ in the $x = 0$ plane.

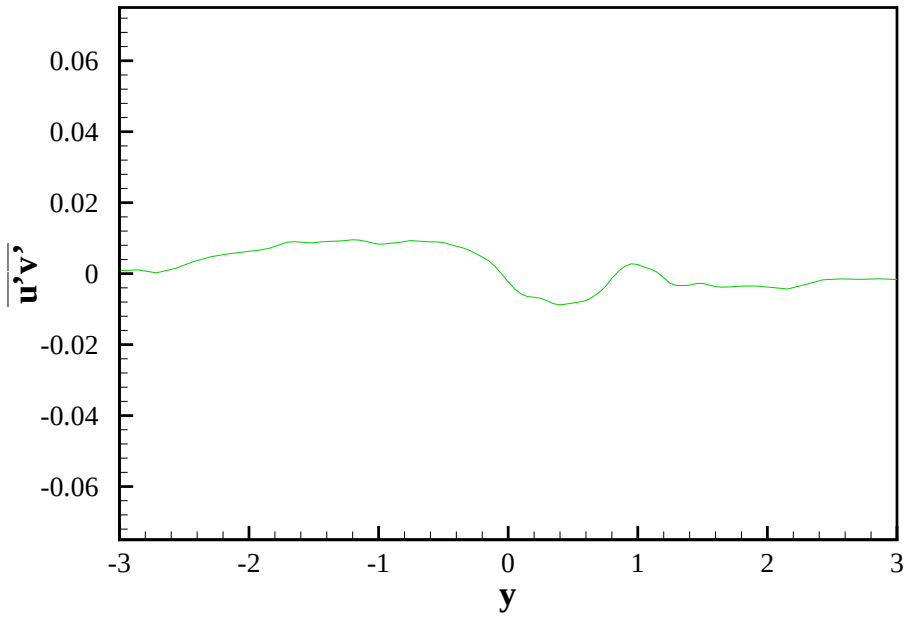

Figure 6.190: Variation of $\overline{u'v'}$ as a function of y at $z = 0.536607$ in the $y = 0$ plane.

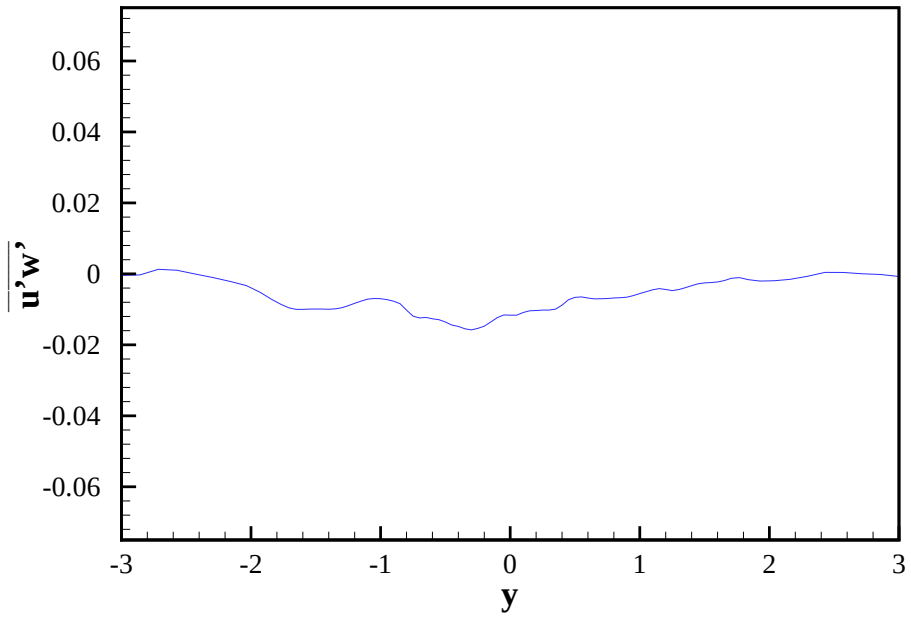

Figure 6.191: Variation of $\overline{u'w'}$ as a function of y at $z = 0.536607$ in the $x = 0$ plane.

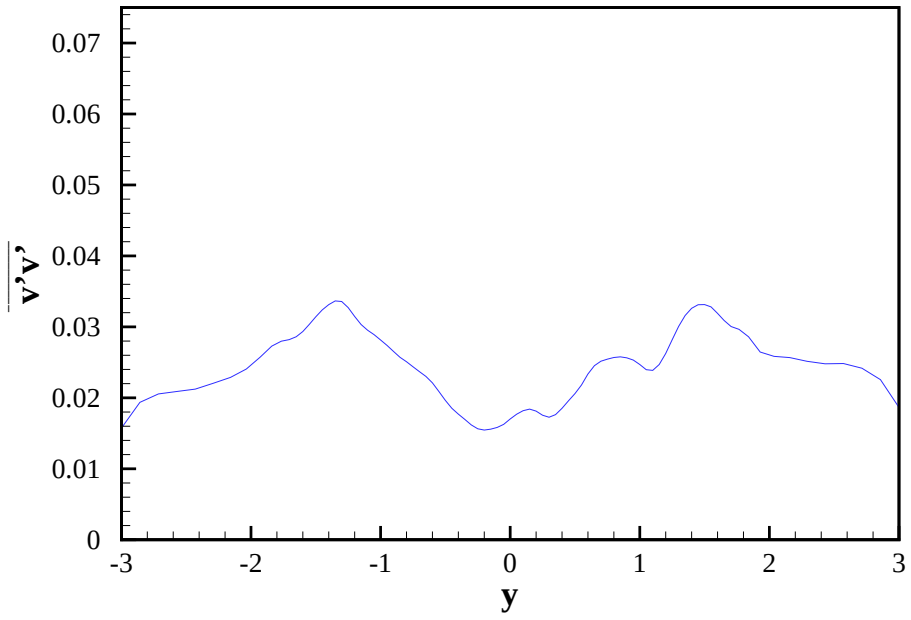

Figure 6.192: Variation of $\overline{v'v'}$ as a function of y at $z = 0.536607$ in the $x = 0$ plane.

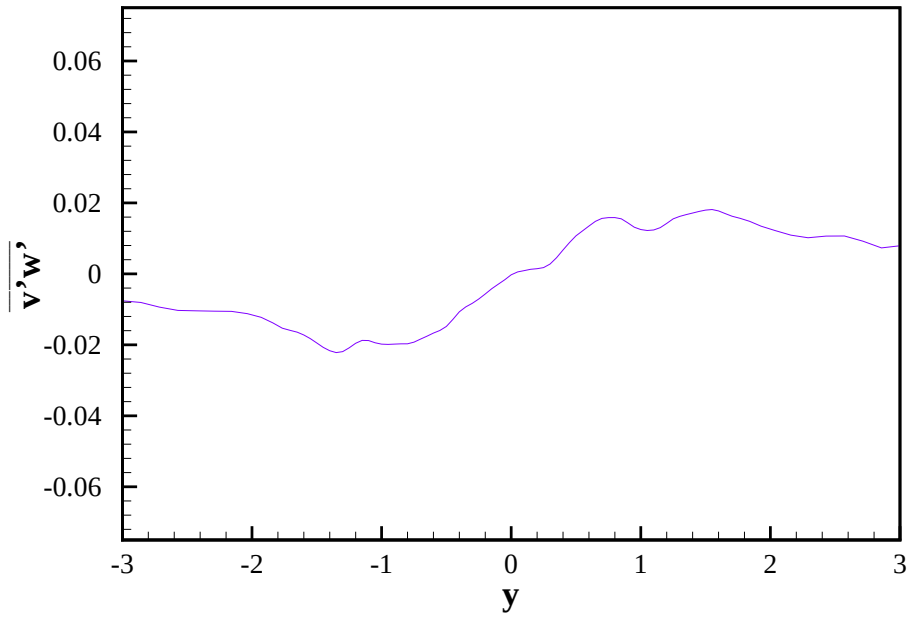

Figure 6.193: Variation of $\overline{v'w'}$ as a function of y at $z = 0.536607$ in the $x = 0$ plane.

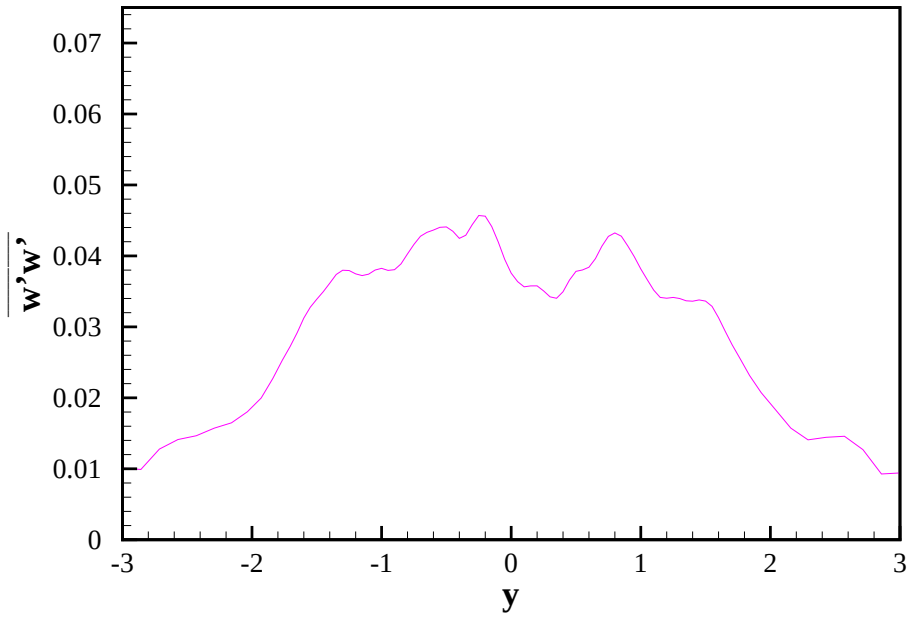

Figure 6.194: Variation of $\overline{w'w'}$ as a function of y at $z = 0.536607$ in the $x = 0$ plane.

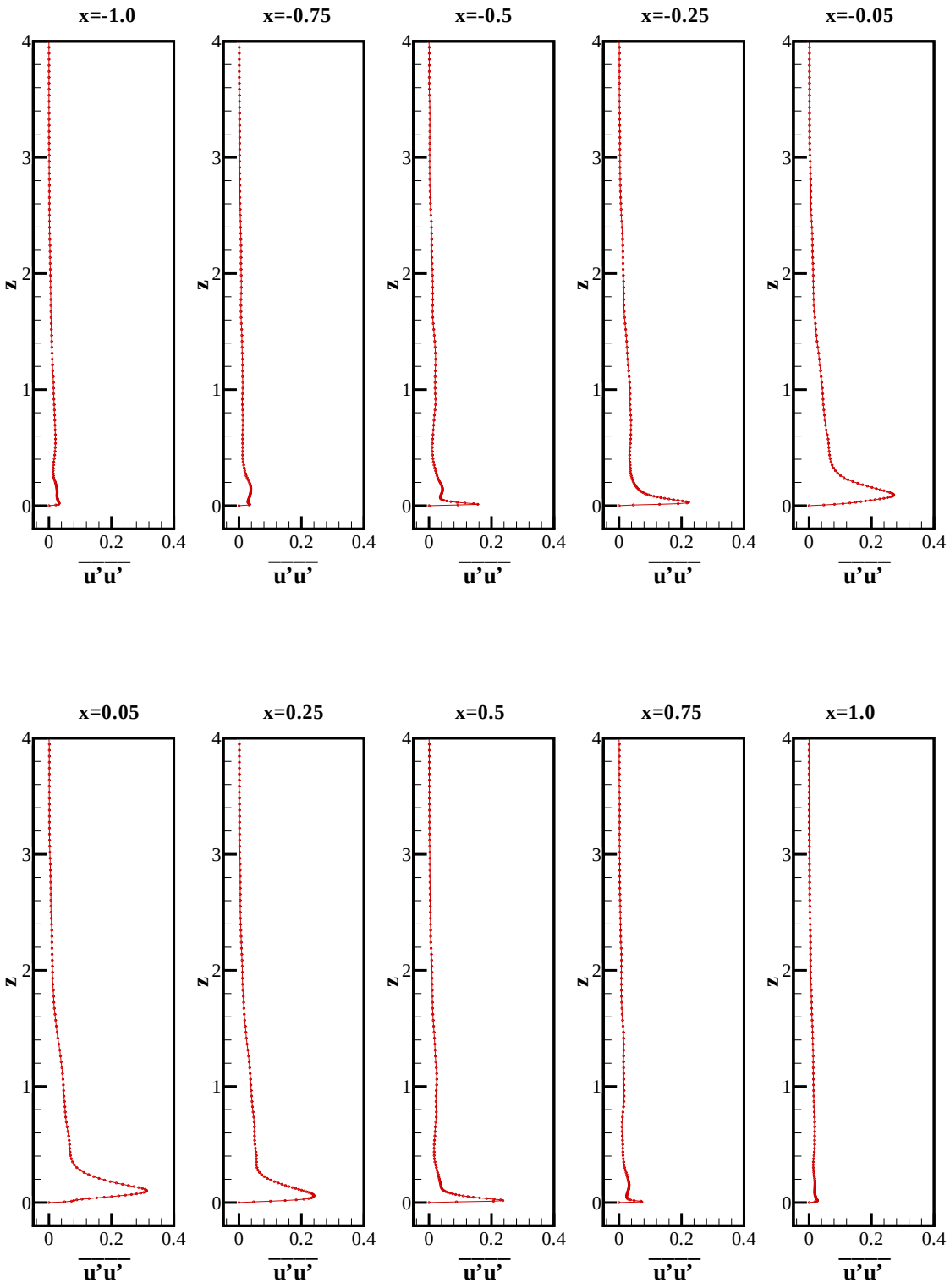

Figure 6.195: Variation of $\overline{u'u'}$ as a function of z at various x-locations between the jets in the $y = 0$ plane.

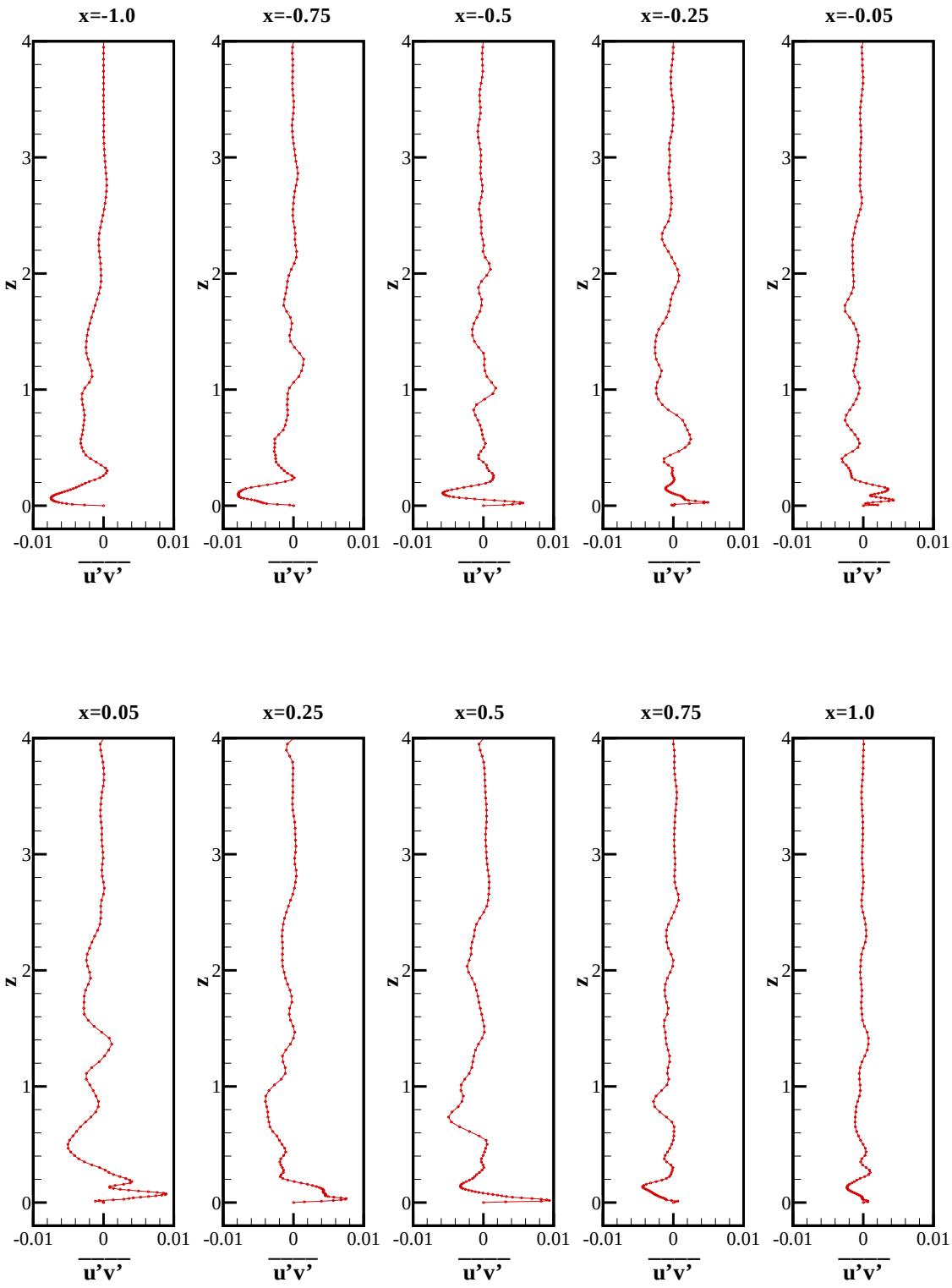

Figure 6.196: Variation of $\overline{u'v'}$ as a function of z at various x-locations between the jets in the $y = 0$ plane.

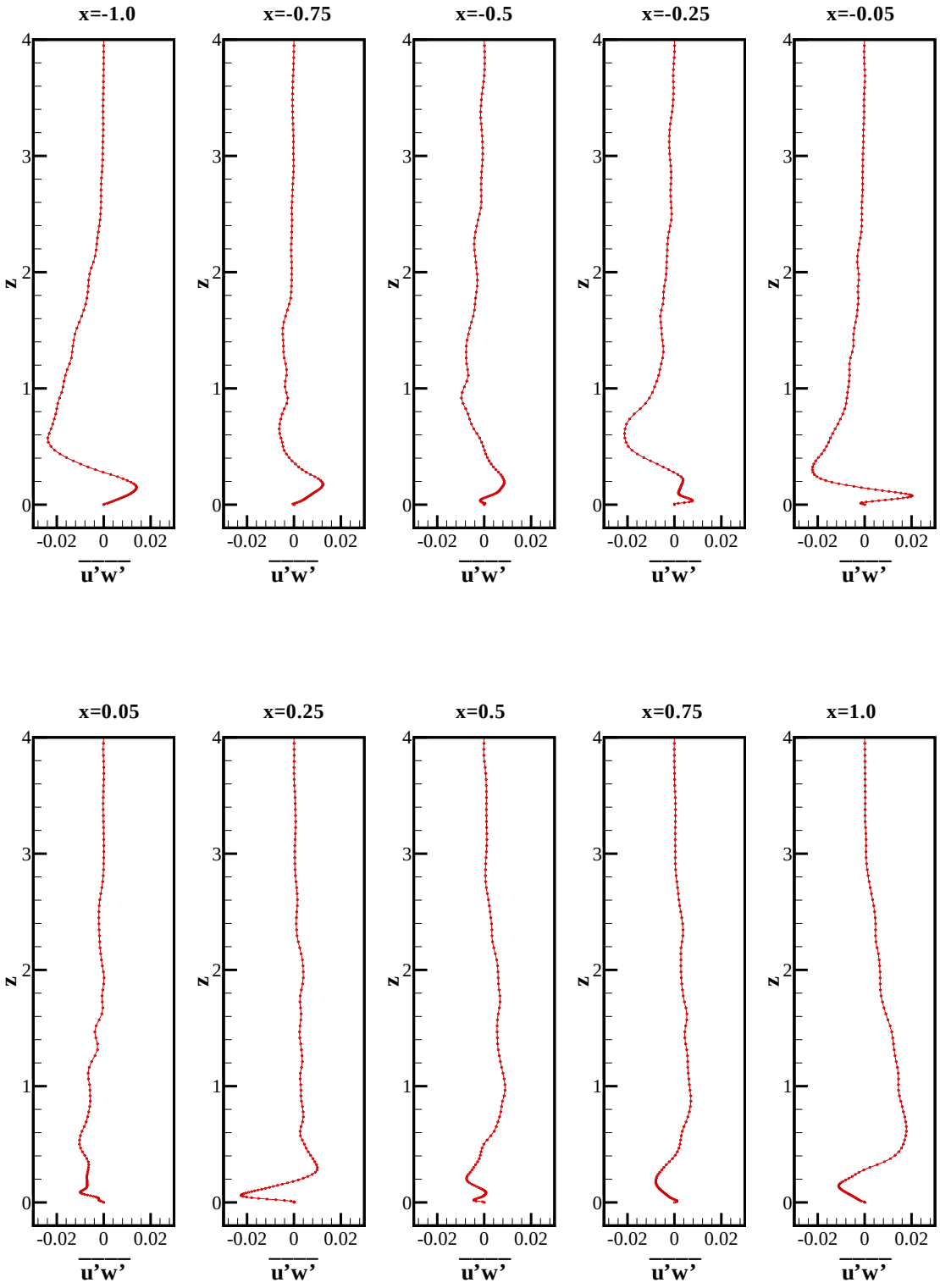

Figure 6.197: Variation of $\overline{u'w'}$ as a function of z at various x-locations between the jets in the $y = 0$ plane.

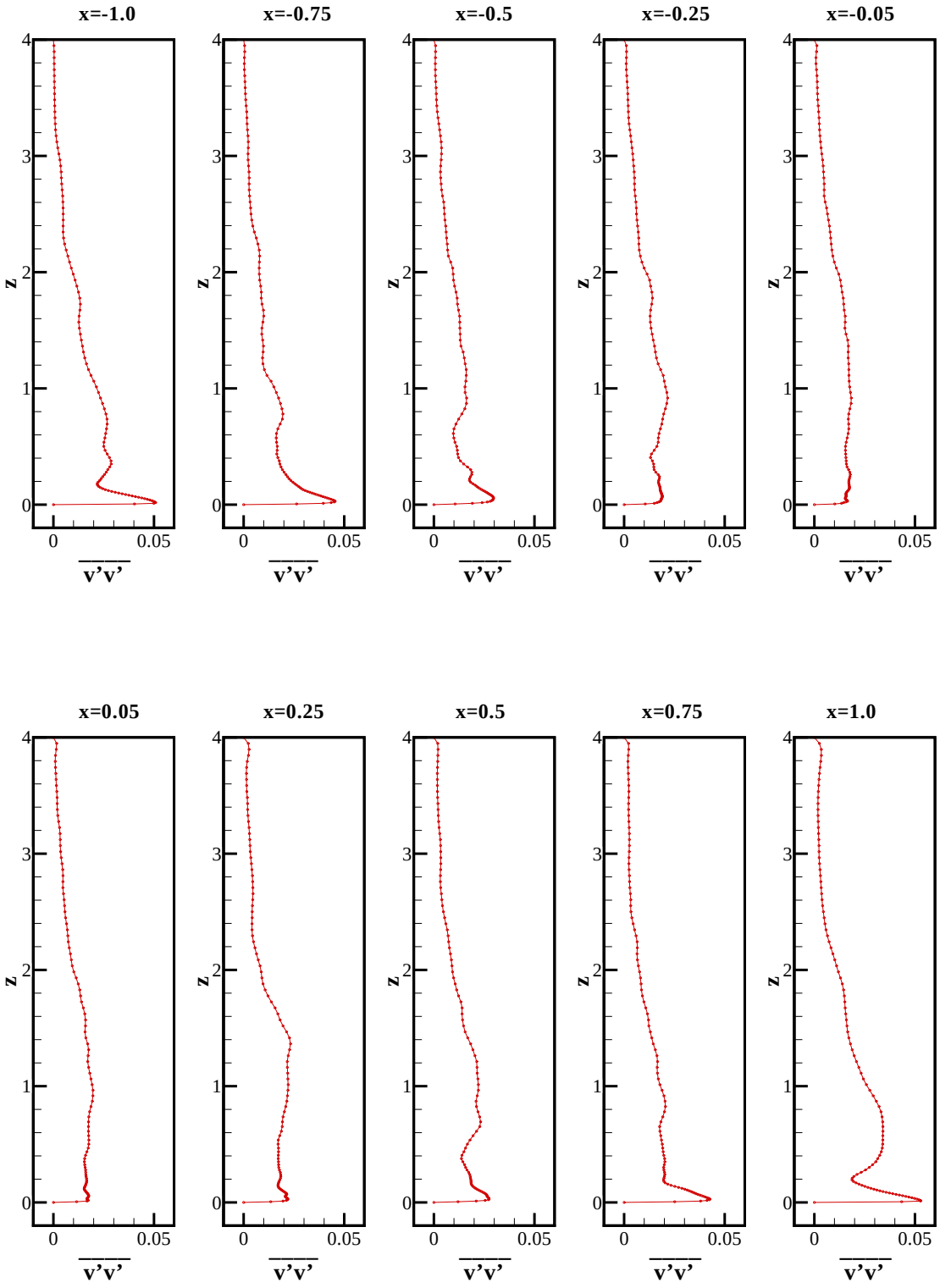

Figure 6.198: Variation of $\overline{v'v'}$ as a function of z at various x-locations between the jets in the $y = 0$ plane.

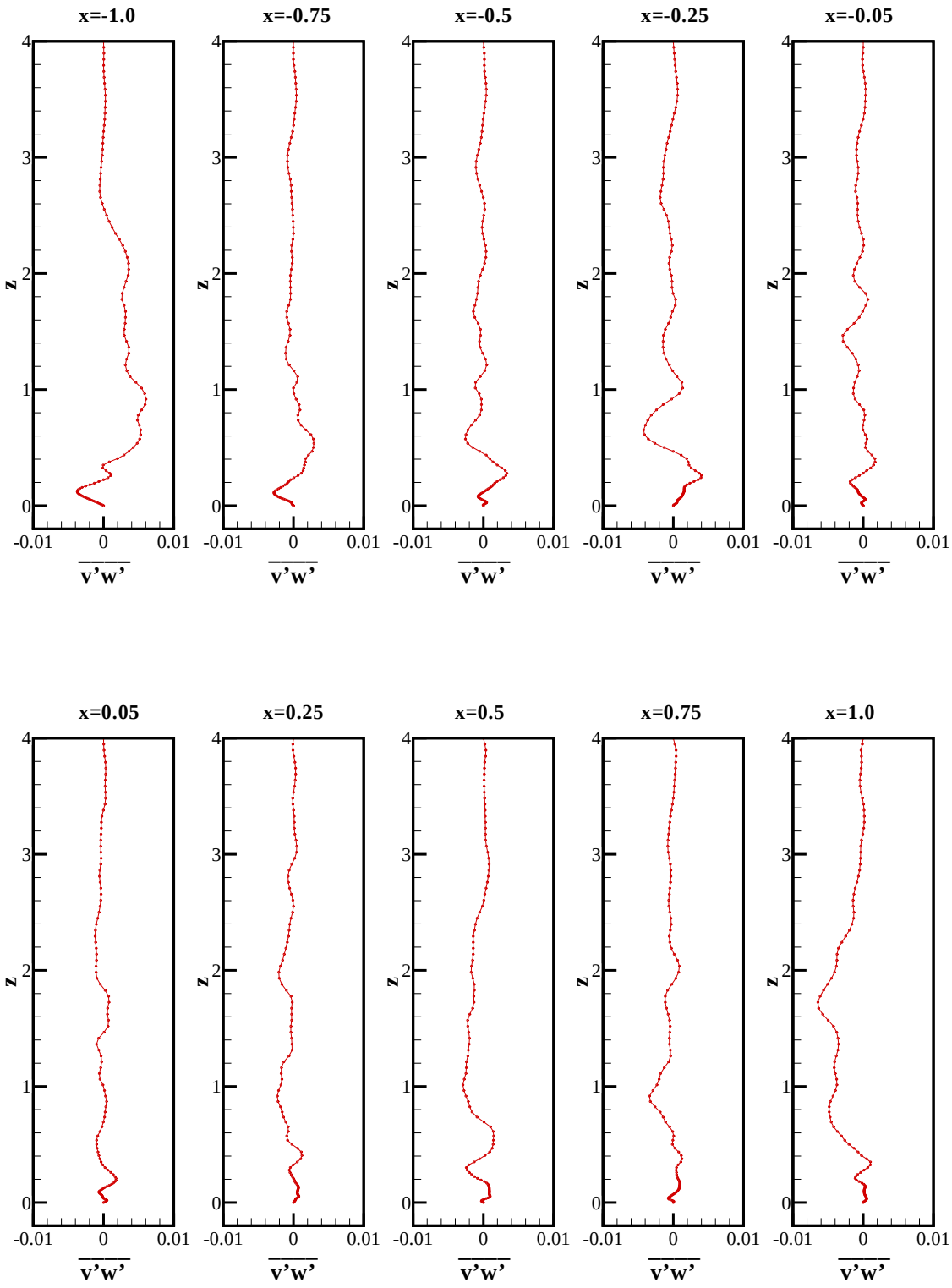

Figure 6.199: Variation of $\overline{v'w'}$ as a function of z at various x-locations between the jets in the $y = 0$ plane.

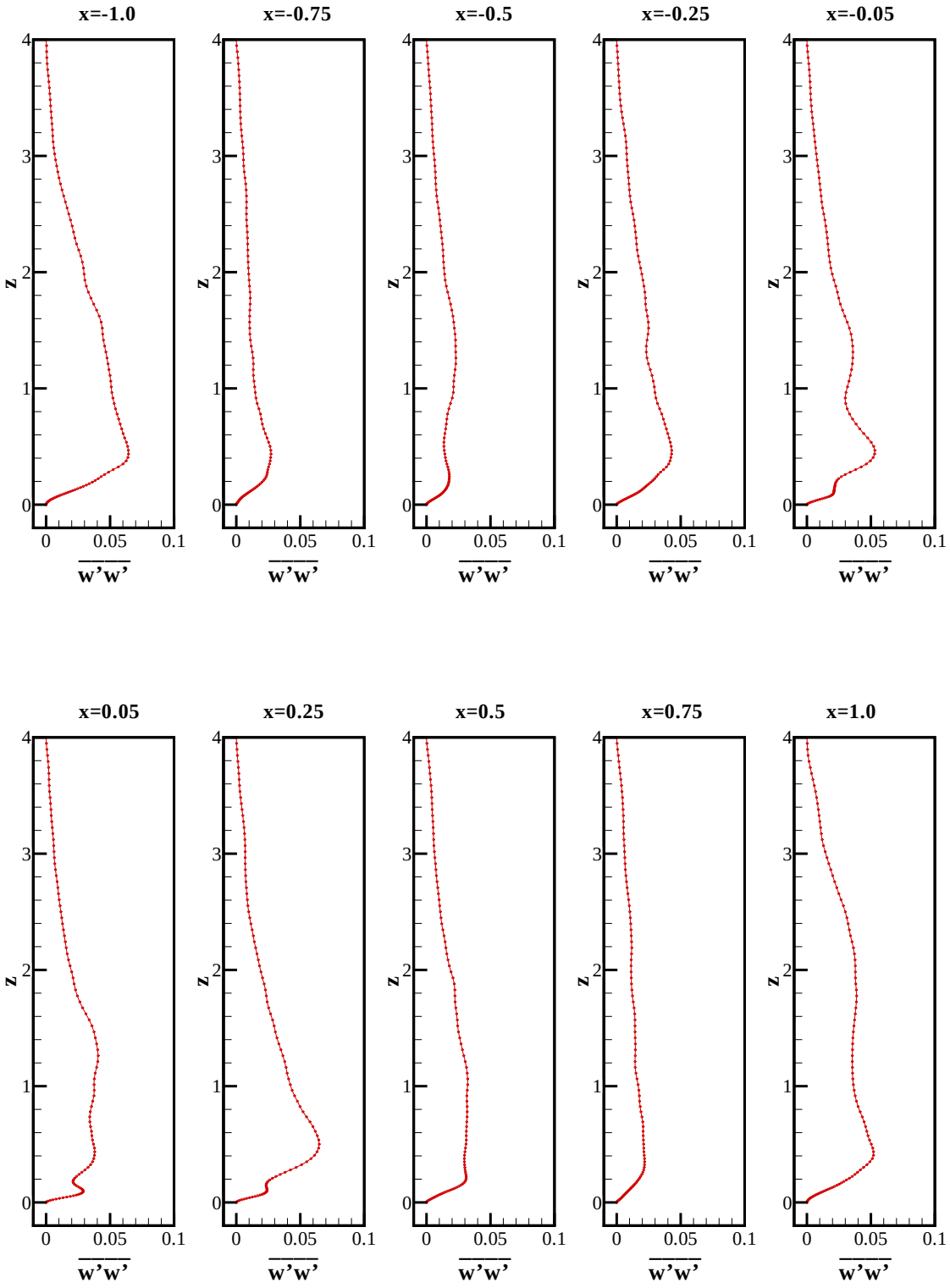

Figure 6.200: Variation of $\overline{w'w'}$ as a function of z at various x-locations between the jets in the $y = 0$ plane.

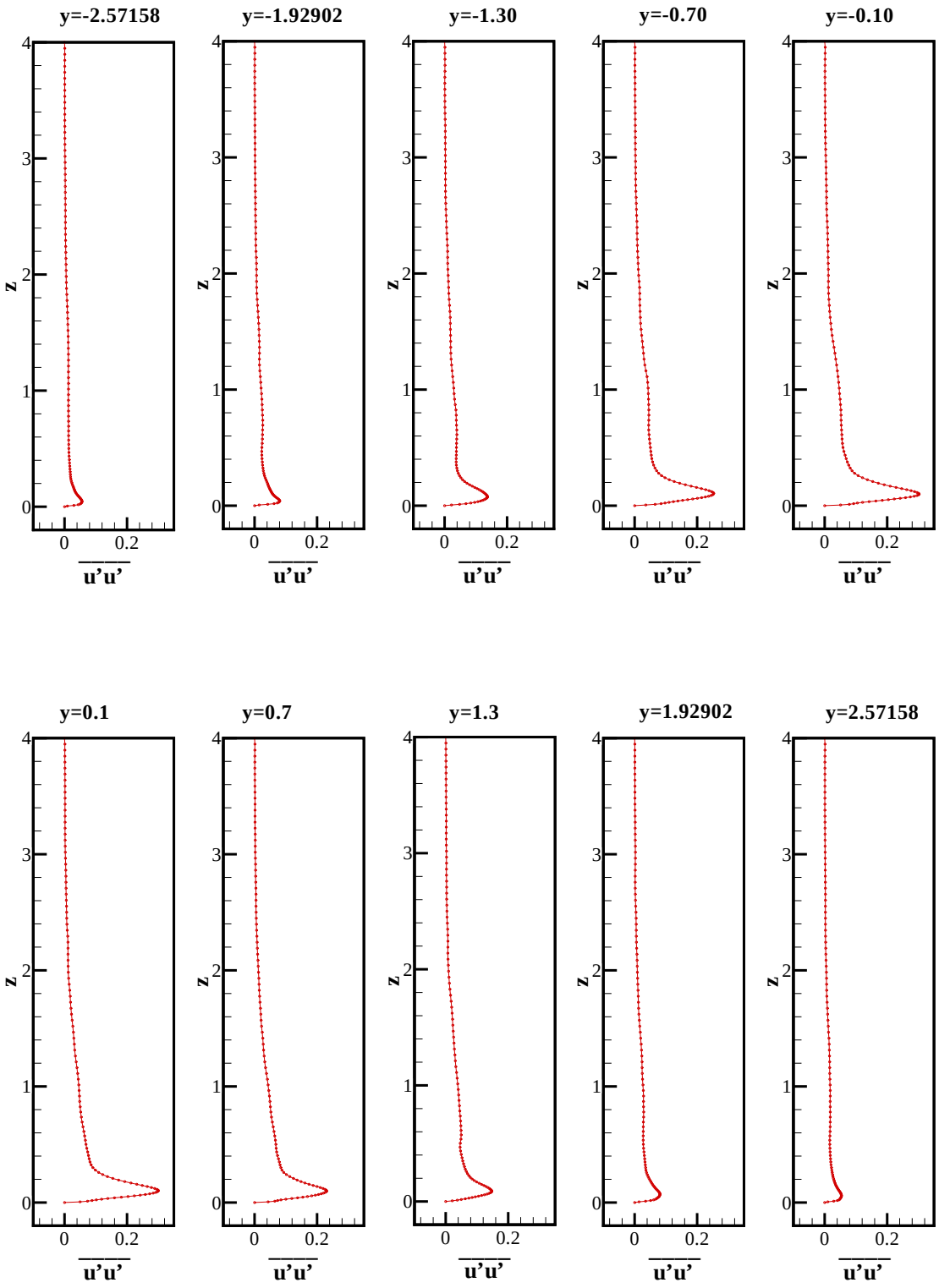

Figure 6.201: Variation of $\overline{u'u'}$ as a function of z at various y-locations in the $x = 0$ plane.

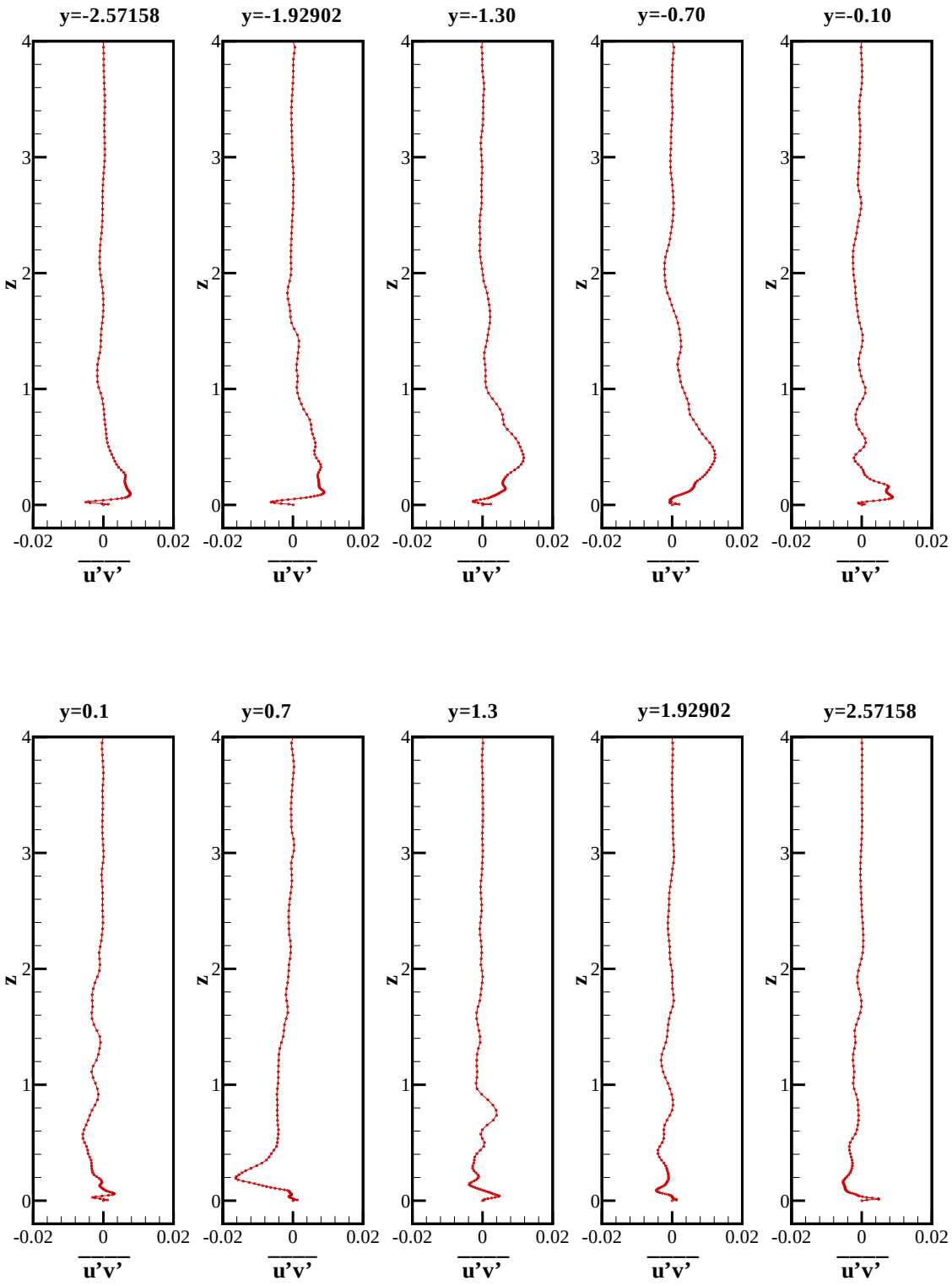

Figure 6.202: Variation of $\overline{u'v'}$ as a function of z at various y-locations in the $x = 0$ plane.

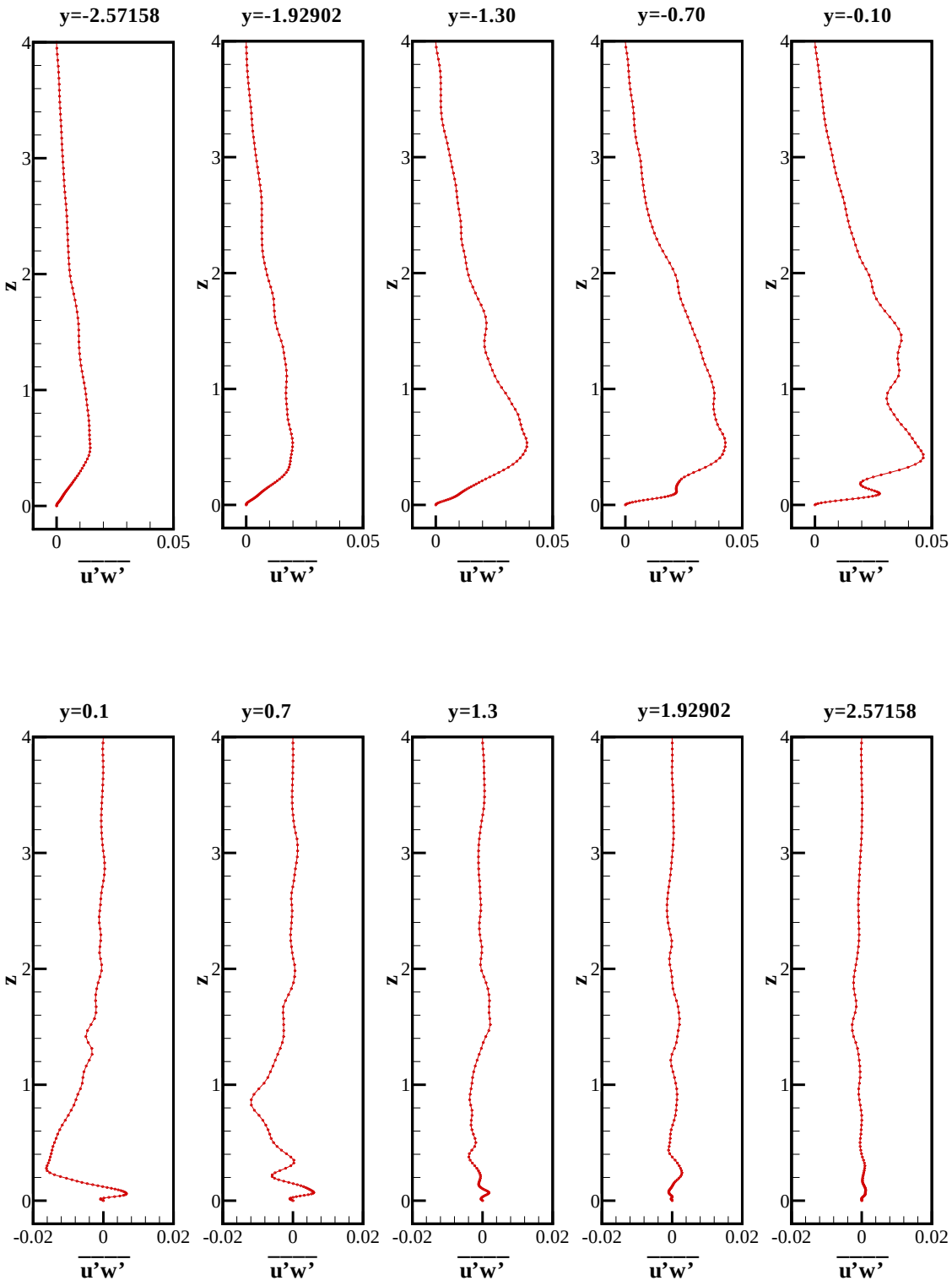

Figure 6.203: Variation of $\overline{u'w'}$ as a function of z at various y-locations in the $x = 0$ plane.

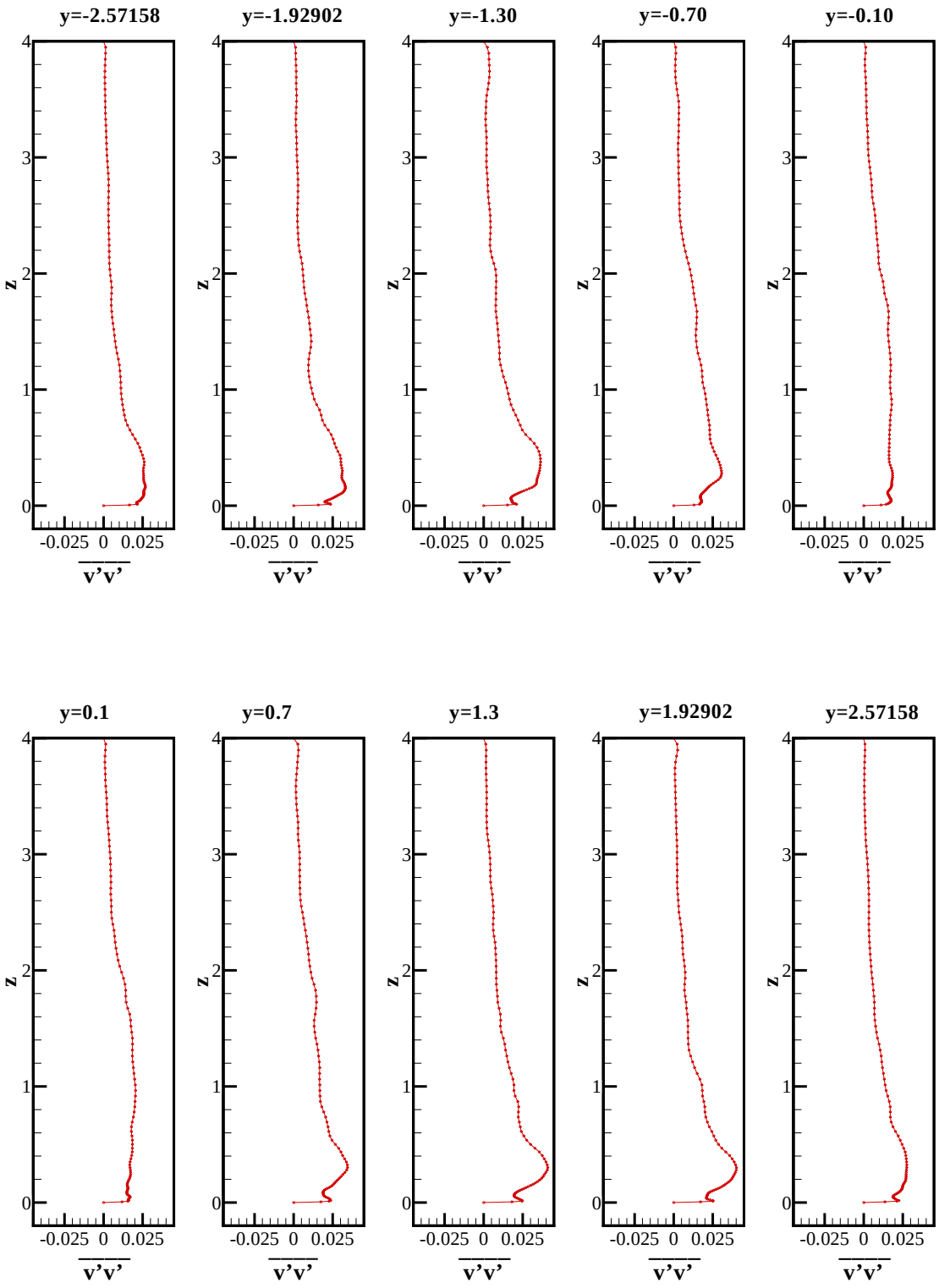

Figure 6.204: Variation of $\overline{v'v'}$ as a function of z at various y-locations between the jets in the $x = 0$ plane.

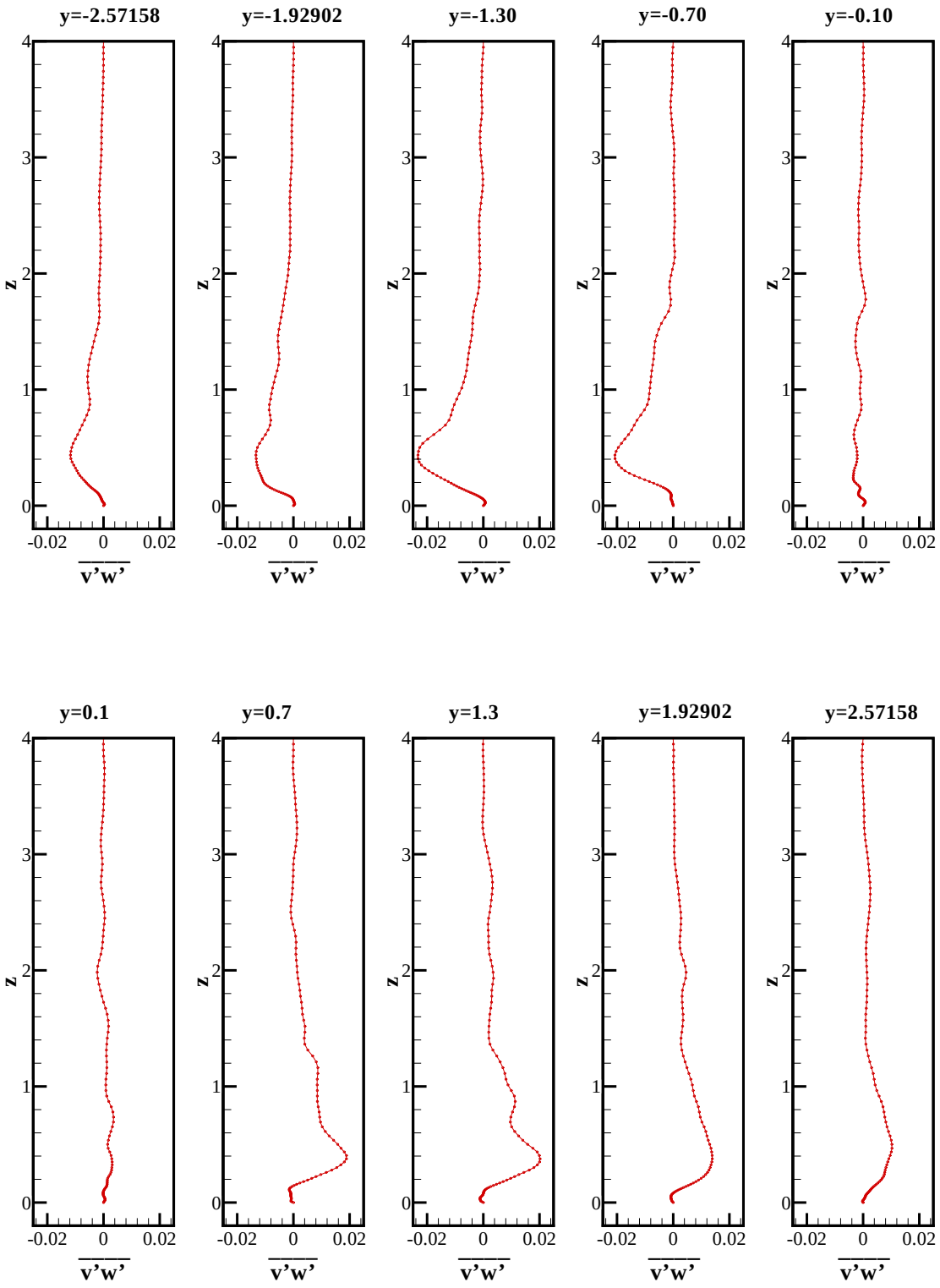

Figure 6.205: Variation of $\overline{v'w'}$ as a function of z at various y-locations between the jets in the $x = 0$ plane .

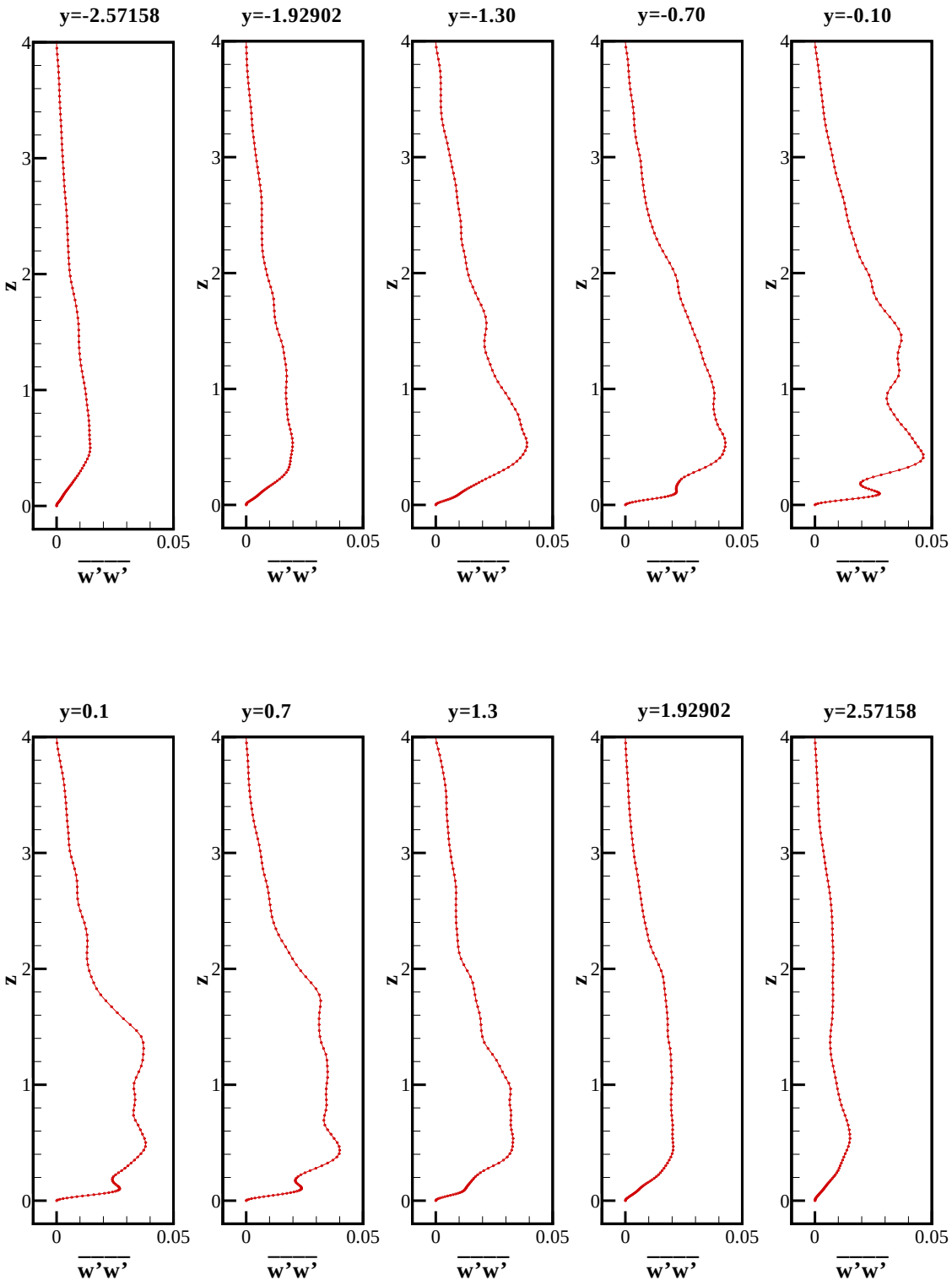

Figure 6.206: Variation of $\overline{w'w'}$ as a function of z at various y-locations between the jets in the $x = 0$ plane.

Chapter 7

CONCLUSIONS

A new LES code suitable for turbulent flow field with embedded shock waves has been developed. The code is based on the fifth order WENO scheme and a dynamic subgrid scale turbulence model. The new filtered dynamic subgrid-scale model proposed by Zhang and Chen[87] for incompressible flow model has been extended to the compressible flow model in the present study.

The main contribution of this dissertation is the large eddy simulation of a three-dimensional supersonic twin-jet impingement ($H^*/D^* = 4$, $S^*/D^* = 3$) at a Mach number of 1.5 and a Reynolds number of 5.5×10^5. The instantaneous flow field, the mean flow field and the Reynolds stresses from the simulation have been presented.

The computer code has been verified by two means. The first verification is done by comparing the numerical results for the simulation of a subsonic three-dimensional compressible turbulent round jet with published results. The second verification is done by comparing the results from the direct numerical simulations of flat-plate boundary layer instability with the results obtained from linear stability analysis.

The results from the simulation of twin-jet impingement show that the main influence of the fountain on the jets is its lateral interactions with the jets. It is found that the fountain flow diffuses very rapidly. This interaction enhances the turbulence production on the inner boundaries of the jets. As a result, the influence of the fountain on the top wall is very weak. The interaction between the fountain and the jets is significant only when $z \leq 3$. This result is in agreement with the experimental finding of Elavarasan and *et al.* [23], who showed that the fountain upwash induced by the interaction of the two jets has significance only when $H^*/D^* < 3$.

The simulation shows that the fountain does not have a dominant large-scale structure. However, a periodic flapping behavior is observed in the fountain. This flapping fountain is the vortical structure formed by the alternating merging of a primary vortex tube with a secondary vortex tube induced by the neighboring primary vortex tube in the collision

region. The period of flapping is found to be $7D^*/W_o^*$.

High unsteadiness and high spreading rate are also observed in the fountain. The presence of high unsteadiness in the fountain flow suggests that unsteadiness must be taken into account when modeling this kind of flow field. Therefore, large eddy simulation is an appropriate tool for the simulation of supersonic twin-jet impingement.

From the mean flow field, it is found that the mean peak velocity in the fountain flow is $0.40406W_o^*$ and it occurs at $z^* = 0.536607D^*$. This result is in a reasonable agreement with the experimental data of Elavarasan and *et al.* [23] who reported that the peak velocity in the fountain is $0.4261W_o^*$ and it occurs at about $0.7692D^*$ from the ground plane for values of H^*/D^* from 1 to 4. However, their mean flow was asymmetric for $H^*/D^* = 4$. These values are also comparable to those of incompressible twin-jet impingement as measured by El-Okda [21], who reported a fountain peak velocity of $0.45W_o^*$ at $z^* = 0.6D^*$.

The mean pressure coefficient on the top plane is found to be varied between -0.008 and -0.013, an indication that the top plane is experiencing a downward force due to flow entrainment into the jets.

Unsteady shock waves are observed at the impingement zones. The mean stand-off distance is found to be $0.4D^*$. The ability of the fifth order WENO scheme used in the present code to capture unsteady shock waves is an indication that WENO scheme is robust enough for simulation of turbulent flow with embedded shocks.

The maximum value of the Reynolds normal stresses, $\overline{u'u'}$, $\overline{v'v'}$ and $\overline{w'w'}$ in the fountain plane ($x = 0$ plane) are 0.3012, 0.0400 and 0.0470, respectively. The largest component of the Reynolds stress tensor is $\overline{u'u'}$. It is equal to 0.3078 and it occurs at (0.05, 0, 0.1), a point in the vicinity of the collision region at $0.1D^*$ above the ground.

Bibliography

[1] D. S. Balsara and C.-W. Shu. Monotonicity preserving weighted essentially non-oscillatory schemes with increasingly high order of accuracy. *Journal of Computational Physcis*, 160(2):405–452, 2000.

[2] J.M.M. Barata, D. F. G. Durao, M. V. Heitor, and J. J. McGuirk. Impingement of single and twin turbulent jets through a cross flow. *AIAA Journal*, 29(4):595–602, 1991.

[3] J. Bardina. Turbulence modelling based on direct simulation of the navier-stokes equations. In *Proceedings of AIAA/ASME/SIAM/APS 1st National Fluid Dynamics Congress*, pages 539–546, Cincinnnati, OH, 25-28 July 1988.

[4] P. Behrouzi. Numerical studies of twin-jet impingement for stovl flow application. *Journal of the Chinese Institute of Engineers*, 23(6):669–676, 2000.

[5] Bendiks J. Boersma and Sanjiva K. Lele. Large eddy simulation of a mach 0.9 turbulent jet. In *AIAA Paper No. 99-1874, 5th AIAA/CEAS Aeroacoustics Conference*, Bellevue(Greater Seattle), WA, 10-12 May 1999.

[6] W. Bower, K. Saripalli, and R. Agarwal. A summary of jet-impingement studies at McDonnell Douglas Research Labs. In *AIAA-81-2613,AIAA 38th Aerospace Sciences Meeting and Exhibit*, Palo Alto, CA, December 1981.

[7] W. W. Bower. Viscous flowfields induced by three-dimensional lift jets in ground effect. Report mdc-q0769; AD-A121026, McDonnell-Douglas Research Labs, Saint Louis, MO, Jan 1982.

[8] W. W. Bower, R. K. Agarwal, G. R. Peters, and D. R. Kotansky. Viscous flowfields induced by two- and three-dimensional lift jets in ground effect. Report onr-cr215-246-3f, McDonnell-Douglas Research Labs, Saint Louis, MO, March 1979.

[9] M. H. Carpenter and C. A. Kennedy. Fourth-order, 2n-storage runge-kutta schemes. NASA TM 109112, ICASE, NASA Langley Research Center, 1994.

[10] K. Chien. Predictions of channel and boundary layer flows with a low Reynolds number turbulence model. *AIAA Journal*, 20(1):33–38, 1982.

[11] E. P. Childs and B. Patel. Turbulence model performance in V/STOL flow field simulation. In *AIAA Paper No. 90-2248,AIAA/SAE/ASME/ASEE 26th joint Propulsion conference*, Orlando, FL, July 1990.

[12] R. E. Childs. Turbulence modeling for complex ground effects flows. In *SAE Paper 901062, SAE, Aerospace Atlantic Meeting*, Dayton, OH, April 1990.

[13] R. E. Childs. Calculation of impinging jet flows with Reynolds-stress models. In *AIAA Paper No. 91-0754,AIAA 29th Aerospace Sciences Meeting*, Reno, NV, January 1991.

[14] R. E. Childs and S.C. Caruso. Assesment of modeling and discretization accuracy for high speed afterbody flows. In *AIAA Paper No. 89-0531,AIAA 29th Aerospace Sciences Meeting*, January 1989.

[15] R.E. Childs and D. Nixon. Simulation of impinging turbulent jets. In *AIAA-85-0047, AIAA 23rd Aerospace Sciences Meeting*, Reno, Nevada, January 1985.

[16] R.E. Childs and D. Nixon. Unsteady three-dimensional simulation of a VTOL upwash fountain. In *AIAA Paper No. 86-0212, AIAA 24th Aerospace Sciences Meeting*, Reno, Nevada, January 1986.

[17] S. H. Cho and S. O. Park. Steady and unsteady computation of a two-dimensional upwash jet. *International Journal for Numerical Methods for Heat and Fluid Flow*, 8(1):64–82, 1998.

[18] S.-H. Chuang and T.-J. Nieh. Numerical simulation and analysis of three-dimensional turbulent impinging square twin-jet flow field with no-crossflow. *International Journal for Numerical Methods in Fluids*, 33:475–498, 2000.

[19] M. K. Chung, S.W. Park, and K. C. Kim. Curvature effects on third-order velocity correlations and its model representaton. *Physics of Fluids*, 30(3):626–628, March 1987.

[20] B. J. Daly and F. H. Harlow. Transport equation of turbulence. *Physics of Fluids*, 13:2634–2649, 1970.

[21] Y. M. El-Okda. Jet/wall interaction: An experimental study with applications to VS-TOL aircraft ground effects. M.S. thesis, Virginia Polytechnic Institute and State University, 2002.

[22] B. E.Launder and D. B. Spalding. *Mathematical Models of Turbulence*. Academic Press, 1972.

[23] R. Elavarasan, L. Venkatakrishnan, A. Krothapalli, and L. Lourenco. Supersonic twin impinging jets. In *AIAA Paper No. 2000-0812,AIAA, 38th Aerospace Sciences Meeting and Exhibit*, Reno, NV, Jan. 10-13 2000.

[24] H. Elbana and J.A. Sabbagh. Flow visualization and measurements in a two-dimensional two-impinging-jet flow. *AIAA Journal*, 27(4):420–426, April 1989.

[25] William H. Foley. Fountain-jet turbulence. Report no. AD-A098098;, General Dynamics Corporation, Fort Worth Division., 1981.

[26] M. Germano. Turbulence : the filtering approach. *Journal of Fluid Mechanics*, 9(12):3932–3934, 1992.

[27] Massimo Germano, Ugo Piomelli, Parviz Moin, and William H. Cabot. A dynamic subgrid-scale eddy viscosity model. *Physics of Fluids*, 3(7):1760–1765, 1991.

[28] M. M. Gibson and B. E. Launder. Ground effects on pressure fluctuations in the atmospheric boundary layer. *Journal of Fluid Mechanics*, 86(Part 3):491–511, 1978.

[29] M. M. Gibson and B. A. Younis. Calculation of swirling jets with a Reynolds stress closure. *Physics of Fluids*, 29(1):36–48, 1986.

[30] B. L. Gilbert. An investigation of turbulence mechanisms in V/STOL upwash flow fields. Report No. AD-A181265; RE-730;AFOSR-87-0603TR, Grumman Aerospace Corp., Bethpage, N.Y., Mar. 1987.

[31] B. L. Gilbert. Turbulence measurements in a two-dimensional upwash. *AIAA Journal*, 26(1):10–14, 1988.

[32] K. Hanjalic and B. E. Launder. A reynolds stress model of turbulence and its application to thin shear flows. *Journal of Fluid Mechanics*, 52:609–638, 1972.

[33] T. M. Houlihan and C. D. Thompson. Jet impingement under VSTOL aircraft. *AIAA Journal*, 10(9):1179–1182, 1972.

[34] G. Jiang and C.-W. Shu. Efficient implementatiion of weighted WENO shemes. *Journal of Computational Physcis*, 126(1):202–228, 1996.

[35] G. Jiang and C.-C. Wu. A high-order weno finite difference shemes for the equations of ideal magnetohydrodynamics. *Journal of Computational Physcis*, 150(2):561–594, 1999.

[36] M. Kato and B. E. Launder. The modelling of turbulent flow around stationary and vibrating square cylinders. In *Proceedings of Ninth Symposium Turbulent Shear Flow*, pages 16–18, Kyoto, August 1993.

[37] R.E. Kuhn. Ground effects on V/STOL and STOL aircraft–a survey. In *AIAA Paper No. 85-4033, AIAA/AHS/ASEE Aircraft Design Systems and Operations Meeting*, Colorado Springs, CO, October 1985.

[38] J. A. Ladd and T. Korakianitis. On the assessment of one- and two-equation turbulence models for the computation of impinging jet flowfields. In *AIAA Paper No. 96-2545,,2nd AIAA,ASME,SAE,and ASEE Joint Propulsion conference and Exhibit*, Lake Buena Vista, FL, July 1996.

[39] B. E. Launder, G. J. Reece, and W. Rodi. Progress in the development of a Reynolds stress turbulence closure. *Journal of Fluid Mechanics*, 68:537–566, 1975.

[40] M.A. Leschziner and W. Rodi. Calculation of annular and twin parallel jets using various discretization schemes and turbulence-model variations. *Journal of Fluid Engineering*, 103:352–355, 1981.

[41] M. Lesieur. *Turbulence in Fluids*. Kluwer Academic Publishers, third revised and enlarged edition edition, 1997.

[42] R. J. Leveque. *Numerical Methods for Conservation Laws*. Birkhäuser Verlag, Boston, 1992.

[43] D. K. Lilly. A proposed modification of the germano subgrid-scale closure method. *Physics of Fluids*, 4(3):633–635, 1992.

[44] X.-D. Liu, S. Osher, and T. Chan. Weighted essentially non-oscillatory schemes. *Journal of Computational Physcis*, 115(1):200–212, 1994.

[45] R. W. MacCormack. A numerical method for solving the equation of compressible flow. In *AIAA Paper No. 81-0110, 19th Aerospace Sciences Meeting*, St Louis, MO, Jan 1981.

[46] Mujeb R. Malik and Steven A. Orszag. Linear stability analysis of three-dimensional compresible boundary layers. *Journal of Scientific Computing*, 2(1):77–97, 1987.

[47] M. P. Martín, U. Piomelli, and G. V. Candler. Subgrid-scale models for compressible large-eddy simulations. *Theoretical and Computational Fluid Dynamics*, 13:361–376, 2000.

[48] M. Meinke and E. Krause. Application of LES to jets and internal turbulent flows. In R. Peyret adn E. Krause, editor, *Advanced Turbulent Flow Computations*, pages 155–208. SpringerWien New York, 2000.

[49] G. L. Mellor and H. J. Herring. A survey of mean turbulent field closure. *AIAA Journal*, 11:590–599, 1973.

[50] F. R. Menter. Zonal two-equation k-ω turbulence models for aerodynamics flows. In *AIAA Paper No. 93-2906*, 1993.

[51] C. M. Milford. Hot gas recirculation inV/STOL. In *SAE Paper 872306*, 1987.

[52] P. Moin, K. Squires, W. Cabot, and S. Lee. Dynamic subgrid-scale model for compressible turbulence and scalar transport. *Physics of Fluids*, 3(11):2746–2757, 1991.

[53] S.W. Park and M. K. Chung. Curvature dependent two-equation model for prediciton of turbulent recirculating flows. *AIAA Journal*, 27(3):340–344, March 1989.

[54] S. V. Patankar. *Numerical Heat Transfer and Fluid Flow*. Hemispher/McGraw-Hill, New York, 1980.

[55] W. J. Pegues and S.P. Vanka. Numerical study of twin-jet impingement upwash flow. *American Society of Mechanical Engineers, Fluids Engineering Division(Publication) FED*, 94:97–103, 1990.

[56] S. A. Ragab and S. Sheen. Large eddy simulation of mixing layers. In B. Galprin and S. Orszag, editors, *Large Eddy Simulation of Complex Engineering and Geophysical Flows*, pages 255–285. Cambridge University Press, 1993.

[57] S. A. Ragab, S. Sheen, and M. Sreedhar. An investigation of finite-difference methods for large-eddy simulation. In *AIAA Paper No. 92-0554*, 1992.

[58] Saad A. Ragab. Numerical simulation of turbulence. In Joseph A. Schetz and Allen E. Fuhs, editors, *Handbook of Fluid Dynamics and Fluid Machinery (Volume 2)*, pages 1506–1527. John Wiley & Sons, Incorporated, 1996.

[59] M. H. Rizk and S. Menon. Large-eddy simulations of excitation effects on a vtol upwash fountain. *Physics of Fluids*, 1(4):732–740, April 1989.

[60] D. W. Roberts and S. T. Imlay. Comparison of turbulence models for powered-lift flow fields. In *AIAA Paper No. 92-3674, AIAA/SAE/ASME/ASEE 28th Joint Propulsion Conference and Exhibit*, Nashville, TN, July 1992.

[61] W. Rodi. A new algebraic relation for calculating the reynolds stresses. *Z. Angew. Math. und Mech.*, 56:219–221, 1976.

[62] P. Sagaut and T. H. Lê. LES-DNS : The aeronautical and defence point of view. In O. Métas and Joe Ferziger, editors, *New Tools in Turbulence Modelling*, pages 183–197. Springer-Verlag, 1997.

[63] K.R. Saripalli. Visualization studies of jet impingement flows at McDonnell Douglas Research Laboratories. In *Flow Visualization III, proceedings of the Third International Symposium on Flow Visualization*, pages 503–509, Ann Arbor, MI, 1983.

[64] K.R. Saripalli. Laser-doppler velocimeter measurements in 3D impingement twin-jet fountain flows. In *AIAA/AHS/ASEE Aircraft Design Systems and Operations Meeting*, Colorado Springs, CO, October 1985.

[65] K.R. Saripalli, J. D. Flood, and G. M. Moss. Inlet hot gas ingestion(HGI) and its control in V/STOL aircraft. In *SAE Paper 975517*, 1997.

[66] S. Sarkar and C. G. Speziale. A simple nonlinear model for the return to isotropy in turbulence. *Physics of Fluids*, 2(1):84–93, 1990.

[67] William E. Schiesser. *The Numerical Method of Lines : Integration of Partial Differential Equations*. Academic Press, Incorporated, 1991.

[68] C.-W. Shu. Essentially non-oscillatory and weighted essentially non-oscillatory schemes for hyperbolic conservation laws. In A. Quarteroni, editor, *Advanced Numerical Approximation of Nonlinear Hyperbolic Equations*, volume 1697 of *Lecture Notes in Mathematics*, pages 325–432. Springer-Verlag, 1998.

[69] C.-W. Shu. High order ENO and WENO schemes for computational fluid dynamics. In T. J. Barth and H. Deconinck, editors, *High-Order Methods for Computational Physics*, Lecture Notes in Computational Science and Engineering, pages 439–582. Springer-Verlag, 1999.

[70] C.-W. Shu. High order finite difference and finite volume weno schemes and discontinuous galerkin methods for cfd. ICASE Report No. 2001-11, ICASE,NASA Langley Research Center, Hampton, VA, 2001.

[71] R. Siegel and M. E. Goldstein. Two dimensional inviscid jet flow from two nozzles at angel to a plane surface. NASA TN D-5064, NASA Lewis Research Center, Cleveland, OH, Oct. 1968.

[72] R. Siegel and M. E. Goldstein. Analysis of two dimensional inviscid model of jet impingement under vertical-takeoff airplane. NASA TN D-5288, NASA Lewis Research Center, Cleveland, OH, March 1969.

[73] J. Smagorinsky. General circulation experiments with the primitive equations. I. The basic experiment. *Monthly Weather Review*, 91(3):99–163, 1963.

[74] P. R. Spalart and S. R. Allmaras. A one-equation turbulence model for aerodynamics flows. In *AIAA Paper No. 92-0439*, 1992.

[75] D. B. Spalding. A single formula for the 'Law of Wall'. *Journal of Applied Mechanics*, 28:455–458, Sept. 1961.

[76] D. B. Spalding. A novel finite-defference formulation for differential expressions involving first and second derivatives. *International Journal for Numerical Methods in Engineering*, 4:551–559, March 1972.

[77] C. G. Speziale, S. Sarkar, and T. B. Gatski. Modelling of the pressure-strain correlation of turbulence: An invariant dynamical system approach. *Journal of Fluid Mechanics*, 227:245–272, 1991.

[78] D. K. Tafti and S. P. Vanka. Hot gas environment around STOVL aircraft in ground proximity-Part2: Numerical study. *Journal of Aircraft*, 29(1):20–27, Jan.-Feb. 1992.

[79] G. Tang, Z.Yang, G. J. page, and J. J. McGuirk. Simulation of an impinging jet in crossflow using an LES method. In *AIAA Paper No. 2002-5959, 2002 International Powered Lift Conference and Exhibit(IPLC)*, Williamsburg, VA, Nov 2002.

[80] T. J. VanOverbeke and J. D. Holdeman. A numerical study of the hot gas environment around a STOVL aircraft in ground proximity. In *AIAA Paper No. 88-2882, AIAA/ASME/SAE/ASEE 24th Joint Propulsion Conference*, Boston, MA, 1988.

[81] Frank M. White. *Viscous Fluid Flow*. McGraw-Hill, 2nd. edition, 1991.

[82] David C. Wilcox. *Turbulence Modeling for CFD*. DCW Industries, Inc., first edition, 1993.

[83] J. Williamson. Low storage runge-kutta schemes. *Journal of Computational Physcis*, 35:48–56, 1980.

[84] R. V. Wilson, A.O. Demuren, and M. Carpenter. Higher-order compact schemes for numerical simulation of incompressible flows. ICASE Report No. 98-13, ICASE,NASA Langley Research Center, Hampton, VA, 1998.

[85] S. Xu, Tariq Aslam, and D. S. Stewart. High resolution numerical simulation of ideal and non-ideal compressible reacting flows with embedded internal boundaries. *Combustion Theory Modelling*, 1:113–142, 1997.

[86] V. Yakhot, S.A. Orszag, S. Thangam, T.B. Gatski, and C. G. Speziale. Developement of turbulence models for shear flows by a double expansion technique. *Physics of Fluids*, 4:1510–1520, 1992.

[87] Wei Zhang and Qingyan Chen. A new filtered dynamic subgrid-scale model for large eddy simulation of indoor airflow. In *Proceedings of Building Simulation '99*, Kyoto, Japan, 1999.

[88] Wei Zhang and Qingyan Chen. Large-eddy simulation of indoor airflow with a filtered dynamic subgrid scale model. *International Journal of Heat and Mass Transfer*, 43(17):3219–3231, 2000.

[89] Wei Zhang and Qingyan Chen. Large eddy simulation of natural and mixed convection airflow indoors with two simple filtered dynamic subgrid scale models. *Numerical Heat Transfer, Part A : Applications*, 37(5):447–463, 2000.

Vita

Hoong Thiam Toh comes from a Chinese family in Malaysia. He completed his primary, secondary and pre-university education in Malaysia, and his tertiary education in Singapore. After receiving his B. Eng. degree in Mechanical Engineering from National University of Singapore, he worked as a mechanical engineer in a construction company and enrolled in a part-time master's degree program at Nanyang Technological University, Singapore. Upon receiving his Master of Science degree in Mechanics and Processing of Materials from Nanyang Technological University, he came to the United States in August 1995 to pursue his Master of Science degree in Aerospace Engineering at Mississippi State University. He began his PhD. program in Engineering Mechanics in the Department of Engineering Science and Mechanics at Virginia Tech in Fall 1998. He will return to Malaysia after completing his PhD. program.